Universität Augsburg
Institut für Physik

Plane-wave approach to the Casimir interaction between colloid particles

Dissertation

zur Erlangung des akademischen Grades
Dr. rer. nat.

eingereicht an der
Mathematisch-Naturwissenschaftlich-Technischen Fakultät
der Universität Augsburg

von

Benjamin Spreng

Augsburg, 18. September 2020

Erstgutachter:	Prof. Dr. Gert-Ludwig Ingold
Zweitgutachter:	Prof. Dr. Thilo Kopp
Tag der mündlichen Prüfung:	30. Oktober 2020

Contents

1 Introduction **1**

2 Casimir interaction within the scattering formalism **7**
2.1 Electromagnetic field in a dielectric medium 7
2.2 Vacuum energy 9
2.3 A determinant formula for a single scatterer 10
2.4 The effective scattering matrix for two scatterers 12
2.5 The scattering formula at zero temperature 15
2.6 Matsubara sum formula for finite temperatures 17
2.7 Padé spectrum decomposition 19
2.8 Scattering formula for the Casimir force and force gradient 21

3 Casimir interaction between parallel planes **23**
3.1 Scattering at a plane 23
3.2 Dielectric function 25
3.3 Fresnel coefficients in the low-frequency limit 28
3.4 Lifshitz formula 29

4 Approximation methods for non-planar surfaces **31**
4.1 Proximity-force approximation 31
4.2 Derivative expansion 33

5 Scattering at a sphere **41**
5.1 Scattering matrix elements 41
5.2 Reflection matrix elements at imaginary frequencies 46
5.3 Low-frequency limit 47
5.4 Scattering at a large sphere 49
5.5 Reflection matrix elements for large spheres 52

6 Asymptotic expansion for two spheres **55**
6.1 Asymptotic expansion of integrals: the saddle-point approximation . . 56
6.2 Expansion in round trips 57
6.3 Leading saddle-point approximation and the PFA 59
6.4 Geometric optical correction to PFA 64
6.5 Perfect reflecting spheres at a vanishing temperature 70
6.6 Plane-sphere limit 71
6.7 Asymptotic expansion for the Casimir force and force gradient 72
6.8 Comparison with the derivative expansion 74
6.9 The role of diffraction 76
6.10 Effective interaction area 79

7 Plane-wave numerical approach **83**
7.1 Arbitrary geometry . . . 83
7.2 Geometry with cylindrical symmetry . . . 84
7.3 Plane-sphere geometry . . . 85
7.4 Sphere-sphere geometry . . . 91
7.5 Numerical evaluation of the scattering amplitudes . . . 93

8 Applications **103**
8.1 Numerical results for the Casimir interaction in colloid systems . . . 103
8.2 Numerical accuracy of the asymptotic expansion . . . 110
8.3 Corrections beyond the PFA at zero temperature . . . 113

9 Conclusions **121**

A Special functions **123**
A.1 Modified Bessel functions . . . 123
A.2 Associated Legendre functions . . . 124
A.3 Polylogarithm . . . 125
A.4 Angular functions . . . 125

B Supplementary material for chapter 2 **127**
B.1 Properties of a unitary matrix . . . 127
B.2 Relation between the scattering and transfer matrix . . . 127
B.3 Convergence analysis for the PSD . . . 128

C Supplementary material for chapter 5 **131**
C.1 Explicit expressions for the polarization transformation coefficients . . . 131
C.2 Scattering amplitudes for large spheres . . . 133

D Supplementary material for chapter 6 **141**
D.1 Uniqueness of the saddle-point condition . . . 141
D.2 Hessian matrix for Fourier transformed variables . . . 142

E Derivation of the NTLO term in the saddle-point approximation **145**
E.1 A differential operator and the chain rule . . . 147
E.2 Derivation of V . . . 149
E.3 Derivation of $U_p^{(i,1)}$ and $U_p^{(i,2)}$ . . . 154
E.4 Derivation of $U^{(ii)}$ . . . 157
E.5 Useful identities . . . 161

F Hybrid numerical approach **165**

Bibliography **171**

List of Abbreviations **181**

List of Symbols **183**

Acknowledgements **185**

Chapter 1

Introduction

Aqueous colloidal suspensions play an important role in our daily lives. They appear naturally as for example milk or blood, and also find many industrial applications such as for paint, pharmaceutical products and in the oil industry. For understanding the physical properties and also the design of such colloidal systems, the knowledge about the relevant forces is necessary, which can be incorporated in a predictive theoretical model. In aqueous suspensions, repulsive electrostatic forces play a major role through double layer forces even when the particles themselves carry no charge [1]. An important omnipresent force for any colloidal systems are the van der Waals forces [1], which are typically attractive but can be repulsive [2–4] for certain combination of materials. These two forces are essential for understanding the stability of colloids.

Colloidal suspensions are composed of nano- to micro-sized particles. The van der Waals force between such macroscopic bodies arises through the interaction of their constituting atoms. For distances smaller than 10 nm between the objects the fluctuating electromagnetic interaction can be treated as instantaneous, but for larger separations retardation effects need to be considered [5]. An early approach describing the van der Waals force relies on the pairwise summation of the interacting dipoles [6]. Since many-body effects are neglected, the method of pair wise summation cannot be correct and can thus serve only as an approximation, which becomes only valid for rather extreme conditions such as for dilute gases [7] or in the weak interaction limit [8].

Later, in 1948, Hendrik Casimir showed through a quantum electrodynamical treatment of the problem that the interaction between metal plates can be directly linked to their optical response [9]. The theory was soon generalized for plates of arbitrary materials [10] and media filling the gap between the planes [11]. This macroscopic theory takes retardation effects through the optical properties of the plates into account and is used for theoretical predictions until today. Acknowledging Casimir's pioneering work, the retarded van der Waals force between macroscopic bodies is often called Casimir force.

In experiments investigating aqueous colloid systems the interaction between two spherical particles [12–14] and also the interaction between a bead and a wall [15, 16] has been studied. These geometries have also been used to study Casimir forces across vacuum and air [17–20]. In order to estimate the Casimir force, the finite curvature of the spherical bodies is usually accounted for by utilizing the proximity-force approximation (PFA), also known as Derjaguin approximation [21]. Within the PFA, the Casimir energy is obtained by averaging the energies of parallel planes over the local distances.

For a long time, the accuracy of the PFA has been unknown, and it was assumed that PFA corrections are of the order of L/R_{eff} [22] with L the surface-to-surface distance and R_{eff} the effective radius of curvature of the surfaces. In many Casimir

experiments, systems with aspect ratios $R_{\text{eff}}/L \sim 1000$ or larger were studied so that the signal of the Casimir interaction is large enough to be measured precisely [17–19]. PFA corrections were thus assumed to be negligible.

Precise measurements of the Casimir forces are not just important to test our fundamental understanding of dispersion forces in regard of their subtle properties such as nonadditivity, their dependence on geometry and temperature, and the optical properties of the involved surfaces [22, 23]. They are also important in the search for non-Newtonian gravity in the submicron distance range, as they provide bounds on such non-Newtonian forces [24–27].

In fact, agreement between theoretical predictions and experimental data has been reported in most cases. However, a surprising observation was made in precise experiments in the plane-sphere configuration with gold coated surfaces. It turned out that the experimental data were better described when the optical data for gold were extrapolated towards zero-frequency using the dissipationless plasma model [17, 18, 20]. An extrapolation towards zero-frequency using the Drude model would be physically better motivated, as that model takes dissipation into account and predicts a finite conductivity at zero-frequency in accordance with experimental facts [28]. In the just mentioned Casimir experiments the Drude model was, however, ruled out for the theoretical description of the Casimir effect. This has become known as the so-called Drude-plasma controversy, which is still a matter of ongoing debate.

A recent refinement in experimental techniques [29, 30] and also a new approach using optical tweezers [13] allow the measurement of the Casimir force with higher precision and thus at larger distances with aspect ratios $R_{\text{eff}}/L \sim 100$ or even smaller. At such larger distances, the accuracy of the PFA becomes insufficient and, therefore, exact methods for predicting the Casimir force are needed. The scattering theory [31, 32] for the fluctuating electromagnetic modes provides for such an exact method and is applicable to in principle arbitrary geometries.

Exact analytical solutions within the scattering theory are rare [33–35]. Thus, there have been efforts in finding analytical corrections to the PFA. Such corrections can be found through asymptotic expansion of the mathematical functions appearing in the scattering formalism. The method, originally developed by Bordag in Ref. [36], was used to obtain analytical beyond the PFA in the plane-sphere [37–39] and sphere-sphere geometry [40]. The experimentally most relevant setups for the two geometries involving real materials at finite temperatures are, however, not covered by these works.

An alternative approach for obtaining an asymptotic expansion of the Casimir force of curved surfaces for short distances is provided by the derivative expansion approach [41–45]. The key idea of this approach is that curvature corrections beyond the PFA are obtained by smoothly deforming the plane-plane configuration. The derivative expansion approach hence assumes the Casimir interaction to be localized around the points of closest approach of the surfaces. While the derivative expansion approach has been verified to make identical predictions as Bordag's asymptotic method at zero temperature [37, 38, 42, 43], it's applicability is limited at finite temperatures [45–47]. For instance, the derivative expansion method cannot be applied to the zero-frequency contribution of the Casimir interaction for metals described by the plasma model [45].

Numerical methods for computing the Casimir interaction complement analytical results beyond the PFA. They do not only serve for checking the quality of approximations, but yield exact results valid for any separation between the objects. Within the scattering theory, a basis needs to be chosen in which the scattering and

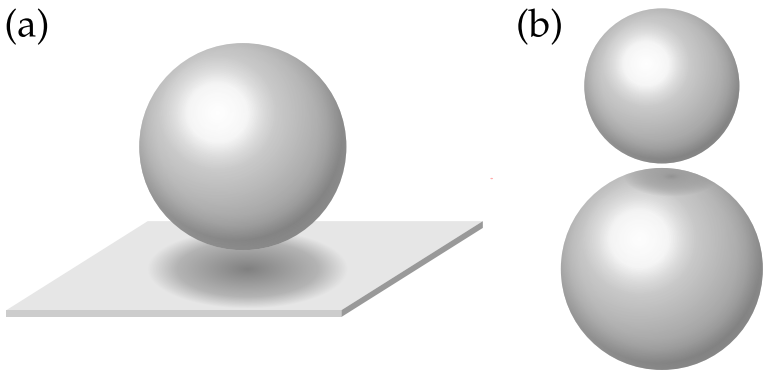

FIGURE 1.1: (a) The geometry of a plane and a sphere and (b) the geometry of two spheres.

translation operators are expressed. Multipolar waves are convenient for numerical calculations since they form a complete set of basis functions which is discrete. Spherical multipolar waves have been the choice for many numerical studies involving spheres, such as in the scattering geometries of a plane and a sphere [48–52], of two spheres [32, 53, 54] and of a grating and a sphere [55]. For large distances, a numerical evaluation of the Casimir interaction is fast, as only a few multipoles need to be considered. The situation changes dramatically at shorter distances. In the typical distance regime of most Casimir experiments, $R_{\text{eff}}/L \sim 1000$, tens of thousands of multipoles need to be included, which was an unfeasible numerical task until recently. With symmetrization of the scattering operator and employing hierarchical low-rank approximation techniques, the large number of multipoles could be dealt with. In this way, a comparison between the experimental results and numerically exact predictions became possible for the first time [56–58].

In this thesis, we explore an alternative approach utilizing the plane-wave basis within the scattering formalism. In the examples of the plane-sphere and the sphere-sphere geometry, depicted in Fig. 1.1, we demonstrate that the plane-wave basis is better suited for the prediction of the Casimir interaction than the multipole basis for typical experimental setups. We offer an analytical and a numerical approach yielding beyond-PFA predictions.

Our analytical approach is built on the asymptotic expansion of the Casimir interaction when the distance between the surfaces becomes small compared to the radius of the sphere(s). The starting point for the asymptotic expansion is the scattering formalism. In contrast to the derivative expansion approach, we do not make assumptions on locality of the interaction. While Bordag's method relied on an expansion of the electromagnetic modes in term of multipoles, we employ the plane-wave basis instead, which further allows a physical interpretation of our results. We find that the PFA arises from a geometric optical picture for plane-wave modes, while the correction to the PFA has its largest contribution from modifications of the geometric optical picture due to diffraction. Since our result is valid for arbitrary materials and temperatures, we are able to provide formulas for the asymptotic expansion, which have not been given in the literature before. The derivation of the asymptotic expansion entails an estimation of the effective interaction area between the two surfaces, which has heuristically been found to scale as $R_{\text{eff}}L$. By our calculation, we can indeed confirm this scaling law for the effective area and can thus deduce that the Casimir interaction is localized around the points of closest approach between the two surfaces.

Moreover, we provide a comparison of the results obtained from the derivative

expansion approach with results from our asymptotic expansion approach. We find agreement as far as finite frequency contributions to the Casimir interaction are concerned. For the zero-frequency contribution, we, however, find that the derivative expansion does not adequately describe the Casimir interaction beyond the PFA in aqueous colloid systems composed of dielectric objects. Our asymptotic method, however, performs well in this case.

On the numerical side, we propose to use plane waves for an evaluation of the scattering formula instead of the commonly employed multipolar waves. We show that the plane-wave numerical approach has far superior convergence properties when compared to approaches using multipolar waves. Another advantage of our approach is that scattering operators are often already known with respect to the plane-wave basis and that the translation between the coordinate systems of the objects is particularly simple. The fact that the plane-wave basis is continuous might seem to be an important drawback. Utilizing a Nyström discretization of the plane-wave momenta, however, allows us to efficiently calculate the Casimir interaction.

We apply the new numerical method to study the Casimir interaction in aqueous colloid systems in the plane-sphere and sphere-sphere geometry. As examples, we consider systems of two polystyrene bodies in water, which is typical for colloid experiments [12, 59, 60], and systems of mercury and polystyrene in water, which show an repulsive force for certain distances. Special attention is paid to the influence of variable salt concentrations on the Casimir interaction. For these systems, we use numerically exact results to test the accuracy of the PFA. We find that, in particular for low salt concentrations, the PFA performs worse than is often assumed in the literature. We further study the dependence on the effective Hamaker parameter on the geometries for the aqueous systems.

Moreover, we study the accuracy of our result for the asymptotic expansion of the Casimir interaction in the plane-sphere and sphere-sphere geometry by comparing its predictions with exact results obtained by the plane-wave numerical method. As expected the asymptotic expansion approach performs significantly better than the PFA. The results of our asymptotic expansion are thus capable of making precise predictions for the Casimir interaction in typical experimental configurations.

Finally, we study the asymptotic series of the Casimir energy between perfectly reflecting spheres in vacuum for short distances at zero temperatures beyond the predictions of our asymptotic expansion. We find that the next-to-next-to-leading-order term in the series is of the form $(L/R_{\text{eff}})^{3/2}$. We can thereby confirm the previously found result in the plane-sphere geometry [58]. Interestingly, we find that the coefficient of that next-to-next-to-leading-order term is constant and does not depend on the ratio of the sphere radii. A possible mechanism explaining the emergence of the fractional power is provided.

The thesis is structured as follows. In chapter 2, we study the Casimir interaction within the scattering approach. We derive the so-called scattering formula, which serves as a basis for the analytical and numerical calculations in the subsequent chapters. In chapter 3, we apply the scattering formula to the geometry of two planes and recover the known results by Dzyaloshinskii, Lifshitz and Pitaevskii [10, 11]. We take the opportunity to discuss important concepts such as reflection of plane-waves on planar interfaces and modeling of realistic dielectric functions. The proximity-force approximation and the derivative expansion approach are outlined in chapter 4. In chapter 5, we study electromagnetic scattering of plane waves on spheres. In chapter 6, we derive the asymptotic expansion of the Casimir interaction between two spheres. The Casimir interaction between a plane and a sphere is obtained as a limiting case. A comparison with the derivative expansion method

and an estimation of the effective area between two bodies is provided. In chapter 7, we discuss the plane-wave numerical approach. We start out by laying out the approach for arbitrary geometries and show how it can be improved when the geometries exhibit a cylindrical symmetry. Then, we discuss the plane-wave approach in the examples of the plane-sphere and sphere-sphere geometry. In chapter 8, we apply our analytical and numerical plane-wave approaches. Using the plane-wave numerical approach, we study aqueous colloid systems containing polystyrene and mercury spheres. Then, we study the accuracy of the analytical approach based on the asymptotic expansion using exact data obtained with our numerical method. Furthermore, we study the Casimir interaction at vanishing temperatures beyond our analytical approach using the plane-wave numerical method. Our results are summarized in chapter 9. The appendices contain technical details supporting the main text of this thesis.

Chapter 2

Casimir interaction within the scattering formalism

In this chapter, we derive the scattering formula for the Casimir interaction between two arbitrary non-intersecting surfaces. In the derivation, a dispersive, dielectric medium between the surfaces is assumed and the temperature is left arbitrary. The formula for the Casimir interaction is derived from a scattering approach for the vacuum and thermal modes. Our derivation is based on the expositions given in Refs. [31, 61–63].

We start out by introducing the classical macroscopic electromagnetic field in the medium. By quantizing this field, we find that the energy density of the quantum field is infinite. This infinity gives rise to the Casimir effect, when boundary conditions for the free fields are introduced. The change of the energy density, due to the presence of the objects, can then be related to the scattering matrix of the problem. This allows us to relate the Casimir energy to the scattering properties of the involved objects integrated over all frequencies. In practice, the integration over real frequencies is ill-behaved. We discuss how to perform a Wick rotation to imaginary frequencies for the zero- and finite-temperature case separately. At finite temperatures, the Casimir interaction is then expressed as a sum over the imaginary Matsubara frequencies. For numerical applications, there exists a more efficient summation scheme based on the Padé spectrum decomposition. We give an outline to that alternative approach. We conclude the chapter by deriving corresponding scattering formulas for the Casimir force and force gradient.

2.1 Electromagnetic field in a dielectric medium

In the absence of sources like charges and currents, the macroscopic Maxwell equations in an infinite medium read

$$\nabla \cdot \mathbf{D} = 0\,, \tag{2.1a}$$

$$\nabla \cdot \mathbf{B} = 0\,, \tag{2.1b}$$

$$\nabla \times \mathbf{E} = -\frac{\partial \mathbf{B}}{\partial t}\,, \tag{2.1c}$$

$$\nabla \times \mathbf{H} = \frac{\partial \mathbf{D}}{\partial t} \tag{2.1d}$$

with the electric field $\mathbf{E}$, the displacement field $\mathbf{D}$, the magnetic field $\mathbf{B}$ and the magnetizing field $\mathbf{H}$. The fields are functions of the position $\mathbf{R} = (x, y, z)$ and time t. We assume an isotropic and homogeneous, dielectric medium, i.e.

$$\mathbf{D} = \varepsilon_0 \varepsilon \mathbf{E}\,, \quad \mathbf{B} = \mu_0 \mathbf{H} \tag{2.2}$$

with the vacuum permittivity ε_0, the relative permittivity ε and the vacuum permeability μ_0. Since we assume a non-magnetic medium, the relative permeability is set to one. By combining the Maxwell equations (2.1a)-(2.1d) with Eq. (2.2), we obtain the wave equations for the electric and magnetic field

$$\begin{aligned} \left(\Delta - \frac{\varepsilon}{c^2}\frac{\partial^2}{\partial t^2}\right)\mathbf{E} = 0\,, \\ \left(\Delta - \frac{\varepsilon}{c^2}\frac{\partial^2}{\partial t^2}\right)\mathbf{B} = 0 \end{aligned} \tag{2.3}$$

where we have used that $\mu_0\varepsilon_0 = 1/c^2$.

Assuming monochromatic waves with angular frequency ω and a harmonic time dependence, $\mathbf{E}(\mathbf{R},t) = \mathrm{Re}\{\mathbf{E}(\mathbf{R})e^{-i\omega t}\}$ and $\mathbf{B}(\mathbf{R},t) = \mathrm{Re}\{\mathbf{B}(\mathbf{R})e^{-i\omega t}\}$, the wave equations (2.3) yield the Helmholtz equations

$$\begin{aligned} \left(\Delta + \frac{\varepsilon\omega^2}{c^2}\right)\mathbf{E}(\mathbf{R}) = 0\,, \\ \left(\Delta + \frac{\varepsilon\omega^2}{c^2}\right)\mathbf{B}(\mathbf{R}) = 0\,. \end{aligned} \tag{2.4}$$

The Helmholtz equations are solved by a superposition of plane waves of the form

$$\begin{aligned} \mathbf{E} &= \mathbf{E}_0 e^{i\mathbf{K}\cdot\mathbf{R}} \\ \mathbf{B} &= \mathbf{B}_0 e^{i\mathbf{K}\cdot\mathbf{R}} \end{aligned} \tag{2.5}$$

which satisfy the dispersion relation

$$|\mathbf{K}| = n\omega/c \tag{2.6}$$

with the refractive index $n = \sqrt{\varepsilon}$ which is in general a complex number. Here and in the following, we will consider the refractive index and thus also $|\mathbf{K}|$ to be a real positive number, which corresponds to the case that the medium is non-dissipative.

Due to the dispersion relation (2.6), the components of the wave vector $\mathbf{K} = (K_x, K_y, K_z)$ are not mutually independent. For instance, its z-component can be expressed in terms of the remaining components:

$$K_z = \phi k_z \quad \text{with} \quad k_z \equiv \sqrt{\mathbf{K}^2 - \mathbf{k}^2} \tag{2.7}$$

where $\phi = \pm$ and $\mathbf{k} = (K_x, K_y, 0)$. The plane waves with $\phi = +$ can be interpreted as traveling towards the positive z direction and those with $\phi = -$ as traveling in the opposite direction. The distinction of the modes by the sign ϕ will be useful when we study quasi-one dimensional scattering problems in Sec. 2.3 and 2.4.

When $|\mathbf{K}| < |\mathbf{k}|$ the z-component of the wave vector K_z becomes an imaginary number. As a consequence, those modes with $\phi = +$ decay exponentially in the positive z direction and those with $\phi = -$ in the negative z direction. These modes are called evanescent waves.

The Maxwell equation (2.1c) connects the field amplitudes of the electric and magnetic plane waves through the relation

$$\mathbf{B}_0 = \frac{1}{\omega}\mathbf{K} \times \mathbf{E}_0\,. \tag{2.8}$$

The divergence equations (2.1a) and (2.1b) demand that $\mathbf{B}_0$ and $\mathbf{E}_0$ are perpendicular to the wave vector $\mathbf{K}$ and thus the electromagnetic field is transverse to the direction of propagation. It is then convenient to introduce orthogonal unit vectors, which span the two-dimensional space perpendicular to $\mathbf{K}$. These two directions give rise to the notion of polarization. The choice of polarization basis is not unique and may be made depending on the problem. In any case, if the unit vector for the polarization component p for a given wave vector is defined as $\hat{\epsilon}_p(\mathbf{K})$ with $\hat{\epsilon}_p(\mathbf{K}) \cdot \mathbf{K} = 0$, then the other independent polarization component q is usually chosen perpendicular and its unit vector is given by the cross product

$$\hat{\epsilon}_q(\mathbf{K}) = \hat{\epsilon}_p(\mathbf{K}) \times \hat{\mathbf{K}}\,. \tag{2.9}$$

Note that here and in the following unit vectors are denoted by a hat.

The electromagnetic modes are now fully specified by their frequency ω, the wave vector transverse to the z-axis $\mathbf{k}$, the polarization p and the sign of the z-component of the wave vector $\phi = \text{sign}(K_z) = \pm$. We thus label the modes by $m \equiv (\omega, \mathbf{k}, p)$ and ϕ and the summation over modes is described by the symbols

$$\sum_{m,\phi} \equiv \sum_p \sum_\phi \int \frac{\mathrm{d}^2\mathbf{k}}{4\pi^2} \int_0^\infty \frac{\mathrm{d}k_z}{2\pi} = \sum_p \sum_\phi \int \frac{\mathrm{d}^2\mathbf{k}}{4\pi^2} \int_0^\infty \frac{\mathrm{d}\omega}{2\pi c} \frac{\varepsilon\omega}{k_z c}\,. \tag{2.10}$$

In the last equality of (2.10), we have used (2.7) to express the integral over the z-component of the wave vector as an integral over frequencies ω. Such representation of the summation over modes is more convenient since the frequency is conserved within the scattering problems considered later in this chapter.

The free macroscopic fields can now be expressed as a superposition of the plane-wave modes

$$\begin{aligned}
\mathbf{E}(\mathbf{r}, z, t) &= \sum_{m,\phi} \hat{\boldsymbol{\epsilon}}_m^\phi \left[\alpha_m^\phi e^{-i(\omega t - \mathbf{k}\cdot\mathbf{r} - \phi k_z z)} + \left(\alpha_m^\phi\right)^* e^{i(\omega t - \mathbf{k}\cdot\mathbf{r} - \phi k_z z)} \right] \\
\mathbf{B}(\mathbf{r}, z, t) &= \frac{n}{c} \sum_{m,\phi} \hat{\boldsymbol{\beta}}_m^\phi \left[\alpha_m^\phi e^{i(\omega t - \mathbf{k}\cdot\mathbf{r} - \phi k_z z)} + \left(\alpha_m^\phi\right)^* e^{-i(\omega t - \mathbf{k}\cdot\mathbf{r} - \phi k_z z)} \right]
\end{aligned} \tag{2.11}$$

with $\mathbf{r} = (x, y, 0)$ and $\hat{\boldsymbol{\beta}}_m^\phi = \hat{\mathbf{K}} \times \hat{\boldsymbol{\epsilon}}_m^\phi$.

A plane-wave mode expansion as given in (2.11) is known as the angular spectrum representation of the fields [64]. Where appropriate, the electromagnetic modes will be represented by the kets $|\omega, \mathbf{k}, \phi, p\rangle$.

2.2 Vacuum energy

For a quantum field theoretical description, the electric and magnetic fields need to be quantized. We follow the quantization scheme for dispersive, dielectric media presented in Refs. [65] and [66]. Because often in applications such as the Casimir interaction the long-wavelength part of the spectrum compared to the problem's characteristic length scales is important, we can regard the electromagnetic field in the medium as macroscopic. The atoms and molecules which constitute the medium will then only interact with the electromagnetic field in an approximative way through the mediums dielectric function ε.

We quantize the classical electromagnetic field as given in the previous section in Eq. (2.11) by promoting its field amplitudes α_m^ϕ to operators. Dimensionless quantum-field amplitudes can then be defined by [66]

$$a_m^\phi \equiv \sqrt{\frac{\hbar\omega}{\varepsilon_0[\varepsilon + \partial_\omega(\omega\varepsilon)]}}\alpha_m^\phi \tag{2.12}$$

with the partial derivative $\partial_\omega = \partial/\partial\omega$. The operators a_m^ϕ and $(a_m^\phi)^\dagger$ can be interpreted as annihilation and creation operators obeying the canonical commutation relations

$$\begin{aligned}\left[a_{m'}^{\phi'}, (a_m^\phi)^\dagger\right] &= (2\pi)^3\delta^{(2)}(\mathbf{k}-\mathbf{k}')\delta(k_z-k_z')\delta_{pp'}\delta_{\phi\phi'} \equiv \delta_{mm'}\delta_{\phi\phi'}\,,\\ \left[a_{m'}^{\phi'}, a_m^\phi\right] &= \left[(a_{m'}^{\phi'})^\dagger, (a_m^\phi)^\dagger\right] = 0\,.\end{aligned} \tag{2.13}$$

In the ground state, which is usually called vacuum state, the electric and magnetic field average to zero,

$$\langle\mathbf{E}\rangle_{\text{vac}} = \langle\mathbf{B}\rangle_{\text{vac}} = 0\,, \tag{2.14}$$

but undergo quantum fluctuations

$$\langle\mathbf{E}^2\rangle_{\text{vac}} = \frac{c^2}{\varepsilon}\langle\mathbf{B}^2\rangle_{\text{vac}} = \sum_{m,\phi}\frac{\hbar\omega}{\varepsilon_0[\varepsilon + \partial_\omega(\omega\varepsilon)]}\,. \tag{2.15}$$

The energy density of the macroscopic electromagnetic field in a dispersive, dielectric medium is given by [67, §80]

$$W = \frac{1}{2}\left[\mu_0\mathbf{H}^2 + \varepsilon_0\partial_\omega(\omega\varepsilon)\mathbf{E}^2\right]\,. \tag{2.16}$$

Earlier, it was suggested that the dispersive second term of W should be omitted in the derivation of the Casimir interaction [68]. However, the form of the energy density given here in (2.16) is in fact necessary to obtain the correct result [69]. The vacuum energy density of the electromagnetic field is then given by the sum over the modes of $\hbar\omega/2$,

$$E_{\text{vac}} = \langle W\rangle_{\text{vac}} = \sum_{m,\phi}\frac{\hbar\omega}{2}\,. \tag{2.17}$$

Note that the dependence of the ground-state energy density on the dispersive medium was canceled out by the normalization factor in (2.12). The presence of the medium thus does not affect the ground-state energy density and it is precisely the same as in vacuum.

Because the number of modes is infinite, the vacuum energy density is an infinite quantity. In quantum field theory, this infinity has often no physical meaning and is then removed by normal ordering of the field operators [70, 71]. However, if boundary conditions are introduced, the zero-point energy cannot be ignored and it gives rise to the Casimir effect as we will discuss in the subsequent sections.

2.3 A determinant formula for a single scatterer

If an object is placed into the medium, the vacuum energy density changes as the object imposes boundary conditions on the fluctuating vacuum modes. Here, we

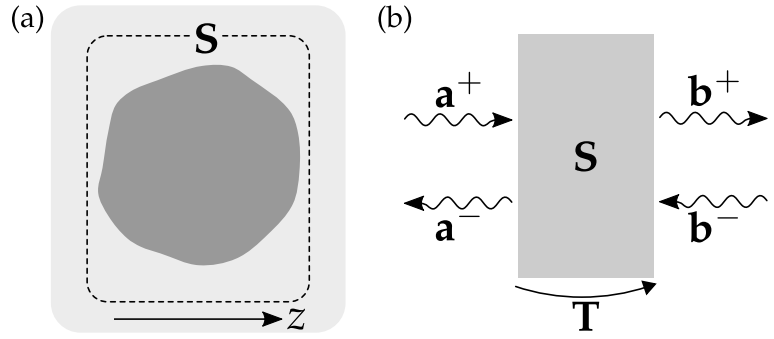

FIGURE 2.1: (a) An object immersed in a dielectric medium described by the scattering matrix **S**. (b) Schematic representation of the corresponding quasi-one dimensional scattering problem. $\mathbf{a}^\phi$ and $\mathbf{b}^\phi$ refer to the modes in the regions left and right of the scatterer, respectively. The superscripts $\phi = \pm$ indicate the direction in which the modes are going. The plus sign is reserved for the modes going to the right, i.e. along the positive z direction, and the negative sign for the opposite direction. The transfer matrix **T** relates the modes left and right of the scatterer.

review how a formula for this change in the vacuum energy can be established for a single scatterer. Our approach is based on the scattering formalism and follows the exposition given in Ref. [63]. Even though the change of vacuum energy will still be divergent for a single scatterer, the formula will be useful for finding the scattering formula for two scatterers.

It is worth recalling that the angular spectrum representation (2.11) for the quantum fields divides the modes in those propagating in the positive and negative z-direction. These modes are respectively labeled with $\phi = \pm$. For a single scatterer, the z-axis can be chosen arbitrarily. For the object in the medium, which is depicted in Fig. 2.1 (a), we can then formulate a quasi-one dimensional scattering problem along the z-axis.

The scattering problem is schematically represented in Fig. 2.1 (b) where the scattering matrix **S** associated to the object relates the in-going and out-going modes on its left and right in terms of the relation

$$\begin{pmatrix} \mathbf{b}^+ \\ \mathbf{a}^- \end{pmatrix} = \mathbf{S} \begin{pmatrix} \mathbf{a}^+ \\ \mathbf{b}^- \end{pmatrix} \tag{2.18}$$

with

$$\mathbf{S} = \begin{pmatrix} \mathbf{S}_{11} & \mathbf{S}_{12} \\ \mathbf{S}_{21} & \mathbf{S}_{22} \end{pmatrix} \equiv \begin{pmatrix} \mathbf{S}^{++} & \mathbf{S}^{+-} \\ \mathbf{S}^{-+} & \mathbf{S}^{--} \end{pmatrix} \tag{2.19}$$

and $\mathbf{a}^\phi$ and $\mathbf{b}^\phi$ are vectors containing all modes of fixed frequency labeled with the sign ϕ to the left and right of the scatterer, respectively. Here, we use the same convention for the scattering matrix as in [62], which is commonly used in quantum field theory. Note that in Ref. [63], $\mathbf{b}^+$ and $\mathbf{a}^-$ in (2.18) are interchanged and thus there, the diagonal entries of the our scattering matrix are on the off-diagonal instead.

Reference [72] establishes a connection between the change of the density of states ΔD in a quasi-one dimensional scattering problem to its scattering matrix at a given energy E:

$$\Delta D(E) = \frac{1}{2\pi i} \frac{\partial}{\partial E} \operatorname{tr} \log \left(\mathbf{S}(E) \right) . \tag{2.20}$$

Since in our problem the energy of the vacuum modes is $E = \hbar\omega/2$, we can make use of this relation to express the change of vacuum energy due to presence of the object as

$$\Delta E_{\text{vac}} = \int_0^\infty \mathrm{d}E\, E\Delta D(E) = \int_0^\infty \mathrm{d}\omega\, \frac{\hbar\omega}{2}\frac{1}{2\pi i}\frac{\partial}{\partial\omega}\,\mathrm{tr}\log\left(\mathbf{S}(\omega)\right)\,. \tag{2.21}$$

By partial integration and using the matrix identity

$$\mathrm{tr}\log(\mathbf{S}) = \log\det(\mathbf{S})\,, \tag{2.22}$$

we then obtain the determinant formula

$$\Delta E_{\text{vac}} = -\hbar\int_0^\infty \frac{\mathrm{d}\omega}{2\pi}\frac{1}{2i}\log\det\left(\mathbf{S}(\omega)\right)\,. \tag{2.23}$$

Note that the determinant formula (2.23) corresponds to the shift in the vacuum energy due to the presence of the object at a *vanishing* temperature. At finite temperatures, thermal fluctuations would need to be taken into account which yield a mean number of photons per mode different than one. Because then the thermal effect would enter as a multiplicative function of ω inside the integral in Eq. (2.23), it would only play a minor role in the following derivation of the scattering formula. We will come back to the thermal effect later in Sec. 2.6.

In order to find an expression for the effective scattering matrix for two scatterers, it is useful to introduce the transfer matrix $\mathbf{T}$ which relates the modes left and right of the scatterer by

$$\begin{pmatrix}\mathbf{b}^+\\ \mathbf{b}^-\end{pmatrix} = \mathbf{T}\begin{pmatrix}\mathbf{a}^+\\ \mathbf{a}^-\end{pmatrix} \tag{2.24}$$

with the block matrix

$$\mathbf{T} = \begin{pmatrix}\mathbf{T}_{11} & \mathbf{T}_{12}\\ \mathbf{T}_{21} & \mathbf{T}_{22}\end{pmatrix}\,. \tag{2.25}$$

The scattering properties of two or more objects can then be conveniently expressed in terms of the product of their transfer matrices.

As shown in appendix B.2, the scattering and transfer matrix are related to one another by the identities

$$\mathbf{T} = \begin{pmatrix}\mathbf{S}/\mathbf{S}_{22} & \mathbf{S}_{12}\mathbf{S}_{22}^{-1}\\ -\mathbf{S}_{22}^{-1}\mathbf{S}_{21} & \mathbf{S}_{22}^{-1}\end{pmatrix} \tag{2.26}$$

and

$$\mathbf{S} = \begin{pmatrix}\mathbf{T}/\mathbf{T}_{22} & \mathbf{T}_{12}\mathbf{T}_{22}^{-1}\\ -\mathbf{T}_{22}^{-1}\mathbf{T}_{21} & \mathbf{T}_{22}^{-1}\end{pmatrix} \tag{2.27}$$

where the block-matrix elements of $\mathbf{S}$ and $\mathbf{T}$ are defined in (2.19) and (2.25), respectively, and

$$\mathbf{X}/\mathbf{X}_{22} = \mathbf{X}_{11} - \mathbf{X}_{12}\mathbf{X}_{22}^{-1}\mathbf{X}_{21} \tag{2.28}$$

for $\mathbf{X} = \mathbf{S}, \mathbf{T}$ is the Schur complement of the block $\mathbf{X}_{22}$ in $\mathbf{X}$.

2.4 The effective scattering matrix for two scatterers

We now consider the situation where two objects 1 and 2 are placed inside the medium at a distance L. The two objects are described by their respective scattering

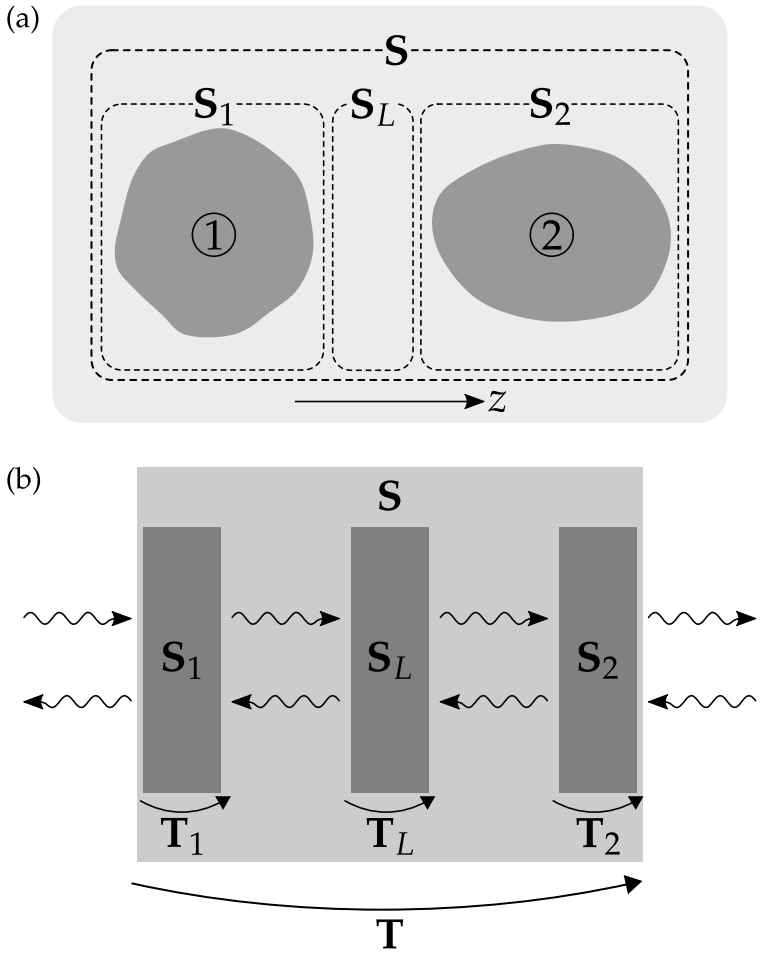

FIGURE 2.2: (a) Two objects 1 and 2 immersed in a dielectric medium separated by a distance $\mathcal{L}$. The effective scattering matrix $\mathbf{S}$ of the problem can be decomposed into the scattering matrices for the two objects $\mathbf{S}_1$ and $\mathbf{S}_2$, respectively, and the scattering matrix $\mathbf{S}_L$ resulting from the translation over their separation L. (b) Schematic representation of the quasi-one dimensional scattering problem.

matrices $\mathbf{S}_1$ and $\mathbf{S}_2$. This setup is depicted in Fig. 2.2 (a). Note that in contrast to what is depicted in the figure, the two objects do not necessarily need to be compact. They may also be infinite surfaces such as, for instance, a grating or a plane.

By choosing the coordinate system such that the two objects are aligned along the z axis, we can formulate a corresponding quasi-one dimensional scattering problem which is schematically represented in Fig. 2.2 (b).

Due to the spatial separation between the objects, the plane waves going out of object 1 and going in on object 2, or vice versa, are subject to a phase shift. This phase shift can be described by the scattering matrix

$$\mathbf{S}_L = \begin{pmatrix} \mathcal{T}_{21} & 0 \\ 0 & \mathcal{T}_{12} \end{pmatrix} \tag{2.29}$$

where $\mathcal{T}_{21}$ denotes the translation matrix for the modes from object 1 to 2 and vice versa for $\mathcal{T}_{12}$. The translation matrices are diagonal, and because the $+$ modes are translated in positive z direction and the $-$ modes in negative z direction, the matrix elements of both translation matrices contain the same phase factors $\exp(ik_z L)$:

$$\begin{aligned} \mathcal{T}_{21} \left|\omega, \mathbf{k}, +, p\right\rangle &= e^{ik_z L} \left|\omega, \mathbf{k}, +, p\right\rangle \,, \\ \mathcal{T}_{12} \left|\omega, \mathbf{k}, -, p\right\rangle &= e^{ik_z L} \left|\omega, \mathbf{k}, -, p\right\rangle \,. \end{aligned} \tag{2.30}$$

Making use of Eq. (2.26), we find the corresponding transfer matrix

$$\mathbf{T}_L = \begin{pmatrix} \mathcal{T}_{21} & 0 \\ 0 & \mathcal{T}_{12}^{-1} \end{pmatrix} . \tag{2.31}$$

In view of Fig. 2.2 (b) we can now write down the problem's effective transfer matrix

$$\mathbf{T} = \mathbf{T}_2 \mathbf{T}_L \mathbf{T}_1 \,. \tag{2.32}$$

Using Eqs. (2.26) and (2.27), it is a straightforward task to find an expression for the effective scattering matrix $\mathbf{S}$ in terms of the entries of the scattering matrices for the two objects and for the translation. We find

$$\mathbf{S}^{++} = \mathbf{S}_2^{++} \mathbf{D}_2 \mathcal{T}_{21} \mathbf{S}_1^{++} \,, \tag{2.33a}$$
$$\mathbf{S}^{+-} = \mathbf{S}_2^{+-} + \mathbf{S}_2^{++} \mathcal{T}_{21} \mathbf{S}_1^{+-} \mathbf{D}_1 \mathcal{T}_{12} \mathbf{S}_2^{--} \,, \tag{2.33b}$$
$$\mathbf{S}^{-+} = \mathbf{S}_1^{-+} + \mathbf{S}_1^{--} \mathcal{T}_{12} \mathbf{S}_2^{-+} \mathbf{D}_2 \mathcal{T}_{21} \mathbf{S}_1^{++} \,, \tag{2.33c}$$
$$\mathbf{S}^{--} = \mathbf{S}_1^{--} \mathbf{D}_1 \mathcal{T}_{12} \mathbf{S}_2^{--} \tag{2.33d}$$

where the two matrices

$$\mathbf{D}_1 = \left(1 - \mathcal{T}_{12} \mathbf{S}_2^{-+} \mathcal{T}_{21} \mathbf{S}_1^{+-}\right)^{-1} \,, \tag{2.34a}$$
$$\mathbf{D}_2 = \left(1 - \mathcal{T}_{21} \mathbf{S}_1^{+-} \mathcal{T}_{12} \mathbf{S}_2^{-+}\right)^{-1} \tag{2.34b}$$

account for an arbitrary number of round trips between the two scatterers which can be seen by expressing them in terms of their series expansion, for instance,

$$\mathbf{D}_1 = 1 + \mathcal{M} + \mathcal{M}^2 + \mathcal{M}^3 + \ldots \tag{2.35}$$

with the round-trip matrix

$$\mathcal{M} = \mathcal{T}_{12} \mathbf{S}_2^{-+} \mathcal{T}_{21} \mathbf{S}_1^{+-} \,. \tag{2.36}$$

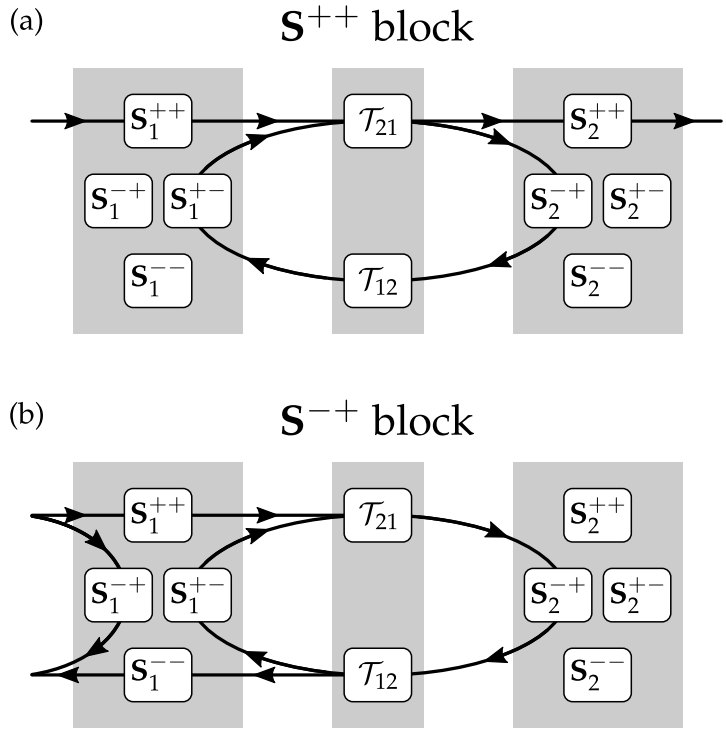

FIGURE 2.3: Schematic representation of the (a) $\mathbf{S}^{++}$ block and (b) $\mathbf{S}^{-+}$ block of the effective scattering matrix $\mathbf{S}$ as given in Eqs. (2.33a) and (2.33c), respectively. The other blocks (2.33b) and (2.33d) can be obtained by interchanging the two objects.

In Fig. 2.3 the relations (2.33a) and (2.33c) are visualized. The other relations are obtained by interchanging object 1 and 2.

2.5 The scattering formula at zero temperature

With Eq. (2.33), we have found an expression which relates the effective scattering matrix to the scattering properties of the two objects. The next step is to use the determinant formula (2.23) to relate those scattering properties of the two objects to the change of the vacuum energy.

Applying the formula [63, Eq. (A7)]

$$\det(\mathbf{S}) = \frac{\det(\mathbf{S}^{--})}{\det(\mathbf{S}^{++})^*} \tag{2.37}$$

to the determinant of the effective scattering matrix, we find that

$$\det(\mathbf{S}) = \frac{\det(\mathbf{S}_1^{--})\det(\mathbf{D}_1)\det(\mathcal{T}_{12})\det(\mathbf{S}_2^{--})}{\det(\mathbf{S}_2^{++})^*\det(\mathbf{D}_2)^*\det(\mathcal{T}_{21})^*\det(\mathbf{S}_1^{++})^*}\,. \tag{2.38}$$

with the asterisk indicating complex conjugation. Since (2.37) applies to any unitary matrix, we can use that formula for the scattering matrices $\mathbf{S}_1$, $\mathbf{S}_2$ and $\mathbf{S}_L$ as well, and we obtain

$$\det(\mathbf{S}) = \det(\mathbf{S}_1)\det(\mathbf{S}_2)\det(\mathbf{S}_L)\frac{\det(\mathbf{D}_1)}{\det(\mathbf{D}_2)^*}\,. \tag{2.39}$$

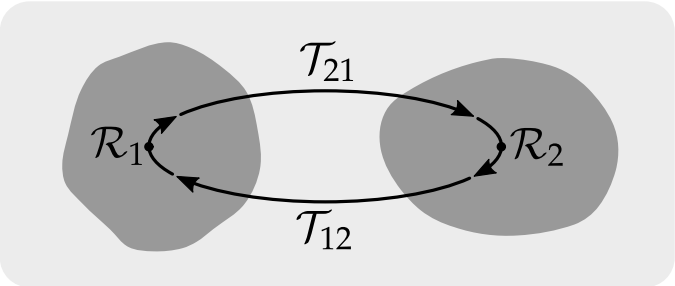

FIGURE 2.4: Schematic representation of the roundtrip operator $\mathcal{M}$ consisting of the reflection operators $\mathcal{R}_1$ and $\mathcal{R}_2$ (where the reference point for the respective reflection is indicated by the dot) and the translation operators $\mathcal{T}_{12}$ and $\mathcal{T}_{12}$.

The first two factors depend only on the respective properties of the objects, and not on their distance L. They will thus not contribute to the Casimir interaction. The middle part, $\det(\mathbf{S_L})$, which is associated to the translation between the objects, obviously depends on that distance. However, if we set the scattering matrices of the two objects to be the identity matrix, which corresponds to the limit of transparent objects, the contribution of $\mathbf{S_L}$ still remains. In order to have a meaningful formula for the Casimir interaction, we discard this contribution as well.

By using Sylvester's determinant identity [73], we have $\det(\mathbf{D}_1) = \det(\mathbf{D}_2)$. In view of the determinant formula (2.23), we then obtain the scattering formula for the Casimir energy at zero temperature

$$E_{\mathrm{Cas}}(L) = \hbar \int_0^\infty \frac{\mathrm{d}\omega}{2\pi} \frac{1}{2i} \left[\log\det\left(1-\mathcal{M}\right) - \log\det\left(1-\mathcal{M}\right)^* \right] \tag{2.40a}$$

$$= \hbar \int_0^\infty \frac{\mathrm{d}\omega}{2\pi} \operatorname{Im} \log\det\left(1-\mathcal{M}\right) . \tag{2.40b}$$

It is convenient to write the round-trip operator as

$$\mathcal{M} = \mathcal{T}_{12}\mathcal{R}_2\mathcal{T}_{21}\mathcal{R}_1 \tag{2.41}$$

where $\mathcal{R}_1$ and $\mathcal{R}_2$ are the reflection operators of the respective objects. From our derivation we have $\mathcal{R}_2 = \mathbf{S}_2^{-+}$ and $\mathcal{R}_1 = \mathbf{S}_1^{+-}$. With the expression (2.41), the round-trip operator does not explicitly depend on the orientation of z-axis, which emphasizes that the Casimir interaction does not depend on such choice either.

In practice, the reference point for describing the scattering at an object is often conveniently placed on its inside. For example, the scattering of electromagnetic waves on spheres, called Mie scattering, is usually described with respect to a coordinate system with origin at the sphere's center. The scattering formula (2.40) does not depend on the choice of the reference points for the objects, as long as $\mathcal{T}_{21}$ accounts for the translation from the reference point at object 1 to the reference point of object 2 and vice versa for $\mathcal{T}_{12}$ (cf. Fig. 2.4).

At this point, we want to mention that the scattering formula as of Eq. (2.40) is valid also for a more general setup, for instance, for a dispersive magnetic medium [74] or even when the medium is dissipative [63].

Even though we have used plane-wave modes for its derivation, the scattering formula (2.40) is independent of the basis in which the electromagnetic fields are expanded. This is due to the fact that the determinant is invariant under similarity transforms. For a given problem, it makes sense to choose a basis for which at least

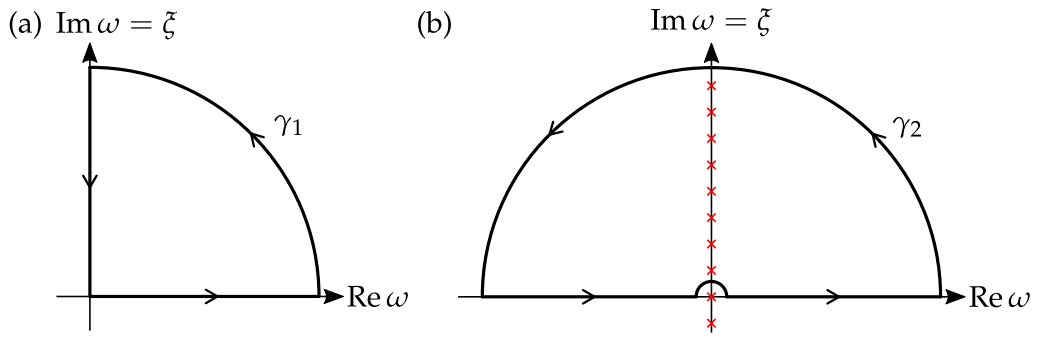

FIGURE 2.5: The complex ω-plane a) for vanishing temperatures with the contour γ_1 and b) for a finite temperature with contour γ_2. The red crosses correspond to the Matsubara frequencies $i\xi_n$.

one of the operators constituting the round-trip operator becomes diagonal. The geometry of two planes is quite special in this regard since for plane waves both reflection and translation operators are diagonal. When spheres are involved, it seems natural to use the basis of spherical multipoles, since then the reflection operator at the sphere is diagonal. However, the translation operator is not diagonal when using the multipole basis. Because the translation operator is diagonal for plane waves, it would appear to be equally natural to use plane waves when spheres are involved. In fact, for this reason plane waves might be a good choice for geometries of two arbitrary objects for which the scattering matrices are known.

For numerical purposes, formula (2.40) is not very practical since $\log\det(1-\mathcal{M})$ is a highly oscillatory complex function. At imaginary frequencies, however, it is real and well-behaved. A rotation to imaginary frequencies is thus desired. Such Wick rotation can be performed by considering an integration contour γ_1 in the complex ω-plane as shown in Fig. 2.5 (a) for the first term in (2.40a). Due to causality and passivity conditions, its integrand has no poles in the upper complex plane [31]. By Cauchy's theorem, the integral over the contour γ_1 thus vanishes. Because of high-frequency transparency of real materials, the arc connecting the contour on the real and imaginary axis yields a vanishing contribution in the limit $|\omega| \to \infty$. The integral along the real-axis can then be expressed in terms of the integral along the imaginary axis. Because the determinant of the round-trip operator is real along the imaginary axis, the contributions for the two terms in (2.40a) are then identical and we find

$$E_{\mathrm{Cas}}(L) = \hbar \int_0^\infty \frac{\mathrm{d}\xi}{2\pi} \log\det\left(1 - \mathcal{M}(i\xi)\right) \tag{2.42}$$

with the imaginary frequency $\xi = -i\omega$.

Note that for a more rigorous derivation of the scattering formula branch points which are introduced by the square-root in (2.7) and possible poles on the real-frequency axis need to be considered [75].

2.6 Matsubara sum formula for finite temperatures

At finite temperatures, one needs to account for thermal fluctuations besides the quantum fluctuations of the electromagnetic fields. In addition to the vacuum energy, each mode at temperature T contributes with the thermal energy $\bar{n}(\omega)\hbar\omega$ where

$$\bar{n}(\omega) = \left[\exp\left(\frac{\hbar\omega}{k_{\mathrm{B}}T}\right) - 1\right]^{-1}. \tag{2.43}$$

is the mean number of thermal photons per mode.

Accounting for this additional thermal energy for each mode, one can write the Casimir free energy at temperature T as [76, 77]

$$\mathcal{F}_{\text{Cas}}(L) = \hbar \int_0^\infty \frac{\mathrm{d}\omega}{2\pi} C(\omega) \frac{1}{2i} \left[\log\det\left(1-\mathcal{M}\right) - \log\det\left(1-\mathcal{M}\right)^* \right] \tag{2.44a}$$

$$= \hbar \int_0^\infty \frac{\mathrm{d}\omega}{2\pi} C(\omega) \, \mathrm{Im} \log\det\left(1-\mathcal{M}\right) . \tag{2.44b}$$

with

$$C(\omega) = 1 + 2\bar{n}(\omega) = \coth\left(\frac{\hbar\omega}{2k_\mathrm{B}T}\right) . \tag{2.45}$$

In the limit of vanishing temperature, the function C goes to one and formula (2.40) is recovered.

The Wick rotation is a bit more involved when the temperature is finite. The reason is that the function C now introduces poles at $i\xi_n$ with $\xi_n = 2\pi n k_\mathrm{B} T/\hbar$ for $n \in \mathbb{Z}$ which are known as the Matsubara frequencies. The poles are simple and equally spaced along the imaginary axis. Because in particular there are now poles in the upper ω-plane, we need to follow a different strategy for the Wick rotation.

First, we note that since the electromagnetic field is real, a complex conjugation of the fields is the same as flipping the sign of the angular frequency, i.e.

$$\mathbf{E}(-\omega) = \mathbf{E}^*(\omega) , \quad \mathbf{B}(-\omega) = \mathbf{B}^*(\omega) . \tag{2.46}$$

Because this applies to all in- and out-going modes with respect to the round-trip, we have that

$$\det\left(1-\mathcal{M}(-\omega)\right) = \det\left(1-\mathcal{M}(\omega)\right)^* . \tag{2.47}$$

Using (2.47) in (2.44a), we can extend the integration domain over the angular frequencies to the whole real line and write

$$\mathcal{F}_{\text{Cas}} = \int_{-\infty}^{+\infty} \mathrm{d}\omega \, f(\omega) \tag{2.48}$$

with

$$f(\omega) = \frac{\hbar}{4\pi i} C(\omega) \log\det\left(1-\mathcal{M}(\omega)\right) . \tag{2.49}$$

Due to the $n = 0$ Matsubara pole, the integrand in (2.48) has a pole at $\omega = 0$, which should be avoided in the integration. The integral (2.48) should thus be understood as the Cauchy principal value. The contour γ_2 in the complex ω-plane as depicted in Fig. 2.5 (b), applied to the integrand of (2.48) will now be helpful to perform the Wick rotation.

On the one hand, as the radius of the outer arc goes to infinity, the integral over the contour γ_2 yields a sum over the residues of all Matsubara frequencies in the upper complex plane by the residue theorem,

$$\int_{\gamma_2} \mathrm{d}\omega \, f(\omega) = 2\pi i \sum_{n=1}^{\infty} \mathrm{Res}[f, i\xi_n] = k_\mathrm{B} T \sum_{n=1}^{\infty} \log\det\left(1-\mathcal{M}(i\xi_n)\right) . \tag{2.50}$$

On the other hand, because the contribution of this outer arc then goes to zero due to the high-frequency transparency of real materials, the contour integral can be alternatively written as the contribution of the integral along the real line plus the small

arc around the origin. Sending the radius of that small arc to zero, we then find

$$\int_{\gamma_2} \mathrm{d}\omega\, f(\omega) = \mathcal{F}_{\mathrm{Cas}} - \pi i \,\mathrm{Res}[f, 0] = \mathcal{F}_{\mathrm{Cas}} - \frac{1}{2}\log\det\left(1 - \mathcal{M}(0)\right) . \tag{2.51}$$

Note that the residue contribution of the zero-Matsubara frequency is weighted by a factor of $1/2$ because the curve is a semi-circle. Due to the orientation of the curve, the sign is negative.

Equating (2.50) and (2.51), we obtain the Matsubara summation formula for the Casimir free energy

$$\mathcal{F}_{\mathrm{Cas}}(L) = k_{\mathrm{B}}T \sum_{n=0}^{\infty}{}' \log\det\left(1 - \mathcal{M}(i\xi_n)\right) , \tag{2.52}$$

where the primed sum indicates that the $n = 0$ term is taken with a factor of $1/2$, i.e.

$$\sum_{n=0}^{\infty}{}'\Phi(i\xi_n) = \frac{1}{2}\Phi(0) + \sum_{n=1}^{\infty}\Phi(i\xi_n) . \tag{2.53}$$

At this point, it shall be noted that by a careful examination of the Wick rotation in the plane-plane configuration, the zero-frequency contribution of the TE-polarized mode gets canceled by the contributions due to poles associated to Foucault currents when the materials are described by the lossless plasma model [78]. As a consequence, the standard Lifshitz-Matsubara sum formula, which corresponds to Eq. (2.52) in the plane-plane geometry, could not be recovered.

In numerical applications, the Matsubara sum needs to be truncated. The translation factor between the two surfaces, which reads $\exp(-2\xi_n L/c)$ for large n provides a frequency cut-off. Convergence will thus be reached when the number of terms included in the Matsubara sum becomes of the order of λ_T/L with the thermal wavelength $\lambda_T = \hbar c/k_{\mathrm{B}}T$. This scaling holds also for dielectric media, but the converge may then also depend on the material properties.

Since Eq. (2.52) is an expansion in terms of the Matsubara spectrum, we may also denote it as the Casimir free energy from the Matsubara spectrum decomposition (MSD). Alternatively one can express the Casimir free energy in terms of the Padé spectrum decomposition (PSD) which is a more efficient sum-over-poles scheme. We will outline this alternative approach in the following section.

2.7 Padé spectrum decomposition

For the PSD, one starts out by expanding the function C in Eq. (2.44) in terms of a Padé approximation [79]. With $\tilde{C}(x) = C(\omega)$ for $x = \hbar\omega/k_{\mathrm{B}}T$ the Padé approximation reads

$$\tilde{C}(x) \approx \frac{2}{x} + 1 + 2x\frac{P_{N-1}(x^2)}{Q_N(x^2)} \tag{2.54}$$

where P_{N-1} and Q_N are polynomials of order $N-1$ and N, respectively. Alternatively, $\tilde{C}$ can then be expressed in terms of a sum over its simple poles

$$\tilde{C}(x) \approx \frac{2}{x} + 1 + 2\sum_{j=1}^{N}\left(\frac{\eta_j}{x + i\chi_j} + \frac{\eta_j}{x - i\chi_j}\right) , \tag{2.55}$$

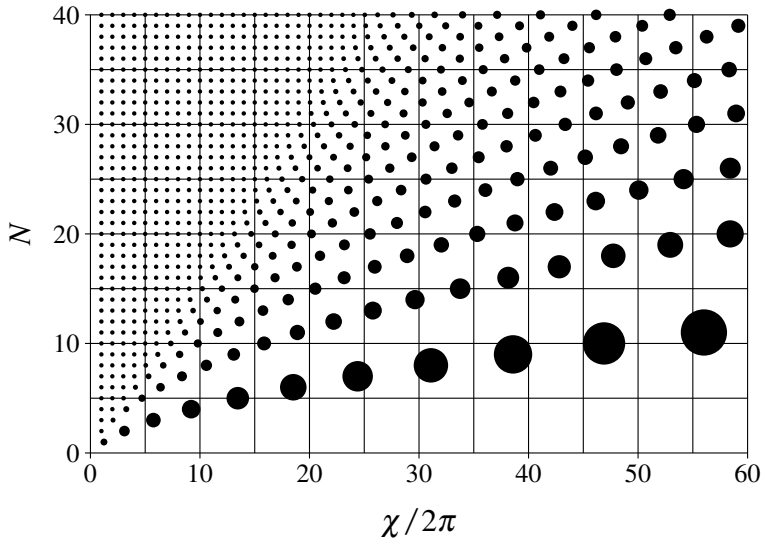

FIGURE 2.6: The PSD frequencies χ are displayed as a function of the order N of the Padé approximation. The center of the circle indicates the position of the pole while the area of the circle is proportional to the weight η associated with the pole. (Taken from Ref. [80].)

where the PSD frequencies χ_j are determined by the roots of Q_N. In practice, those PSD frequencies can be computed via the eigenvalues, $\{\lambda_j \equiv \pm 2/\chi_j\}$, of the symmetric tridiagonal matrix [79]

$$\Lambda_{jk} = \frac{\delta_{j,k\pm1}}{\sqrt{(2j+1)(2k+1)}}, \quad j,k = 1,\ldots,2N\,. \tag{2.56}$$

The PSD weights η_j are given by [79]

$$\eta_j = \left.\frac{P_{N-1}(z)}{2Q'_N(z)}\right|_{z=-\chi_j^2} \tag{2.57}$$

where the prime indicates a z-derivative. The polynomials $P_{N-1}(z)$ and $Q_N(z)$ can be efficiently computed through a recursive relation. For the starting values $A_1(z) = 1/4$, $A_2(z) = 5/4$, $B_1(z) = 3$, $B_2(z) = 15 + z/4$, the recursion

$$X_{M\geq 3}(z) = (2M+1)X_{M-1}(z) + \frac{z}{4}X_{M-2}(z) \tag{2.58}$$

for both $X = A, B$ can be used to find [79]

$$P_{N-1}(z) = A_{2N}(z)\,, \qquad Q_N(z) = B_{2N}(z)\,. \tag{2.59}$$

In order to obtain $Q'_N(z)$ one needs to additionally use the corresponding recursion for B'_M which can be found by taking the derivative of (2.58).

Figure 2.6 visualizes the PSD frequencies χ as a function of the order of the Padé approximation N. The center of the circles represent the position of the poles and the circle area is proportional to the associated weights. For small enough frequencies, the PSD frequencies are close to the regularly spaced Matsubara frequencies. For larger frequencies, the spacing between the PSD frequencies increases and so does their associated weight. Due to the irregular spacing of the poles, the PSD order has to be fixed beforehand.

The Wick rotation can then be performed in the same way as in the derivation of the Matsubara sum formula. The integration over the contour γ_2 as depicted in Fig. 2.5 (b) then yields the sum over the residues of the finite number of PSD poles instead. Any subtleties regarding the contour integration remain unchanged with respect to the MSD. In particular, a discussion of the zero-frequency contribution would be exactly the same, since the pole at $x = 0$ in (2.55) is identical to the $n = 0$ Matsubara frequency.

Within the PSD, the Casimir free energy then reads

$$\mathcal{F} = \frac{k_B T}{2} \left[\Phi(0) + 2 \sum_{j=1}^{N} \eta_j \Phi(i k_\mathrm{B} T \chi_j / \hbar) \right] \tag{2.60}$$

with

$$\Phi(\omega) = \log\det(1 - \mathcal{M}(\omega)) \,. \tag{2.61}$$

Though the computation of the PSD frequencies and weights is considerably more complicated than for the MSD, the PSD scheme comes with the reward of a faster convergence of the frequency sum. Namely, as we show in Appendix B.3 convergence will be typically reached when the PSD order scales only as $N \propto \sqrt{\lambda_T / L}$. Thus, the PSD is superior to the MSD, in particular, for non-planar surfaces at experimentally relevant distances.

2.8 Scattering formula for the Casimir force and force gradient

So far, we have only considered the Casimir free energy. The Casimir force can be obtained from the Casimir energy by taking the negative derivative with respect to the distance between the objects. In numerical applications, one could compute the force by calculating the numerical derivative. Depending on the numerical differentiation scheme, this would require the computation of several Casimir energies around a given distance, to obtain the force at a single distance. Because the evaluation of the Casimir (free) energy may be computationally demanding for non-trivial geometries (cf. Ch. 6), a formula which gives the force directly would be more efficient.

Using Jacobi's formula,

$$\partial_L \log\det\left(1 - \mathcal{M}\right) = -\operatorname{tr}\left(\frac{\partial_L \mathcal{M}}{1 - \mathcal{M}}\right) , \tag{2.62}$$

we obtain a scattering formula for the force at finite temperatures,

$$F_\mathrm{Cas} = k_\mathrm{B} T \sum_{n=0}^{\infty}{}' \operatorname{tr}\left(\frac{\partial_L \mathcal{M}}{1 - \mathcal{M}}\right) . \tag{2.63}$$

The force gradient of the Casimir interaction is a quantity which is often experimentally investigated. Taking another derivative of the Casimir force, the force gradient reads

$$F'_\mathrm{Cas} = k_\mathrm{B} T \sum_{n=0}^{\infty}{}' \operatorname{tr}\left[\frac{\partial_L^2 \mathcal{M}}{1 - \mathcal{M}} + \left(\frac{\partial_L \mathcal{M}}{1 - \mathcal{M}}\right)^2\right] . \tag{2.64}$$

Note that in (2.63) and (2.64) the dependence of the round-trip operator $\mathcal{M}$ on the imaginary frequencies $i\xi_n$ was dropped for brevity.

By the replacement

$$k_{\mathrm{B}}T \sum_{n=0}^{\infty}{}' \to \hbar \int_0^\infty \frac{\mathrm{d}\xi}{2\pi}\,. \tag{2.65}$$

in (2.63) and (2.64), the corresponding formulas for a vanishing temperature can be obtained.

Chapter 3

Casimir interaction between parallel planes

The prime example for the Casimir effect is the setup which was considered by Henrik Casimir in his pioneering work: two perfectly conducting, parallel planes in vacuum at zero temperature. In fact, due to its theoretical simplicity, the setup of two parallel planes is the most studied geometry for the Casimir interaction. On the experimental side, however, due to the issue of parallelism between the planes, the geometry of a sphere and plane has been most commonly studied. Recently, the geometry of two spheres has gained more attention. The theoretical prediction of the Casimir interaction in those geometries is a challenging task. Thus, almost exclusively the proximity force approximation (PFA) is employed for the analysis of experiments. Within the PFA, the Casimir energy is expressed as the average of the plane-plane Casimir energy over the local distances between two surfaces. In this way, the Casimir interaction between two parallel planes plays an important role for the Casimir interaction even when non-planar surfaces are involved.

In this chapter, the Casimir interaction for the geometry of two parallel planes is studied. This gives us the opportunity to familiarize ourselves with the scattering formalism in a particularly simple example. In fact, this geometry is one of few examples where both the reflection and translation operators are diagonal in the same basis. For this geometry, this basis is composed of plane waves. We start out by discussing the reflection of plane waves on a planar interface. We then introduce the dielectric function and discuss important models for dielectrics and metals. The low-frequency limit of the reflection coefficients on the plane depends on the material model and we find expressions for it. Finally, we derive the formulas for the plane-plane interaction and recover the well-known Lifshitz formula for the Casimir free energy and the force.

3.1 Scattering at a plane

Consider two half-spaces filled with dielectric media of refractive indices n_1 and n_2. The z-axis is chosen perpendicular to the interface plane. This setup is illustrated in Fig. 3.1. The plane of incidence, also sometimes called Fresnel plane, is spanned by the incidence wave vector $\mathbf{K}$ and the normal vector to the interface (here: $\mathbf{z}$). We consider the two polarizations for the fields: the electric field perpendicular and parallel to the plane of incidence. These polarizations are commonly called transverse

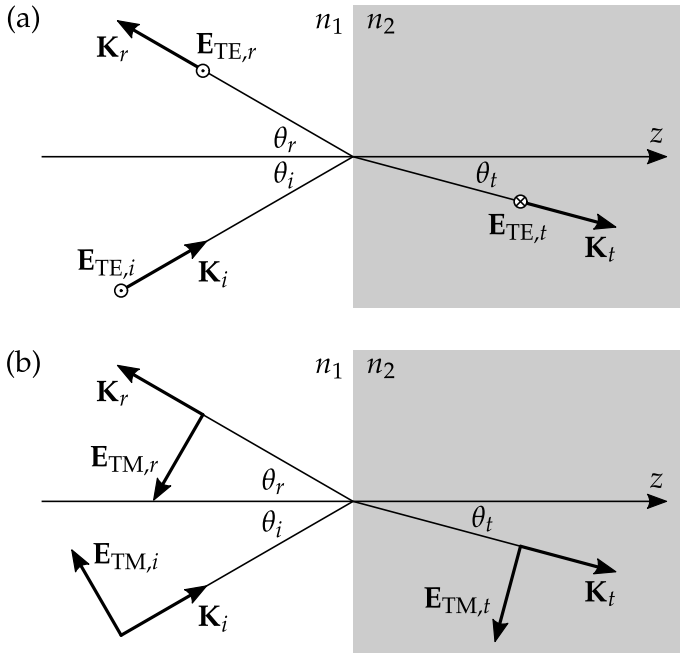

FIGURE 3.1: Reflection and transmission of an incident electric wave on a plane boundary between two media with respective refractive index n_1 and n_2 for (a) the transverse electric (TE) and (b) the transverse magnetic (TM) field components.

electric (TE) and transverse magnetic (TM) and they can be defined as

$$\begin{aligned} \hat{\boldsymbol{\epsilon}}_{\mathrm{TE}}(\mathbf{K}) &= \frac{\hat{\mathbf{z}} \times \hat{\mathbf{K}}}{|\hat{\mathbf{z}} \times \hat{\mathbf{K}}|}, \\ \hat{\boldsymbol{\epsilon}}_{\mathrm{TM}}(\mathbf{K}) &= \hat{\boldsymbol{\epsilon}}_{\mathrm{TE}} \times \hat{\mathbf{K}} \end{aligned} \tag{3.1}$$

with unit vectors denoted by a hat. The field components with respect to this choice of polarization are conserved for reflection and transmission on the plane interface. This means that reflected and transmitted field of a TE-polarized incident wave are also TE-polarized. And the same is true for a TM-polarized incident field.

The Fresnel reflection coefficients r_{TE} and r_{TM} describe the relative amplitudes of TE- and TM-polarized plane waves reflected on the interface between the two media, respectively. Using the law of specular reflection, $\theta_i = \theta_r$, and Snell's law,

$$n_1 \sin(\theta_i) = n_2 \sin(\theta_t) \tag{3.2}$$

the Fresnel reflection coefficients can be solely expressed in terms of the incidence angle [81]

$$r_{\mathrm{TE}}(\theta_i) = \frac{\cos(\theta_i) - \sqrt{\varepsilon - 1 + \cos^2(\theta_i)}}{\cos(\theta_i) + \sqrt{\varepsilon - 1 + \cos^2(\theta_i)}}, \tag{3.3}$$

$$r_{\mathrm{TM}}(\theta_i) = \frac{\varepsilon \cos(\theta_i) - \sqrt{\varepsilon - 1 + \cos^2(\theta_i)}}{\varepsilon \cos(\theta_i) + \sqrt{\varepsilon - 1 + \cos^2(\theta_i)}} \tag{3.4}$$

where $\varepsilon = \varepsilon_2/\varepsilon_1 = n_2^2/n_1^2$.

The incidence angle can be expressed in terms of the incidence wave vector through the relation

$$\cos\theta_i = \frac{k_z}{K}\,. \tag{3.5}$$

At imaginary frequencies $\xi = -i\omega$, this relation becomes

$$\cos\theta_i = \frac{\kappa}{\mathcal{K}} \tag{3.6}$$

with the axial wave vector after Wick rotation

$$\kappa = \sqrt{\mathcal{K}^2 + k^2} \tag{3.7}$$

and the imaginary wave number

$$\mathcal{K} = n_1(i\xi)\xi/c\,. \tag{3.8}$$

At imaginary frequencies, the Fresnel coefficients can then be expressed in terms of the imaginary wave number and the magnitude of the in-plane wave number k:

$$\begin{aligned} r_{\mathrm{TE}}(i\xi,k) &= \frac{\kappa - \sqrt{(\varepsilon-1)\mathcal{K}^2+\kappa^2}}{\kappa + \sqrt{(\varepsilon-1)\mathcal{K}^2+\kappa^2}}\,,\\ r_{\mathrm{TM}}(i\xi,k) &= \frac{\varepsilon\kappa - \sqrt{(\varepsilon-1)\mathcal{K}^2+\kappa^2}}{\varepsilon\kappa + \sqrt{(\varepsilon-1)\mathcal{K}^2+\kappa^2}}\,. \end{aligned} \tag{3.9}$$

where $\varepsilon = \varepsilon(i\xi) = \varepsilon_2(i\xi)/\varepsilon_1(i\xi)$. In the special case of a perfectly reflecting interface, i.e. $\varepsilon_2 \to -\infty$, the Fresnel reflection coefficients become

$$r_{\mathrm{TE}}^{(\mathrm{PR})} = -1\,, \quad r_{\mathrm{TM}}^{(\mathrm{PR})} = 1\,. \tag{3.10}$$

Due to specular reflection, the in-plane wave vector $\mathbf{k}$ is conserved upon reflection on the plane. Since, in view of the angular spectrum representation, only the sign ϕ changes, the action of the reflection operator of the plane $\mathcal{R}_{\mathrm{P}}$ on a plane-wave mode can be written as

$$\mathcal{R}_{\mathrm{P}}\,|\mathbf{k},p,+\rangle = r_p\,|\mathbf{k},p,-\rangle\ . \tag{3.11}$$

If we interchange the two half-spaces and have an incident plane-wave traveling in negative z-direction, the Fresnel reflection coefficients are identical, and the action of the reflection operator on the corresponding plane-wave modes reads

$$\mathcal{R}_{\mathrm{P}}\,|\mathbf{k},p,-\rangle = r_p\,|\mathbf{k},p,+\rangle\ . \tag{3.12}$$

3.2 Dielectric function

In the last section, the reflection matrix elements for a plane were derived. We have seen that the Fresnel reflection coefficients depend on the dielectric function which generally depends further on the frequency. In order to evaluate the Casimir interaction by means of an integral or sum along the imaginary frequency axis, we then also need to know how the dielectric function transforms under the Wick rotation.

Due to causality, the dielectric function, $\varepsilon(\omega) = \varepsilon'(\omega) + i\varepsilon''(\omega)$ with real part ε' and imaginary part ε'', is required to be analytic in the upper complex ω-plane. The real and imaginary parts are then connected by the Kramers-Kronig relations [67]. These relations allow one to link the dielectric function for real and imaginary

frequencies through the expression

$$\varepsilon(i\xi) = 1 + \frac{2}{\pi}\int_0^\infty \frac{\omega\varepsilon''(\omega)}{\xi^2+\omega^2}\mathrm{d}\omega\,. \tag{3.13}$$

In principle, one can now find the dielectric function along the imaginary frequency axis using tabulated experimental data. There are, however, practical limitation as experimental data are known only for a finite frequency window $\omega_{\min} < \omega < \omega_{\max}$. Below $\omega_{\min}$ and above $\omega_{\max}$ an extrapolation using appropriate models for the dielectric function is required. A detailed description on this approach, which is commonly used for metals such as gold, can be found for instance in Ref. [82].

For dielectrics, a different approach is usually used, and an oscillator model is fitted to the experimental data set instead. Once the fitting parameters have been obtained, one then simply evaluates the dielectric function within the oscillator model on the imaginary frequency axis [83–85].

In the following, we will discuss the commonly employed oscillator model for dielectrics, the Drude and plasma model for solid metals, and the Drude-Smith model for liquid metals. In Chapter 7, where we apply the numerical and analytical methods developed in this thesis, we will use these models to describe the materials.

Dielectrics

The optical response of dielectrics is well described by the Debye and damped oscillator model [23]

$$\varepsilon(\omega) = 1 + \sum_d \frac{c_d}{1-i\omega\tau_d} + \sum_j \frac{c_j\omega_j^2}{\omega_j^2 - i\omega\gamma_j - \omega^2} \tag{3.14}$$

As pointed out above, the parameters c_d, τ_d, c_j, ω_j and γ_j are determined by fitting the dielectric function obtained from tabulated experimental data.

The individual oscillators contributing to the dielectric function may have a physical origin. For instance, the Debye oscillators, $c_d/(1-i\omega\tau_d)$, describe polarization by rotation of permanent dipoles with relaxation time τ_d [86], and the damped oscillators, $c_j\omega_j^2/(\omega_j^2 - i\omega\gamma_j - \omega^2)$ with resonance frequency ω_j and damping constant γ_j, describe polarization due to excitation of quantum states where c_j is related to the transition probability between states [85]. Two distinct regimes can be typically identified for the damped oscillators: the IR spectrum corresponding to excitation in vibration states, and the UV spectrum corresponding to electronic excitations. In general, one should however not overinterpret the fitting parameters for they are obtained from a formal mathematical fitting procedure [83, 84].

In the static limit, $\omega \to 0$, the dielectric function goes to a constant value determined by the coefficients c_d and c_j,

$$\varepsilon(0) = 1 + \sum_d c_d + \sum_j c_j\,. \tag{3.15}$$

At imaginary frequencies, the oscillator model reads

$$\varepsilon(i\xi) = 1 + \sum_d \frac{c_d}{1+\xi\tau_d} + \sum_j \frac{c_j\omega_j^2}{\omega_j^2 + \xi\gamma_j + \xi^2}\,. \tag{3.16}$$

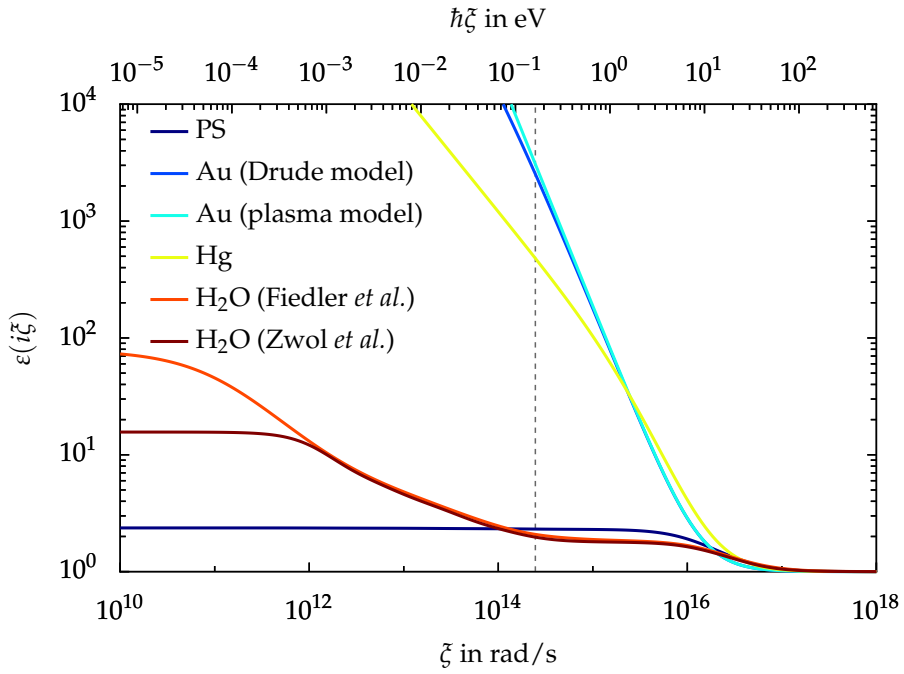

FIGURE 3.2: The dielectric function for imaginary frequencies ξ for various materials. The vertical dashed line indicates the $n = 1$ Matsubara frequency at room temperature.

In this thesis, the oscillator model without Debye terms will be used for polystyrene using the fitting parameters of data set 1 from Ref. [84]. For water, we will use two different models. One model is based on the fitting parameters from Zwol *et al.* (c.f. Ref. [84]) where no Debye terms are used and the static value of the dielectric function is set to $\varepsilon(0) = 78.7$. The other model has two Debye terms with fitting parameters from Fiedler *et al.* (cf. Ref. [85]).

The dielectric function of polystyrene and the two models of water is depicted in Fig. 3.2 as a function of the imaginary frequency ξ.

Metals

Plasma model

The lossless plasma model for the dielectric function is given by

$$\varepsilon(\omega) = 1 - \frac{\omega_p^2}{\omega^2} \tag{3.17}$$

with plasma frequency ω_p, and captures the optical properties of metals at high frequencies. Despite missing physical motivation, the low-frequency extrapolation of the Casimir interaction based on this model agrees very well with experimental results.

At imaginary frequencies, the plasma model reads

$$\varepsilon(i\xi) = 1 + \frac{\omega_p^2}{\xi^2}\,. \tag{3.18}$$

When we use this model for gold, we take the plasma frequency at $9\,\mathrm{eV}/\hbar$. The corresponding dielectric function is depicted in Fig. 3.2.

The conductivity $\sigma(\omega)$ is related to the dielectric function by the relation

$$\varepsilon(\omega) = 1 + i\frac{\sigma(\omega)}{\varepsilon_0 \omega}\,. \tag{3.19}$$

This implies that conductivity diverges like $\propto 1/\omega$ as $\omega \to 0$ for the plasma model. However, real metals have a finite dc conductivity. A simple model which takes the finite dc conductivity into account is the Drude model.

Drude model

The dielectric function for the Drude model is given by

$$\varepsilon(\omega) = 1 - \frac{\omega_p^2}{\omega(\omega + i\gamma)} \tag{3.20}$$

with the plasma frequency ω_p and damping coefficient γ. At imaginary frequencies, this dielectric function reads

$$\varepsilon(i\xi) = 1 + \frac{\omega_p^2}{\xi(\xi + \gamma)}\,. \tag{3.21}$$

A typical value for the damping coefficient for gold is $0.035\,\mathrm{eV}/\hbar$. The dielectric function for gold based on the Drude model is shown Fig. 3.2.

Drude-Smith model

Liquid metals such as mercury display a qualitatively different conductivity from the one predicted by the Drude model [87, 88]. Namely, a peak at infrared frequencies was observed. To account for this observation Smith proposed to modify the Drude model as [89]

$$\varepsilon(\omega) = 1 - \frac{\omega_p^2}{\omega(\omega + i\gamma)}\left[1 + \sum_{n=1}^{\infty} \frac{i^n \gamma^n c_n}{(\omega + i\gamma)^n}\right] \tag{3.22}$$

where the coefficients c_n describe the persistence of the velocity of the conduction electrons. When $c_n = 0$ for all n, the Drude model is recovered. At imaginary frequencies, the Drude-Smith model reads

$$\varepsilon(i\xi) = 1 + \frac{\omega_p^2}{\xi(\xi + \gamma)}\left[1 + \sum_{n=1}^{\infty} \frac{\gamma^n c_n}{(\xi + \gamma)^n}\right]\,. \tag{3.23}$$

For mercury, we use the parameters as given in Ref. [90] where only the first value of the coefficients c_n contributes, $c_1 = -0.49$. The value of the plasma frequency and the damping coefficient is $\omega_p = 13\,\mathrm{eV}/\hbar$ and $\gamma = 1.084\,\mathrm{eV}/\hbar$, respectively. The dielectric function of mercury along the imaginary frequency axis is depicted in Fig. 3.2.

3.3 Fresnel coefficients in the low-frequency limit

When computing the Casimir interaction at finite temperatures, we need to know the matrix elements of the reflection operators at finite imaginary frequencies and also in the zero-frequency limit. When planes are involved, one needs to know how the

Fresnel reflection coefficients behave in that limit. In fact, there are different results for the low-frequency limit for the Fresnel coefficients depending on the material model under consideration.

Here, it will be assumed that the medium is dielectric and thus its dielectric function takes a constant value $\varepsilon_{\mathrm{m}}(0)$ for vanishing frequencies. Depending on whether the plane is dielectric or a metal described by the plasma or Drude model, we will derive expressions for the Fresnel coefficients in the low-frequency limit.

Dielectric half-space

When the half-space is a dielectric, its permittivity ε_{d} assumes also a constant value $\varepsilon_{\mathrm{d}}(0)$ at a vanishing frequency. In this limit, the Fresnel coefficients (3.9) become

$$\begin{aligned} r_{\mathrm{TE}}(0,k) &= 0\,, \\ r_{\mathrm{TM}}(0,k) &= \frac{\varepsilon(0)-1}{\varepsilon(0)+1} \end{aligned} \tag{3.24}$$

where $\varepsilon(0) = \varepsilon_{\mathrm{d}}(0)/\varepsilon_{\mathrm{m}}(0)$.

Drude model

Within the Drude model the dielectric function behaves like $\varepsilon \propto 1/\xi$ as $\xi \to 0$. The TE Fresnel coefficient thus vanishes as for the dielectric plane, and the TM Fresnel coefficient becomes perfectly reflecting,

$$\begin{aligned} r_{\mathrm{TE}}(0,k) &= 0\,, \\ r_{\mathrm{TM}}(0,k) &= 1\,. \end{aligned} \tag{3.25}$$

Because the Drude-Smith model has the same low-frequency behavior as the Drude model, the Frensel coefficients take the same limit as given in Eq. (3.25).

Plasma model

When the dielectric function of the metallic plane is described by the plasma model, the relative permittivity diverges for low frequencies as $\varepsilon \propto 1/\xi^2$. The TM Fresnel coefficient then takes the same limit as for the Drude model. However, the TE Fresnel coefficient is now different and it depends on the in-plane wave number k and the plasma frequency ω_p. In the low-frequency limit, the Fresnel coefficients thus read

$$\begin{aligned} r_{\mathrm{TE}}(0,k) &= \frac{k-\sqrt{K_{\mathrm{p}}^2+k^2}}{k+\sqrt{K_{\mathrm{p}}^2+k^2}}\,, \\ r_{\mathrm{TM}}(0,k) &= 1 \end{aligned} \tag{3.26}$$

with the plasma wave number $K_{\mathrm{p}} = \omega_{\mathrm{p}}/c$.

3.4 Lifshitz formula

Now, we are ready to evaluate the scattering formula for two planes. The setup is depicted in Fig. 3.3. Due to the translational invariance of the setup in the direction parallel to the planes, the Casimir free energy expressed through scattering formula (2.52) needs to be understood per unit area.

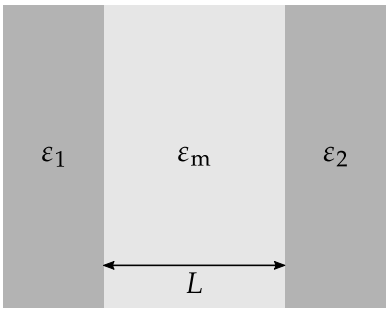

FIGURE 3.3: The plane-plane geometry consisting of two dielectric half-spaces with respective relative permittivities ε_1 and ε_2. The two planes are at a distance L. In between there is a dielectric medium with relative permittivity ε_m.

Because the reflection and translation operators are diagonal for plane waves, the round-trip operator is also diagonal. Using the identity for the translation matrices (2.30) at imaginary frequencies, and (3.11) and (3.12) for the reflection operators at the two planes, we can express the action of the round-trip operator on a plane-wave mode as

$$\mathcal{M}\,|\mathbf{k},p,-\rangle = r_p^{(1)}(i\xi,k)r_p^{(2)}(i\xi,k)e^{-2\kappa L}\,|\mathbf{k},p,-\rangle\ . \tag{3.27}$$

The determinant in the scattering formula then factorizes and we find

$$\log\det(1-\mathcal{M}(i\xi)) = \sum_{p\in\{\mathrm{TE,TM}\}}\int\frac{\mathrm{d}^2\mathbf{k}}{(2\pi)^2}\log\left(1-r_p^{(1)}(i\xi,k)r_p^{(2)}(i\xi,k)e^{-2\kappa L}\right)\ . \tag{3.28}$$

It is now convenient to express the in-plane momenta $\mathbf{k}$ in polar coordinates, since then the angular integration can be performed yielding a factor of 2π. Consequently, the Casimir free energy per unit area between two parallel planes becomes

$$\mathcal{F}_{\mathrm{PP}} = k_{\mathrm{B}}T{\sum_{n=0}^{\infty}}'\sum_{p\in\{\mathrm{TE,TM}\}}\int_0^\infty\frac{\mathrm{d}k}{2\pi}k\log\left(1-r_p^{(1)}(i\xi_n,k)r_p^{(2)}(i\xi_n,k)e^{-2\kappa L}\right)\ . \tag{3.29}$$

The pressure, i.e. force per unit area, between the two planes is obtained by taking the negative derivative with respect to the distance and we find

$$F_{\mathrm{PP}} = -2k_{\mathrm{B}}T{\sum_{n=0}^{\infty}}'\sum_{p\in\{\mathrm{TE,TM}\}}\int_0^\infty\frac{\mathrm{d}k}{2\pi}\kappa k\frac{r_p^{(1)}r_p^{(2)}e^{-2\kappa L}}{1-r_p^{(1)}r_p^{(2)}e^{-2\kappa L}}\,. \tag{3.30}$$

The expressions (3.29) and (3.30) are known as the Lifshitz formulas for the free energy per unit area and the pressure, respectively [10, 11].

Chapter 4

Approximation methods for non-planar surfaces

Approximation methods are usually used to estimate the Casimir interaction for non-planar surfaces at short distances. One reason is that hardly any exact analytical results are known. Another reason is that the numerically exact computation of the interaction is a challenging task.

The most popular approximation method is the proximity-force approximation (PFA). It has been employed for almost all experiments reported in the literature so far. The PFA is applicable when the interacting surfaces are smooth and it becomes valid when the distance between the surfaces is much smaller than the radii of curvature of the surfaces. In the literature the PFA is often also called Derjaguin approximation (DA). The derivative expansion (DE) approach is a related approximation method which can be understood as a generalization of the PFA. As such it yields asymptotic corrections to the PFA for small distances.

Another approximation method of the Casimir interaction is the pairwise summation (PWS) method. This method is built on expressing the Casimir force between the two macroscopic bodies in terms of a sum over the forces acting between their constituents, which can be atoms or molecules. The PWS is known to become precise only in rather extreme cases, for example, for weakly interacting atoms [8] or when the materials involved are infinitely dilute [7]. In the experimentally relevant cases, it was shown that the PWS does not match with the exact Casimir forces for the atom-plane, plane-plane and plane-sphere geometry [91].

In this chapter we focus on the DA, the PFA and the DE. In order to avoid confusion, we will not use the acronyms DA and PFA interchangeably. We will rather define the PFA as the leading order asymptotic term of the DA for short distances. In Sec. 4.1, the common heuristic derivation of the DA is outlined in the example of two spheres. We then find the leading order contribution the PFA. Then, in Sec. 4.2, DE approach is discussed which can be understood as a systematic way of improving on the DA and thus also on the PFA. The DE is then illustrated for two dielectric spheres in the high temperature limit. The corresponding results for the PFA and DE in the plane-sphere geometry can be obtained as the limiting case for one sphere radius going to infinity.

4.1 Proximity-force approximation

Derjaguin proposed to determine the Casimir free energy between two non-planar surfaces by averaging the plane-plane free energy over the local distances [21]. With

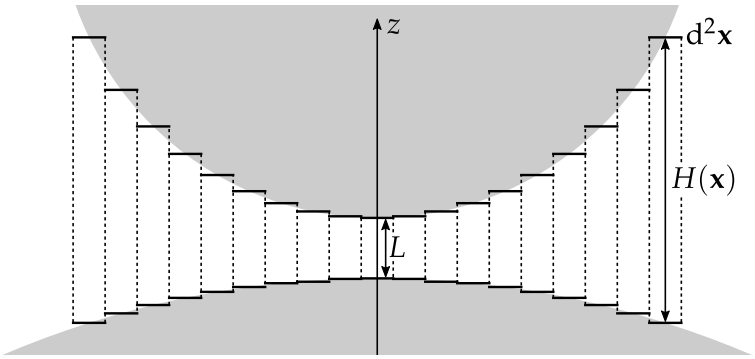

FIGURE 4.1: Within the DA the Casimir energy is expressed in terms of the energy of parallel planes averaged over the local distances $H(\mathbf{x})$ between the two non-planar surfaces.

the local-distance function $H(\mathbf{x})$ the DA free energy is given as

$$\mathcal{F}_{\mathrm{DA}} = \int_{\Sigma} \mathrm{d}^2\mathbf{x} \mathcal{F}_{\mathrm{PP}}(H(\mathbf{x}))\,, \tag{4.1}$$

where Σ is the area in the x-y-plane for which $H(\mathbf{x})$ is defined and $\mathcal{F}_{\mathrm{PP}}$ is the Casimir free energy per unit area between parallel planes as given in (3.29). In Fig. 4.1, the DA is illustrated for the example of two spheres with radii R_1 and R_2, respectively.

Due to rotational symmetry around the z-axis in the example of two spheres, it is convenient to parametrize the surface Σ in polar coordinates with radial component ρ and angular component ϕ. The radial component then runs from 0 to the smaller sphere radius. The local-distance function is independent of the angle and given by

$$H(\rho) = L + R_1 \left[1 - \sqrt{1 - (\rho/R_1)^2}\right] + R_2 \left[1 - \sqrt{1 - (\rho/R_2)^2}\right]\,. \tag{4.2}$$

Introducing the distance variable $l = H(\rho)$ and expanding the local-distance function around $\rho = 0$,

$$H(\rho) \approx L + \frac{1}{2R_{\mathrm{eff}}}\rho^2 + \mathcal{O}(\rho^4) \tag{4.3}$$

with the effective radius

$$R_{\mathrm{eff}} = \frac{R_1 R_2}{R_1 + R_2}\,, \tag{4.4}$$

yields the well-known PFA free energy for two spheres [92]

$$\mathcal{F}_{\mathrm{PFA}}(L) = 2\pi R_{\mathrm{eff}} \int_L^{\infty} \mathrm{d}l\, \mathcal{F}_{\mathrm{PP}}(l)\,. \tag{4.5}$$

Note that the upper integration limit was set to infinity here. In doing so, we account only for the leading order contribution in the limit of large radii. The integral can be performed and we obtain

$$\mathcal{F}_{\mathrm{PFA}}(L) = -R_{\mathrm{eff}} \frac{k_{\mathrm{B}}T}{2} {\sum_{n=0}^{\infty}}' \sum_{p\in\{\mathrm{TE,TM}\}} \int_0^{\infty} \mathrm{d}k\, \frac{k}{\kappa}\, \mathrm{Li}_2\left(r^{(1)}(i\xi_n,k) r^{(2)}(i\xi_n,k) e^{-2\kappa L}\right) \tag{4.6}$$

with the dilogarithm Li_2 (see Appendix A.3). The PFA force is then given by

$$F_{\mathrm{PFA}}(L) = 2\pi R_{\mathrm{eff}} \mathcal{F}_{\mathrm{PP}}(L)\,. \tag{4.7}$$

It is worth mentioning that one could also choose a curved surface as Σ such as the surface of either of the two surfaces. The pairs of infinitesimal surface elements are then not mutually parallel anymore. In the example of a plane and a sphere, it has been shown that the DA result depends on such choice, but the leading order PFA result does not [93]. In fact, the choice of a plane Σ which was made here is the base for the derivative expansion approach which we will discuss in the next section.

It is clear that the DA can only be an approximation to the Casimir interaction since the curvature of the surfaces is only partly taken into account through the distance function. The exact Casimir interaction should also take diffraction into account. Indeed diffraction effects are neglected within the DA since it involves only the interaction of parallel planes for which only specular reflection is considered. As a further consequence of the plane-plane geometry, polarization mixing is suppressed within the DA, which may in general give a contribution to the exact Casimir interaction.

Despite these shortcomings and the fact that the Casimir interaction is non-additive [22], it is remarkable that the PFA yet provides the correct leading order asymptotic behavior of the exact Casimir interaction. Starting from the exact scattering formula, we will prove in Sec. 6.3 that this is indeed true for the plane-sphere and the sphere-sphere geometry.

4.2 Derivative expansion

The derivative expansion approach has been first suggested to be used for the Casimir interaction in Ref. [41] where corrections to the Casimir energy for scalar fields obeying the Dirichlet boundary condition have been computed. The results agreed with those obtained from an asymptotic expansion of the exact Casimir energy in the plane-cylinder [36] and plane-sphere geometry [94]. The derivative expansion approach was soon generalized for the electromagnetic field where corrections to the Casimir interactions have been obtained for perfectly reflecting objects [42] and real materials [43]. A concise overview over the DE approach is given in [44] where also applications to nuclear and colloidal physics are discussed.

In Ref. [45] the DE approach was studied for the zero-frequency Matsubara contribution to the Casimir free energy which corresponds to the high temperature limit. It was found that the DE is applicable in this case only if the dielectric function of at least one of the two surfaces times the frequency squared goes to zero in the limit of vanishing frequencies, i.e. if $\omega^2\varepsilon(\omega) \to 0$ as $\omega \to 0$. This means that the DE is applicable for dielectrics and metals described by the Drude model, but not to two perfectly reflecting objects or metallic surfaces described by the plasma model.

More recently, Bimonte has suggested to use the DE for the calculation of the finite imaginary frequency contributions while using exact results or numerical methods for the evaluation of the zero-frequency contributions for metallic surfaces [46, 47, 95].

In this section, the DE approach will be described in more detail. First, we provide an outline of the method which will be rather formal. Then, we apply the DE approach to the Casimir free energy between two dielectric spheres in the high-temperature limit. In section 6.8, the results obtained here will be compared to an asymptotic expansion of the Casimir interaction between two spheres with radii much larger than the surface-to-surface distance.

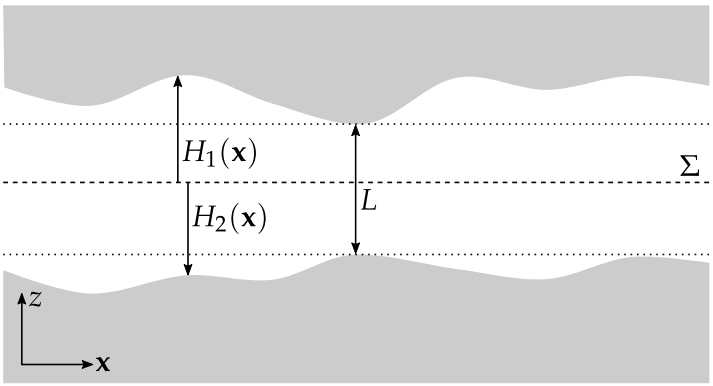

FIGURE 4.2: Parametrization of two opposing, gently curved surfaces with respect to a reference plane Σ. The distance of closest approach between the surfaces is denoted as L.

Outline of the method

We outline the DE approach following the expositions in Refs. [42–44, 46]. We consider two surfaces which are described by the smooth height profiles $z = H_1(\mathbf{x})$ and $z = H_2(\mathbf{x})$. Here, $\mathbf{x} = (x, y)$ are the coordinates spanning some reference plane Σ and the z-axis is chosen perpendicular to Σ (see Fig. 4.2). Because the two surfaces do not intersect, we can always assume that $H_2(\mathbf{x}) < H_1(\mathbf{x})$.

The Casimir free energy between the two surfaces can be expressed as a functional of the two height profiles, $\mathcal{F}[H_1, H_2]$. The idea behind the DE is that for surfaces of small slopes, $|\nabla H_i| \ll 1$ for $i = 1, 2$, the functional $\mathcal{F}[H_1, H_2]$ can be expanded in derivatives of the height profiles [41]. Considering that $\mathcal{F}[H_1, H_2]$ be invariant under simultaneous rotations and translations of H_1 and H_2 in the reference plane Σ, the most general expression for the derivative expansion up to second order in the derivatives of the height profiles takes the form [42, 46]

$$\mathcal{F}[H_1, H_2] = \int_\Sigma \mathrm{d}^2\mathbf{x}\big[\mathcal{F}_{\mathrm{PP}}(H) + \alpha_1(H)(\nabla H_1)^2 + \alpha_2(H)(\nabla H_2)^2 + \alpha_\times(H)\nabla H_1 \cdot \nabla H_2 + \alpha_-(H)(\nabla H_1 \times \nabla H_2)\cdot\hat{\mathbf{z}}\big] \quad (4.8)$$

where the difference between the height functions is denoted by $H \equiv H_1 - H_2$. Note that here, $\mathcal{F}_{\mathrm{PP}}$ and the α's can only be a function of H and not the individual height profiles to ensure that the $\mathcal{F}[H_1, H_2]$ is invariant under translation of the reference plane Σ along the z-direction.

The first term in (4.8) is precisely the DA as defined in Eq. (4.1). The integrals in (4.8) proportional to the α's represent curvature corrections beyond the DA. Note that for consistency and in order to find the correction to the PFA, we need to include the subleading term within the DA here and cannot neglect it like we did in Sec. 4.1.

The coefficients α are further constrained due to the invariance of $\mathcal{F}[H_1, H_2]$ with respect to tilting the reference plane Σ [42]:

$$\begin{aligned} 2\left[\alpha_1(H) + \alpha_2(H) + \alpha_\times(H)\right] + H\frac{\partial \mathcal{F}_{\mathrm{PP}}}{\partial H} - \mathcal{F}_{\mathrm{PP}} = 0\,, \\ \alpha_-(H) = 0\,. \end{aligned} \quad (4.9)$$

Using the above relations, we can eliminate $\alpha_\times$ and α_- in (4.8). The interaction between the two surfaces thus reduces to the simpler problem of a curved surface

in front of a plane for which case the coefficients α_1 and α_2 are determined (c.f. the derivation of α below).

We now make a simplification of the problem and assume both surfaces to be made of the same materials. Then

$$\alpha_1(H) = \alpha_2(H) \equiv \alpha(H)\,. \tag{4.10}$$

Using (4.9) and (4.10) the DE can be recast into the form

$$\mathcal{F}[H_1, H_2] = \mathcal{F}_{\mathrm{DA}} + \int_\Sigma \mathrm{d}^2\mathbf{x}\, \alpha(H)(\nabla H)^2 + \frac{1}{2}\int_\Sigma \mathrm{d}^2\mathbf{x}\, \left(\mathcal{F}_{\mathrm{PP}} - H\frac{\partial \mathcal{F}_{\mathrm{PP}}}{\partial H}\right) \nabla H_1 \cdot \nabla H_2\,. \tag{4.11}$$

where $\mathcal{F}_{\mathrm{DA}}$ is the Casimir free energy within the DA as given in (4.1).

The remaining unknown in the above expression is the coefficient $\alpha(H)$. It can be determined by a comparison of (4.11) with a perturbative expansion of the functional $\mathcal{F}[H, 0]$ with $H(\mathbf{x}) = L + h(\mathbf{x})$, which is the functional for a curved surface in front of a plane, to second order for small deformation amplitudes $h(\mathbf{x})$. Note that while this latter expansion relies on small amplitudes $h(\mathbf{x})/L \ll 1$, the DE as given in (4.11) assumes that the slopes of the surfaces are small. Nevertheless, both expansions can be shown to be formally equivalent by resumming the pertubative expansion for small in-plane momenta [44].

To second order in h, the perturbative expansion of the free energy is given by

$$\mathcal{F}[L + h(\mathbf{x}), 0] = A\mathcal{F}_{\mathrm{PP}}(L) + \mu(L)\tilde{h}(\mathbf{0}) + \int \frac{\mathrm{d}^2\mathbf{k}}{(2\pi)^2}\tilde{G}(k; L)|\tilde{h}(\mathbf{k})|^2 \tag{4.12}$$

where A is the surface area and $\mathbf{k}$ is the in-plane wave vector and $\tilde{h}(\mathbf{k})$ is the Fourier transform of $h(\mathbf{x})$. In order for the DE to work, it is now required that the kernel $\tilde{G}$ can be expanded up to second order in k,

$$\tilde{G}(k; L) = \gamma(L) + \delta(L)k^2 + o(k^2)\,. \tag{4.13}$$

If the second-order derivative in k of the kernel exists, we can obtain $\alpha(L)$ by matching (4.11) with (4.12) which yields

$$\mathcal{F}'_{\mathrm{PP}}(L) = \mu(L)\,, \quad \mathcal{F}''_{\mathrm{PP}}(L) = 2\gamma(L)\,, \quad \alpha(L) = \delta(L) \tag{4.14}$$

where the prime indicates a derivative with respect to the distance L.

Now, we have successfully reduced the problem of determining $\alpha(L)$ to the problem of finding the kernel $\tilde{G}$. At first sight, that may not seem like progress, but in fact the kernel can be determined using the scattering formalism for a gently curved surface in front of a plane. The matrix elements of the reflection operator on the gently curved surface can be expanded in powers of the height profile h as [43, 96]

$$\begin{aligned}\langle \mathbf{k}', p', -|\mathcal{R}^{(1)}|\mathbf{k}, p, -\rangle = {} & (2\pi)^2\delta(\mathbf{k} - \mathbf{k}')\delta_{pp'}r_p^{(1)}(i\xi_n, k) \\ & + \kappa\kappa'\Big[-2B_{pp'}(\mathbf{k}, \mathbf{k}')\tilde{h}(\mathbf{k} - \mathbf{k}') \\ & + \int \frac{\mathrm{d}^2\mathbf{k}''}{(2\pi)^2}(B_2)_{pp'}(\mathbf{k}, \mathbf{k}'; \mathbf{k}'')\tilde{h}(\mathbf{k} - \mathbf{k}'')\tilde{h}(\mathbf{k}'' - \mathbf{k}') + \dots\Big]\,.\end{aligned} \tag{4.15}$$

The coefficients $B_{pp'}(\mathbf{k},\mathbf{k}')$ and $(B_2)_{pp'}(\mathbf{k},\mathbf{k}';\mathbf{k}'')$ depend on the relative orientation of the in-plane wave vectors $\mathbf{k}$ and $\mathbf{k}'$, on the corresponding k and κ, and on the dielectric functions itself. Note that in Ref. [96] a slightly different notation is used: $B_{pp'} \to B^{22}_{\alpha\alpha_0}$ and $(B_2)_{pp'} \to i(B_2)^{22}_{\alpha\alpha_0}$. The coefficient $B_{pp'}$ is given in Eq. (4.15) in Ref. [96] and an expression for $(B_2)_{pp'}$ can be found in the Appendix D in Ref. [96].

Substituting the above expansion into the scattering formula (2.52), one obtains [43]

$$\tilde{G}(k;L) = k_\mathrm{B}T {\sum_{n=0}^{\infty}}' \int \frac{\mathrm{d}^2\mathbf{k}'}{(2\pi)^2} \frac{f_n(\mathbf{k}',\mathbf{k}'+\mathbf{k}) + f_n(\mathbf{k}',\mathbf{k}'-\mathbf{k})}{2} \tag{4.16}$$

where

$$f_n(\mathbf{k}',\mathbf{k}'') = -\sum_p \frac{\kappa' r_p^{(2)}(k')}{g_p(k')} e^{-2\kappa' L} \Big[(B_2)_{pp}(\mathbf{k}',\mathbf{k}';\mathbf{k}'') + 2\sum_{p'} \frac{\kappa'' r_{p'}^{(2)}(k'')}{g_{p'}(k'')} e^{-2\kappa'' L} B_{pp'}(\mathbf{k}',\mathbf{k}'') B_{p'p}(\mathbf{k}'',\mathbf{k}') \Big] \tag{4.17}$$

with $g_p(k) = 1 - r_p^{(1)} r_p^{(2)} \exp(-2\kappa L)$. For brevity, the explicit dependence on $i\xi_n$ of several quantities was dropped. Now that we have found an expression for the kernel $\tilde{G}(k;L)$, the coefficient $\alpha(L)$ can be found by evaluation of the second order derivative

$$\alpha(L) = \frac{1}{2} \frac{\partial^2 \tilde{G}}{\partial k^2}\bigg|_{k=0} = \frac{k_\mathrm{B}T}{2} {\sum_{n=0}^{\infty}}' \int \frac{\mathrm{d}^2\mathbf{k}'}{(2\pi)^2} \frac{\partial^2 f_n(\mathbf{k}',\mathbf{k}'+\mathbf{k})}{\partial k^2}\bigg|_{k=0} . \tag{4.18}$$

Note that an alternative approach on deriving the kernel $\tilde{G}$ is provided in Ref. [97] where roughness effects in the plane-plane geometry were studied.

Application to two dielectric spheres at high temperatures

Derivation of α and $\mathcal{F}_\mathrm{PP}/A$ for dielectrics

In the limit of high temperatures only the zero-Matsubara frequency contributes. For dielectrics, the TE contribution vanishes and the relevant scattering coefficients are then [45, Eq. (A4)]

$$\begin{aligned} B_{\mathrm{TM,TM}}(\mathbf{k},\mathbf{k}') &= -\frac{r_\mathrm{TM}}{\varepsilon+1}\left(\varepsilon + \frac{\mathbf{k}\cdot\mathbf{k}'}{kk'}\right) \\ (B_2)_{\mathrm{TM,TM}}(\mathbf{k},\mathbf{k};\mathbf{k}') &= \frac{2r_\mathrm{TM}}{(\varepsilon+1)k^2}\left[\frac{r_\mathrm{TM}}{k'}\left(\varepsilon k^2 k'^2 - (\mathbf{k}\cdot\mathbf{k}')^2\right) + \frac{4\varepsilon k}{\varepsilon+1}\mathbf{k}\cdot\mathbf{k}'\right] \end{aligned} \tag{4.19}$$

with relative permittivity $\varepsilon = \varepsilon(0)$ and the Fresnel coefficient (see Sec. 3.3)

$$r_\mathrm{TM} = \frac{\varepsilon - 1}{\varepsilon + 1} . \tag{4.20}$$

With that at hand, we can evaluate the $n = 0$ Matsubara contribution for $\alpha(L)$ in (4.18).

For convenience, we choose a coordinate system such that $\mathbf{k}$ is aligned with the x-axis. Using polar coordinates we can then write

$$\begin{aligned} \mathbf{k}' \cdot (\mathbf{k}' + \mathbf{k}) &= k'^2 + kk' \cos(\theta) \,, \\ |\mathbf{k}' + \mathbf{k}| &= \sqrt{k'^2 + k^2 + 2kk' \cos(\theta)} \,, \end{aligned} \tag{4.21}$$

where θ is the polar angle of $\mathbf{k}'$. We carry the following calculation out using Mathematica [98].

After computing the second derivative of f_0 defined in (4.17) with subsequent evaluation at $k = 0$, the integral over θ can be carried out. By introducing the rescaled variable $q = Lk'$, we find

$$\alpha(L) = -\frac{k_\mathrm{B} T}{8\pi L^2} a(\varepsilon) \tag{4.22}$$

with

$$a(\varepsilon) = r_\mathrm{TM}^3 \int_0^\infty \mathrm{d}q \, q \, e^{-2q} \frac{1 + 2r_\mathrm{TM} \left(2q^2 - 3q - r_\mathrm{TM}\right) e^{-2q} + r_\mathrm{TM}^3 \left(4q^2 + 6q + r_\mathrm{TM}\right) e^{-4q}}{\left(1 - r_\mathrm{TM}^2 e^{-2q}\right)^4} \,. \tag{4.23}$$

In the limit of $\varepsilon \to \infty$, i.e. $r_\mathrm{TM} \to 1$, the integral becomes

$$a^{(\mathrm{D})} = \int_0^\infty \mathrm{d}q \, q \, e^{-2q} \frac{1 + 2\left(2q^2 - 3q - 1\right) e^{-2q} + \left(4q^2 + 6q + 1\right) e^{-4q}}{\left(1 - e^{-2q}\right)^4} = \frac{1 + 6\,\zeta(3)}{24} \,. \tag{4.24}$$

In this limit, the known result for a Dirichlet scalar field is recovered [45, 99]

$$\alpha^{(\mathrm{D})}(L) = -\frac{k_\mathrm{B} T}{192\pi L^2} [1 + 6\,\zeta(3)] \approx -0.0136 \, \frac{k_\mathrm{B} T}{L^2} \,. \tag{4.25}$$

However, we find that the limit of $\varepsilon \to \infty$ does not yield the same expression if taken after computing derivative expansion. This can be seen in Fig. 4.3 (a) where α is plotted as a function of the relative permittivity. In the figure, $\alpha(\varepsilon \to \infty) \approx -0.0120 \, k_\mathrm{B} T / L^2$, which is different from $\alpha^{(\mathrm{D})}$ corresponding to the dashed line. Note that this finding does not agree with the results from Ref. [45] where α (called Z_s there) converges to the Dirichlet value as $\varepsilon \to \infty$. We will see in Sec. 7.2, however, that our result obtained here matches with the results from numerical calculations.

In the opposite limit, $\varepsilon \to 0$, the field obeys the Neumann boundary conditions for which the DE is known to break down [45, 99]. This can also be seen in Fig. 4.3 (b) by the fact that α diverges in this limit.

To find the correction beyond PFA with the DE, we will also need an expression for the Casimir free energy between two parallel dielectric planes in the high-temperature limit. In view of (3.29), we have

$$\mathcal{F}_\mathrm{PP} = \frac{k_\mathrm{B} T}{2} \int_0^\infty \frac{\mathrm{d}k}{2\pi} k \log\left(1 - r_\mathrm{TM}^2 e^{-2kL}\right) \,. \tag{4.26}$$

Since r_TM does not depend on k, we can carry out the integration to find

$$\mathcal{F}_\mathrm{PP} = -\frac{k_\mathrm{B} T}{16\pi L^2} \, \mathrm{Li}_3(r_\mathrm{TM}^2) \,, \tag{4.27}$$

where Li_3 is the trilogarithm.

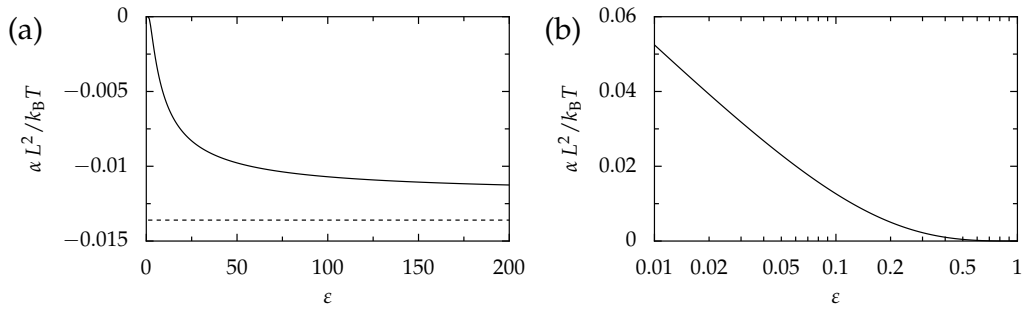

FIGURE 4.3: The function α in the high temperature limit for two identical dielectrics as a function of the relative permittivity for (a) $\varepsilon > 1$ with the dashed line being the limiting case for the Dirichlet scalar field and (b) $\varepsilon < 1$.

Correction to the PFA for two spheres

Since we now have found expressions for α and $\mathcal{F}_{\mathrm{PP}}/A$, we are fully equipped to find the DE for any smooth geometry of two dielectric bodies in the high-temperature limit. Here, we will focus on the geometry of two spheres which includes the geometry of a plane and a sphere as a limiting case.

The remaining task is to evaluate the integrals in (4.11). Since α and $\mathcal{F}_{\mathrm{PP}}/A$ are both proportional to H^{-2}, the integrals which need to be solved are of the form

$$\int_\Sigma \mathrm{d}^2\mathbf{x}\frac{1}{H^2}\,, \quad \int_\Sigma \mathrm{d}^2\mathbf{x}\frac{(\nabla H)^2}{H^2}\,, \quad \int_\Sigma \mathrm{d}^2\mathbf{x}\frac{\nabla H_1\cdot\nabla H_2}{H^2}\,. \tag{4.28}$$

It is convenient to use polar coordinates due to the axial symmetry of the problem. Then, the integration over the polar coordinates yields a factor of 2π. We choose the reference plane Σ at the point on the surface of sphere 2, which is closest to sphere 1, such that the surfaces can be parametrized in terms of the radial coordinate ρ:

$$\begin{aligned} H_1(\rho) &= L + R_1\left[1-\sqrt{1-(\rho/R_1)^2}\right]\,,\\ H_2(\rho) &= -R_2\left[1-\sqrt{1-(\rho/R_2)^2}\right]\,. \end{aligned} \tag{4.29}$$

For the integration over the radial component ρ we cannot perform the integration up to the smaller radius R_1 since then the derivative of the height profiles would diverge. The integration interval thus needs to be bounded by some $\rho_{\max} < R_1$. Fortunately, the leading and subleading order term within the DE will not depend on the value of $\rho_{\max}$.

Assuming that the Casimir interaction is localized near the point of closest approach, we expand the gradients of the height profiles for small ρ:

$$(\nabla H)^2 \sim \frac{\rho^2}{R_{\mathrm{eff}}^2}\,, \qquad \nabla H_1\cdot\nabla H_2 \sim -\frac{\rho^2}{R_1R_2}\,. \tag{4.30}$$

In fact, if we would take the exact expressions for the gradients, the integrals would not yield a finite value. Using (4.30) with the exact expression for the height profile

$H = H_1 - H_2$, we find

$$\begin{aligned}\int_\Sigma \mathrm{d}^2\mathbf{x}\frac{1}{H^2} &\sim 2\pi\left[\frac{R_{\mathrm{eff}}}{L} - (1-3u)\log\left(\frac{R_{\mathrm{eff}}}{L}\right)\right],\\ \int_\Sigma \mathrm{d}^2\mathbf{x}\frac{(\nabla H)^2}{H^2} &\sim 4\pi\log\left(\frac{R_{\mathrm{eff}}}{L}\right),\\ \int_\Sigma \mathrm{d}^2\mathbf{x}\frac{\nabla H_1\cdot\nabla H_2}{H^2} &\sim -4\pi u\log\left(\frac{R_{\mathrm{eff}}}{L}\right)\end{aligned} \tag{4.31}$$

with the dimensionless quantity

$$u = \frac{R_{\mathrm{eff}}^2}{R_1R_2} = \frac{R_1R_2}{(R_1+R_2)^2}\,. \tag{4.32}$$

The individual contributions to (4.11) are then

$$\begin{aligned}\mathcal{F}_{\mathrm{DA}} &\sim -\frac{k_{\mathrm{B}}T}{8}\,\mathrm{Li}_3(r_{\mathrm{TM}}^2)\left[\frac{R_{\mathrm{eff}}}{L} - (1-3u)\log\left(\frac{R_{\mathrm{eff}}}{L}\right)\right],\\ \int_\Sigma \mathrm{d}^2\mathbf{x}\alpha(H)(\nabla H)^2 &\sim -\frac{k_{\mathrm{B}}T}{2}a(\varepsilon)\log\left(\frac{R_{\mathrm{eff}}}{L}\right)\end{aligned} \tag{4.33}$$

and

$$\frac{1}{2}\int_\Sigma \mathrm{d}^2\mathbf{x}\left(\mathcal{F}_{\mathrm{PP}} - H\frac{\partial\mathcal{F}_{\mathrm{PP}}}{\partial H}\right)\nabla H_1\cdot\nabla H_2 \sim \frac{3k_{\mathrm{B}}T}{8}\,\mathrm{Li}_3(r_{\mathrm{TM}}^2)u\log\left(\frac{R_{\mathrm{eff}}}{L}\right). \tag{4.34}$$

The final result for the Casimir free energy between two dielectric spheres then reads

$$\mathcal{F} \sim \mathcal{F}_{\mathrm{PFA}} + \mathcal{F}_1 \tag{4.35}$$

with the PFA

$$\mathcal{F}_{\mathrm{PFA}} = -\frac{k_{\mathrm{B}}T}{8}\,\mathrm{Li}_3(r_{\mathrm{TM}}^2)\frac{R_{\mathrm{eff}}}{L} \tag{4.36}$$

and the first correction to the PFA

$$\mathcal{F}_1 = \frac{k_{\mathrm{B}}T}{8}\left[\mathrm{Li}_3(r_{\mathrm{TM}}^2) - 4a(\varepsilon)\right]\log\left(\frac{R_{\mathrm{eff}}}{L}\right). \tag{4.37}$$

Interestingly, like for the PFA, the dependence on u drops out for the correction and it only depends on the sphere radii through the effective radius R_{eff}. When we send $\varepsilon \to \infty$, the result is consistent with a short-distance expansion of the exact result for two spheres with Dirichlet boundary condition [46].

The result for the plane-sphere geometry can be obtained by formally sending one sphere radius to infinity. The effective radius then becomes the radius of the remaining sphere, $R_{\mathrm{eff}} \to R$.

Chapter 5

Scattering at a sphere

The goal of the subsequent chapters is to study the Casimir interaction in the sphere-sphere and the plane-sphere geometry within the scattering formalism. The scattering formula requires the reflection matrix elements for a sphere, which will be derived in this chapter.

We start out by introducing the sphere scattering matrix elements for planar waves. These scattering matrix elements involve the well-known Mie scattering amplitudes. The exact reflection matrix elements are then given for imaginary frequencies and expressions in the low-frequency limit are worked out. For the asymptotic expansion of the Casimir interaction between two spheres for short distances in Ch. 6, the asymptotics of the reflection matrix elements for large radii are needed. The asymptotics of the Mie scattering amplitudes in the real frequency domain is known from the literature. The leading order term in the asymptotic expansion can be derived within a WKB approximation allowing an interpretation within a geometric optical picture, while the first correction takes diffraction into account.

After a brief review of these results from the literature, it is shown that the leading order WKB approximation evaluated at imaginary frequencies agrees with the asymptotic expressions derived from the scattering amplitudes at imaginary frequencies. While this is also true for the first correction to the WKB approximation when the sphere is perfectly reflecting, our results for the correction for general dielectric spheres differ from the ones found in the literature. The chapter is concluded by giving the expression of the reflection matrix elements for large spheres at imaginary frequencies.

5.1 Scattering matrix elements

Consider a plane wave with wave vector $\mathbf{K}^{(\mathrm{in})}$ and electric field $\mathbf{E}^{(\mathrm{in})}$ incident on a sphere with radius R and a scattered plane wave with wave vector $\mathbf{K}^{(\mathrm{sc})}$ and electric field $\mathbf{E}^{(\mathrm{sc})}$. The pair of wave vectors $(\mathbf{K}^{(\mathrm{in})}, \mathbf{K}^{(\mathrm{sc})})$ forms the scattering plane. The angle between the two vectors in that scattering plane is the scattering angle Θ. The setup is depicted in Fig. 5.1. Note that the scattering plane is not defined if $\Theta = 0$ and π that is when the vectors a collinear.

To describe the scattering of plane waves on a sphere, it is convenient to make use of a polarization basis which is defined with respect to the scattering plane. The polarization components can then be defined to be parallel or perpendicular to that plane. The perpendicular polarization vector is identical for the incident and scattered wave, but the parallel polarization vector is in general different. The polarization unit vectors are shown for the incident and scattered wave vector in

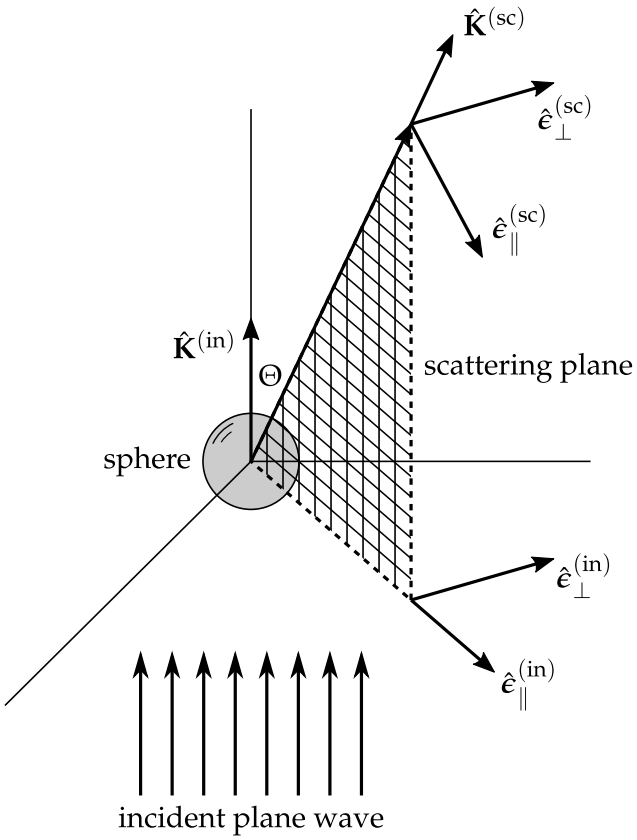

FIGURE 5.1: Schematic representation of an incident and scattered plane wave on a sphere. The wave vectors of the incident and scattered plane waves, $\mathbf{K}^{(\mathrm{in})}$ and $\mathbf{K}^{(\mathrm{sc})}$, respectively, define a scattering plane. The angle between the two wave vectors is the scattering angle Θ. The polarization basis $\{\hat{\boldsymbol{\epsilon}}_{\parallel}, \hat{\boldsymbol{\epsilon}}_{\perp}\}$ is defined with respect to the scattering plane.

Fig 5.1. Specifically, we define

$$\begin{aligned}\hat{\boldsymbol{\epsilon}}_{\perp}^{(\mathrm{in})} &= \hat{\boldsymbol{\epsilon}}_{\perp}^{(\mathrm{sc})} = \frac{\hat{\mathbf{K}}^{(\mathrm{sc})} \times \hat{\mathbf{K}}^{(\mathrm{in})}}{|\hat{\mathbf{K}}^{(\mathrm{sc})} \times \hat{\mathbf{K}}^{(\mathrm{in})}|}\,, \\ \hat{\boldsymbol{\epsilon}}_{\parallel}^{(\mathrm{in})} &= \hat{\boldsymbol{\epsilon}}_{\perp}^{(\mathrm{in})} \times \hat{\mathbf{K}}^{(\mathrm{in})}\,, \\ \hat{\boldsymbol{\epsilon}}_{\parallel}^{(\mathrm{sc})} &= \hat{\boldsymbol{\epsilon}}_{\perp}^{(\mathrm{sc})} \times \hat{\mathbf{K}}^{(\mathrm{sc})}\,.\end{aligned} \tag{5.1}$$

The three vectors $(\hat{\boldsymbol{\epsilon}}_{\parallel}, \hat{\boldsymbol{\epsilon}}_{\perp}, \hat{\mathbf{K}})$ then form a right-handed triad. One can now decompose the electric field vectors $\mathbf{E}^{(\mathrm{in})}$ and $\mathbf{E}^{(\mathrm{sc})}$ with respect to the polarization basis (5.1). A similar decomposition can be found for the magnetic field vectors.

The linearity of the Maxwell's equations implies that the scattering process mixes the field components $E_{\perp}$ and $E_{\parallel}$ in a linear way. The relation between incident and scattered fields can then be written in matrix form. If the origin of the coordinate system is placed at the sphere center, this relation reads [81, 100]

$$\begin{pmatrix} E_{\parallel}^{(\mathrm{sc})} \\ E_{\perp}^{(\mathrm{sc})} \end{pmatrix} = \frac{e^{iK|\mathbf{R}|}}{-iK|\mathbf{R}|} \begin{pmatrix} S_2 & 0 \\ 0 & S_1 \end{pmatrix} \begin{pmatrix} E_{\parallel}^{(\mathrm{in})} \\ E_{\perp}^{(\mathrm{in})} \end{pmatrix}\,. \tag{5.2}$$

where $|\mathbf{R}| = \sqrt{x^2+y^2+z^2}$. The scattering matrix is diagonal for the polarization basis perpendicular and parallel to the scattering plane. The scattered field is a spherical wave where the amplitudes in each direction is modulated by the scattering amplitudes S_1 and S_2 which are functions of the size parameter KR and the scattering angle Θ. The scattering amplitudes are defined in terms of the expansion of partial waves with angular momentum ℓ and read [81, 100]

$$\begin{aligned} S_1 &= \sum_{\ell=1}^{\infty} \frac{2\ell+1}{\ell(\ell+1)} \left[a_\ell(KR)\pi_\ell(\cos(\Theta)) + b_\ell(KR)\tau_\ell(\cos(\Theta))\right]\,, \\ S_2 &= \sum_{\ell=1}^{\infty} \frac{2\ell+1}{\ell(\ell+1)} \left[a_\ell(KR)\tau_\ell(\cos(\Theta)) + b_\ell(KR)\pi_\ell(\cos(\Theta))\right]\,. \end{aligned} \tag{5.3}$$

Here, a_ℓ and b_ℓ are the partial-wave scattering amplitudes, called Mie coefficients, for electric and magnetic polarization, respectively. Explicit expressions for the Mie coefficients for imaginary frequencies will be given in Sec. 5.2. The angular distribution of the scattered radiations is described by the functions [81]

$$\begin{aligned} \pi_\ell(z) &= P_\ell{}'(z) \\ \tau_\ell(z) &= -(1-z^2)P_\ell{}''(z) + zP_\ell{}'(z)\,, \end{aligned} \tag{5.4}$$

where $P_\ell(z)$ are Legendre polynomials and the prime indicates a derivative with respect to the argument $z = \cos(\Theta)$. The functions $\pi_\ell(z)$ and $\tau_\ell(z)$ are thus usually called angular functions.

Within the angular spectrum representation, the scattering angle Θ is defined through the relation

$$\cos(\Theta) = \frac{1}{K^2}\left(\mathbf{k}^{(\mathrm{in})} \cdot \mathbf{k}^{(\mathrm{sc})} + \phi^{(\mathrm{in})}\phi^{(\mathrm{sc})}k_z^{(\mathrm{in})}k_z^{(\mathrm{sc})}\right)\,. \tag{5.5}$$

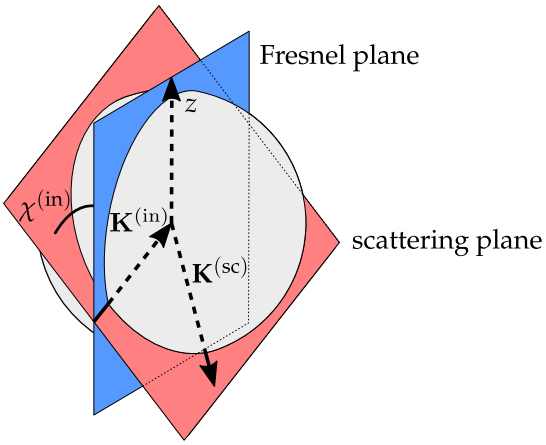

FIGURE 5.2: The Fresnel plane for the incoming wave vector $\mathbf{K}^{(\mathrm{in})}$ in general does not coincide with the scattering plane. The two planes are at an angle $\chi^{(\mathrm{in})}$. The corresponding Fresnel plane for the scattered wave vector $\mathbf{K}^{(\mathrm{sc})}$ is not shown. (from [104])

Using Weyl's identity [101], the spherical wave can be expanded in terms of the angular spectrum representation for planar waves [102, §2.2.2]

$$\frac{e^{iKr}}{-iKr} = -\int \frac{\mathrm{d}^2\mathbf{k}}{(2\pi)^2}\frac{2\pi}{Kk_z}e^{i(\mathbf{k}\cdot\mathbf{r}+\phi k_z z)}\,, \tag{5.6}$$

which also includes evanescent waves. Note that for evanescent waves the scattering angle Θ defined by (5.5) does not correspond to an actual angle like it does for propagating waves.

Within the angular spectrum representation, the matrix elements of the sphere scattering matrix $\mathbf{S}_\mathrm{S}$ can now be identified as [103]

$$\begin{aligned}\langle \mathbf{k}^{(\mathrm{sc})}, \phi^{(\mathrm{sc})}, \parallel |\mathbf{S}_\mathrm{S}| \mathbf{k}^{(\mathrm{in})}, \phi^{(\mathrm{in})}, \parallel \rangle &= -\frac{2\pi}{Kk_z^{(\mathrm{sc})}} S_2\,,\\ \langle \mathbf{k}^{(\mathrm{sc})}, \phi^{(\mathrm{sc})}, \perp |\mathbf{S}_\mathrm{S}| \mathbf{k}^{(\mathrm{in})}, \phi^{(\mathrm{in})}, \perp \rangle &= -\frac{2\pi}{Kk_z^{(\mathrm{sc})}} S_1\,.\end{aligned} \tag{5.7}$$

Note that, because the frequency ω is conserved upon scattering, it was dropped in the notation of the plane-wave basis elements.

For the purpose of applying these results to the Casimir effect, the polarization basis (5.1) is not convenient as it depends on both the incident and scattered wave vector. The TE-TM polarization basis defined in Eq. (3.1) is better suited because once the z-axis is fixed, the polarization components only depend on the wave vector itself. Obviously, this choice is convenient for plane-sphere geometry because scattering at the plane is already diagonal with respect to this polarization basis. When two spheres are involved, the TE-TM polarization basis is also very practical for describing the round trip because then the scattered mode from one sphere is identical to the incident mode on the other sphere. Inspired by the scattering on a plane, we denote the plane spanned by the wave vector and the z-axis as Fresnel plane.

In order to express the scattering matrix elements (5.7) in terms of the TE-TM-polarization basis, we need to perform the rotation

$$\begin{pmatrix} \hat{\boldsymbol{\epsilon}}_{\mathrm{TM}} \\ \hat{\boldsymbol{\epsilon}}_{\mathrm{TE}} \end{pmatrix} = \begin{pmatrix} \cos(\chi) & -\sin(\chi) \\ \sin(\chi) & \cos(\chi) \end{pmatrix} \begin{pmatrix} \hat{\boldsymbol{\epsilon}}_{\parallel} \\ \hat{\boldsymbol{\epsilon}}_{\perp} \end{pmatrix} \tag{5.8}$$

on both the incident and scattered modes. Noting that the field components then transform with the inverse rotation matrix, the scattering matrix elements with respect to the TE and TM polarization can be expressed as

$$\langle \mathbf{k}^{(\mathrm{sc})}, \phi^{(\mathrm{sc})}, \mathrm{TM} | \mathbf{S}_{\mathrm{S}} | \mathbf{k}^{(\mathrm{in})}, \phi^{(\mathrm{in})}, \mathrm{TM} \rangle = -\frac{2\pi}{K k_z^{(\mathrm{sc})}} \left(A S_2 + B S_1 \right) , \tag{5.9a}$$

$$\langle \mathbf{k}^{(\mathrm{sc})}, \phi^{(\mathrm{sc})}, \mathrm{TE} | \mathbf{S}_{\mathrm{S}} | \mathbf{k}^{(\mathrm{in})}, \phi^{(\mathrm{in})}, \mathrm{TE} \rangle = -\frac{2\pi}{K k_z^{(\mathrm{sc})}} \left(A S_1 + B S_2 \right) , \tag{5.9b}$$

$$\langle \mathbf{k}^{(\mathrm{sc})}, \phi^{(\mathrm{sc})}, \mathrm{TM} | \mathbf{S}_{\mathrm{S}} | \mathbf{k}^{(\mathrm{in})}, \phi^{(\mathrm{in})}, \mathrm{TE} \rangle = +\frac{2\pi}{K k_z^{(\mathrm{sc})}} \left(C S_1 + D S_2 \right) , \tag{5.9c}$$

$$\langle \mathbf{k}^{(\mathrm{sc})}, \phi^{(\mathrm{sc})}, \mathrm{TE} | \mathbf{S}_{\mathrm{S}} | \mathbf{k}^{(\mathrm{in})}, \phi^{(\mathrm{in})}, \mathrm{TM} \rangle = -\frac{2\pi}{K k_z^{(\mathrm{sc})}} \left(C S_2 + D S_1 \right) , \tag{5.9d}$$

where the rotation between the polarization bases is described by the coefficients

$$\begin{aligned} A &= \cos(\chi^{(\mathrm{sc})}) \cos(\chi^{(\mathrm{in})}) , \\ B &= \sin(\chi^{(\mathrm{sc})}) \sin(\chi^{(\mathrm{in})}) , \\ C &= -\sin(\chi^{(\mathrm{sc})}) \cos(\chi^{(\mathrm{in})}) , \\ D &= \cos(\chi^{(\mathrm{sc})}) \sin(\chi^{(\mathrm{in})}) \end{aligned} \tag{5.10}$$

with $\chi^{(\mathrm{in})}$ and $\chi^{(\mathrm{sc})}$ being the angles between the Fresnel and scattering plane for the incident and scattered wave vectors, respectively. Note that $\chi^{(\mathrm{in})}$ and $\chi^{(\mathrm{sc})}$ depend on both wave vectors $\mathbf{K}^{(\mathrm{in})}$ and $\mathbf{K}^{(\mathrm{sc})}$, but explicit expressions for the angles will not be needed. However, expressions for the coefficients A, B, C and D as functions of the incident and scattered wave vectors will be needed. Those are worked out in Appendix C.1.

The effect of TE-TM polarization mixing is controlled by the angles $\chi^{(\mathrm{in})}$ and $\chi^{(\mathrm{sc})}$ and only appears when those angles do not vanish.

The scattering matrix elements at the sphere are not all mutually independent as they need to fulfill reciprocity relations [55, 105, 106]. To check for consistency, we now verify that the reciprocity relations are fulfilled. These relations read

$$\begin{aligned} k_z^{(\mathrm{sc})} &\langle \mathbf{k}^{(\mathrm{sc})}, \phi^{(\mathrm{sc})}, p^{(\mathrm{sc})} | \mathbf{S}_{\mathrm{S}} | \mathbf{k}^{(\mathrm{in})}, \phi^{(\mathrm{in})}, p^{(\mathrm{in})} \rangle \\ &= (-1)^{p^{(\mathrm{sc})}+p^{(\mathrm{in})}} k_z^{(\mathrm{in})} \langle -\mathbf{k}^{(\mathrm{in})}, -\phi^{(\mathrm{in})}, p^{(\mathrm{in})} | \mathbf{S}_{\mathrm{S}} | -\mathbf{k}^{(\mathrm{sc})}, -\phi^{(\mathrm{sc})}, p^{(\mathrm{sc})} \rangle \end{aligned} \tag{5.11}$$

where $(-1)^{p^{(\mathrm{sc})}+p^{(\mathrm{in})}}$ is $+1$ if the polarizations are equal and -1 otherwise. When $(\mathbf{K}^{(\mathrm{sc})}, \mathbf{K}^{(\mathrm{in})})$ is mapped to $(-\mathbf{K}^{(\mathrm{in})}, -\mathbf{K}^{(\mathrm{sc})})$ the angles between the incident and scattering plane change as

$$\begin{aligned} \chi^{(\mathrm{sc})} &\to -\chi^{(\mathrm{in})} , \\ \chi^{(\mathrm{in})} &\to -\chi^{(\mathrm{sc})} . \end{aligned} \tag{5.12}$$

Then, the polarization transformation coefficients are mapped as

$$\begin{aligned} A &\to A\,, \\ B &\to B\,, \\ C &\to D\,, \\ D &\to C\,. \end{aligned} \tag{5.13}$$

Because moreover the scattering angle Θ stays invariant under such transformation, the reciprocity relations are readily verified for the scattering matrix elements (5.9).

5.2 Reflection matrix elements at imaginary frequencies

The evaluation of the scattering formula requires the matrix elements for a reflection on the sphere. Those reflection matrix elements are obtained from the scattering matrix elements for which the direction of propagation along the z-axis changes between the incident and scattered wave vector, i.e. $\phi^{(\mathrm{in})}$ and $\phi^{(\mathrm{sc})}$ have opposite sign. At imaginary frequencies, the reflection matrix elements read

$$\langle \mathbf{k}^{(\mathrm{sc})}, \mp, \mathrm{TM} | \mathcal{R}_\mathrm{S} | \mathbf{k}^{(\mathrm{in})}, \pm, \mathrm{TM} \rangle = \frac{2\pi}{\mathcal{K}\kappa^{(\mathrm{sc})}} \left(A S_2 + B S_1 \right) , \tag{5.14a}$$

$$\langle \mathbf{k}^{(\mathrm{sc})}, \mp, \mathrm{TE} | \mathcal{R}_\mathrm{S} | \mathbf{k}^{(\mathrm{in})}, \pm, \mathrm{TE} \rangle = \frac{2\pi}{\mathcal{K}\kappa^{(\mathrm{sc})}} \left(A S_1 + B S_2 \right) , \tag{5.14b}$$

$$\langle \mathbf{k}^{(\mathrm{sc})}, \mp, \mathrm{TM} | \mathcal{R}_\mathrm{S} | \mathbf{k}^{(\mathrm{in})}, \pm, \mathrm{TE} \rangle = -\frac{2\pi}{\mathcal{K}\kappa^{(\mathrm{sc})}} \left(C S_1 + D S_2 \right) , \tag{5.14c}$$

$$\langle \mathbf{k}^{(\mathrm{sc})}, \mp, \mathrm{TE} | \mathcal{R}_\mathrm{S} | \mathbf{k}^{(\mathrm{in})}, \pm, \mathrm{TM} \rangle = \frac{2\pi}{\mathcal{K}\kappa^{(\mathrm{sc})}} \left(C S_2 + D S_1 \right) . \tag{5.14d}$$

In polar coordinates, $\mathbf{k}^{(\mathrm{in})} = (k^{(\mathrm{in})}, \varphi^{(\mathrm{in})})$ and $\mathbf{k}^{(\mathrm{sc})} = (k^{(\mathrm{sc})}, \varphi^{(\mathrm{sc})})$, the polarization transformation coefficients derived in appendix C.1 are given by

$$\begin{aligned} A &= \frac{\mathcal{K}^4 \cos(\varphi) - [k^{(\mathrm{in})} k^{(\mathrm{sc})} \cos(\varphi) - \kappa^{(\mathrm{in})} \kappa^{(\mathrm{sc})}][k^{(\mathrm{in})} k^{(\mathrm{sc})} - \kappa^{(\mathrm{in})} \kappa^{(\mathrm{sc})} \cos(\varphi)]}{\mathcal{K}^4 - [k^{(\mathrm{in})} k^{(\mathrm{sc})} \cos(\varphi) - \kappa^{(\mathrm{in})} \kappa^{(\mathrm{sc})}]^2} , \\ B &= -\frac{\mathcal{K}^2 k^{(\mathrm{in})} k^{(\mathrm{sc})} \sin^2(\varphi)}{\mathcal{K}^4 - [k^{(\mathrm{in})} k^{(\mathrm{sc})} \cos(\varphi) - \kappa^{(\mathrm{in})} \kappa^{(\mathrm{sc})}]^2} , \\ C &= \pm \mathcal{K} \sin(\varphi) \frac{k^{(\mathrm{in})} k^{(\mathrm{sc})} \kappa^{(\mathrm{in})} \cos(\varphi) + (k^{(\mathrm{in})})^2 \kappa^{(\mathrm{sc})}}{\mathcal{K}^4 - [k^{(\mathrm{in})} k^{(\mathrm{sc})} \cos(\varphi) - \kappa^{(\mathrm{in})} \kappa^{(\mathrm{sc})}]^2} , \\ D &= \mp \mathcal{K} \sin(\varphi) \frac{k^{(\mathrm{in})} k^{(\mathrm{sc})} \kappa^{(\mathrm{sc})} \cos(\varphi) + (k^{(\mathrm{sc})})^2 \kappa^{(\mathrm{in})}}{\mathcal{K}^4 - [k^{(\mathrm{in})} k^{(\mathrm{sc})} \cos(\varphi) - \kappa^{(\mathrm{in})} \kappa^{(\mathrm{sc})}]^2} , \end{aligned} \tag{5.15}$$

where $\varphi = \varphi^{(\mathrm{sc})} - \varphi^{(\mathrm{in})}$. The upper sign in the coefficients C and D is taken for an incident plane wave traveling in positive z-direction, while the lower sign is reserved for incident plane waves traveling in the opposite direction.

Corresponding expressions for the coefficients A, B, C and D for Cartesian coordinates, $\mathbf{k}^{(\mathrm{in})} = (k_x^{(\mathrm{in})}, k_y^{(\mathrm{in})})$ and $\mathbf{k}^{(\mathrm{sc})} = (k_x^{(\mathrm{sc})}, k_y^{(\mathrm{sc})})$, can be found by replacing

$$\begin{aligned} k^{(\mathrm{in/sc})} &= \sqrt{\left(k_x^{(\mathrm{in/sc})}\right)^2 + \left(k_y^{(\mathrm{in/sc})}\right)^2}, \\ \cos(\varphi) &= \frac{k_x^{(\mathrm{in})} k_x^{(\mathrm{sc})} + k_y^{(\mathrm{in})} k_y^{(\mathrm{sc})}}{k^{(\mathrm{in})} k^{(\mathrm{sc})}}, \\ \sin(\varphi) &= \frac{k_x^{(\mathrm{in})} k_y^{(\mathrm{sc})} - k_x^{(\mathrm{sc})} k_y^{(\mathrm{in})}}{k^{(\mathrm{in})} k^{(\mathrm{sc})}}. \end{aligned} \tag{5.16}$$

At imaginary frequencies, the angular functions π_ℓ and τ_ℓ appearing in the Mie scattering amplitudes (5.3) are evaluated at

$$\cos(\Theta) = -\frac{1}{\mathcal{K}^2}\left(\mathbf{k}^{(\mathrm{in})} \cdot \mathbf{k}^{(\mathrm{sc})} + \kappa^{(\mathrm{in})}\kappa^{(\mathrm{sc})}\right). \tag{5.17}$$

For homogeneous dielectric spheres, the electric and magnetic Mie coefficients are given by [50, 107]

$$\begin{aligned} a_\ell(ix) &= (-1)^\ell \frac{\pi}{2} \frac{n^2 s_\ell^{(a)} - s_\ell^{(b)}}{n^2 s_\ell^{(c)} + s_\ell^{(d)}}, \\ b_\ell(ix) &= (-1)^{\ell+1} \frac{\pi}{2} \frac{s_\ell^{(b)} - s_\ell^{(a)}}{s_\ell^{(c)} + s_\ell^{(d)}}, \end{aligned} \tag{5.18}$$

respectively, with the imaginary size parameter $x = -iKR = \mathcal{K}R$ and

$$\begin{aligned} s_\ell^{(a)} &= I_{\ell+\frac{1}{2}}(nx)\left[xI_{\ell-\frac{1}{2}}(x) - \ell I_{\ell+\frac{1}{2}}(x)\right], \\ s_\ell^{(b)} &= I_{\ell+\frac{1}{2}}(x)\left[nxI_{\ell-\frac{1}{2}}(nx) - \ell I_{\ell+\frac{1}{2}}(nx)\right], \\ s_\ell^{(c)} &= I_{\ell+\frac{1}{2}}(nx)\left[xK_{\ell-\frac{1}{2}}(x) + \ell K_{\ell+\frac{1}{2}}(x)\right], \\ s_\ell^{(d)} &= K_{\ell+\frac{1}{2}}(x)\left[nxI_{\ell-\frac{1}{2}}(nx) - \ell I_{\ell+\frac{1}{2}}(nx)\right]. \end{aligned} \tag{5.19}$$

Here, $n = n_{\mathrm{sphere}}/n_{\mathrm{medium}}$ is the relative refractive index, and the functions I_ℓ and K_ℓ are the modified Bessel function of first and second kind, respectively.

In the limit of a perfectly reflecting sphere, $n \to i\infty$, the Mie coefficients become

$$\begin{aligned} a_\ell^{(\mathrm{PR})}(ix) &= (-1)^\ell \frac{\pi}{2} \frac{xI_{\ell-1/2}(x) - \ell I_{\ell+1/2}(x)}{xK_{\ell-1/2}(x) + \ell K_{\ell+1/2}(x)}, \\ b_\ell^{(\mathrm{PR})}(ix) &= (-1)^{\ell+1} \frac{\pi}{2} \frac{I_{\ell+1/2}(x)}{K_{\ell+1/2}(x)}. \end{aligned} \tag{5.20}$$

5.3 Low-frequency limit

To compute the contribution of the round trip operator at $\xi_0 = 0$ in the Matsubara sum, the low-frequency limit of the reflection matrix elements (5.14) is required. Even though the scattering amplitudes vanish in the limit $\xi \to 0$, this is not the case for the reflection matrix elements. Therefore, we need to keep terms linear in ξ in the low-frequency expression for the scattering amplitudes.

model	$\mathcal{A}_\ell^{\text{model}}$	$\mathcal{B}_\ell^{\text{model}}$
perfect reflectors	1	$-\dfrac{\ell}{\ell+1}$
Drude model	1	0
plasma model	1	$-\dfrac{\ell}{\ell+1}\left[1-\dfrac{2\ell+1}{\alpha}\dfrac{I_{\ell+1/2}(\alpha)}{I_{\ell-1/2}(\alpha)}\right]$
dielectrics	$\dfrac{\varepsilon(0)-1}{\varepsilon(0)+1+\frac{1}{\ell}}$	0

TABLE 5.1: The coefficients $\mathcal{A}_\ell^{\text{model}}$ and $\mathcal{B}_\ell^{\text{model}}$ depending on the material model under consideration. For the plasma model, the variable $\alpha = \omega_p R/c$ was introduced and, for dielectrics, $\varepsilon(0) = \varepsilon_{\text{sphere}}(0)/\varepsilon_{\text{medium}}(0)$ denotes the relative dielectric function in the static limit.

We start by expanding the angular functions π_ℓ and τ_ℓ. According to (5.17), $\cos(\Theta)$ diverges like $1/\xi^2$ at low frequencies. Thus, we can employ the asymptotics of the angular functions for large arguments (A.22) and find

$$\begin{aligned}\pi_\ell\big(\cos(\Theta)\big) &\sim \frac{(2\ell)!}{2^\ell(\ell-1)!\ell!}\cos^{\ell-1}(\Theta) \propto \frac{1}{\xi^{2\ell-2}}\,,\\ \tau_\ell\big(\cos(\Theta)\big) &\sim \frac{(2\ell)!}{2^\ell[(\ell-1)!]^2}\cos^{\ell}(\Theta) \propto \frac{1}{\xi^{2\ell}}\,.\end{aligned} \tag{5.21}$$

As a consequence, among the four combinations of these two functions and the two Mie coefficients a_ℓ and b_ℓ, only those involving τ_ℓ can potentially lead to contributions linear in ξ. Terms involving π_ℓ yield an additional factor ξ^2 and can thus be disregarded.

At low frequencies, the Mie coefficient are of the form (see [51, §7] for a detailed discussion)

$$\begin{aligned}a_\ell(ix) &= (-1)^\ell\frac{(\ell+1)(\ell!)^2}{2\ell(2\ell+1)[(2\ell)!]^2}\mathcal{A}_\ell^{\text{model}}(2x)^{2\ell+1}+\mathcal{O}(x^{2\ell+2})\,,\\ b_\ell(ix) &= (-1)^\ell\frac{(\ell+1)(\ell!)^2}{2\ell(2\ell+1)[(2\ell)!]^2}\mathcal{B}_\ell^{\text{model}}(2x)^{2\ell+1}+\mathcal{O}(x^{2\ell+2})\,,\end{aligned} \tag{5.22}$$

where $x = n\xi R/c$ and the coefficients $\mathcal{A}_\ell^{\text{model}}$ and $\mathcal{B}_\ell^{\text{model}}$ depend on the model used for the material under consideration. In Table 5.1 these coefficients are listed for a sphere made of a perfectly reflecting material, a metal described by either the Drude or the plasma model, or a dielectric material.

With the low-frequency asymptotics (5.21) and (5.22), the scattering amplitudes in the low-frequency limit read

$$\begin{aligned}S_1 &= x\sum_{\ell=1}^{\infty}\mathcal{B}_\ell^{\text{model}}\frac{y^{2\ell}}{(2\ell)!}\,,\\ S_2 &= x\sum_{\ell=1}^{\infty}\mathcal{A}_\ell^{\text{model}}\frac{y^{2\ell}}{(2\ell)!}\,,\end{aligned} \tag{5.23}$$

where $y = \sqrt{-2x^2\cos(\Theta)} = R\sqrt{2(\mathbf{k}^{(\mathrm{in})}\cdot\mathbf{k}^{(\mathrm{sc})} + k^{(\mathrm{in})}k^{(\mathrm{sc})})}$.

Because the imaginary wave number $\mathcal{K}$ contained in the prefactor x in (5.23) cancels with the one in the matrix elements, it is convenient to define scaled scattering amplitudes as $\tilde{S}_p = S_p/x$ in the low-frequency limit. Noting that for $\xi = 0$ the polarization transformation coefficients evaluate to

$$A = 1\,, \quad B = C = D = 0\,, \tag{5.24}$$

the reflection matrix elements become

$$\begin{aligned}\langle \mathbf{k}^{(\mathrm{sc})}, \mp, \mathrm{TM}|\mathcal{R}_{\mathrm{S}}|\mathbf{k}^{(\mathrm{in})}, \pm, \mathrm{TM}\rangle &= \frac{2\pi R}{k^{(\mathrm{sc})}}\tilde{S}_2\,,\\ \langle \mathbf{k}^{(\mathrm{sc})}, \mp, \mathrm{TE}|\mathcal{R}_{\mathrm{S}}|\mathbf{k}^{(\mathrm{in})}, \pm, \mathrm{TE}\rangle &= \frac{2\pi R}{k^{(\mathrm{sc})}}\tilde{S}_1\end{aligned} \tag{5.25}$$

with the scaled scattering amplitudes

$$\begin{aligned}\tilde{S}_1 &= \sum_{\ell=1}^{\infty} \mathcal{B}_\ell^{\mathrm{model}} \frac{y^{2\ell}}{(2\ell)!}\,,\\ \tilde{S}_2 &= \sum_{\ell=1}^{\infty} \mathcal{A}_\ell^{\mathrm{model}} \frac{y^{2\ell}}{(2\ell)!}\,.\end{aligned} \tag{5.26}$$

For perfect reflectors, the sum over ℓ can be performed yielding

$$\begin{aligned}\tilde{S}_1^{(\mathrm{PR})} &= -\frac{y^2\cosh(y) - 2y\sinh(y) + 2\cosh(y) - 2}{y^2}\,,\\ \tilde{S}_2^{(\mathrm{PR})} &= \cosh(y) - 1\,.\end{aligned} \tag{5.27}$$

5.4 Scattering at a large sphere

In order to find an asymptotic expansion of the Casimir free energy for $R_1, R_2 \gg L$, we need asymptotic expressions for the matrix elements (5.14). For this purpose, it is convenient to express the scattering amplitudes (5.3) in terms of the so-called Debye expansion. Within this Debye expansion, the scattering amplitudes are decomposed in an infinite series of terms representing multiple internal reflections of the spherical waves [108]:

$$S_p = S_{p,0} + \sum_{n=0}^{N} S_{p,n} + \Delta S_{p,N} \tag{5.28}$$

for $p = 1, 2$ where $S_{p,0}$ and $S_{p,1}$ represent the direct reflection and transmission amplitude, respectively. The terms $S_{p,n}$ for $n \geq 2$ correspond to transmission into the sphere followed by $(n-1)$ internal reflections and $\Delta S_{p,N}$ is a remainder term.

Except for the case when resonances are involved, the Debye expansion yields a rapidly converging series in contrast to performing the summation over ℓ in (5.3). Moreover, within the expansion many optical effects for water droplets in air can be explained. For instance, the primary bow of the meteorological rainbow can be explained with the third term of the Debye expansion $S_{p,2}$ [108, 109].

For the Casimir interaction only the direct reflection term contributes to the asymptotic expansion. This is because higher order terms contain phase factors associated to propagation over the sphere's radius which become exponentially small after Wick rotation. For large size parameters $KR \gg 1$, the asymptotic expansion of

the direct reflection term reads

$$S_p \sim S_p^{(\mathrm{WKB})} \left(1 + s_p \frac{i}{KR} + \mathcal{O}((KR)^{-2})\right) \tag{5.29}$$

with

$$S_p^{(\mathrm{WKB})} = -\frac{iKR}{2} r_p((\pi - \Theta)/2) \exp(-2iKR \sin(\Theta/2)) \tag{5.30}$$

where r_p are the Fresnel coefficients (3.3) for which $p = 1, 2$ corresponds to TE and TM modes, respectively. Expressions for the correction s_p can be found in Ref. [110] or [111]. While the results from the two references agree for perfect reflectors,

$$\begin{aligned} s_1^{(\mathrm{PR})} &= \frac{1}{2} \frac{\cos(\Theta)}{\sin^3(\Theta/2)}, \\ s_2^{(\mathrm{PR})} &= -\frac{1}{2} \frac{1}{\sin^3(\Theta/2)}, \end{aligned} \tag{5.31}$$

they are not consistent for transparent spheres.

The asymptotic expansion of the direct reflection term of the scattering amplitudes (5.29) is derived from the WKB approximation for the Mie coefficients and angular functions by taking the saddle-point approximation and its correction for the integral over angular momenta [110, 112]. For a given scattering angle Θ, the main contribution to the scattering amplitudes (5.3) comes from the neighbordhood of the angular momentum value $\ell = KR \cos(\Theta/2)$ [113]. In the semiclassical approximation, the localization principle [100] connects waves with angular momentum $\ell \gg 1$ to localized rays defining an impact parameter $b = \ell/K$. Thus, the leading order WKB approximation (5.30) defines rays corresponding to the impact parameter $b = R \cos(\Theta/2)$ shown in Fig. 5.3. Such rays hit the sphere surface with an incidence angle of $(\pi - \Theta)/2$, which is precisely the value required for obtaining the scattering angle Θ from the condition of specular reflection at the tangent plane indicated in the figure. Comparing the reflection at the tangent plane (thick lines) and at the sphere with its center as a reference point, one finds a difference in path length amounting to $2(\omega R/c) \sin(\Theta/2)$. In this way, the last two factors of (5.30) find their natural explanation. The first factor is responsible for providing the correct scattering cross section proportional to R^2.

While the leading order term in (5.29) is described by geometrical optics, the subleading term takes diffraction into account.

In view of the expression (5.29) one would expect the WKB expansion to break down when the first order correction becomes larger than the leading order term. Indeed this is the case when the scattering angle is close to the forward direction, $\Theta \approx 0$. In fact, it was shown that the result holds uniformly for $(KR)^{-1/3} \ll \Theta \leq \pi$, i.e. all scattering directions except close to the forward direction [110].

For the Casimir effect, we expect that the near forward direction plays a minor role in the asymptotic expansion since the corresponding amplitude for the round-trip would be small. Thus, in order to find the asymptotic expression for the scattering amplitudes along the imaginary axis, we can simply evaluate the asymptotics (5.29) at imaginary frequencies. To double check that this is indeed true, we independently derive the asymptotic expansion corresponding to (5.29) for imaginary frequencies by starting out with the representation of the exact scattering amplitudes for imaginary frequencies. In the derivation, which is given in Appendix C.2, it is assumed that $\cos(\Theta)$ does not take values close to -1. In Sec. 7.5, we will verify that our result is correct for any values of $\cos(\Theta)$.

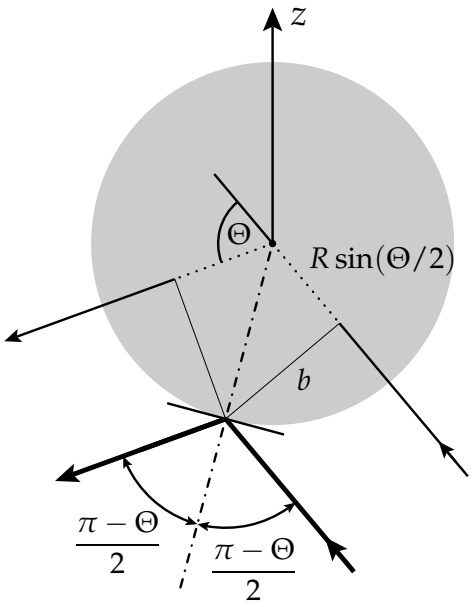

FIGURE 5.3: Geometrical optics limit for the direct reflection by a sphere of radius R. Within the WKB approximation, a given scattering angle Θ defines the impact parameter $b = R\cos(\Theta/2)$. Seen from the tangent plane to the sphere, the angle of incidence is given by $(\pi - \Theta)/2$. The missing phase of a ray with frequency ω reflected on the sphere's surface with respect to a corresponding ray passing via the sphere's center before being deflected amounts to $2(\omega R/c)\sin(\Theta/2)$. (from Ref. [114])

For large imaginary size parameters $x \gg 1$, we find

$$S_p \sim S_p^{(\mathrm{WKB})} \left(1 + s_p \frac{1}{x} + \mathcal{O}(1/x^2)\right) \tag{5.32}$$

with

$$S_p^{(\mathrm{WKB})} = \frac{x}{2} r_p((\pi - \Theta)/2) \exp(2x \sin(\Theta/2)) \tag{5.33}$$

and

$$\begin{aligned} s_1 &= s_1^{(\mathrm{PR})} + \frac{1/s}{c^2 + s\sqrt{n^2 - c^2}} - \frac{2n^2 - c^2}{2(n^2 - c^2)^{3/2}}\,, \\ s_2 &= s_2^{(\mathrm{PR})} + \frac{1/s}{c^2 - s\sqrt{n^2 - c^2}} - \frac{c^2}{s^3} \frac{2n^4 s^2 - n^2 c^2 (1 + s^2 - s^4) + c^6}{(n^2 - c^2)(n^2 s^2 - c^2)^2} \\ &\quad + \frac{n^2}{2(n^2 - c^2)^{3/2}} \frac{2n^4 - n^2 c^2 (1 + c^2) - c^4}{(n^2 s^2 - c^2)^2}\,. \end{aligned} \tag{5.34}$$

In the formulas (5.34), we have made use of the abbreviations

$$s = \sin(\Theta/2)\,, \quad c = \cos(\Theta/2)\,. \tag{5.35}$$

In fact, while we were able to reproduce the correction in the perfect reflector limit, the correction for transparent spheres does not agree with any of the two results in Ref. [110] or [111]. For a comparison, we give the two different expressions in Eqs. (C.28) and (C.29), respectively.

When applying the asymptotics of the scattering amplitudes (5.32) to the Casimir

effect, it is useful to express the trigonometric functions of Θ with respect to $\cos(\Theta)$ for which an expression at imaginary frequencies is given in (5.17). For instance,

$$\sin(\Theta/2) = \sqrt{\frac{1-\cos(\Theta)}{2}}\,, \tag{5.36}$$

$$\cos^2(\Theta/2) = 1 - \sin^2(\Theta/2) = \frac{\cos(\Theta)+1}{2}\,. \tag{5.37}$$

The asymptotic expansion of the Mie scattering amplitudes (5.32) does *a priori* not cover the zero-frequency case because the requirement $x \gg 1$ cannot be met when $\xi = 0$. In Appendix C.2, the asymptotics of the scaled scattering amplitudes (5.26) for large radii is derived. The result valid at vanishing frequencies is found to be

$$\begin{aligned} \tilde{S}_1 &\sim \frac{1}{2}\mathcal{B}^{\text{model}}_{y/2} e^y\,, \\ \tilde{S}_2 &\sim \frac{1}{2}\mathcal{A}^{\text{model}}_{y/2} e^y\,. \end{aligned} \tag{5.38}$$

where $y = R\sqrt{2(\mathbf{k}^{(\text{in})}\cdot\mathbf{k}^{(\text{sc})} + k^{(\text{in})}k^{(\text{sc})})}$ is assumed to be the large parameter and the coefficients $\mathcal{A}^{\text{model}}_\ell$ and $\mathcal{B}^{\text{model}}_\ell$ are given in Table 5.1. As shown in Appendix C.2, to leading order they agree with the leading order term in (5.32) taken at $\xi = 0$. However, the correction to the WKB result is now different. In the special case of perfect reflectors (including Drude and plasma-type metals), the asymptotics of $\tilde{S}_2$ in (5.38) contains only the leading order asymptotic term. In view of the exact result (5.27), the subleading terms are exponentially small in the large parameter y.

It is worth noting that, for the application of computing the asymptotic expansion of the Casimir interaction involving spheres, it is important to keep the asymptotics (5.38) for the zero-frequency contribution in this form. The correction to the PFA can only be obtained in this way. Otherwise, if the coefficients $\mathcal{A}^{\text{model}}_{y/2}$ and $\mathcal{B}^{\text{model}}_{y/2}$ are expanded for large y, the NTLO term would give rise to infrared divergences.

5.5 Reflection matrix elements for large spheres

The matrix elements of the reflection operator at the sphere can be obtained by using the asymptotic expansion of the scattering amplitudes given in Sec. 5.4 in the exact reflection matrix elements. Here, we summarize the asymptotics of the reflection matrix elements for finite and vanishing frequencies. These results will be used in the following chapter.

For finite imaginary frequencies, (5.14) with (5.34) yields

$$\langle \mathbf{k}^{(\text{sc})}, \mp, p^{(\text{sc})} | \mathcal{R}_S | \mathbf{k}^{(\text{in})}, \pm, p^{(\text{in})} \rangle \sim \frac{\pi R}{\kappa^{(\text{sc})}} \exp\left(2x\sin\left(\frac{\Theta}{2}\right)\right) \rho_{p^{(\text{out})},p^{(\text{in})}} \tag{5.39}$$

where

$$2x\sin\left(\frac{\Theta}{2}\right) = R\sqrt{2(\mathcal{K}^2 + \mathbf{k}^{(\text{in})}\cdot\mathbf{k}^{(\text{sc})} + \kappa^{(\text{in})}\kappa^{(\text{sc})})} \tag{5.40}$$

and

$$\begin{aligned}
\rho_{\mathrm{TE,TE}} &\sim (Ar_{\mathrm{TE}} + Br_{\mathrm{TM}}) + (Ar_{\mathrm{TE}}s_1 + Br_{\mathrm{TM}}s_2)\,\frac{1}{x} + \mathcal{O}\left(x^{-2}\right) \\
\rho_{\mathrm{TM,TM}} &\sim (Ar_{\mathrm{TM}} + Br_{\mathrm{TE}}) + (Ar_{\mathrm{TM}}s_2 + Br_{\mathrm{TE}}s_1)\,\frac{1}{x} + \mathcal{O}\left(x^{-2}\right) \\
\rho_{\mathrm{TM,TE}} &\sim -(Cr_{\mathrm{TE}} + Dr_{\mathrm{TM}}) - (Cr_{\mathrm{TE}}s_1 + Dr_{\mathrm{TM}}s_2)\,\frac{1}{x} + \mathcal{O}\left(x^{-2}\right) \\
\rho_{\mathrm{TE,TM}} &\sim (Cr_{\mathrm{TM}} + Dr_{\mathrm{TE}}) + (Cr_{\mathrm{TM}}s_2 + Dr_{\mathrm{TE}}s_1)\,\frac{1}{x} + \mathcal{O}\left(x^{-2}\right)\,.
\end{aligned} \tag{5.41}$$

The Fresnel coefficients r_{TE} and r_{TM} as given in (3.3) are evaluated at the incidence angle $(\pi - \Theta)/2$, the coefficients in the WKB correction s_1 and s_2 are given in (5.34), and the polarization transformation coefficients A, B, C and D can be found in (5.15).

In the zero-frequency limit, (5.25) with (5.38) yields

$$\begin{aligned}
\langle \mathbf{k}^{(\mathrm{sc})}, \mp, \mathrm{TM} | \mathcal{R}_{\mathrm{S}} | \mathbf{K}^{(\mathrm{in})}, \pm, \mathrm{TM} \rangle &\sim \frac{\pi R}{k^{(\mathrm{sc})}} \mathcal{A}^{\mathrm{model}}_{y/2} e^{y}\,, \\
\langle \mathbf{k}^{(\mathrm{sc})}, \mp, \mathrm{TE} | \mathcal{R}_{\mathrm{S}} | \mathbf{K}^{(\mathrm{in})}, \pm, \mathrm{TE} \rangle &\sim \frac{\pi R}{k^{(\mathrm{sc})}} \mathcal{B}^{\mathrm{model}}_{y/2} e^{y}
\end{aligned} \tag{5.42}$$

with $y = R\sqrt{2(\mathbf{k}^{(\mathrm{in})} \cdot \mathbf{k}^{(\mathrm{sc})} + k^{(\mathrm{in})}k^{(\mathrm{sc})})}$ and the coefficients $\mathcal{A}^{\mathrm{model}}_{\ell}$ and $\mathcal{B}^{\mathrm{model}}_{\ell}$ are given in Table 5.1.

Chapter 6

Asymptotic expansion of the Casimir interaction between two spheres

In this chapter, we determine the first two terms in the asymptotic expansion of the Casimir interaction between two spheres, when the radii of the spheres R_1 and R_2 become large compared to the surface-to-surface distance L. In contrast to the derivative expansion approach presented in Sec. 4.2, we start out from the exact Casimir interaction in terms of the scattering formula without making any assumptions on locality.

In the literature, such asymptotic expansions have been calculated exclusively by utilizing a multipole representation of the fields. This multipole-based method, originally developed by Bordag in [36] for a cylinder in front of a plane, has been employed for the plane-sphere [37, 94] and sphere-sphere geometry [40] for scalar and electromagnetic fields with perfectly reflecting boundary conditions. For the plane-sphere geometry, the results have been generalized to the electromagnetic field with boundary conditions imposed by real materials [38]. In all of these works, the PFA was obtained as the asymptotic leading order term for short distances.

The setups for which the PFA correction have been obtained for the electromagnetic case in the literature are summarized in Tab. 6.1. In the table, we distinguish between (A) the plane-sphere and (B) the sphere-sphere geometry, between vanishing ($T = 0$) and finite temperature ($T > 0$) and between idealized objects with perfectly reflecting boundary condition and objects made of real materials. Drude-type metals are not considered in the table since exact results for zero-frequency Matsubara contribution to the Casimir interaction are known for both geometries [33–35]. Note that, although in Ref. [39] the PFA correction has been obtained for the zero-frequency contribution of the Casimir interaction between a perfectly reflecting plane and sphere, the result can be combined with the PFA correction at finite frequencies given in [104] to find the PFA correction at finite temperatures.

In contrast to the method developed by Bordag, we perform the asymptotic expansion using the representation of the electromagnetic field in terms of plane waves further allowing for a physical interpretation of the calculated results. We prove that the PFA provides the correct leading-order term in the small-distance limit for arbitrary materials and temperatures. Moreover, we obtain explicit expressions for the PFA correction for arbitrary materials and temperatures, thus completing table 6.1. As special cases, we recover the results for the plane-sphere geometry known from

TABLE 6.1: Known results in the literature for PFA correction from an asymptotic expansion of the exact Casimir interaction in the plane-sphere and sphere-sphere geometry.

(A) plane-sphere geometry

	$T=0$	$T>0$
perfect reflectors	[37]	[39]
real materials	[38]	–

(B) sphere-sphere geometry

	$T=0$	$T>0$
perfect reflectors	[40]	–
real materials	–	–

the literature [37, 38, 42], and the sphere-sphere result for perfect reflectors at vanishing temperatures [40, 42]:

$$E \sim E_{\mathrm{PFA}} \left[1 + \left(\frac{1}{3} - \frac{20}{\pi^2} - u \right) \frac{L}{R_{\mathrm{eff}}} + \ldots \right] \tag{6.1}$$

with the PFA result

$$E_{\mathrm{PFA}} = -\frac{\hbar c \pi^3 R_{\mathrm{eff}}}{720 L^2}, \tag{6.2}$$

the dimensionless parameter u defined in (4.32) and the effective radius R_{eff} as defined in (4.4). When real materials at finite temperatures are involved, we demonstrate that within our approach the PFA correction is valid even in situations where the derivative expansion approach fails or becomes non-applicable.

The chapter starts out by introducing the saddle-point method for an asymptotic expansion of integrals. A formula which goes beyond the commonly employed leading order saddle-point approximation is provided. The Casimir free energy is then expressed in terms of a trace over round trips for which the saddle-point method can be applied. The leading order contribution due to the saddle-point integral is derived where the cases of finite and vanishing frequencies are treated separately. The leading order saddle-point approximation of the trace over round trips contains the PFA to leading order and a subleading term due to diffraction. The remaining PFA correction is calculated using the next-to-leading-order term in the saddle-point method. It is shown that the correction is consistent with (6.1) in the perfect reflector limit at vanishing temperatures. Taking the plane-sphere limit from the sphere-sphere result we obtain the result found by Teo [40]. We then compare the results obtained by means of the asymptotic expansion with the derivative expansion approach. As an application, we analyze the relative contributions entering the PFA correction. Finally, we estimate the effective interaction area on the two spheres contributing to the leading two terms in the asymptotic expansion of the Casimir interaction.

6.1 Asymptotic expansion of integrals: the saddle-point approximation

Consider a d-dimensional integral of the form

$$I(\lambda) = \int_{\mathbb{R}^d} \mathrm{d}\mathbf{x}\, g(\mathbf{x}) e^{-\lambda f(\mathbf{x})} \tag{6.3}$$

with the differentiable functions f and g. We assume that f has a *unique* minimum at $\mathbf{x}_{\mathrm{sp}}$ called saddle-point, which is determined by the saddle-point condition $\nabla f(\mathbf{x}) =$

0, and the Hessian matrix of f

$$\mathsf{H} \equiv \left(\frac{\partial^2 f}{\partial x_i \partial x_j} \right)_{i,j=1,\dots,d} \tag{6.4}$$

has no vanishing eigenvalues, i.e. it is *non-singular*.

We are interested in the asymptotic behavior of such integrals for large values of λ. Away from the saddle-point $\mathbf{x}_{\mathrm{sp}}$, the integrand becomes exponentially small. Thus, the main contribution of the integral comes from a close neighborhood around $\mathbf{x}_{\mathrm{sp}}$. A Taylor expansion of the functions f and g around that point then allows one to find an asymptotic expansion of $I(\lambda)$ for large λ. Due to the saddle-point condition, the first order term in the Taylor expansion of f vanishes. Expanding f up to second order and g to zeroth order, the integral can be identified as a Gaussian integral and can thus be evaluated. This yields the leading order asymptotic behavior of $I(\lambda)$ as $\lambda \to \infty$.

To obtain the next-to-leading-order term in the expansion, one has to expand f to fourth and g to second order. Keeping the second order term of f in the exponent, the evaluation of the integrals of Gaussian form multiplied by polynomials yields the formula [115, 116]

$$I(\lambda) \sim \left(\frac{2\pi}{\lambda}\right)^{d/2} \frac{e^{-\lambda f_{\mathrm{sp}}}}{\sqrt{\det \mathsf{H}}} \left(g_{\mathrm{sp}} + \frac{1}{2\lambda} \left[g_{ij} \mathsf{H}^{ij} - \frac{1}{4} (g_{\mathrm{sp}} f_{ijkl} + 4 f_{ijk} g_l) \mathsf{H}^{ij} \mathsf{H}^{kl} + \frac{g_{\mathrm{sp}}}{12} f_{ijk} f_{lmn} \left(3 \mathsf{H}^{ij} \mathsf{H}^{kl} \mathsf{H}^{mn} + 2 \mathsf{H}^{il} \mathsf{H}^{jm} \mathsf{H}^{kn} \right) \right] \right). \tag{6.5}$$

Here, the subscript "sp" denotes the evaluation of the function at $\mathbf{x} = \mathbf{x}_{\mathrm{sp}}$. A derivative with respect to the i-th component of $\mathbf{x}$ with subsequent evaluation at the saddle-point is represent by a lower index i: $f_i \equiv \partial f / \partial x_i |_{\mathbf{x}=\mathbf{x}_{\mathrm{sp}}}$ or equivalently for g. Likewise, higher order derivatives are denoted by multiple lower indices. Two upper indices denote the matrix elements of the inverse matrix, $\mathsf{H}^{ij} \equiv (\mathsf{H}^{-1})_{i,j}$, and, finally, repeated indices are summed over the values from 1 to d.

In the special case of $d = 1$, we have [117, 118]

$$I(\lambda) \sim \left(\frac{2\pi}{\lambda f''_{\mathrm{sp}}}\right)^{1/2} g_{\mathrm{sp}} e^{-\lambda f_{\mathrm{sp}}} \left(1 + \frac{1}{2\lambda} \left[\frac{g''_{\mathrm{sp}}}{g_{\mathrm{sp}} f''_{\mathrm{sp}}} - \frac{g'_{\mathrm{sp}} f'''_{\mathrm{sp}}}{g_{\mathrm{sp}} (f''_{\mathrm{sp}})^2} - \frac{1}{4} \frac{f''''_{\mathrm{sp}}}{(f''_{\mathrm{sp}})^2} + \frac{5}{12} \frac{(f'''_{\mathrm{sp}})^2}{(f''_{\mathrm{sp}})^3} \right] \right) \tag{6.6}$$

where the prime denotes a derivative.

6.2 Expansion in round trips

In order to facilitate the asymptotic expansion of the Casimir free energy, we use the identity (2.22) to express the logarithm of the determinant as the trace of the logarithm in the scattering formula (2.52). The Casimir free energy then becomes

$$\mathcal{F} = k_{\mathrm{B}} T {\sum_{n=0}^{\infty}}' \mathcal{F}(\xi_n) \quad \text{with} \quad \mathcal{F}(\xi) = \operatorname{tr} \log(1 - \mathcal{M}(i\xi)) \tag{6.7}$$

and the Matsubara frequencies ξ_n. Here, $\mathcal{M}$ is the round-trip operator defined in (2.41). Without loss of generality, we assume a finite temperature for the asymptotic

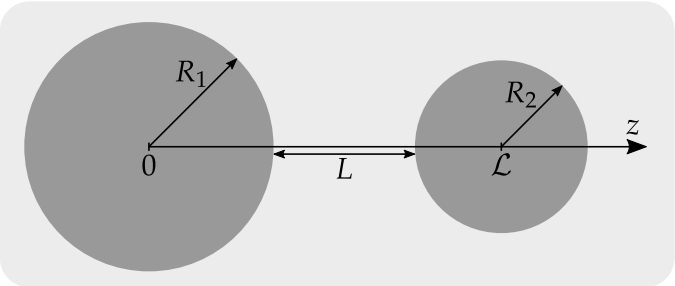

FIGURE 6.1: The geometry of two spheres with radii R_1 and R_2 at a surface-to-surface distance L. The coordinate system's origin is placed at the center of sphere 1 and the z-axis is chosen such that it connects the two sphere centers. The center of sphere 2 is located at $z = \mathcal{L}$.

expansion. The zero temperature result can always be obtained by replacing the Matsubara sum by an integral over the imaginary frequencies as in (2.65).

Expanding the logarithm in a Mercator series,

$$\mathcal{F}(\xi) = -\sum_{r=1}^{\infty} \frac{1}{r} \operatorname{tr} \mathcal{M}^r \,, \tag{6.8}$$

the Casimir free energy can be interpreted in terms of contributions of a single round-trip within the cavity imposed by the two spheres, up to an infinitely large number of round-trips.

The trace of the r-th power of the round-trip operator then reads

$$\begin{aligned} \operatorname{tr}\mathcal{M}^r = \sum_{p_0,\dots,p_{2r-1}} \int \frac{d\mathbf{k}_0 \dots d\mathbf{k}_{2r-1}}{(2\pi)^{4r}} \prod_{j=0}^{r-1} e^{-(\kappa_{2j}+\kappa_{2j-1})\mathcal{L}} \\ \times \langle \mathbf{k}_{2j+1}, +, p_{2j+1} | \mathcal{R}_1 | \mathbf{k}_{2j}, -, p_{2j} \rangle \\ \times \langle \mathbf{k}_{2j}, -, p_{2j} | \mathcal{R}_2 | \mathbf{k}_{2j-1}, +, p_{2j-1} \rangle \,. \end{aligned} \tag{6.9}$$

Within the round-trip expansion a scattered plane wave from one sphere becomes the incident plane wave for the subsequent reflection on the other sphere. For this reason, we have dropped the superscripts (in) and (sc) in (6.9) and labeled different modes with different indices instead. Note that we have used the convention of cyclic indices $p_{2r} \equiv p_0$ and $\mathbf{k}_{2r} \equiv \mathbf{k}_0$.

Since within Mie scattering, the reflection at the spheres is described with respect to a coordinate system with origin at the sphere centers, the translation operators (2.30) are required over the distance $\mathcal{L} = L + R_1 + R_2$. At imaginary frequencies, the matrix elements of the translation operators read $e^{-\kappa\mathcal{L}}$ with the axial wave vector after Wick rotation κ as given in (3.7).

With the asymptotics of the reflection matrix elements for spheres with large radii (5.39) and (5.42), the trace of the r-th round trip can be expressed as

$$\operatorname{tr}\mathcal{M}^r = \left(\frac{R_1 R_2}{16\pi^2}\right)^r \int \mathrm{d}\mathbf{k}_0 \dots \mathrm{d}\mathbf{k}_{2r-1}\, g(\mathbf{k}_0, \dots, \mathbf{k}_{2r-1}) \exp\left(-f(\mathbf{k}_0, \dots, \mathbf{k}_{2r-1})\right) \,. \tag{6.10}$$

At finite frequencies, the function in the exponent of (6.10) is given by

$$f(\mathbf{k}_0,\ldots,\mathbf{k}_{2r-1}) = \sum_{j=0}^{r-1}\left(R_1\eta_{2j,2j+1} + R_2\eta_{2j-1,2j}\right) \tag{6.11}$$

where the terms proportional to R_s are contributions from sphere $s = 1, 2$ and

$$\eta_{j,j+1} = \kappa_j + \kappa_{j+1} - \sqrt{2\left[\mathcal{K}^2 + \kappa_j\kappa_{j+1} + \mathbf{k}_j\cdot\mathbf{k}_{j+1}\right]}\,. \tag{6.12}$$

The corresponding function of f for vanishing frequencies can be simply obtained by taking the low-frequency limit in (6.12), i.e. replacing $\mathcal{K} \to 0$ and $\kappa_j \to k_j$. The situation is different for the function g and the cases of a finite and a vanishing frequency have to be considered separately. At finite frequencies, the function g reads

$$g|_{\xi>0}(\mathbf{k}_0,\ldots,\mathbf{k}_{2r-1}) = \sum_{p_0,\ldots,p_{2r-1}}\prod_{j=0}^{r-1}\frac{e^{-(\kappa_{2j}+\kappa_{2j-1})L}}{\kappa_{2j}\kappa_{2j-1}}\rho^{(1)}_{p_{2j+1},p_{2j}}(\mathbf{k}_{2j+1},\mathbf{k}_{2j})\rho^{(2)}_{p_{2j},p_{2j-1}}(\mathbf{k}_{2j},\mathbf{k}_{2j-1}) \tag{6.13}$$

where $\rho_{p,p'}$ is defined in (5.41). The superscript (s) denotes that the relative refractive index in the reflection matrix elements corresponds to the one of the sphere $s = 1, 2$. Also, for sphere 1 the lower sign in the coefficients C and D, given in (5.15), has to be chosen and for sphere 2 the upper sign.

On the other hand, at vanishing frequencies the function g is expressed as

$$g|_{\xi=0}(\mathbf{k}_0,\ldots,\mathbf{k}_{2r-1}) = \sum_{\mathcal{X}=\mathcal{A},\,\mathcal{B}}\prod_{j=0}^{r-1}\frac{e^{-(k_{2j}+k_{2j-1})L}}{k_{2j}k_{2j-1}}\mathcal{X}^{(1)}_{R_1\sigma_{2j+1,2j}}\mathcal{X}^{(2)}_{R_2\sigma_{2j,2j-1}} \tag{6.14}$$

with

$$\sigma_{j,j+1} = \sqrt{(\mathbf{k}_j\cdot\mathbf{k}_{j+1} + k_jk_{j+1})/2} \tag{6.15}$$

and the functions $\mathcal{A}$ and $\mathcal{B}$ as given in Tab. 5.1. Similar to the finite frequency case, the superscript (s) denotes that the functions $\mathcal{A}$ and $\mathcal{B}$ are to be chosen depending on the modeling of the material properties of sphere s.

Even though a large parameter has not been explicitly factored out in the exponent of (6.10), the expression for the trace of the r-th round trip is now suitable for a saddle-point approximation. In principle either of the two radii, or a combination of both, could be used as the larger parameter while keeping the ratio of the sphere radii fixed. In order to make the formulas appearing in the calculations of the correction of the saddle-point approximation more transparent, we will not make an explicit choice for the large parameter here and use the saddle-point formula (6.5) with the large parameter λ being absorbed into the function f.

6.3 Leading saddle-point approximation and the PFA

We compute the asymptotics of the trace of the r-th round trip (6.10) for large radii by means of the leading order saddle-point approximation in (6.5). The cases of a finite and a vanishing frequency are considered separately. The derivation is based on Refs. [104, 114].

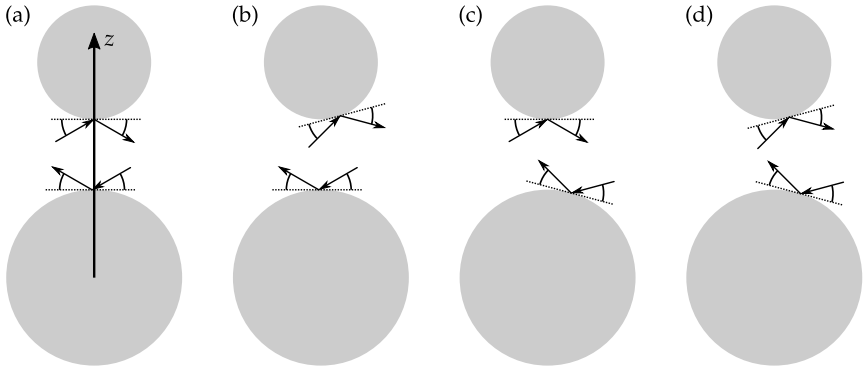

FIGURE 6.2: Specular reflection at (a) the tangent planes at the bottom and top of the spheres, respectively, (b) and (c) at a slightly tilted tangent plane on one of the two spheres and (d) at tilted tangent planes on both spheres.

Finite frequencies

In order to employ the asymptotic expansion of the saddle-point integral, we first need to determine the saddle-points of the $4r$-dimensional integral over the momenta transverse to the z-axis as given in (6.10). In fact, as shown in appendix D.1, there exists a unique family of saddle points,

$$\mathbf{k}_0 = \cdots = \mathbf{k}_{2r-1} \equiv \mathbf{k}_{\mathrm{sp}}\,, \tag{6.16}$$

parametrized by $\mathbf{k}_{\mathrm{sp}}$.

The saddle-point manifold implies that within the leading order geometric optical picture of the Mie scattering amplitudes discussed in Sec. 5.4, the plane-waves are reflected at tangent planes perpendicular to the z-axis as depicted in Fig. 6.2 (a). As a consequence, the scattering plane and the Fresnel planes for the incident and scattered plane waves coincide, and the angle between those planes vanishes, $\chi^{(\mathrm{in})} = \chi^{(\mathrm{sc})} = 0$. In this case, according to (5.10), the polarization transformation coefficients evaluate to

$$A = 1\,, \quad B = C = D = 0\,, \tag{6.17}$$

for each reflection at the two spheres. Then, the polarization mixing reflection matrix elements vanish as $\rho^{(s)}_{p,p'}|_{\mathrm{sp}} = 0$ if $p \neq p'$ for both spheres $s = 1, 2$ and the polarization preserving matrix elements contribute additively. Using that $\rho^{(s)}_{p,p}|_{\mathrm{sp}} = r^{(s)}_p$ for $p = \mathrm{TM}, \mathrm{TE}$ and $s = 1, 2$, the function g evaluated at the saddle-point manifold (6.16) can be decomposed as

$$g_{\mathrm{sp}} = g_{\mathrm{TE}} + g_{\mathrm{TM}} \tag{6.18}$$

with

$$g_p \sim \left(\frac{r^{(1)}_p r^{(2)}_p e^{-2\kappa_{\mathrm{sp}} L}}{(\kappa_{\mathrm{sp}})^2}\right)^r \left[1 + \frac{r}{\mathcal{K}}\left(\frac{s^{(1)}_p|_{\mathrm{sp}}}{R_1} + \frac{s^{(2)}_p|_{\mathrm{sp}}}{R_2}\right)\right]. \tag{6.19}$$

Here and in the following, the Fresnel reflection coefficients r_p as of (3.9) are evaluated at $(i\xi, k_{\mathrm{sp}})$. Expression (6.19) results from a sequence of r reflections on the two spheres with at most one of them picking the diffractive WKB correction in (5.32). Terms for which the diffractive correction is picked up more than once would contribute to higher order corrections to the PFA which are not considered here.

The function f vanishes when evaluated at the saddle-point manifold,

$$f_{\mathrm{sp}} = 0\,, \tag{6.20}$$

and, by arranging rows and columns in the order of $(k_{0,x}, \ldots, k_{2r-1,x}, k_{0,y}, \ldots, k_{2r-1,y})$, the Hessian matrix can be brought to block-diagonal form

$$\mathsf{H} = \begin{pmatrix} \mathsf{H}_{xx} & 0 \\ 0 & \mathsf{H}_{yy} \end{pmatrix}. \tag{6.21}$$

The matrix blocks are given by the second derivative of f evaluated at the saddle point

$$\left(\mathsf{H}_{xx}\right)_{ij} = \left.\frac{\partial^2 f}{\partial k_{i,x} \partial k_{j,x}}\right|_{\mathrm{sp}} \tag{6.22}$$

with a corresponding expression for H_{yy}. Due to the block structure of the Hessian matrix, we can perform the integrations over the x- and y-components of the wave vectors separately.

An explicit calculation shows that the blocks of the Hessian matrix can be expressed as $\mathsf{H}_{xx} = \mathsf{H}_{yy} = (1/2\kappa_{\mathrm{sp}})\Gamma_r$ with the $2r \times 2r$ matrix

$$\Gamma_r = \begin{pmatrix} R_1+R_2 & -R_1 & & & -R_2 \\ -R_1 & R_1+R_2 & -R_2 & & \\ & -R_2 & \ddots & \ddots & \\ & & \ddots & \ddots & -R_1 \\ -R_2 & & & -R_1 & R_1+R_2 \end{pmatrix}, \tag{6.23}$$

where the matrix elements not shown are zero. In the special case of a single round-trip, $r = 1$, the two off-diagonal matrix elements add up yielding

$$\Gamma_1 = (R_1+R_2)\begin{pmatrix} 1 & -1 \\ -1 & 1 \end{pmatrix}. \tag{6.24}$$

The eigenvalues of the matrix Γ_r are found as

$$\lambda_{j,\pm} = R_1 + R_2 \pm \sqrt{(R_1+R_2)^2 - 4R_1R_2\sin^2\left(\frac{\pi j}{r}\right)} \tag{6.25}$$

for $j = 0, \ldots, r-1$.

With $\lambda_{0,-} = 0$, both blocks H_{xx} and H_{yy} have a vanishing eigenvalue corresponding to the saddle-point manifold (6.16). In order to employ the saddle-point formula, it is necessary to first transform the integration variables $\mathbf{k}_j$ in such a way, that the direction corresponding to the vanishing eigenvalues can be singled out. Then, the multidimensional integral over the perpendicular directions can be evaluated by means of the saddle-point method, while the integration over the saddle-point manifold needs to be performed exactly.

If we choose the transformation to be unitary, the coordinate corresponding to the direction of the vanishing eigenvalues is

$$\mathbf{v}_0 = \frac{1}{\sqrt{2r}}(\mathbf{k}_0 + \mathbf{k}_1 + \ldots + \mathbf{k}_{2r-1})\,. \tag{6.26}$$

The variables corresponding to the perpendicular directions depend on the details of the transformation, which do not need to be specified at this point. When the saddle-point condition (6.16) is met, the zero eigenvalue coordinates (6.26) evaluate to $\mathbf{v}_0|_{\mathrm{sp}} = \sqrt{2r}\mathbf{k}_{\mathrm{sp}}$. Changing the integration variable from $\mathbf{v}_0$ to $\mathbf{k}_{\mathrm{sp}}$ then yields a factor of $2r$.

With the variable change to the coordinates $\mathbf{v}_j$ the Hessian matrix also transforms. Here, we do not need to know the exact form of the transformed Hessian, since all we need is its determinant. The determinant of the transformed Hessian is identical to the product of the non-vanishing eigenvalues of the singular Hessian H. Such a quantity is also known as a pseudo-determinant of H denoted by $\mathrm{pdet}(\mathsf{H})$ [119, p. 529].[1]

The leading order saddle-point approximation for the trace of the r-th round trip now reads

$$\operatorname{tr}\mathcal{M}^r \sim \frac{r}{\pi}\left(\frac{R_1R_2}{4}\right)^r \int \mathrm{d}\mathbf{k}_{\mathrm{sp}} \frac{g_{\mathrm{sp}}}{\sqrt{\mathrm{pdet}(\mathsf{H})}} e^{-f_{\mathrm{sp}}}\,. \tag{6.27}$$

We are left with the evaluation of the pseudo-determinant. Since we know the eigenvalues of the Hessian with (6.25), the square root of the pseudo-determinant can be expressed as

$$\sqrt{\mathrm{pdet}(\mathsf{H})} = \left(\prod_{\lambda\neq 0}\lambda\right)^{1/2} = \left(\frac{1}{2\kappa_{\mathrm{sp}}}\right)^{2r-1} \lambda_{0,+}\prod_{j=1}^{r-1}\lambda_{j,-}\lambda_{j,+}\,. \tag{6.28}$$

By first evaluating the product $\lambda_{j,-}\lambda_{j,+}$, we can make use of the identity

$$\prod_{j=1}^{r-1}\sin\left(\frac{\pi j}{r}\right) = \frac{r}{2^{r-1}} \tag{6.29}$$

to find

$$\sqrt{\mathrm{pdet}(\mathsf{H})} = \frac{4r^2\kappa_{\mathrm{sp}}}{R_{\mathrm{eff}}}\left(\frac{R_1R_2}{4\kappa_{\mathrm{sp}}^2}\right)^r\,. \tag{6.30}$$

When we change the integration variable in (6.27) to polar coordinates $\mathbf{k}_{\mathrm{sp}} = (k_{\mathrm{sp}}, \varphi_{\mathrm{sp}})$, the integration over the angular component φ_{sp} can be carried out yielding a factor of 2π. The trace of the r-th round trip then becomes

$$\operatorname{tr}\mathcal{M}^r \sim \frac{R_{\mathrm{eff}}}{2r}\int_{\mathcal{K}}^{\infty}\mathrm{d}\kappa_{\mathrm{sp}} \sum_{p=\mathrm{TM,\,TE}}\left[r_p^{(1)}r_p^{(2)}e^{-2\kappa_{\mathrm{sp}}L}\right]^r\left[1+\frac{r}{\mathcal{K}}\left(\frac{s_p^{(1)}|_{\mathrm{sp}}}{R_1}+\frac{s_p^{(2)}|_{\mathrm{sp}}}{R_2}\right)\right]\,, \tag{6.31}$$

where we have used $\kappa_{\mathrm{sp}}\mathrm{d}\kappa_{\mathrm{sp}} = k_{\mathrm{sp}}\mathrm{d}k_{\mathrm{sp}}$ to change the integration over the radial component k_{sp} to κ_{sp}.

[1] Alternatively, the pseudo-determinant of a $n \times n$ matrix A can be computed through its definition [119, p. 529]

$$\mathrm{pdet}(\mathsf{A}) = \lim_{\alpha\to 0}\frac{\det(\mathsf{A}+\alpha 1)}{\alpha^{n-\mathrm{rank}(\mathsf{A})}}\,,$$

where $\mathrm{rank}(\mathsf{A})$ denotes the rank of A.

The sum over round trips (6.8) can now be expressed in terms of polylogarithms and we find

$$\mathcal{F}(\xi) \sim -\frac{R_{\text{eff}}}{2} \sum_{p=\text{TM, TE}} \int_{\mathcal{K}}^{\infty} \mathrm{d}\kappa_{\text{sp}} \left[\text{Li}_2\left(\Phi_p\right) - \frac{1}{\mathcal{K}} \left(\frac{s_p^{(1)}|_{\text{sp}}}{R_1} + \frac{s_p^{(2)}|_{\text{sp}}}{R_2} \right) \log\left(1-\Phi_p\right) \right] \tag{6.32}$$

for $\xi > 0$ where

$$\Phi_p = r_p^{(1)} r_p^{(2)} e^{-2\kappa_{\text{sp}} L} \,. \tag{6.33}$$

Vanishing frequencies

The calculations above leading up to Eq. (6.27) carry over for a vanishing frequency, only that now κ_{sp} is replaced by k_{sp} in the square root of the pseudo-determinant (6.30) and that g_{sp} is obtained from (6.14) by evaluation at the saddle-point manifold. Like in the finite-frequency case with (6.18), the contributions due to the two polarizations

$$\begin{aligned} g_{\text{TM}} &= \frac{e^{-2k_{\text{sp}}Lr}}{(k_{\text{sp}})^{2r}} \left[\mathcal{A}^{(1)}_{R_1 k_{\text{sp}}} \mathcal{A}^{(2)}_{R_2 k_{\text{sp}}} \right]^r , \\ g_{\text{TE}} &= \frac{e^{-2k_{\text{sp}}Lr}}{(k_{\text{sp}})^{2r}} \left[\mathcal{B}^{(1)}_{R_1 k_{\text{sp}}} \mathcal{B}^{(2)}_{R_2 k_{\text{sp}}} \right]^r \end{aligned} \tag{6.34}$$

contribute additively to g_{sp}. The trace of the r-th round trip then becomes

$$\operatorname{tr} \mathcal{M}^r \sim \frac{R_{\text{eff}}}{2r} \int_0^{\infty} \mathrm{d}k_{\text{sp}} \sum_{\mathcal{X}=\mathcal{A},\,\mathcal{B}} \left[\mathcal{X}^{(1)}_{R_1 k_{\text{sp}}} \mathcal{X}^{(2)}_{R_2 k_{\text{sp}}} e^{-2k_{\text{sp}}L} \right]^r . \tag{6.35}$$

Performing the summation over the round trips, we obtain

$$\mathcal{F}(0) \sim -\frac{R_{\text{eff}}}{2} \sum_{\mathcal{X}=\mathcal{A},\,\mathcal{B}} \int_0^{\infty} \mathrm{d}k_{\text{sp}}\, \text{Li}_2\left(\mathcal{X}^{(1)}_{R_1 k_{\text{sp}}} \mathcal{X}^{(2)}_{R_2 k_{\text{sp}}} e^{-2k_{\text{sp}}L} \right) . \tag{6.36}$$

For Drude-type metals, we find from Tab. 5.1 that $\mathcal{A}^{(\text{Drude})} = 1$ and $\mathcal{B}^{(\text{Drude})} = 0$. In this case, expression (6.36) is identical to the PFA and thus does not provide a correction to the PFA. In all other cases, the PFA and the PFA correction is implicitly contained in (6.36).

PFA as the leading order contribution

In Sec. 5.4, we have discussed that the functions $\mathcal{A}$ and $\mathcal{B}$ in (6.36) are asymptotic to the low-frequency expressions of the Fresnel coefficients r_{TM} and r_{TE}, respectively, when the sphere radii are large compared to the distance. Together with the leading order term in (6.32), the leading order asymptotics of the Casimir free energy then becomes

$$\mathcal{F} \sim -\frac{k_{\text{B}} T R_{\text{eff}}}{2} {\sum_{n=0}^{\infty}}' \sum_{p=\text{TM, TE}} \int_{\mathcal{K}_n}^{\infty} \mathrm{d}\kappa_{\text{sp}}\, \text{Li}_2\left(r_p^{(1)} r_p^{(2)} e^{-2\kappa_{\text{sp}}L} \right) \tag{6.37}$$

where $\mathcal{K}_n = \sqrt{\varepsilon_{\text{m}}}\xi_n/c$. The expression (6.37) is precisely the PFA for two spheres given in (4.6). Without assumptions on locality, we have thus proven that the PFA corresponds to the leading order asymptotics of the exact Casimir free energy for arbitrary materials. It is straightforward to extend this result to the zero temperature case. The result is also valid in the plane-sphere limit where the effective radius R_{eff} is replaced by the sphere radius.

While for low frequencies expression (6.36) already contains PFA corrections, the expression for finite frequencies only contains corrections to the PFA due to diffraction. This diffractive contribution to the corrections reads

$$\mathcal{F}_{\mathrm{d}} = \frac{k_{\mathrm{B}} T R_{\mathrm{eff}}}{2} \sum_{n=1}^{\infty} \sum_{p=\mathrm{TM,\,TE}} \int_{\mathcal{K}_n}^{\infty} \mathrm{d}\kappa_{\mathrm{sp}} \frac{1}{\mathcal{K}_n} \left(\frac{s_p^{(1)}|_{\mathrm{sp}}}{R_1} + \frac{s_p^{(2)}|_{\mathrm{sp}}}{R_2} \right) \log\left(1 - r_p^{(1)} r_p^{(2)} e^{-2\kappa_{\mathrm{sp}} L}\right) . \tag{6.38}$$

Due to the evaluation at the saddle-point manifold (6.16), expression (6.38) can still be interpreted as arising from reflections localized at the points of closest approach on the two spheres as depicted in Fig. 6.2 (a). These reflections are, however, not specular as the finite curvature of the spheres are taken into account.

The remaining contributions to the PFA correction at finite frequencies are due to the next-to-leading-order term in the saddle-point approximation (6.5). The derivation of this contribution will be discussed in the following section.

6.4 Geometric optical correction to PFA

For the remaining PFA correction due to the subleading term in the saddle-point approximation, we need to consider only the leading order asymptotic contributions of the function $g|_{\xi>0}$ in (6.13). As the subleading terms in $g|_{\xi>0}$ are proportional to the the inverse radii, they would contribute to higher order corrections to the PFA when included here. Since the leading order term in $g|_{\xi>0}$ describes specular reflections on the two spheres, the contribution to the PFA correction calculated here can be given an interpretation within geometrical optics. In the following part of this section, the frequency ξ will always be finite and thus the subscript $\xi > 0$ will be dropped for the function $g|_{\xi>0}$. The derivation in this section is partly based on the exposition in Ref. [104] where the PFA correction was calculated for a perfectly reflecting plane and sphere.

Variable transformation and the Hessian matrix

Since for the subleading term in the saddle-point formula (6.5) the calculation of derivatives and the Hessian matrix is required, we now need to specify a transformation which singles out the saddle-point manifold and thus leads to formula (6.27). It is convenient to use a discrete Fourier transform to perform such transformation. The transformed variables v are then defined by

$$k_{j,\alpha} = \sum_{l=0}^{2r-1} \mathsf{W}_{j,l} v_{l,\alpha} \tag{6.39}$$

for $\alpha = x, y$, where the Fourier matrix is given by

$$\mathsf{W}_{j,l} = \frac{1}{\sqrt{2r}} \exp\left(\frac{2\pi i}{2r} jl\right) . \tag{6.40}$$

Indeed, the direction of the saddle-point manifold is then given by $\mathbf{v}_0$ as in (6.26). Because the Fourier matrix is unitary, all other directions are in particular orthogonal to $\mathbf{v}_0$. The saddle-point approximation is now applied to the integrals with respect to the variables $\mathbf{v}_j$ for $j = 1, \ldots, 2r-1$.

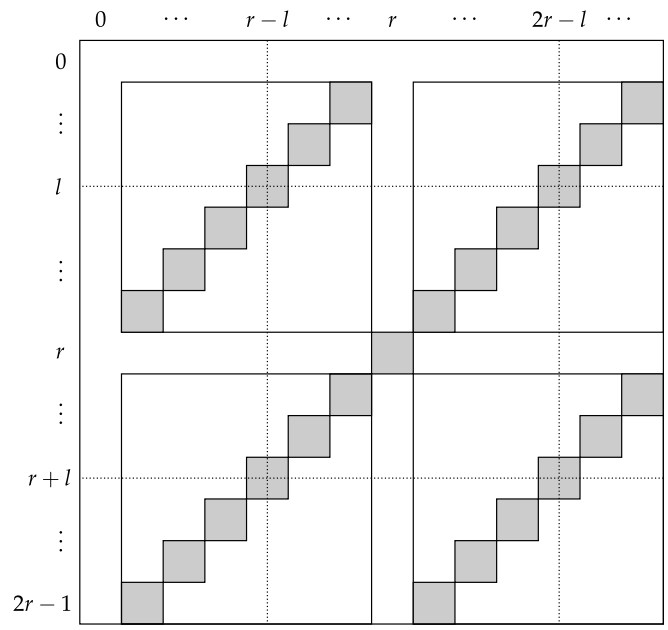

FIGURE 6.3: Schematic representation of the Hessian matrix after Fourier transform. The numbers on the left and top label the row and column indices, respectively. The matrix elements in grey are the only non-vanishing ones. The dotted lines highlight the sub-block of the matrix associated to the index l.

With the discrete Fourier transform, the non-vanishing diagonal blocks of the Hessian matrix transform as

$$\mathsf{H}_{\alpha\alpha} \to \mathsf{W}^T \mathsf{H}_{\alpha\alpha} \mathsf{W} \tag{6.41}$$

for $\alpha = x, y$. In appendix D.2, it is shown that after the transformation the Hessian matrix becomes the anti-diagonal block matrix

$$(\mathsf{W}^T \mathsf{H}_{\alpha\alpha} \mathsf{W})_{j,k} = \frac{1}{\kappa_{\mathrm{sp}}} \begin{cases} i(R_2 - R_1) \sin(\pi k/2r) \cos(\pi k/2r) & \text{for } j+k = r, 3r \\ (R_2 + R_1) \sin^2(\pi k/2r) & \text{for } j+k = 2r \\ 0 & \text{else} \end{cases} \tag{6.42}$$

for $\alpha = x, y$.

The $\alpha\alpha$-blocks of the transformed Hessian are schematically represented in figure 6.3. The matrix elements in grey represent those which are non-zero. The first row and column of the matrix is zero and corresponds to the variable $\mathbf{v}_0$. The remaining part of the Hessian will be required for the saddle-point method. It corresponds to the Hessian with respect to the variables $\mathbf{v}_j$ for $j > 0$ and will be denoted as $(\tilde{\mathsf{H}}_{\alpha\alpha})_{jk}$ for $\alpha = x, y$ and $j, k = 1, \ldots, 2r-1$. Apart from $\tilde{\mathsf{H}}_{r,r} = (R_1 + R_2)/\kappa_{\mathrm{sp}}$, the non-vanishing entries of the transformed Hessian matrix form 2×2 blocks along the anti-diagonal, which can be expressed as

$$\begin{pmatrix} \tilde{\mathsf{H}}_{l,r-l} & \tilde{\mathsf{H}}_{l,2r-l} \\ \tilde{\mathsf{H}}_{r+l,r-l} & \tilde{\mathsf{H}}_{r+l,2r-l} \end{pmatrix} = \frac{1}{\kappa_{\mathrm{sp}}} \begin{pmatrix} -i(R_1 - R_2) s_l c_l & (R_1 + R_2) s_l^2 \\ (R_1 + R_2) c_l^2 & i(R_1 - R_2) s_l c_l \end{pmatrix} \tag{6.43}$$

for $l = 1, \ldots, r-1$ where

$$s_l = \sin\left(\frac{\pi l}{2r}\right) \quad \text{and} \quad c_l = \cos\left(\frac{\pi l}{2r}\right). \tag{6.44}$$

The inversion of the Hessian can be performed block-wise and we find

$$\begin{aligned}\begin{pmatrix} \tilde{\mathsf{H}}^{-1}_{l,r-l} & \tilde{\mathsf{H}}^{-1}_{l,2r-l} \\ \tilde{\mathsf{H}}^{-1}_{r+l,r-l} & \tilde{\mathsf{H}}^{-1}_{r+l,2r-l} \end{pmatrix} &= \begin{pmatrix} \tilde{\mathsf{H}}_{r-l,l} & \tilde{\mathsf{H}}_{r-l,r+l} \\ \tilde{\mathsf{H}}_{2r-l,l} & \tilde{\mathsf{H}}_{2r-l,r+l} \end{pmatrix}^{-1} \\ &= \frac{\kappa_{\mathrm{sp}}}{4R_1R_2} \begin{pmatrix} -i(R_1-R_2)/s_l c_l & (R_1+R_2)/s_l^2 \\ (R_1+R_2)/c_l^2 & i(R_1-R_2)/s_l c_l \end{pmatrix}\end{aligned} \tag{6.45}$$

for $l = 1, \ldots, r-1$ and

$$\tilde{\mathsf{H}}^{-1}_{r,r} = \kappa_{\mathrm{sp}}/(R_1+R_2)\,. \tag{6.46}$$

Geometric optical contribution to the trace over round trips

Having found an expression for the inverse Hessian, we can now evaluate the subleading term of the saddle-point formula (6.5). A closer analysis reveals that two of the terms in this subleading term vanish because the functions g and f are symmetric with respect to their arguments. For instance, after employing the chain rule, the first derivative of the function g reads

$$\left.\frac{\partial g}{\partial v_{i,\alpha}}\right|_{\mathrm{sp}} = \sum_{l=0}^{2r-1} W_{i,l} \left.\frac{\partial g}{\partial k_{l,\alpha}}\right|_{\mathrm{sp}}\,, \tag{6.47}$$

where $i \neq 0$, i.e. the derivative is not taken along the saddle-point manifold. Because of the symmetry of g just mentioned, the derivative on the right-hand side evaluated at the saddle point is independent of l. The resulting sum over the Fourier factors (6.40) vanishes, so that $g_i = 0$. For the same reason the derivative with respect to $v_{i,\alpha}$ in $f_{ijk}\tilde{\mathsf{H}}^{jk}$ evaluates to zero. Because this argument will be used more often when calculating the contribution of the term proportional to g_{ij}, we summarize it as Lemma 1.2 in Appendix E.5.

In the subleading term of the saddle-point formula (6.5) only three terms remain. The geometric optical correction can then be expressed as (6.27) with g_{sp} being replaced by the subleading terms in (6.5), containing the derivatives with respect to f and g. Making use of (6.20) and (6.30), the corresponding expression for the trace of the r-th round trip becomes

$$(\operatorname{tr}\mathcal{M}^r)_{\mathrm{go}} = \frac{R_{\mathrm{eff}}}{4r}\int_{\mathcal{K}}^{\infty} \mathrm{d}\kappa_{\mathrm{sp}}\kappa_{\mathrm{sp}}^{2r}\left[g_{ij}\tilde{\mathsf{H}}^{ij} - \frac{1}{4}g_{\mathrm{sp}}f_{ijkl}\tilde{\mathsf{H}}^{ij}\tilde{\mathsf{H}}^{kl} + \frac{1}{6}g_{\mathrm{sp}}f_{ijk}f_{lmn}\tilde{\mathsf{H}}^{il}\tilde{\mathsf{H}}^{jm}\tilde{\mathsf{H}}^{kn}\right] \tag{6.48}$$

where we use a similar convention as in Sec. 6.1. A lower index, say i, represents derivatives with respect to $v_{i,\alpha}$ evaluated at the saddle-point manifold, and multiple lower indices correspond to higher order derivatives. $\tilde{\mathsf{H}}^{ij}$ is the matrix element of the inverse Fourier transformed Hessian with row index i and column index j. Repeated indices are summed over the values from 1 to $2r-1$ and a summation over $\alpha = x, y$ for each index pair is implicit as well.

The calculation of the terms in the square bracket in (6.48) is somewhat involved. Technical details are provided in Appendix E. There, it is shown that the square bracket in (6.48) can be split into the two terms $U^{(i)}$ and $U^{(ii)}$.

In the first term, $U^{(i)}$, derivatives are taken of all functions but the polarization transformation coefficients (5.15) appearing in (5.41) through (6.13). As shown in Sec. 6.3, the PFA result (6.37) arises from ray-optical specular reflections at the points of closest approach between the two spheres, i.e. scattering channel (a) in Fig. 6.2. The correction due to $U^{(i)}$ can still be understood within geometrical optics, but now

the specular reflections may also occur at tangent planes slightly tilted with respect to the x-y-plane, as illustrated by channels (b)-(d) in Fig. 6.2.

We find its explicit contribution as

$$U^{(i)} = U^{(i,0)} + \sum_{p=\mathrm{TM,TE}} \left(U_p^{(i,1)} + U_p^{(i,2)} \right) \tag{6.49}$$

with

$$U^{(i,0)} = -g_{\mathrm{sp}} \frac{rL\kappa_{\mathrm{sp}}(\kappa_{\mathrm{sp}}^2 + \mathcal{K}^2) + \mathcal{K}^2}{3r\kappa_{\mathrm{sp}}^3} \left(\frac{r^2-1}{R_{\mathrm{eff}}} + \frac{3}{R_1+R_2} \right) \tag{6.50}$$

and

$$U_p^{(1/2)} = 2rg_p \left[d(0) Q_{p,0}^{(1/2)} + d_\pm(1) Q_{p,1}^{(1/2)} \right] . \tag{6.51}$$

Here, g_p is the leading order term in (6.19),

$$\begin{aligned} d(0) &= \frac{\kappa_{\mathrm{sp}}}{2r} \left(\frac{1}{R_1+R_2} + \frac{r^2-1}{3R_{\mathrm{eff}}} \right) , \\ d_\pm(1) &= \frac{\kappa_{\mathrm{sp}}}{2r} \left(-\frac{1}{R_1+R_2} \pm (r-1) \frac{R_1-R_2}{R_1R_2} + \frac{(r-1)(r-2)}{3R_{\mathrm{eff}}} \right) \end{aligned} \tag{6.52}$$

and

$$\begin{aligned} Q_{\mathrm{TE},0}^{(s)} &= Q_{\mathrm{TE},1}^{(s)} + \frac{k_{\mathrm{sp}}^2}{\kappa_{\mathrm{sp}}^3 \varkappa_{\mathrm{sp}}} , \\ Q_{\mathrm{TE},1}^{(s)} &= \frac{k_{\mathrm{sp}}^2 - 2\varkappa_{\mathrm{sp}}^2}{2\kappa_{\mathrm{sp}} \varkappa_{\mathrm{sp}}^3} , \\ Q_{\mathrm{TM},0}^{(s)} &= Q_{\mathrm{TM},1}^{(s)} - \frac{n_s^2 k_{\mathrm{sp}}^2 \mathcal{K}^2}{\kappa_{\mathrm{sp}}^3 \varkappa_{\mathrm{sp}} (\varkappa_{\mathrm{sp}}^2 + n_s^2 k_{\mathrm{sp}}^2)} , \\ Q_{\mathrm{TM},1}^{(s)} &= n_s^2 \mathcal{K}^2 \frac{k_{\mathrm{sp}}^2 (n_s^2 k_{\mathrm{sp}}^2 - 3\varkappa_{\mathrm{sp}}^2) + 2\varkappa_{\mathrm{sp}}^4}{2\kappa_{\mathrm{sp}} \varkappa_{\mathrm{sp}}^3 \left(\varkappa_{\mathrm{sp}}^2 + n_s^2 k_{\mathrm{sp}}^2 \right)^2} \end{aligned} \tag{6.53}$$

with the relative refractive index n_s for sphere s and

$$\varkappa_{\mathrm{sp}} = \sqrt{n_s^2 \mathcal{K}^2 + k_{\mathrm{sp}}^2} . \tag{6.54}$$

For the second contribution to the square bracket, $U^{(ii)}$, derivatives are only taken of the polarization transformation coefficients. Its contribution may thus be interpreted due to scattering channels, which experience a tilt between the Fresnel and scattering planes of successive reflections (see Fig. 5.2). The contribution due to $U^{(ii)}$ thus also takes the effect of polarization mixing into account.

The calculation of $U^{(ii)}$ is outlined in appendix E.4. We find

$$U^{(ii)} = U^{(ii,0)} + \sum_{p=\mathrm{TM,TE}} \left(U_p^{(ii,1)} + U_p^{(ii,2)} \right) \tag{6.55}$$

where the first term reads

$$U^{(ii,0)} = \frac{\mathcal{K}^2 \exp(-2r\kappa_{\rm sp}L)}{k_{\rm sp}^2 \kappa_{\rm sp}^{2r+1}} \frac{1}{R_1+R_2} \times \left[2\Delta r^{(1)}\Delta r^{(2)} Y - X \left(\frac{\left[\Delta r^{(1)}\right]^2}{r_{\rm TE}^{(1)} r_{\rm TM}^{(1)}} \frac{R_2}{R_1} + \frac{\left[\Delta r^{(2)}\right]^2}{r_{\rm TE}^{(2)} r_{\rm TM}^{(2)}} \frac{R_1}{R_2} \right) \right] \tag{6.56}$$

with

$$\begin{aligned} X &= \frac{x_{\rm TE}^r x_{\rm TM} - x_{\rm TM}^r x_{\rm TE}}{x_{\rm TE} - x_{\rm TM}}, \\ Y &= \frac{x_{\rm TE}^r - x_{\rm TM}^r}{x_{\rm TE} - x_{\rm TM}} \end{aligned} \tag{6.57}$$

for $x_p = r_p^{(1)} r_p^{(2)}$, and

$$\Delta r^{(1/2)} = r_{\rm TE}^{(1/2)} - r_{\rm TM}^{(1/2)}. \tag{6.58}$$

The remaining terms in (6.55) can be expressed as

$$U_p^{(1/2)} = -g_p \frac{\mathcal{K}^2}{k_{\rm sp}^2 \kappa_{\rm sp}} \left(r + (r-1)\frac{R_{2/1}}{R_{1/2}} \right) \frac{1}{R_1+R_2} \frac{r_p^{(1/2)} - r_{\bar{p}}^{(1/2)}}{r_p^{(1/2)}}, \tag{6.59}$$

where $\bar{p} = \mathrm{TE}$ if $p = \mathrm{TM}$ and vice versa, and g_p as above.

In the special case of two perfectly reflecting spheres, only the term $U^{(i,0)}$ contributes to the geometric optical correction as the derivatives on the Fresnel coefficients appearing in $U_p^{(i,1/2)}$ vanish. As shown in the final part of Appendix E.4, the term $U^{(ii)}$ entirely cancels out in this case. Thus, the effect of a possible tilt between the scattering and Fresnel planes does not enter the PFA correction. Since such tilt gives rise to polarization mixing scattering channels, it follows that polarization mixing has no effect on the PFA correction. This does not carry over to spheres made of real materials for which $U^{(ii)}$ has a finite contribution and polarization mixing scattering channels contribute to the Casimir interaction.

Geometric optical contribution to the free energy

With (6.48), where the expression in the bracket can be expressed as a sum of the two contributions $U^{(i)}$ and $U^{(ii)}$ given in (6.49) and (6.55), respectively, we have obtained an expression for the r-th round trip due to the correction of the saddle-point integral. Expressing the sum over round trips (6.8) in terms of polylogarithms, we can write the geometric optical correction to the Casimir free energy as

$$\mathcal{F}_{\rm go} = \mathcal{F}_{\rm go}^{(i)} + \mathcal{F}_{\rm go}^{(ii)} \tag{6.60}$$

with $\mathcal{F}_{\rm go}^{(i/ii)}$ being the contribution to the free energy due to $U^{(i/ii)}$ defined in (6.49) and (6.55), respectively.

In analogy to (6.49), we subdivide those contributions as

$$\mathcal{F}_{\rm go}^{(i)} = k_{\rm B}T \sum_{n=1}^{\infty} \left[\mathcal{F}_{\rm go}^{(i,0)}(\xi_n) + \mathcal{F}_{\rm go}^{(i,1)}(\xi_n) + \mathcal{F}_{\rm go}^{(i,2)}(\xi_n) \right], \tag{6.61}$$

where

$$\mathcal{F}_{\mathrm{go}}^{(i,0)}(\xi) = \frac{1}{12}\int_{\mathcal{K}}^{\infty} \mathrm{d}\kappa_{\mathrm{sp}} \frac{1}{\kappa_{\mathrm{sp}}^3} \sum_{p=\mathrm{TM,TE}} \big\{ L\kappa_{\mathrm{sp}}(\kappa_{\mathrm{sp}}^2 + \mathcal{K}^2)[\mathrm{Li}_0(\Phi_p) + (3u-1)\,\mathrm{Li}_2(\Phi_p)] + \mathcal{K}^2[\mathrm{Li}_1(\Phi_p) + (3u-1)\,\mathrm{Li}_3(\Phi_p)]\big\} \quad (6.62)$$

with the dimensionless parameter u as defined in (4.32) and

$$\mathcal{F}_{\mathrm{go}}^{(i,1/2)}(\xi) = -\frac{1}{12}\int_{\mathcal{K}}^{\infty} \mathrm{d}\kappa_{\mathrm{sp}}\kappa_{\mathrm{sp}} \sum_{p=\mathrm{TM,TE}} [q_p^{(0)} Q_{p,0}^{(1/2)} + q_p^{(1/2)} Q_{p,1}^{(1/2)}] \quad (6.63)$$

with the coefficients Q given above in (6.53) and

$$\begin{aligned} q_p^{(0)} &= \mathrm{Li}_0(\Phi_p) + (3u-1)\,\mathrm{Li}_2(\Phi_p)\,, \\ q_p^{(1/2)} &= \mathrm{Li}_0(\Phi_p) + 3\left(-1 \pm \frac{R_1 - R_2}{R_1 + R_2}\right)\mathrm{Li}_1(\Phi_p) + \left(2 - 3u \mp 3\frac{R_1 - R_2}{R_1 + R_2}\right)\mathrm{Li}_2(\Phi_p)\,. \end{aligned} \quad (6.64)$$

The second term in (6.60) reads

$$\mathcal{F}_{\mathrm{go}}^{(ii)} = k_{\mathrm{B}}T \sum_{n=1}^{\infty} \Big[\mathcal{F}_{\mathrm{go}}^{(ii,0)}(\xi_n) + \mathcal{F}_{\mathrm{go}}^{(ii,1)}(\xi_n) + \mathcal{F}_{\mathrm{go}}^{(ii,2)}(\xi_n)\Big] \quad (6.65)$$

with

$$\mathcal{F}_{\mathrm{go}}^{(ii,0)}(\xi) = -\frac{u}{4}\int_{\mathcal{K}}^{\infty} \mathrm{d}\kappa_{\mathrm{sp}} \frac{\mathcal{K}^2}{k_{\mathrm{sp}}^2\kappa_{\mathrm{sp}}} \frac{1}{x_{\mathrm{TE}} - x_{\mathrm{TM}}} \Bigg\{ 2\Delta r^{(1)}\Delta r^{(2)}\,[\mathrm{Li}_2(\Phi_{\mathrm{TE}}) - \mathrm{Li}_2(\Phi_{\mathrm{TM}})] - \left(\frac{[\Delta r^{(1)}]^2}{r_{\mathrm{TE}}^{(1)} r_{\mathrm{TM}}^{(1)}}\frac{R_2}{R_1} + \frac{[\Delta r^{(2)}]^2}{r_{\mathrm{TE}}^{(2)} r_{\mathrm{TM}}^{(2)}}\frac{R_1}{R_2}\right)[x_{\mathrm{TM}}\,\mathrm{Li}_2(\Phi_{\mathrm{TE}}) - x_{\mathrm{TE}}\,\mathrm{Li}_2(\Phi_{\mathrm{TM}})] \Bigg\} \quad (6.66)$$

and

$$\mathcal{F}_{\mathrm{go}}^{(ii,1/2)}(\xi) = \frac{u}{4}\int_{\mathcal{K}}^{\infty} \mathrm{d}\kappa_{\mathrm{sp}} \frac{\mathcal{K}^2}{k_{\mathrm{sp}}^2\kappa_{\mathrm{sp}}} \sum_{p=\mathrm{TM,TE}} \frac{r_p^{(1/2)} - r_{\bar{p}}^{(1/2)}}{r_p^{(1/2)}} \times \left[\left(1 + \frac{R_{2/1}}{R_{1/2}}\right)\mathrm{Li}_1(\Phi_p) - \frac{R_{2/1}}{R_{1/2}}\,\mathrm{Li}_2(\Phi_p)\right]. \quad (6.67)$$

With (6.32), (6.36) and (6.60), we now have found the first two terms in the asymptotic expansion of the Casimir free energy for two dielectric spheres at a finite temperature T. Expressions for a vanishing temperature can be found by replacing the Matsubara sum by means of (2.65). We thus have found asymptotic expansion for the remaining cases in Tab. 6.1 (B), which have not been derived in the literature before.

In the special case of two spheres made of identical materials, the PFA correction depends only on the radii of the spheres through the effective radius R_{eff} and the dimensionless parameter u. This can be seen by using

$$\frac{R_1}{R_2} + \frac{R_2}{R_1} = \frac{1}{u} + 2 \quad (6.68)$$

in the contributions constituting $\mathcal{F}_{\mathrm{go}}^{(i)}$ in (6.61) and noting that the dependence on

$(R_1 - R_2)/(R_1 + R_2)$ through $q_p^{(1)}$ and $q_p^{(2)}$ defined in (6.64) drops out in (6.61) because $Q_{p,1}^{(1)} = Q_{p,1}^{(2)}$.

6.5 Perfect reflecting spheres at a vanishing temperature

For perfectly reflecting spheres in vacuum at a vanishing temperature, the expressions for the asymptotics of the finite-frequency contributions simplify considerably. In this section, we reproduce the corresponding result (6.1) known from the literature. The results obtained in this section will also be important for the analysis of the PFA corrections beyond expression (6.1), which will be discussed in Sec. 8.3.

For the calculations in this section, it is convenient to rescale the imaginary wave number $\mathcal{K} = \xi/c$ and introduce the dimensionless variable

$$s = rL\mathcal{K} \tag{6.69}$$

with the round-trip index r and the surface-to-surface distance L. When the Casimir energy is expressed in terms of the round-trip expansion (6.8), the integral over imaginary frequencies can be written as an integral over s. The Casimir energy then reads

$$E = -\frac{\hbar c}{2\pi L}\int_0^\infty \mathrm{d}s \sum_{r=1}^{\infty} \frac{1}{r^2}\,\mathrm{tr}\,\mathcal{M}^r\,. \tag{6.70}$$

For perfect reflectors, the Fresnel coefficients are $r_{\mathrm{TM}} = -r_{\mathrm{TE}} = 1$ and the coefficients (5.31), appearing in the WKB correction of the Mie scattering amplitudes, can be expressed as

$$\begin{aligned} s_1^{(\mathrm{PR})}\Big|_{\mathrm{sp}} &= \frac{\mathcal{K}(\mathcal{K}^2 - 2\kappa_{\mathrm{sp}}^2)}{2\kappa_{\mathrm{sp}}^3}\,, \\ s_2^{(\mathrm{PR})}\Big|_{\mathrm{sp}} &= -\frac{\mathcal{K}^3}{2\kappa_{\mathrm{sp}}^3}\,. \end{aligned} \tag{6.71}$$

In analogy to (6.69), we introduce another dimensionless variable defined as

$$t = rL\kappa_{\mathrm{sp}}\,. \tag{6.72}$$

The contribution to the trace over the r-th round trip due to the leading order saddle-point approximation as given in (6.31) can then be expressed in terms of the new variables s and t. After summation over the two polarization contributions, we find

$$(\mathrm{tr}\,\mathcal{M}^r)_{\mathrm{LO}} = \frac{1}{r^2}\int_s^\infty \mathrm{d}t\, e^{-2t}\left(\frac{R_{\mathrm{eff}}}{L} - \frac{r^2}{2t}\right)\,. \tag{6.73}$$

In the same way, we obtain an expression for the trace of the r-th round trip due to the subleading contribution to the saddle-point approximation (6.48):

$$(\mathrm{tr}\,\mathcal{M}^r)_{\mathrm{NTLO}} = -\frac{1}{6r^2}\int_s^\infty \mathrm{d}t\, e^{-2t}\,\frac{t(t^2+s^2)+s^2}{t^3}\left(r^2+3u-1\right) \tag{6.74}$$

Here, we have used that, for perfect reflectors, only (6.50) contributes to the square bracket in (6.48).

Finally, inserting (6.73) and (6.74) in (6.70) yields the first two terms in the asymptotic expansion of the Casimir energy

$$E \sim E_{\mathrm{PFA}} + E_1 \,, \tag{6.75}$$

where the leading order asymptotic term is associated with the PFA and given by the leading term in (6.73):

$$E_{\mathrm{PFA}} = -\frac{\hbar c R_{\mathrm{eff}}}{2\pi L^2} \int_0^\infty \mathrm{d}s \int_s^\infty \mathrm{d}t\, e^{-2t} \sum_{r=1}^\infty \frac{1}{r^4} = -\frac{\hbar c R_{\mathrm{eff}} \pi^3}{720 L^2} \,. \tag{6.76}$$

In the last equality of (6.76) we have used that the integrals over s and t evaluate to $1/4$ and the sum over r is given by

$$\sum_{r=1}^\infty \frac{1}{r^4} = \frac{\pi^4}{90} \,. \tag{6.77}$$

The subleading term in (6.75) is given by

$$E_1 = \frac{\hbar c}{24\pi L} \left(4 \sum_{r=1}^\infty \frac{1}{r^2} + (3u-1) \sum_{r=1}^\infty \frac{1}{r^4} \right) = E_{\mathrm{PFA}} \left(\frac{1}{3} - \frac{20}{\pi^2} - u \right) \frac{L}{R_{\mathrm{eff}}} \,, \tag{6.78}$$

where in the first equality the integrals over s and t yield the values

$$\begin{aligned} \int_0^\infty \mathrm{d}s \int_s^\infty \mathrm{d}t\, \frac{e^{-2t}}{t} &= \frac{1}{2} \,, \\ \int_0^\infty \mathrm{d}s \int_s^\infty \mathrm{d}t\, e^{-2t} \frac{t(t^2+s^2)+s^2}{t^3} &= \frac{1}{2} \,. \end{aligned} \tag{6.79}$$

In the second equality of (6.78), we have evaluated the sum over round trips using (6.77) and

$$\sum_{r=1}^\infty \frac{1}{r^2} = \frac{\pi^2}{6} \,. \tag{6.80}$$

With the asymptotic expansion of the Casimir energy for two perfectly reflecting spheres in vacuum at a vanishing temperature as given in (6.75), we have now reproduced the result (6.1) known from the literature.

6.6 Plane-sphere limit

The plane-sphere geometry can be obtained as a limiting case from the geometry of two spheres. If we take the limit $R_1 \to \infty$, the surface of sphere 1 becomes a plane. We denote the radius of the remaining sphere as $R = R_2$. In this limit, the effective radius becomes the sphere radius, $R_{\mathrm{eff}} \to R$, and the parameter u defined in (4.32) goes to zero as R_2/R_1.

The asymptotics of the zero-frequency contribution (6.36) then becomes

$$\mathcal{F}(0) \sim -\frac{R}{2} \sum_{\mathcal{X}=\mathcal{A},\mathcal{B}} \int_0^\infty \mathrm{d}k_{\mathrm{sp}}\, \mathrm{Li}_2 \left(r_p^{(1)}(0,k_{\mathrm{sp}}) \mathcal{X}^{(2)}_{R_2 k_{\mathrm{sp}}} e^{-2k_{\mathrm{sp}}L} \right) \,, \tag{6.81}$$

where $p = \mathrm{TM}$ when $\mathcal{X} = \mathcal{A}$, and $p = \mathrm{TE}$ when $\mathcal{X} = \mathcal{B}$. Here, we used that $\mathcal{A}_{R_1 k_{\mathrm{sp}}} \to r_{\mathrm{TM}}(0,k_{\mathrm{sp}})$ and $\mathcal{B}_{R_1 k_{\mathrm{sp}}} \to r_{\mathrm{TE}}(0,k_{\mathrm{sp}})$ as $R_1 \to \infty$.

For finite frequencies, the result from the leading order saddle-point approximation (6.32) is now given

$$\mathcal{F}(\xi) \sim -\frac{R}{2} \sum_{p=\mathrm{TM,\,TE}} \int_{\mathcal{K}}^{\infty} \mathrm{d}\kappa_{\mathrm{sp}} \left[\mathrm{Li}_2\left(\Phi_p\right) - \frac{s_p^{(2)}|_{\mathrm{sp}}}{R} \log\left(1-\Phi_p\right) \right] \tag{6.82}$$

with Φ_p as given in (6.33). The terms constituting the geometric optical contribution to the correction through (6.61) become in the plane-sphere limit

$$\mathcal{F}_{\mathrm{go}}^{(i,0)}(\xi) = \frac{1}{12} \int_{\mathcal{K}}^{\infty} \mathrm{d}\kappa_{\mathrm{sp}} \frac{1}{\kappa_{\mathrm{sp}}^3} \big\{ L\kappa_{\mathrm{sp}} (\kappa_{\mathrm{sp}}^2 + \mathcal{K}^2) [\mathrm{Li}_0(\Phi_p) - \mathrm{Li}_2(\Phi_p)] + \mathcal{K}^2 [\mathrm{Li}_1(\Phi_p) - \mathrm{Li}_3(\Phi_p)] \big\} \tag{6.83}$$

and

$$\mathcal{F}_{\mathrm{go}}^{(i,1/2)}(\xi) = -\frac{1}{12} \int_{\mathcal{K}}^{\infty} \mathrm{d}\kappa_{\mathrm{sp}} \kappa_{\mathrm{sp}} [q_p^0 Q_{p,0}^{(1/2)} + q_p^{(1/2)} Q_{p,1}^{(1/2)}] \tag{6.84}$$

where the coefficients Q are given above in (6.53) and

$$\begin{aligned} q_p^{(0)} &= q_p^{(1)} = \mathrm{Li}_0(\Phi_p) - \mathrm{Li}_2(\Phi_p)\,, \\ q_p^{(2)} &= \mathrm{Li}_0(\Phi_p) - 6\,\mathrm{Li}_1(\Phi_p) + 5\,\mathrm{Li}_2(\Phi_p)\,. \end{aligned}$$

The terms constituting (6.65) are now given by

$$\mathcal{F}_{\mathrm{go}}^{(ii,0)}(\xi) = \frac{1}{4} \int_{\mathcal{K}}^{\infty} \mathrm{d}\kappa_{\mathrm{sp}} \frac{\mathcal{K}^2}{k_{\mathrm{sp}}^2 \kappa_{\mathrm{sp}}} \frac{x_{\mathrm{TM}}\,\mathrm{Li}_2(\Phi_{\mathrm{TE}}) - x_{\mathrm{TE}}\,\mathrm{Li}_2(\Phi_{\mathrm{TM}})}{x_{\mathrm{TE}} - x_{\mathrm{TM}}} \frac{[\Delta r^{(2)}]^2}{r_{\mathrm{TE}}^{(2)} r_{\mathrm{TM}}^{(2)}} \tag{6.85}$$

and

$$\mathcal{F}_{\mathrm{go}}^{(ii,2)}(\xi) = \frac{1}{4} \int_{\mathcal{K}}^{\infty} \mathrm{d}\kappa_{\mathrm{sp}} \frac{\mathcal{K}^2}{k_{\mathrm{sp}}^2 \kappa_{\mathrm{sp}}} \sum_{p=\mathrm{TM,TE}} \frac{r_p^{(2)} - r_{\bar{p}}^{(2)}}{r_p^{(2)}} [\mathrm{Li}_1(\Phi_p) - \mathrm{Li}_2(\Phi_p)]\,. \tag{6.86}$$

The remaining term $\mathcal{F}_{\mathrm{go}}^{(ii,1)}(\xi)$ vanishes as the reflection matrix on the plane is given by the Fresnel coefficients and thus does not contain the polarization transformation coefficients.

Consistent with the results for two spheres, the contributions $\mathcal{F}_{\mathrm{go}}^{(ii)}$ drop out in the perfect reflector limit. At $T = 0$, the PFA correction agrees with the results given in Ref. [38]. The result given here yields the PFA correction also for finite temperatures which has not been derived in the literature before. Therefore, we complete Tab. 6.1 (A).

6.7 Asymptotic expansion for the Casimir force and force gradient

So far, we have found the first two terms of the asymptotic expansion of the Casimir free energy for two spheres and a sphere in front of a plane. In Casimir experiments, commonly the Casimir force F and force gradient F' are measured [20, 22]. The asymptotic expansion of those quantities can be obtained from the free energy by

taking derivatives with respect to the distance L:

$$\begin{aligned} F &= -\frac{\partial \mathcal{F}}{\partial L} \\ F' &= -\frac{\partial^2 \mathcal{F}}{\partial L^2}\,. \end{aligned} \tag{6.87}$$

Apart from the expression (6.62) and (6.83) for the sphere-sphere and plane-sphere geometry, respectively, the asymptotic expansion of the Casimir free energy depends on the distance L only through the argument of the polylogarithms

$$\Phi_p = r_p^{(1)} r_p^{(2)} e^{-2\kappa_{\rm sp} L} \tag{6.88}$$

for $p = \mathrm{TE}, \mathrm{TM}$. Using the identity for the derivative of the polylogarithm (A.16), we can express the derivatives with respect to the distance as

$$\begin{aligned} -\frac{\partial \operatorname{Li}_s(\Phi_p)}{\partial L} &= 2\kappa_{\rm sp} \operatorname{Li}_{s-1}(\Phi_p) \\ -\frac{\partial^2 \operatorname{Li}_s(\Phi_p)}{\partial L^2} &= -4\kappa_{\rm sp}^2 \operatorname{Li}_{s-2}(\Phi_p)\,. \end{aligned} \tag{6.89}$$

The corresponding expression of (6.62) for the force is then obtained as

$$\begin{aligned} -\frac{\partial}{\partial L}\mathcal{F}_{\rm go}^{(i,0)}(\xi) = \\ \frac{1}{12}\int_{\mathcal{K}}^{\infty} \mathrm{d}\kappa_{\rm sp} \frac{1}{\kappa_{\rm sp}^2} \sum_{p=\mathrm{TM,TE}} \big\{ 2L\kappa_{\rm sp}(\kappa_{\rm sp}^2 + \mathcal{K}^2)[\operatorname{Li}_{-1}(\Phi_p) + (3u-1)\operatorname{Li}_1(\Phi_p)] \\ - k_{\rm sp}^2[\operatorname{Li}_0(\Phi_p) + (3u-1)\operatorname{Li}_2(\Phi_p)]\big\}\,. \end{aligned} \tag{6.90}$$

The corresponding expression for the force gradient reads

$$\begin{aligned} -\frac{\partial^2}{\partial L^2}\mathcal{F}_{\rm go}^{(i,0)}(\xi) = \frac{1}{3}\int_{\mathcal{K}}^{\infty} \mathrm{d}\kappa_{\rm sp} \sum_{p=\mathrm{TM,TE}} \big\{ \kappa_{\rm sp}[\operatorname{Li}_{-1}(\Phi_p) + (3u-1)\operatorname{Li}_1(\Phi_p)] \\ - L(\kappa_{\rm sp}^2 + \mathcal{K}^2)[\operatorname{Li}_{-2}(\Phi_p) + (3u-1)\operatorname{Li}_0(\Phi_p)]\big\} \end{aligned} \tag{6.91}$$

The result for the plane-sphere geometry is obtained by setting $u = 0$ in the above expressions.

In the remaining terms, a short-distance formula for the Casimir force is obtained from the formula for the Casimir free energy by the replacement

$$\operatorname{Li}_s(\Phi_p) \to 2\kappa_{\rm sp} \operatorname{Li}_{s-1}(\Phi_p) \tag{6.92}$$

and similarly one obtains a formula for the Casimir force gradient by the replacement

$$\operatorname{Li}_s(\Phi_p) \to -4\kappa_{\rm sp}^2 \operatorname{Li}_{s-2}(\Phi_p)\,. \tag{6.93}$$

This replacement rule can also be used to obtain the force and force gradient contribution in the zero-frequency limit. In (6.36) and (6.81), the polylogarithms can be replaced with the same rule above except that the function arguments would be different and $\kappa_{\rm sp}$ would be replaced by $k_{\rm sp}$ instead.

6.8 Comparison with the derivative expansion

The derivative expansion (DE) approach, which was discussed in Sec. 4.2, is an alternative approach for obtaining an asymptotic expansion of the Casimir interaction. For electromagnetic fields, it is only applicable for obtaining the first two terms in the asymptotic expansion. It is not possible to obtain any higher order asymptotic terms since the kernel $\tilde{G}$ in (4.16) is non-analytic and cannot be expanded beyond second order [44, 120]. In this section, we make a closer comparison between the results for the asymptotic expansion (AE), which were obtained in this chapter, with the DE.

In the literature, no explicit results are given for the DE of the Casimir interaction between two spheres. There, a direct comparison on the analytical level is not possible. In Ref. [38], Teo has compared her result for the asymptotic expansion in the plane-sphere geometry with the corresponding results from the DE, given in [43], numerically and has found good agreement.

For metallic spheres, the DE is not very useful. Although it is applicable for Drude-type metals yielding a logarithmic PFA-correction, subleading logarithmic terms dominate the leading PFA correction at distances which are typical for experiments [33]. Thus, in Refs. [46, 47, 95], Bimonte proposes to use exact results or numerical methods to evaluate the zero-frequency contribution. For finite Matsubara frequencies, $n > 0$, he proposes to use the DE to compute the Casimir interaction. Within the DE, the PFA correction can be expressed as

$$\frac{F_{1,n>0}}{F_{\mathrm{PFA},n>0}} = -\left[\theta(L) + u\kappa(L)\right] \frac{L}{R_{\mathrm{eff}}} \tag{6.94}$$

for the Casimir force, and

$$\frac{F'_{1,n>0}}{F'_{\mathrm{PFA},n>0}} = -\left[\tilde{\theta}(L) + u\tilde{\kappa}(L)\right] \frac{L}{R_{\mathrm{eff}}}\,, \tag{6.95}$$

for the force gradient with the effective radius R_{eff} and the dimensionless parameter u defined in (4.4) and (4.32), respectively. The functions θ, κ, $\tilde{\theta}$ and $\tilde{\kappa}$ depend only on the distance, the material properties of the objects and the temperature T. As detailed in [47], they can be expressed in terms of the function α given in (4.18) and the plane-plane energy $\mathcal{F}_{\mathrm{PP}}$ given in (3.29). Bimonte gives the values of those functions for gold in vacuum in the distance range of $0.1\,\mu$m to $2\,\mu$m in [47]. To model the dielectric function of gold, tabulated optical data [121] were used. In order to yield the dielectric function at imaginary frequencies, the optical data has been suitably extrapolated towards zero frequency using the Drude (with plasma frequency $\omega_p = 9\,\mathrm{eV}/\hbar$ and damping constant $\gamma = 0.035\,\mathrm{eV}/\hbar$) or the plasma prescription.

In Fig. 6.4, we compare Bimonte's tabulated results from [47] with our AE result using the same optical data with the Drude prescription. We assume two spheres with equal radii $R_1 = R_2 = 30\,\mu$m. Figure 6.4 (a) shows the comparison for the Casimir force and (b) for the force gradient. Bimonte's result for the DE is represented by the circles, while the crosses represent our AE result. We find good agreement with the results from the derivative expansion for both the force and the force gradient. The relative difference between our results and the DE results is within the accuracy to which the functions θ, κ, $\tilde{\theta}$ and $\tilde{\kappa}$ in Ref. [47] were given, which is about 3 digits.

For the zero-frequency contribution, we compare the DE with the AE for dielectrics, as both methods are applicable in this case. We have worked out the DE result with (4.35). The AE result for the zero-frequency contribution is given in (6.36)

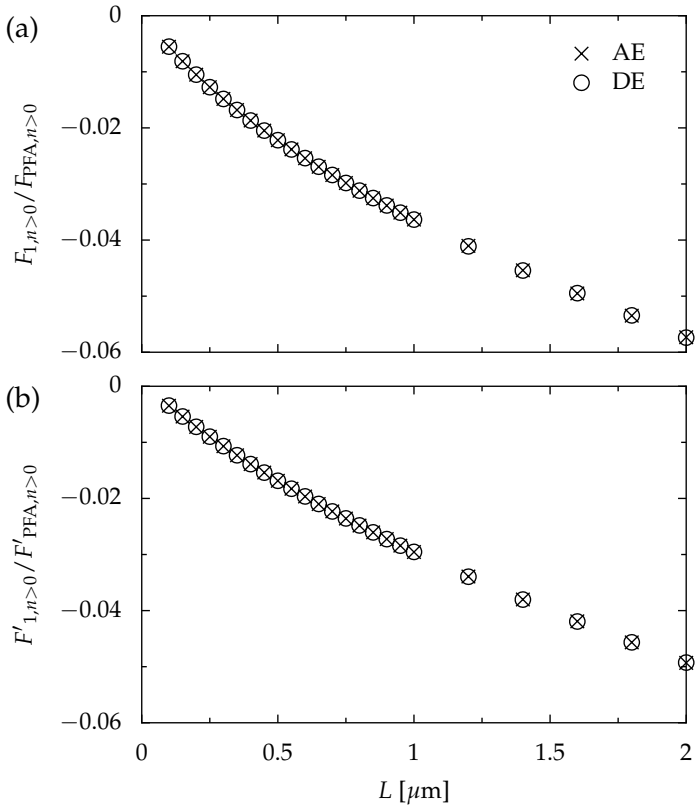

FIGURE 6.4: Comparison of the asymptotic expansion (AE) and derivative expansion (DE) approach for two gold spheres with equal radii $R_1 = R_2 = 30\,\mu$m in Vacuum. The PFA-correction from both methods is depicted relative to the PFA as a function of the distance L for (a) the Casimir force and (b) the force gradient. For the quantities involved, the Matsubara sum runs over all non-zero frequencies, $n > 0$, at $T = 300\,$K.

and (6.81) for the sphere-sphere and plane-sphere geometry, respectively. Since the DE and AE result produce rather different predictions when the relative refractive index of the object is smaller than one, we compare these predictions with exact numerical results obtained by the method which will be developed in chapter 7.

In Fig. 6.5 (a) and (b) the relative error made by the DE (dash-dotted lines), the AE (solid lines) and the PFA (dashed lines) is shown for polystyrene in vacuum in the plane-sphere and sphere-sphere geometry, respectively. In Fig. 6.5 (c) and (d) the corresponding results are shown for polystyrene in water.

For polystyrene in vacuum, which has a relative dielectric function of about $\varepsilon(0) = 2.37$, the DE and AE yield very similar results for both geometries. Both methods improve on the PFA by almost an order of magnitude in the relative error at shorter distances. The situation is different for polystyrene in water, which has a relative dielectric function of $\varepsilon(0) = 0.030$. While the AE again improves significantly on the PFA, the DE does not do as well as the AE.

The reason why the DE does not perform as well as the AE for polystyrene in water is that the DE does not provide the correct asymptotics for the PFA correction. When $\varepsilon(0) = 0$, the Casimir free energy is equivalent to the TE contribution for perfect reflectors for which the DE is not applicable. Bimonte has shown that the correction in this case is proportional to $\log^2(L/R)$ for the plane-sphere geometry [39]. It seems plausible that a correction of such form dominates over the logarithmic correction predicted by the DE when $\varepsilon(0)$ is small. In contrast to the DE, the AE provides the correct asymptotics which is uniformly valid for any value of $\varepsilon(0)$.

6.9 The role of diffraction

For a perfectly reflecting plane and sphere in vacuum at zero temperature, it was found that the correction to the PFA is dominated by the term associated to diffraction as it contributes with almost 90% [104]. With the correction to the PFA obtained in Secs. 6.3 and 6.4, we can now study how the results from Ref. [104] carry over to the geometry of two spheres made of a perfectly reflecting or real materials. For simplicity, we assume a vanishing temperature, $T = 0$, and the two spheres be made of an identical non-dispersive dielectric with relative permittivity ε.

The total PFA correction $\mathcal{F}_1$ is then composed of the diffractive contribution $\mathcal{F}_\mathrm{d}$ given in (6.38) and the geometric optical contribution $\mathcal{F}_\mathrm{go} = \mathcal{F}_\mathrm{go}^{(i)} + \mathcal{F}_\mathrm{go}^{(ii)}$. The term $\mathcal{F}_\mathrm{go}^{(i)}$, which measures the influence of the tilting of the tangent planes on which the modes are reflected, is given in (6.61). The other term, $\mathcal{F}_\mathrm{go}^{(ii)}$, amounts to the contribution to the correction due to a tilt between the scattering planes for multiple reflections during the round trips. It is given in (6.65). Expressions for zero temperature can be obtained from these by replacing the sum over the positive Matsubara frequencies with an integral over imaginary frequencies as

$$k_\mathrm{B} T \sum_{n=1}^{\infty} \to \hbar \int_0^\infty \frac{\mathrm{d}\xi}{2\pi} \,. \tag{6.96}$$

In Fig. 6.6 (a), the diffractive contribution $\mathcal{F}_\mathrm{d}$ along with the geometric optical contribution $\mathcal{F}_\mathrm{go}^{(i)}$ is depicted as a function of the ratio of the radii R_1/R_2 from 1 to 100. Figure 6.6 (b) shows the geometric optical contribution $\mathcal{F}_\mathrm{go}^{(ii)}$. The individual contributions are depicted relative to the total contribution $\mathcal{F}_1 = \mathcal{F}_\mathrm{d} + \mathcal{F}_\mathrm{go}^{(i)} + \mathcal{F}_\mathrm{go}^{(ii)}$. The chosen values for the relative permittivities are taken as the low-frequency limit

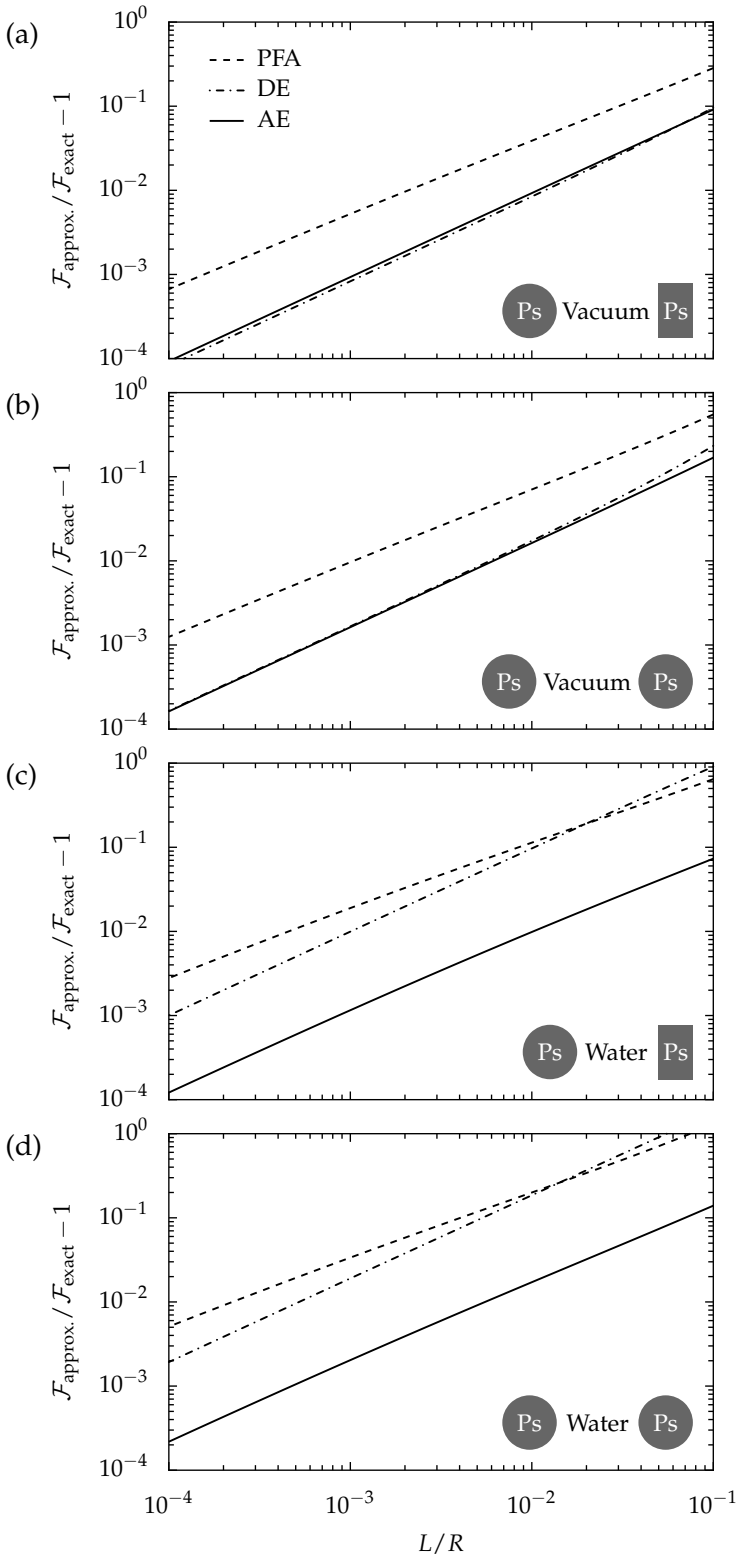

FIGURE 6.5: The relative error of the proximity-force approximation (PFA), the derivative expansion (DE) and the asymptotic expansion (AE) is shown as a function of the the aspect ratio L/R where L is the surface-to-surface distance and R the radius of the sphere(s). The radius of the sphere(s) is taken to be $1\,\mu$m. The four subfigures differ in the medium materials and geometry: polystyrene in vacuum for (a) the plane-sphere and (b) the sphere-sphere geometry, and polystyrene in water for (c) plane-sphere and (d) sphere-sphere geometry.

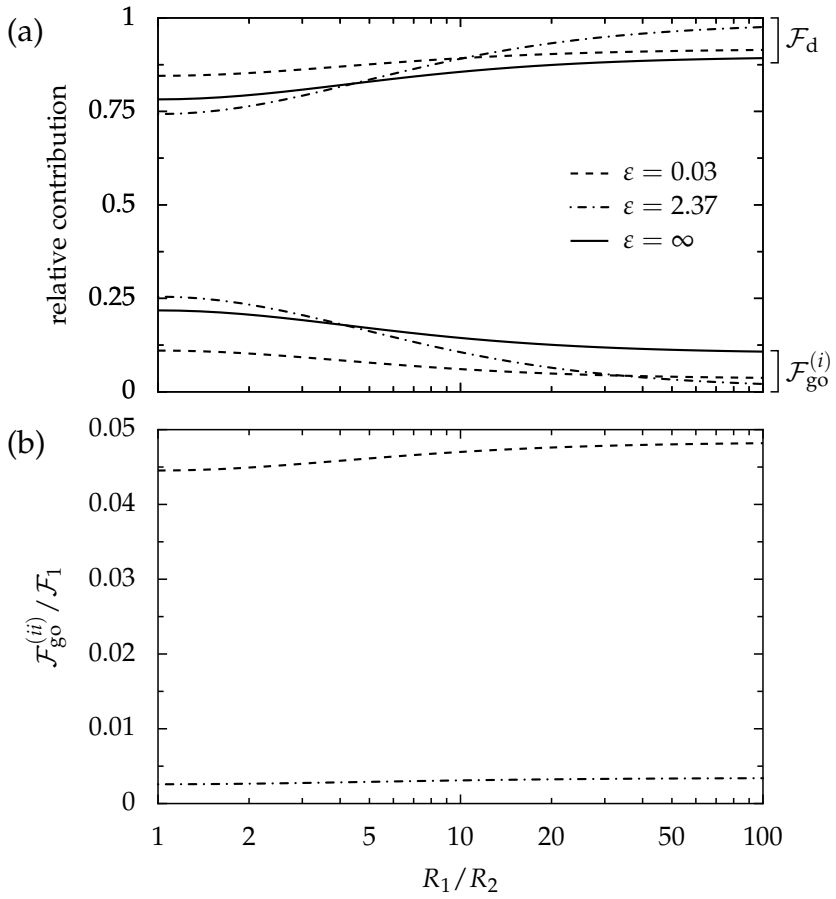

FIGURE 6.6: The contributions to the PFA correction between two spheres with radii R_1 and R_2 and relative permittivity ε as a function of the ratio of the radii, R_1/R_2. The temperature is assumed to be zero and the contributions are given relative to the total correction $\mathcal{F}_1 = \mathcal{F}_{\rm d} + \mathcal{F}_{\rm go}^{(i)} + \mathcal{F}_{\rm go}^{(ii)}$. (a) The contribution due to diffraction $\mathcal{F}_{\rm d}$ and the geometric optical contribution $\mathcal{F}_{\rm go}^{(i)}$. (b) The geometric optical contribution $\mathcal{F}_{\rm go}^{(ii)}$. Note the difference in scale of the vertical axis.

for polystyrene in water ($\varepsilon = 0.030$) and polystyrene in vacuum ($\varepsilon = 2.37$). The result for perfectly reflecting spheres is indicated by the black line. Note that, for non-dispersive dielectrics at $T = 0$, the relative contributions do not depend on the surface-to-surface distance L.

We observe that also for two spheres, the diffractive correction contributes the most to the total correction. In the plane-sphere limit $R_1/R_2 \gg 1$, its contribution exceeds the value for perfect reflectors of 90% when the relative permittivity is finite. The relative diffractive contribution monotonically decreases as the sphere radii become equal, but it still amounts to the largest contribution.

The geometric optical term $\mathcal{F}_{\rm go}^{(ii)}$ contributes typically to less than one percent to the PFA correction. $\mathcal{F}_{\rm go}^{(i)}$ makes the second largest contribution, which is largest for two spheres with equal radii, and decreases monotonically as one sphere radius becomes larger than the other (see $\varepsilon = 2.37$ in Fig 6.6). When the relative permittivity ε approaches zero, the geometric optical contribution $\mathcal{F}_{\rm go}^{(ii)}$ may become much larger and may even exceed the contribution of $\mathcal{F}_{\rm go}^{(i)}$.

For dispersive dielectrics, we find qualitatively similar result for which an additional dependence on the distance between the two spheres can be observed.

6.10 Effective interaction area

The most precise Casimir experiments employ spherical lenses [122] or coated microspheres attached to a cantilever beam [123–126] instead of whole spherical surfaces. Since the experimental data are analyzed with the help of the PFA, it is important to understand what section of the spherical surface actually contributes to the leading asymptotics. For instance, in the case of a spherical lens, such analysis would define the minimum transverse lens size required for equivalence with a complete spherical surface. Here, we estimate the size of the sphere section relevant not just for the PFA but also for the correction derived in the previous parts of this chapter.[2] We proceed in two steps. First, we employ our saddle-point calculation to estimate the typical change in the projection of the wave vector onto the x-y-plane during reflection at one of the spheres. Second, we use geometric arguments to obtain the corresponding size of the sphere section in real space.

Even though we first consider the reflection at a single sphere, this reflection is still to be taken in the context of the sphere-sphere setup. Therefore, we keep the saddle-point manifold (6.16) obtained in Sec. 6.3. Considering only a single reflection, we denote the incident and scattered wave vectors as $\mathbf{K}^{(\mathrm{in})}$ and $\mathbf{K}^{(\mathrm{sc})}$, respectively, as indicated in Fig. 6.7. For simplicity, we take $k_y^{(\mathrm{in})} = k_y^{(\mathrm{sc})} = k_{y,\mathrm{sp}}$ and concentrate on k_x. As the x-axis is arbitrary, we replace k_x by the modulus of $\mathbf{k}$ in the following. From (6.10) and (6.11), the Gaussian contribution of a single reflection at a sphere with radius R_j, $j = 1, 2$ can then be identified as

$$\exp\left(-\eta R_j\right) = \exp\left(-\frac{R_j}{4\kappa_{\mathrm{sp}}}(k^{(\mathrm{in})} - k^{(\mathrm{sc})})^2\right). \tag{6.97}$$

Here, η is defined in analogy to (6.12) with the two wave-vector components replaced by $k^{(\mathrm{in})}$ and $k^{(\mathrm{sc})}$.

Neglecting numerical factors of order one, the width around the saddle-point manifold is thus $\delta k^{(j)} \propto \sqrt{\kappa_{\mathrm{sp}}/R_j}$. The typical scale of κ_{sp} is set by the integral on the right-hand side of (6.31), finally leading to the change of the projection of the wave vector onto the x-y-plane

$$\delta k^{(j)} = |\mathbf{k}^{(\mathrm{sc})} - \mathbf{k}^{(\mathrm{in})}| \propto (LR_j)^{-1/2}. \tag{6.98}$$

As expected, the scattering at the smaller sphere provides the larger deviations from the saddle-point manifold. Thus, the effective area contributing to the Casimir interaction is fixed by the smaller radius which we refer to as R_1 in the following.

We now explore the implications of (6.98) in real space based on specular reflection. The saddle-point manifold (6.16) corresponds to reflections between the points on the two spheres corresponding to the closest distance L (cf. Fig. 6.7). Deviations from the saddle-point manifold as allowed by the Gaussian (6.97) implicate the surroundings of these two points in the scattering process. We estimate the dimension of the spherical cap on the surface of the smaller sphere 1 by considering the scattering of propagating waves in the real frequency domain with the help of Fig. 6.7.

[2] The analysis in this section is taken from Ref. [114].

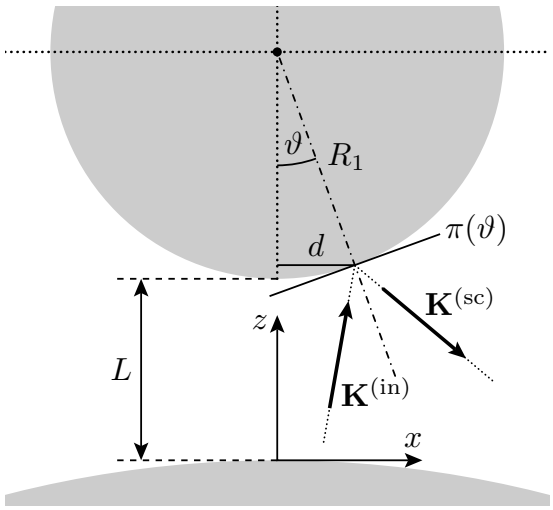

FIGURE 6.7: Estimation of the effective area contributing to the Casimir interaction between two spheres. $\mathbf{K}^{(\mathrm{in})}$ and $\mathbf{K}^{(\mathrm{sc})}$ denote the incident and scattered wave vectors, respectively. To be definite, the reflection is shown at the smaller sphere of radius R_1. Specular reflection at the tangent plane $\pi(\vartheta)$ entails that the projections of $\mathbf{K}^{(\mathrm{in})}$ and $\mathbf{K}^{(\mathrm{sc})}$ on $\pi(\vartheta)$ are equal. On the other hand, the wave vector projections on the x-y-plane are generally different: $\delta k = |\mathbf{k}^{(\mathrm{sc})} - \mathbf{k}^{(\mathrm{in})}| \approx 2\vartheta k_z$ for $\vartheta \ll 1$. We can estimate the angular sector effectively contributing to the Casimir interaction from the width δk of the Gaussian integrand in the saddle-point approximation (see text). (from Ref. [114])

As above, we assume $\mathbf{k}^{(\mathrm{in})}$ and $\mathbf{k}^{(\mathrm{sc})}$ to be parallel and for simplicity omit the index $j = 1$ when writing $\delta k = |\mathbf{k}^{(\mathrm{sc})} - \mathbf{k}^{(\mathrm{in})}|$. As shown in Sec. 5.4, the WKB approximation for the direct reflection term amounts to a specular reflection at a tangent plane $\pi(\vartheta)$ making an angle ϑ with the x-y-plane. For parallel vectors and small values of δk, a simple relation between ϑ and δk can be derived by noting that while the projection of the wave vector onto the plane $\pi(\vartheta)$ is conserved during a scattering process, this is not the case for the projection onto the x-y-plane for non-vanishing values of ϑ. Assuming $\vartheta \ll 1$, we find

$$\delta k \approx 2\vartheta k_z \,. \tag{6.99}$$

This relation together with the scaling $k_z \propto 1/L$ allow us to estimate the width of the angular sector effectively contributing to the Casimir interaction from the Gaussian width (6.98).

We find that the spherical cap around the point of closest distance corresponds to the angular sector bounded by the angle $\vartheta \propto (L/R_1)^{1/2} \ll 1$. As indicated by Fig. 6.7, its transverse size is $d \approx R_1\vartheta \propto (R_1 L)^{1/2} \ll R_1 < R_2$. The same scaling was found by an heuristic geometric argument [127]. The area of the spherical surface effectively contributing to the interaction is then $A \propto R_1 L$, which coincides, except for a numerical factor of order one, with the ratio between the Casimir force for two spheres within PFA and the Casimir pressure for parallel planes, as long as the interaction obeys a power law.[3]

[3]Since we have neglected numerical factors of order one, we are unable to distinguish between the smallest radius R_1 and the effective radius R_{eff} defined in (4.4), given that their ratio is bounded by $1 < R_1/R_{\mathrm{eff}} \leq 2$.

Although the discussion above holds for arbitrary temperatures, we show in the remaining part of this section that the effective area for the thermal corrections scales in a different way in the low-temperature regime. The difference arises from the typical scale for $\kappa_{\rm sp}$, which is no longer set by $1/L$, but rather by $1/\lambda_T$, where $\lambda_T = \hbar c/k_B T$ is the thermal wavelength. In order to illustrate this property, we consider the thermal correction of the Casimir force $\delta F \equiv F(L,T) - F(L,0)$ as an example. We start from Eqs. (4.7) with (3.29) and employ the Poisson summation formula [77] to write

$$\delta F = 2\hbar\, R_{\rm eff} \sum_{m=1}^{\infty} \sum_{p} \int_0^{\infty} d\xi \cos(m\lambda_T \xi/c) \int_{\xi/c}^{\infty} \frac{d\kappa}{2\pi} \kappa \log\left(1 - r_p^{(1)} r_p^{(2)} e^{-2\kappa L}\right) . \quad (6.100)$$

In the low-temperature limit, $L \ll \lambda_T$, the exponential $\exp(-2\kappa L)$ can be taken to be approximately constant and does not provide a cutoff for the κ integration in (6.100). For instance, in the case of plasma metals, the correction δF can be written in terms of simple integrals involving trigonometric functions of $m\lambda_T\kappa$, which are similar to the expressions derived for the Casimir pressure between parallel planes in Ref. [77]. The derivation of the low-temperature limit of (6.100) for Drude metals is more involved [128], but $1/\lambda_T$ also provides the typical scale of κ in this case.

As a consequence, the effective area contributing to the thermal correction δF is found to be of the order of $A^{(T)} \propto R_1 \lambda_T$ and thus much larger than the area relevant for $F(L,T)$, which is dominated by the zero-temperature (vacuum) contribution in the low-temperature limit. This result is consistent with the numerical examples for a scalar field presented in Ref. [129].

The thermal correction to the Casimir force has been measured in the plane-sphere geometry by employing a coated lens with $R_1 = 15.6\,\text{cm}$ [122]. The results were analyzed with the help of the PFA, which can be expected to provide an accurate description of the thermal correction if the transverse size of the lens is much larger than $\sqrt{R_1\lambda_T} \propto 1\,\text{mm}$. If our estimate valid for $L \ll \lambda_T$ applies to the experiment where $L \lesssim 0.4\,\lambda_T$, we can conclude that the lens was indeed of sufficient size.

In most Casimir force measurements, thermal corrections are typically very small. Nevertheless, our estimation of an enlarged effective area is still relevant for thermodynamic quantities vanishing in the zero-temperature limit, in particular for the Casimir entropy.

Chapter 7

Plane-wave numerical approach

For the numerical evaluation of the scattering formula, usually a multipole basis is employed. Spherical multipolar waves have been applied to the geometries of a plane and a sphere [48–52], two spheres [32, 53, 54], and a sphere and a grating [55]. Bispherical multipolar waves have also found numerical application in the plane-sphere and the sphere-sphere geometry [39, 47]. The approaches using bispherical multipoles show an improved convergence rate compared to approaches using spherical multipoles. They, however, are only limited to the evaluation of the zero-frequenciy contributing to the high temperature limit of the Casimir interaction. This is because bispherical coordinates solve only the Laplace equation and not the more general Helmholtz equation [130].

In this chapter, we propose to employ the plane-wave basis for a numerical evaluation of the scattering formula. It turns out that the convergence properties of the plane-wave numerical approach are superior over the method using spherical multipoles. In the examples of the plane-sphere and sphere-sphere geometry, the convergence properties of the plane-wave approach are similar to those observed in the method utilizing bispherical multipoles. The plane-wave approach is, however, applicable for all frequencies and thus useful for making predictions of the Casimir interaction at any temperature.

We start out by explaining the plane-wave numerical approach for arbitrary geometries. The key idea for the method is the Nyström discretization of the plane-wave momenta. For geometries which exhibit cylindrical symmetry, we explain that the method can be improved using a discrete Fourier transform. Then, the plane-wave numerical approach is applied to the plane-sphere and the sphere-sphere geometry, which both are cylindrical symmetric. Finally, we address numerical issues appearing in the numerical calculations with special focus on the numerical evaluation of the Mie scattering amplitudes. Most parts of this chapter were adapted from Ref. [80].

7.1 Arbitrary geometry

Within the continuous plane-wave basis, the operators constituting the round-trip, and thus also the round-trip operator itself, are integral operators. As such, the action of the round-trip operator (2.41) on a given plane-wave basis elements can be expressed as

$$\mathcal{M}\,|\mathbf{k}, p\rangle = \sum_{p'} \int \frac{d^2\mathbf{k}'}{(2\pi)^2}\, K_{\mathcal{M}}(\mathbf{k}', p'; \mathbf{k}, p)\,|\mathbf{k}', p'\rangle \tag{7.1}$$

with its kernel function

$$K_{\mathcal{M}}(\mathbf{k}', p'; \mathbf{k}, p) = e^{-\kappa' \mathcal{L}} \sum_{p''} \int \frac{d^2\mathbf{k}''}{(2\pi)^2} K_{\mathcal{R}_2}(\mathbf{k}', p'; \mathbf{k}'', p'') e^{-\kappa'' \mathcal{L}} K_{\mathcal{R}_1}(\mathbf{k}'', p''; \mathbf{k}, p)\,, \quad (7.2)$$

where $K_{\mathcal{R}_j}$ is the kernel of the reflection operator $\mathcal{R}_j$ for $j = 1, 2$ and κ' as well as κ'' are defined according to (3.7). Note that we have dropped the dependence of the plane-wave basis elements on the sign ϕ, representing the propagation of the plane waves with respect to the z-axis, as it is the same before and after the round trip. Note also that the kernel functions depend also on the frequency ξ which is suppressed in the arguments to not overload the notation. In the continuous case, the kernel functions can be identified with the matrix elements of the corresponding operators.

For numerical purposes, a Nyström discretization needs to be applied to the integral appearing in (7.1). The discrete matrix elements of the round trip operator then differ from its kernel function by a numerical factor as we will see in the following. With the Nyström discretization, the action of the round-trip operator is expressed in terms of

$$\mathcal{M} \, |\mathbf{k}_\alpha, p\rangle = \sum_{p', \alpha'} \frac{w_{\alpha'}}{(2\pi)^2} K_{\mathcal{M}}(\mathbf{k}_{\alpha'}, p'; \mathbf{k}_\alpha, p) \, |\mathbf{k}_{\alpha'}, p'\rangle \quad (7.3)$$

with the nodes $\mathbf{k}_\alpha$ and weights w_α of a quadrature rule for the two-dimensional integral. Later, when carrying out the integration over $\mathbf{k}$ in polar coordinates, it will be appropriate to use two different one-dimensional quadrature rules for the radial and the angular integration.

Within this approximation the matrix elements of the round-trip operator become the corresponding kernel function multiplied by the quadrature weights [131]

$$\langle \mathbf{k}_{\alpha'}, p' | \mathcal{M} | \mathbf{k}_\alpha, p \rangle = \frac{w_{\alpha'}}{(2\pi)^2} K_{\mathcal{M}}(\mathbf{k}_{\alpha'}, p'; \mathbf{k}_\alpha, p)\,. \quad (7.4)$$

After discretization the matrix elements thus form a block matrix with respect to the index α and the polarization p. The Casimir free energy an then be approximated by replacing the round-trip operator $\mathcal{M}$ in (2.52) by the finite matrix (7.4). Likewise, an approximation for the Casimir force and force gradient can be found doing the same replacement in the formulas (2.63) and (2.64), respectively.

In general, the reflection operators pertaining to the two objects are non-diagonal in the plane-wave basis as is the case for example in the geometry of two spheres. The integral over $\mathbf{k}''$ appearing inside the kernel of the round-trip operator (7.2) can usually not be performed analytically. Thus, for numerical applications this integral needs to be discretized as well where the quadrature rule with indices α'' may differ from the one chosen in (7.3). The summation over α'' and p'' then allows the round-trip matrix to be expressed in terms of a product of two block matrices representing the reflection operators.

7.2 Geometry with cylindrical symmetry

Casimir and van der Waals experiments are often carried out in set-ups with a certain symmetry. The cylindrical symmetry is particularly common as it appears in the plane-sphere and sphere-sphere geometries. At first sight, the spherical-wave basis appears to be better adapted for those geometries since the azimuthal number m is conserved through the round trip, yielding a block-diagonal round-trip matrix.

However, this symmetry can also be exploited in the plane-wave basis as will be explained in the following.

For a cylindrically symmetric geometry it is natural to express the transverse wave vector $\mathbf{k}$ in polar coordinates with radial component k and angular component φ, where the latter is relevant for the following considerations. A suitable quadrature rule for the integration over φ is the trapezoidal rule which at order M has nodes at $\varphi_j = (2\pi/M)j$ with constant weights $w_j = 2\pi/M$ where $j = 1, \ldots, M$. In fact, the trapezoidal rule converges exponentially fast for periodic functions as given here [132, 133].

Due to the cylindrical symmetry, the kernel functions depend only on the difference of the angular components $\Delta\varphi = \varphi' - \varphi$. Because the weights of the trapezoidal rule are constant and its nodes proportional to the indices, the discretized block matrix then depends through the difference of the angles only on the difference of the indices, i.e. $\Delta\varphi_{i,j} = \Delta\varphi_{i-j}$. Such a block matrix is called circulant and can be block-diagonalized by a discrete Fourier transform. The blocks on the diagonal then correspond to the contributions for each azimuthal number starting from $m = 0, \pm 1, \ldots$ up to $\pm(M-1)/2$ when M is odd or $M/2$ when M is even. Note that opposite signs in the azimuthal number contribute equally. This is due to the fact that azimuthal numbers of opposite signs are connected through the Fourier transform by the transformation $\Delta\varphi \to -\Delta\varphi$. Such a transformation, however, leaves the Casimir interaction unchanged, since it corresponds to a flip in the sign of the z-coordinates.

The reflection operators of the two objects may in general be non-diagonal as it is the case in the geometry of two spheres. In Sec. 7.1 it was argued that the discretized round-trip matrix can then be written in terms of a product of two block matrices. In order to exploit the cylindrical symmetry, the quadrature rule of the angular component of the $\mathbf{k}''$-integral in (7.2) needs to be a trapezoidal rule of the same order M as above. Only then both block matrices become circulant such that after the discrete Fourier transform their block matrix product can be simplified to a product of block-diagonal matrices.

It is possible to perform the discrete Fourier transform analytically, which opens the possibility for a hybrid numerical method in which the matrix elements are constructed by discretizing the radial transverse momentum k for each angular momentum index m. At first sight, one might favor such a hybrid approach over the pure plane-wave approach discussed above, since one can save on the computation time of the discrete Fourier transform. In practice, however, the time needed for the discrete Fourier transform in the plane-wave approach is dominated by the computation of the matrix elements. Numerical tests on the plane-sphere geometry indicate that the hybrid approach is slower than the plane-wave approach. Details on the hybrid approach in the example of the plane-sphere geometry can be found in appendix F.

In the following, we apply the plane-wave numerical method in the examples of the plane-sphere and the sphere-sphere geometry. Both geometries are cylindrically symmetric so that the simplification discussed in this section applies.

7.3 Plane-sphere geometry

As a first example to which we apply the plane-wave method described above, we consider a sphere with radius R above a plane at a surface-to-surface distance L. The cylindrically symmetric geometry is depicted in Fig. 7.1. The kernel of the round-trip

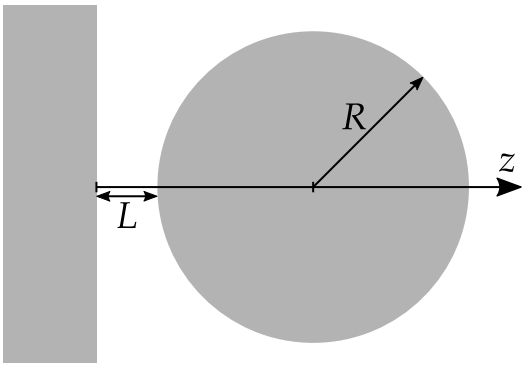

FIGURE 7.1: Geometry of a sphere with radius R in front of a plane at a surface-to-surface distance L.

operator is given by

$$K_{\mathcal{M}}(\mathbf{k}, p; \mathbf{k}', p') = r_p(i\xi, k) e^{-(\kappa+\kappa')(L+R)} K_{\mathcal{R}_S}(\mathbf{k}, p; \mathbf{k}', p') \tag{7.5}$$

with the Fresnel coefficients r_p given in (3.9) and, in view of the matrix elements (5.14), the kernel of the reflection operator at the sphere $K_{\mathcal{R}_S}$ reads

$$\begin{aligned}
K_{\mathcal{R}_S}(k', \varphi', \mathrm{TM}; k, \varphi, \mathrm{TM}) &= \frac{2\pi k}{\mathcal{K}\kappa'} \left[AS_2 + BS_1\right] , \\
K_{\mathcal{R}_S}(k', \varphi', \mathrm{TE}; k, \varphi, \mathrm{TE}) &= \frac{2\pi k'}{\mathcal{K}\kappa'} \left[AS_1 + BS_2\right] , \\
K_{\mathcal{R}_S}(k', \varphi', \mathrm{TM}; k, \varphi, \mathrm{TE}) &= -\frac{2\pi k'}{\mathcal{K}\kappa'} \left[CS_1 + DS_2\right] , \\
K_{\mathcal{R}_S}(k', \varphi', \mathrm{TE}; k, \varphi, \mathrm{TM}) &= \frac{2\pi k'}{\mathcal{K}\kappa'} \left[CS_2 + DS_1\right] ,
\end{aligned} \tag{7.6}$$

with the Mie scattering amplitudes (5.3) and the polarization transformation coefficients (5.15). For convenience, the factor k' arising from the integration measure in polar coordinates has been absorbed into the kernel functions.

In (7.5), we chose the reference point of the sphere at its center and the reference point of the plane as the point on its surface closest to the sphere. The exponential function in (7.5) corresponds to the translation of the plane waves from the plane's surface to the sphere center and back.

In the multipole method, a symmetrization of the round-trip operator is important for a fast and stable numerical evaluation of the Casimir interaction because otherwise the matrices appearing in the calculation are ill-conditioned [57]. This symmetrization is not as crucial in the plane-wave method where it merely gives a factor of two in run-time speed-up because only half of the matrix elements need to be computed.

It is however important to write the translation over the sphere radius in (7.5) symmetrically with respect to the two momenta κ and κ'. Only then the matrix elements in the plane-wave method are well-conditioned and take their maximum around $\mathbf{k} = \mathbf{k}'$. This can be understood by examining the asymptotic behavior of the round-trip operator when $R \gg L$.

Following the line of reasoning from the discussion of the effective interaction area in Sec. 6.10 around Eq. (6.97), the Gaussian contribution of the reflection at the

sphere can be identified as

$$\exp\left(-\frac{R}{4\kappa}\left[(k-k')^2+k^2(\varphi-\varphi')^2\right]\right). \tag{7.7}$$

Its main contribution comes from $k = k'$ and $\varphi = \varphi'$ where the exponent vanishes. When the translation operator is not expressed symmetrically with respect to the momenta, the kernel would grow exponentially with κ and decrease exponentially with κ' or vice versa, resulting in an ill-conditioned matrix.

Quadrature rule for radial wave vector component

Before the Casimir interaction can be determined numerically, the quadrature rule for the integration over the radial component of the transverse wave vectors in (7.3) needs to be specified. In principle, any quadrature rule for the semi-infinite interval $[0,\infty)$ can be used. The Fourier-Chebyshev scheme described in Ref. [134] turned out to be particularly well suited. Defining

$$t_n = \frac{\pi n}{N+1}, \tag{7.8}$$

the quadrature rule is specified by its nodes

$$k_n = b\cot^2(t_n/2) \tag{7.9}$$

and weights

$$w_n = \frac{8b\sin(t_n)}{[1-\cos(t_n)]^2}\frac{1}{N+1}\sum_{\substack{j=1\\ j\,\mathrm{odd}}}^{N}\frac{\sin(jt_n)}{j} \tag{7.10}$$

for $n = 1,\ldots,N$. An optimal choice for the free parameter b can boost the convergence of the computation.

For dimensional reasons, the transverse wave vector and thus b should scale like the inverse surface-to-surface distance $1/L$. In fact, the choice $b = 1/L$ already yields a fast convergence rate and will be used in the following discussion.

Estimation of the convergence rate

In order to understand how well the plane-wave method performs when $R \gg L$, one needs to know how the quadrature orders N and M for the integration over the angular and radial wave vector component, respectively, scale with the aspect ratio R/L for a maximally allowed relative error. We refer to this scaling as the convergence rate of the quadrature schemes.

In the multipole method, the number of multipoles needs to be truncated in order to make the calculation of the Casimir interaction amenable to linear algebra routines. Convergence will then be reached when the highest multipole order $\ell_{\max}$ and the highest azimuthal number $m_{\max}$ included in the computation take values which scale as $\ell_{\max} \propto R/L$ and $m_{\max} \propto \sqrt{R/L}$, respectively [37, 38, 40]. Since the angular quadrature order M in the plane-wave approach is related to $m_{\max}$ through a Fourier transform, one can expect that it exhibits the same convergence rate as $m_{\max}$. The scaling behavior of the radial quadrature order N, however, is a priori not known and will be determined in the following.

Within the plane-wave approach, convergence can only be reached once the nodes associated to the quadrature rules are able to resolve the structure of the kernel functions. The important contributions of the round-trip kernel come from a region around its maximum at $\kappa = \kappa' \approx 1/L$. This region corresponds to indices of the Fourier-Chebyshev quadrature rule around $n = n' \approx N/2$, where for large N the spacing between neighboring quadrature nodes is given by

$$\delta k \approx \frac{2\pi}{LN}\,. \tag{7.11}$$

Furthermore, when $R \gg L$, the kernel can be approximated by a Gaussian with width $\sqrt{\kappa/R} \propto 1/\sqrt{LR}$. This can be seen by expanding the exponent in (7.7) around $k = k'$. Requiring δk to be of the order of that Gaussian width, we find that the quadrature order N scales like $\sqrt{R/L}$. Along the same lines, it can be verified that the angular quadrature order M obeys the same scaling law.

The quadrature orders for angular and radial integration can thus be expressed as

$$N = \left\lceil \eta_N \left(\frac{R}{L}\right)^{1/2} \right\rceil\,, \quad M = \left\lceil \eta_M \left(\frac{R}{L}\right)^{1/2} \right\rceil \tag{7.12}$$

respectively, where the ceiling function ensures that the orders are integers. The two coefficients η_N and η_M control the numerical accuracy with larger values corresponding to higher accuracy.

These expectations for the convergence rate can be verified numerically. We specifically consider perfect reflectors in vacuum, a sphere radius of 1 μm, i.e. a typical value for colloids, and room temperature, $T = 293\,\mathrm{K}$. Figure 7.2 (a) shows the relative error of the Casimir free energy as a function of η_N and η_M for the aspect ratios $R/L = 50$ and 500. The errors have been computed relative to energies with much larger values of the coefficients, namely $\eta_N = \eta_M = 14$ for all points in the figure. For the points where the relative errors are shown as a function of η_N, the coefficient of the angular quadrature order was kept fixed at $\eta_M = 14$, and vice versa. One can indeed see that the coefficients depend only weakly on the aspect ratio R/L. This also holds for other system parameters and real materials as can be seen in the example of a polystyrene sphere and plane in water depicted in Fig. 7.2 (b). The figures can be further used as a guide to choose η_N and η_M in order to obtain a given numerical accuracy. The formulas (7.12) only work when R/L is larger than 50. For smaller aspect ratios, one can simply set R/L to 50 in Eq. (7.12), which gives a sufficiently high accuracy depending on the coefficients η_N and η_M.

Based on the curves depicted in Fig. 7.2 we establish a rule of thumb for which the η's can be determined for a given desired relative error ϵ:

$$\begin{aligned} \eta_M &= -0.38\log(\epsilon) - 0.13\,, \\ \eta_N &= 0.007\log^2(\epsilon) - 0.27\log(\epsilon) + 0.42\,. \end{aligned} \tag{7.13}$$

For convenience, required values of η_N and η_M for specific relative errors ϵ are listed in Tab. 7.1.

In comparison to the multipole method we conclude that the matrix sizes appearing in the plane-wave approach are smaller by a factor of $\sqrt{R/L}$. This reduction in the matrix size becomes particularly relevant when typical aspect ratios appearing in experiments are considered.

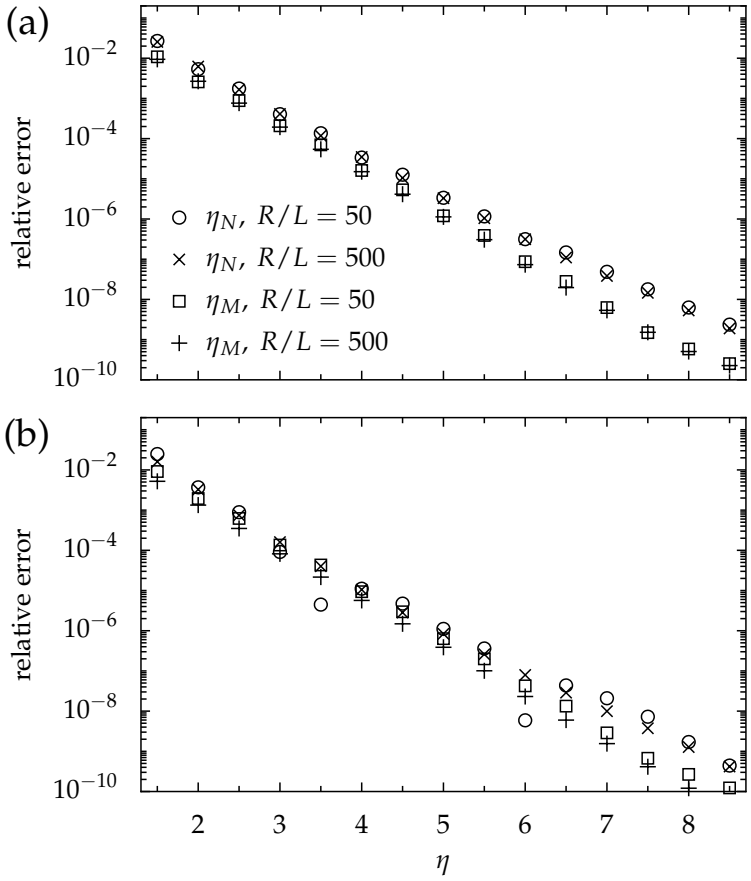

FIGURE 7.2: The relative error as a function of η_N (circles and crosses) and η_M (squares and pluses) for the aspect ratios $R/L = 50$ and 500 for (a) perfectly reflectors in vacuum (taken from [80]) and (b) polystyrene in water.

ϵ	10^{-2}	10^{-3}	10^{-4}	10^{-5}	10^{-6}	10^{-7}	10^{-8}
η_M	1.6	2.5	3.4	4.2	5.1	6.0	6.9
η_N	1.9	2.7	3.6	4.6	5.6	6.8	8.0

TABLE 7.1: Required values of η_N and η_M to achieve a numerical relative error of ϵ.

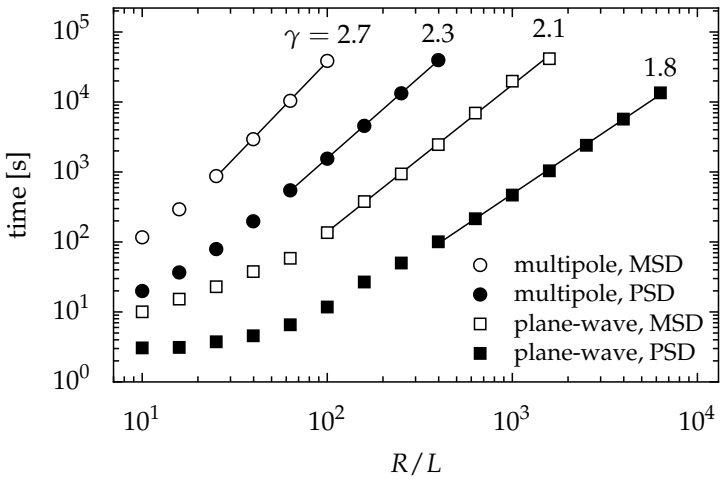

FIGURE 7.3: Runtime comparison between the plane-wave method (squares) and the multipole method (circles) using MSD (open symbols) and PSD (filled symbols). The solid lines indicate a power-law fit $\propto (R/L)^\gamma$ on the basis of the data points shown on top of the lines. The value of the exponent γ is indicated at the end of the lines. The timing experiments were carried out on a computer with an Intel Core i7-2600 processor. The four cores running at 3.4 GHz were fully exploited by running eight threads or processes in parallel. (taken from [80])

Runtime analysis: plane-wave versus multipole method

We now further quantify the advantages of the plane-wave method over the multipole method by analyzing their respective runtimes. The plane-wave method was implemented in Python using the scientific libraries NumPy [135], SciPy [136] as well as Numba [137] for just-in-time compilation. For the multipole method the implementation of Ref. [138] in C was used. Because the latter only supports the computation of the Casimir free energy, we restrict the analysis to this quantity.

We consider the same plane-sphere setup as in the previous section with perfect reflectors in vacuum, a sphere radius of $R = 1\,\mu$m and temperature $T = 293\,$K. The Casimir free energy at finite temperatures can be evaluated in different ways. We consider the Matsubara spectrum decomposition (MSD) represented by Eq. (2.52), and the Padé spectrum decomposition (PSD) [79] outlined in Sec. 2.7. When using PSD, only $\sqrt{\lambda_T/L}$ terms in the frequency summation need to be considered, where $\lambda_T = \hbar c/k_B T$ is the thermal wavelength. Thus, PSD is expected to be significantly faster than MSD for all experimentally relevant distances since the latter requires a summation over λ_T/L terms to ensure convergence.

To ensure comparability, the Casimir free energy is computed with both methods to the same numerical precision of about six correct digits. Figure 7.3 shows the runtime of the Casimir free energy for the multipole method (circles) and the plane-wave method (squares) for aspect ratios $R/L \geq 10$ using MSD (open symbols) and PSD (filled symbols). For all timing experiments a machine with an Intel Core i7-2600 processor was used. The four cores running at 3.4 GHz were fully exploited by either running eight threads or processes in parallel depending on the implementation. We find that the plane-wave method is significantly faster than the multipole method. As expected, the PSD performs better than the MSD. For instance, at the aspect ratio $R/L = 100$, the multipole methods takes about 11 hours to compute the free energy using MSD and only 25 minutes with PSD. The plane-wave method,

however, needs only about two minutes to compute the same quantity when using MSD and 12 seconds with PSD. For other system parameters and real materials we come to similar conclusions for the runtime.

The black lines in Fig. 7.3 are fits to the points they overspan. The timings of the multipole method are consistent with the timing experiment in Ref. [57] where it was found that for a given frequency and azimuthal number the timing scales as $\propto (R/L)^{1.31}$. The sum over the azimuthal numbers scales with $\propto (R/L)^{0.5}$. The above mentioned scaling behavior for the frequency sum in the MSD and PSD is thus consistent with the observed over-all scaling of $(R/L)^{2.7}$ and $(R/L)^{2.3}$, respectively.

The method based on plane waves scales as $(R/L)^{2.1}$ for MSD and $(R/L)^{1.8}$ using PSD, allowing the computation of higher aspect ratios with ordinary hardware. The difference between the scaling behavior of the MSD and PSD for the plane-wave method of about $(R/L)^{0.3}$ is notably smaller than the expected difference of $(R/L)^{0.5}$. While the PSD requires the evaluation of fewer frequency contributions to the Casimir energy, some of the frequencies to be considered are higher than those required for the MSD (see discussion in Sec. 2.7). Numerical tests show that the time needed to evaluate matrix elements increases with increasing frequency, thus offering an explanation for the reduced improvement of the PSD over the MSD.

Note that for the calculations of the determinants, we did not use the sophisticated algorithm using hierarchical matrices which was crucial to boost the performance for Casimir computations in the multipole basis [56, 57]. Since we are dealing with much smaller matrices and our computation time is dominated by the calculation of the matrix elements itself, such method is not expected to bring a significant improvement. Instead we speed up the calculation of the matrix elements by first estimating their values in terms of their asymptotic behavior given in Eq. (7.7). Since the matrices are well-conditioned and their dominant contributions come from matrix elements around the diagonal, we can set matrix-elements to zero if their asymptotic behavior predicts a value smaller than the machine precision. Otherwise, the computed matrix elements are numerically exact. Numerical tests reveal that this scheme yields a speed-up scaling as $(R/L)^{0.5}$.

7.4 Sphere-sphere geometry

Another example of a Casimir setup with cylindrical symmetry consists of two spheres with radii R_1 and R_2. As in the plane-sphere geometry, we denote the surface-to-surface distance as L. The setup is depicted in Fig. 6.1. When the two reference points are placed at the spheres' centers, the kernel of the round-trip operator is of the form (7.2) with the kernel functions of the reflection operators of the respective spheres given in (7.6). Note that the sign of the coefficients C and D differs for the two spheres.

We recall that, because the reflection operator at both objects is now non-diagonal, a discretization of two integrals over the transverse momenta is required. Firstly, the discretization of the integral over $\mathbf{k}'$ in Eq. (7.1) results in a finite matrix representation of the round-trip operator. Secondly, the discretization of the integral over $\mathbf{k}''$ in Eq. (7.2) allows to express the round-trip matrix in terms of a product of two block-matrices. As before, we express $\mathbf{k}'$ and $\mathbf{k}''$ in polar coordinates. For the radial components we employ the Fourier-Chebyshev quadrature scheme presented in Sec. 7.3. The quadrature orders, however, do not need to coincide and thus we use the quadratures of order N' and N'' for the integrations over k' and k'', respectively. Likewise we employ trapezoidal rules of order M' and M'' for the discretization of

the angular components. In order to exploit the cylindrical symmetry of the problem by means of the discrete Fourier transform, the quadrature orders M' and M'' will be required to be equal. However, for the sake of the following analysis we assume them to be different.

The convergence rate of the quadrature orders can be determined with the same line of reasoning as in section 7.3. When the sphere radii become large, the kernel functions of the reflection operators can be approximated by Gaussians for which the width is controlled by the respective radii. The kernel of the round-trip operator is then a convolution of these two Gaussians, resulting in a Gaussian where the width is controlled by the effective radius defined in (4.4) instead. We then find the scaling

$$N' \propto M' \propto \sqrt{R_{\text{eff}}/L}\,. \tag{7.14}$$

The quadrature orders N'' and M'' can be estimated from the convolution integral. The integrand is a Gaussian where the two radii appear as a sum, $R_1 + R_2$ and thus the quadrature orders scale as

$$N'' \propto M'' \propto \sqrt{(R_1 + R_2)/L}\,. \tag{7.15}$$

Note that in the plane-sphere limit, where one radius is much larger than the other, the quadrature orders N' and M' become the same as in the plane-sphere geometry (7.12) where $R = R_1$. The quadrature orders N'' and M'' then become very large, reflecting the fact that the kernel functions of the sphere with the larger radius R_2 become strongly peaked around $\mathbf{k} = \mathbf{k}'$ as expected from the reflection properties of a plane. A more detailed discussion of this limiting procedure in connection with the PFA can be found in Ref. [114].

Finally, we need to go back to equal orders M' and M''. Since $R_1 + R_2 > R_{\text{eff}}$, the quadrature order of the trapezoidal rule thus scales as $M' = M'' \propto \sqrt{(R_1 + R_2)/L}$ to ensure convergence.

In analogy to (7.12), we can express the quadrature orders for the angular and radial integrations as

$$\begin{aligned} N' &= \left\lceil \eta_{N'} \left(\frac{R_{\text{eff}}}{L} \right)^{1/2} \right\rceil , \\ N'' &= \left\lceil \eta_{N''} \left(\frac{R_1 + R_2}{L} \right)^{1/2} \right\rceil , \\ M' &= \left\lceil \eta_{M'} \left(\frac{R_1 + R_2}{L} \right)^{1/2} \right\rceil , \end{aligned} \tag{7.16}$$

where the functions $\eta_{N'}$, $\eta_{N''}$ and $\eta_{M'}$ control the numerical accuracy.

These expectations can again be numerically verified. Considering perfectly reflecting spheres at $T = 293\,\text{K}$ and sphere 1 with radius $1\,\mu\text{m}$, the relative error for the Casimir free energy is shown in Fig. 7.4.

The functions $\eta_{N'}$, $\eta_{N''}$ and $\eta_{M'}$ are represented by the blue, green and red symbols, respectively. Crosses and circles stand for aspect ratio $R_1/L = 100$, and crosses and circles for $R_1/L = 500$. For the crosses and pluses, the ratio of the sphere radii R_1/R_2 is one, while it is two for the circles and squares. The errors have been computed relative to free energies with much larger values of the coefficients, namely $\eta_{N'} = \eta_{N''} = \eta_{M'} = 14$ for all points in the figure. For the points where the relative errors are shown as a function of $\eta_{N'}$, the other functions were kept fixed at $\eta_{N''} = \eta_{M'} = 14$. The same procedure was applied to the relative error as a function

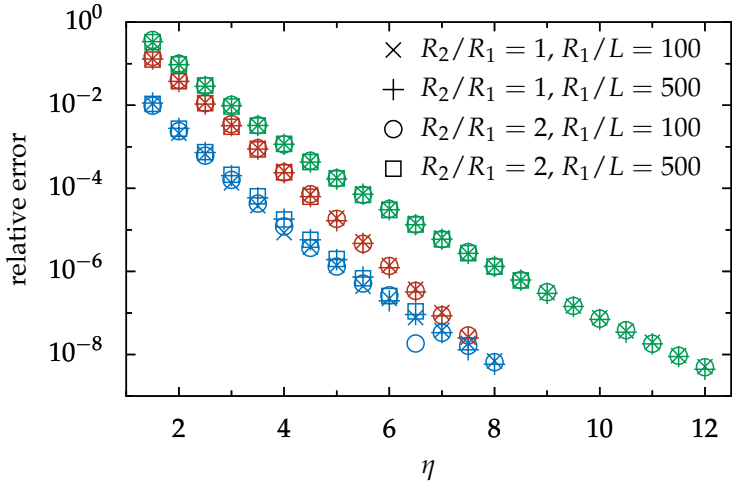

FIGURE 7.4: The relative error as a function of $\eta_{N'}$ (blue), $\eta_{N''}$ (green) and $\eta_{M'}$ (red) for aspect ratios $R_1/L = 100$ (crosses and circles) and $R_1/L = 500$ (pluses and squares). For the crosses and pluses, the ratio of the sphere radii R_1/R_2 is one, while it is two for the circles and squares.

ϵ	10^{-2}	10^{-3}	10^{-4}	10^{-5}	10^{-6}	10^{-7}	10^{-8}
$\eta_{N'}$	1.5	2.3	3.2	4.2	5.2	6.4	7.6
$\eta_{N''}$	2.9	4.0	5.3	6.6	8.0	9.6	11
$\eta_{M'}$	2.5	3.4	4.3	5.2	6.0	6.9	7.8

TABLE 7.2: Required values of $\eta_{N'}$, $\eta_{N''}$ and $\eta_{M'}$ to achieve a numerical relative error of ϵ.

of $\eta_{N''}$ and $\eta_{M'}$. Figure 7.4 shows that the coefficients depend only weakly on the system parameters, thus verifying the scaling law (7.16). For other system parameters and real materials we find similar results.

Based on Fig. 7.4, we establish a rule of thumb for which the coefficients in (7.16) can be determined given a desired relative error ϵ:

$$\begin{aligned} \eta_{N'} &= 0.0076 \log^2(\epsilon) - 0.27 \log(\epsilon) + 0.060 \,, \\ \eta_{N''} &= 0.011 \log^2(\epsilon) - 0.35 \log(\epsilon) + 1.1 \,, \\ \eta_{M'} &= -0.0009 \log^2(\epsilon) - 0.40 \log(\epsilon) + 0.69 \,. \end{aligned} \tag{7.17}$$

For convenience, the values of the coefficients $\eta_{N'}$, $\eta_{N''}$ and $\eta_{M'}$ according to (7.17) can be found in Tab. 7.2 for certain values of ϵ.

7.5 Numerical evaluation of the scattering amplitudes

In this section, we address a few numerical issues arising in the plane-sphere and sphere-sphere calculations discussed above. Apart from the numerical evaluation of the Mie scattering amplitudes (5.3), we use routines provided by standard python packages. For instance, we use the Fast Fourier Transform routine provided by the numpy package to perform the discrete Fouier transform as described in Sec. 7.2 and the linear algebra routines from scipy [136] for the evaluation of the Casimir interaction by means of the scattering formula once the round-trip matrix has been computed.

A fast and stable numerical evaluation of the Mie scattering amplitudes (5.3) requires more work. We discuss our implementation in more detail in the following. We start out by discussing the numerical evaluation of the Mie coefficients and the angular functions. Then, we explain how we perform the summation over ℓ. Finally, we compare the numerically evaluated Mie scattering amplitudes with their asymptotics obtained in Sec. 5.4 and analyze for which parameters the numerical difference is so small that the scattering amplitudes can be replaced by their asymptotics.

Numerical evaluation of the Mie coefficients/Bessel functions

Besides the material properties encoded through the refractive index, the Mie coefficients a_ℓ and b_ℓ as given in (5.18) depend only on the imaginary size parameter $x = \mathcal{K}R$, where $\mathcal{K}$ is the imaginary wave number in the medium and R is the sphere radius. For a given frequency, the Mie coefficients are the same for all matrix elements of the round-trip operator. Thus, they can be precomputed for each frequency contribution to the Casimir interaction.

For practical purposes, it is convenient to limit the summation over the partial-wave indices ℓ by a highest value $\ell_{\max}$ up to which the Mie coefficients are computed. In Sec. 5.4, we have disussed in more detail that, within the semiclassical approximation, the localization principle [100] connects waves with angular momentum $\ell \gg 1$ to localized rays defining an impact parameter $b = \ell/\mathcal{K}$. Since large impact parameters $b \gg R$ correspond to rays passing by the sphere, their contribution to the scattering amplitudes is negligible. Thus, the main contributions to the scattering amplitudes come from angular momenta $\ell \lesssim R\mathcal{K}$. Because the wave numbers contributing to the Casimir interaction scale as the inverse surface-to-surface distance, $\mathcal{K} \propto 1/L$, we can set the highest angular momentum considered in the summation to $\ell_{\max} = \lceil \eta R/L \rceil$, where the coefficient η controls the numerical error.

In view of the numerical approaches based on the multipolar representation of the electromagnetic fields [51, 54, 58], where the numerical error as a function of η was analyzed, we set $\eta = 12$, and $\ell_{\max}$ to at least 200 here. Then, the scattering amplitudes are evaluated to high enough accuracy, such that the numerical error due to the finite $\ell_{\max}$, does not interfere with the numerical error induced by the Nyström discretization discussed in sections 7.3 and 7.4. While the choice for the proportionality constant η is crucial for performance in the multipole based approaches as it determines the matrix sizes involved in the calculations, it does not affect performance that notably here allowing the conservative choice for η.

By their definition (5.18), the evaluation of the Mie coefficients themselves can be reduced to the numerical evaluation of Bessel functions. We implement the routines for the evaluation of the Bessel functions as given in [51, 54, 58]. We refer the reader interested in details to the expositions in those references.

Numerical evaluation of the angular functions

The angular functions π_ℓ and τ_ℓ, as defined in (5.4), are numerically evaluated in different ways depending if the index ℓ is small or large. For small $\ell < 1000$, we evaluate the angular functions by means of the recurrence relations [81]

$$\begin{aligned} \pi_\ell(z) &= \frac{2\ell-1}{\ell-1} z\pi_{\ell-1}(z) - \frac{\ell}{\ell-1}\pi_{\ell-2}(z)\,, \\ \tau_\ell(z) &= \ell z\pi_\ell(z) - (\ell+1)\pi_{\ell-1}(z) \end{aligned} \tag{7.18}$$

starting with $\pi_0(z) = \tau_0(z) = 0$, $\pi_1(z) = 1$ and $\tau_1(z) = z$. By our experience, the recurrence relations (7.18) are stable in the upward direction.

For large $\ell \geq 1000$, we evaluate the angular functions by means of asymptotic expansions. The reason for this is that we do not perform the summation over ℓ in the scattering amplitudes (5.3) starting from $\ell = 1$ up to $\ell_{\max}$, but rather sum only over the relevant terms contained in a smaller interval between the lower and upper summation bound. This summation technique will be discussed in more detail below.

An asymptotic expansion of the angular functions can be found by alternatively expressing them as

$$\begin{aligned} \pi_\ell(z) &= \frac{1}{\sqrt{z^2-1}} P_\ell^1(z)\,, \\ \tau_\ell(z) &= -z\pi_\ell(z) + \ell(\ell+1)P_\ell(z) \end{aligned} \tag{7.19}$$

and using asymptotic expansions of the (associated) Legendre functions found in the literature.

Asymptotic expansion of the associated Legendre function

With an asymptotic expansion of the associated Legendre function $P_\ell^1(z)$, we immediately find an asymptotic expansion for the angular function π_ℓ as defined in (7.19).

In [139, §29.3.3], a uniform asymptotic expansion of the associated Legendre function $P_\ell^{-1}(z)$ for large ℓ is given by

$$P_\ell^{-1}(\cosh x) = \frac{1}{\lambda}\left(\frac{x}{\sinh x}\right)^{1/2} \sum_{k=0}^{\infty} c_k(x) \left(\frac{3}{2}\right)^{(k)} I_{m+k}(\lambda x) \left(\frac{2x}{\lambda}\right)^k \tag{7.20}$$

with $\lambda = \ell + 1/2$ and the rising factorials defined by

$$\left(\frac{3}{2}\right)^{(k)} = \frac{\Gamma(k+3/2)}{\Gamma(3/2)}\,. \tag{7.21}$$

The coefficients $c_k(x)$ can be obtained from the series expansion [139, §29.3.2]

$$\left(2x\frac{\cosh x - \cosh\left(\sqrt{x^2-y}\right)}{y\sinh x}\right)^{1/2} = \sum_{k=0}^{\infty} c_k(x) y^k\,. \tag{7.22}$$

The first few coefficients read

$$\begin{aligned} c_0 &= 1\,, \\ c_1 &= \frac{1 - x\coth(x)}{8x^2}\,, \\ c_2 &= \frac{8x^2 - 3x^2\coth^2(x) - 18x\coth(x) + 21}{384x^4}\,, \\ c_3 &= \frac{-3x^3\coth^3(x) + 40x^2 - 15x^2\coth^2(x) - 81x\coth(x) + 99}{3072x^6}\,, \\ c_4 &= \frac{d_4}{1474560x^8}\,, \\ c_5 &= \frac{d_5}{3932160x^{10}} \end{aligned} \tag{7.23}$$

with

$$\begin{aligned} d_4 &= 64x^4 - 225x^4\coth^4(x) - 1260x^3\coth^3(x) + 13200x^2 \\ &\quad + 30\left(8x^2 - 165\right)x^2\coth^2(x) - 25740x\coth(x) + 32175\,, \\ d_5 &= -105x^5\coth^5(x) + 192x^4 - 675x^4\coth^4(x) - x\left(64x^4 + 49725\right)\coth(x) \\ &\quad + 26000x^2 + 30x^2\left(24x^2 - 325\right)\coth^2(x) + 10x^3\left(16x^2 - 273\right)\coth^3(x) + 62985\,. \end{aligned} \tag{7.24}$$

With the connection formula

$$P_\ell^m(z) = \frac{\Gamma(1+\ell+m)}{\Gamma(1+\ell-m)}P_\ell^{-m}(z)\,, \tag{7.25}$$

we then find the asymptotic expansion of the angular function π_ℓ as

$$\begin{aligned} \pi_\ell(\cosh x) &= \frac{1}{\sinh x}P_\ell^1(\cosh x) \sim \\ &\quad \frac{\ell(\ell+1)}{\lambda}\left(\frac{x}{\sinh^3 x}\right)^{1/2}\sum_{k=0}^{5}c_k(x)\left(\frac{3}{2}\right)^{(k)}I_{k+1}(\lambda x)\left(\frac{2x}{\lambda}\right)^k\,. \end{aligned} \tag{7.26}$$

Six terms in the asymptotic expansion are enough to determine π_ℓ to machine precision when $\ell \geq 1000$.

For the asymptotic expansion of the angular function τ_ℓ by means of the corresponding formula in (7.19), we need to find the asymptotic expansion of the Legendre functions. We follow the procedure of evaluating the Legendre functions $P_\ell(z)$ as outlined in [140]. There, two different asymptotic expansions are used depending on how the index ℓ compares with the argument z.

Legendre functions for small arguments

For small arguments,

$$(\ell+1)\sinh x < 25\,, \tag{7.27}$$

the Legendre polynomials can be evaluated using the asymptotic expansion [140]

$$P_\ell(\cosh x) \sim \sum_{n=0}^{6}\frac{f_n(x\lambda)}{\lambda^n} \tag{7.28}$$

where $\lambda = \ell + 1/2$. The functions $f_n(x)$ vanish for odd values of n and for even values of n they are given by

$$\begin{aligned} f_0(x) &= h_0(x)\,, \\ f_2(x) &= -\frac{1}{8}h_1(x) - \frac{1}{12}h_2(x)\,, \\ f_4(x) &= \frac{11}{384}h_2(x) + \frac{7}{160}h_3(x) + \frac{1}{160}h_4(x)\,, \\ f_6(x) &= -\frac{173}{15360}h_3(x) - \frac{101}{3584}h_4(x) - \frac{671}{80640}h_5(x) - \frac{61}{120960}h_6(x)\,, \end{aligned} \tag{7.29}$$

with $h_n(x) = x^n I_n(x)$ and the modified Bessel function of the first kind $I_n(x)$.

Legendre functions for large arguments

For large arguments,

$$(\ell+1)\sinh x \geq 25\,, \tag{7.30}$$

we make use of the asymptotic expansion [140]

$$P_\ell(\cosh x) \sim \left(\frac{2}{\pi \sinh x}\right)^{1/2} \sum_{m=0}^{M-1} C_{\ell,m} \frac{\cosh[(m+\ell+1/2)x]}{\sinh^m x}\,. \tag{7.31}$$

The coefficients $C_{\ell,m}$ are given in terms of the recurrence relation

$$C_{\ell,m+1} = \frac{(m+1/2)^2}{2(m+1)(\ell+m+3/2)} C_{\ell,m} \tag{7.32}$$

with initial value

$$C_{\ell,0} = \frac{\Gamma(\ell+1)}{\Gamma(\ell+3/2)}\,. \tag{7.33}$$

For $\ell \geq 1000$, it turns out that setting $M = 16$ in (7.31) yields numerical values for the Legendre functions which are accurate to machine precision.

In practice, it is faster and more precise to compute the initial value $C_{\ell,0}$ via the asymptotic series

$$C_{\ell,0} \sim \frac{1}{\sqrt{\ell}}\left(1 - \frac{3}{8\,\ell} + \frac{25}{128\,\ell^2} - \frac{105}{1024\,\ell^3} + \frac{1659}{32768\,\ell^4} - \frac{6237}{262144\,\ell^5} + \ldots\right) \tag{7.34}$$

than calculating it by means of implementations of the gamma function. The asymptotic series (7.34) has been obtained with Mathematica. For $\ell \geq 1000$, it yields numerical values at machine precision.

Performing the summation over ℓ

Now we discuss the summation over partial-wave indices ℓ appearing in the Mie scattering amplitudes (5.3). In the discussion about the numerical evaluation of the Mie coefficients above, we have argued that the summation over ℓ can be truncated by $\ell_{\max} = \lceil 12R/L \rceil$. If we were to compute the sum starting from $\ell = 1$ up to $\ell_{\max}$, the computation time would scale proportional to R/L. We can do better than that by using our knowledge from the analytical derivation of the asymptotics of the scattering amplitudes discussed in Sec. 5.4.

There, we have seen that the largest contribution comes from an index ℓ close to $\ell_{\mathrm{sp}} = \mathcal{K}R\sqrt{-(\cos(\Theta)+1)/2}$. Thus, it makes sense to start the evaluation of the scattering amplitudes close to ℓ_{sp} and perform an upward and downward summation over ℓ. The upward summation is terminated either if the value $\ell_{\max}$ or convergence is reached. Similarly, the downward summation is terminated either if $\ell = 1$ or convergence is reached. In the special case that $\ell_{\mathrm{sp}} > \ell_{\max}$, we only perform a downward summation starting from $\ell_{\max}$.

In this way, the number of terms which need to be considered in the evaluation of the scattering amplitudes scales as $\sqrt{\mathcal{K}R}\sqrt{(1-\cos(\Theta))/2}$, which corresponds to the Gaussian width around ℓ_{sp} (see App C.2 for details). Since $\mathcal{K} \propto 1/L$, the number of terms included in the calculation of the scattering amplitudes thus scales as $\sqrt{R/L}$ and so does the total computation time. Using this method for the summation over ℓ, we accomplish a speedup of $\sqrt{R/L}$ compared to the naive summation from $\ell = 1$ to $\ell_{\max}$.

Employing asymptotics for the evaluation of the scattering amplitudes

Here, we explore for which parameters the asymptotic expansion (5.32) is accurate enough to be used for the numerical evaluation of the scattering amplitudes instead of the exact evaluation discussed above. It is worth recalling that the Mie scattering amplitudes are functions of the imaginary size parameter $x = \mathcal{K}R$, the scattering angle Θ through $\cos(\Theta)$ and the relative refractive index n.

We start out by comparing the asymptotics of the Mie scattering amplitudes (5.32), which were derived in appendix C.2, with the numerical exact evaluation explained aboved. In order to show that the asymptotics (5.32) are correct, we subtract the numerical exact values of the scattering amplitudes and check whether the remainder is asymptotically subleading compared to the WKB correction in (5.32). As representative examples, we consider the scattering angles $\cos(\Theta) = -1$ and $\cos(\Theta) = -2$, and the values $n = 0.2,\, 2,\, \infty$ for the refractive index, while varying the size parameter x.

In Fig. 7.5 (a), the next-to-leading order (NTLO) correction of the Mie scattering amplitudes is shown relative to the WKB approximation (5.33) for $\cos(\Theta) = -1$ as a function of the imaginary size parameter x. The results for the refractive index with values $n = 0.2,\, 2$ and ∞ are represented by pluses, crosses and circles, respectively. The results for S_1 and S_2 in the figure are identical since, for $\cos(\Theta) = -1$, the two Mie scattering amplitudes only differ by their sign, $S_1 = -S_2$. In Fig. 7.5 (b) and (c), the NTLO correction to S_1 and S_2, respectively, is shown for $\cos(\Theta) = -2$. The solid lines represent functions proportional to $1/x^2$, while the dashed line in Fig. 7.5 (a) is proportional to $1/x^4$.

Fig. 7.5 shows that the NTLO correction is asymptotic to $1/x^4$ for perfect reflectors ($n = \infty$) when $\cos(\Theta) = -1$ and asymptotic to $1/x^2$ in the other cases. Such asymptotics are subleading compared to the WKB correction term in (5.33), which is proportional to $1/x$. Thus, we have numerically verified that the asymptotics of the Mie scattering amplitudes as of Eq. (5.32) are indeed correct.

Since we have numerically verified that the asymptotics of the scattering amplitudes (5.32) holds uniformly for any values of $\cos(\Theta)$, we can now analyze for which parameters the asymptotics are close enough to the numerical exact values, so that they can be used for the numerical evaluation of the scattering amplitudes in the calculation of the Casimir interaction.

In Fig. 7.6, the asymptotics of the Mie scattering amplitudes, denoted by $S_p^{(\text{asymptot.})}$, is compared to the numerical exact evaluation of the scattering amplitudes S_p. The relative error of the asymptotics compared to the exact evaluation is depicted for a fixed refractive index n and size parameter x as a function of the scattering angle Θ through the parameter $z = -\cos(\Theta) - 1$. Figures 7.6 (a) and (b) show the relative error for the asymptotics of S_1, while Figs. 7.6 (c) and (d) show the relative error for the asymptotics of S_2. For (a) and (c) the size parameter is kept fixed at $x = 500$ and for (b) and (d) at $x = 5000$. Pluses, crosses and circles represent the refractive index of $n = 0.2,\, 2$ and ∞, respectively.

The plots in Fig. 7.6 on the left show a similar qualitative behavior compared to those on the right. Quantitatively, the plots on the right show a smaller relative error, which is expected as they correspond to the larger value of the size parameter x. In all plots, we observe that, when $z > 1$, the relative error generally decreases as z increases and, when n is finite, the relative error goes to a constant value for small z. Similar to the observations made in Fig. 7.5, the perfect reflector limit is also special here, as the relative error decreases further with decreasing z.

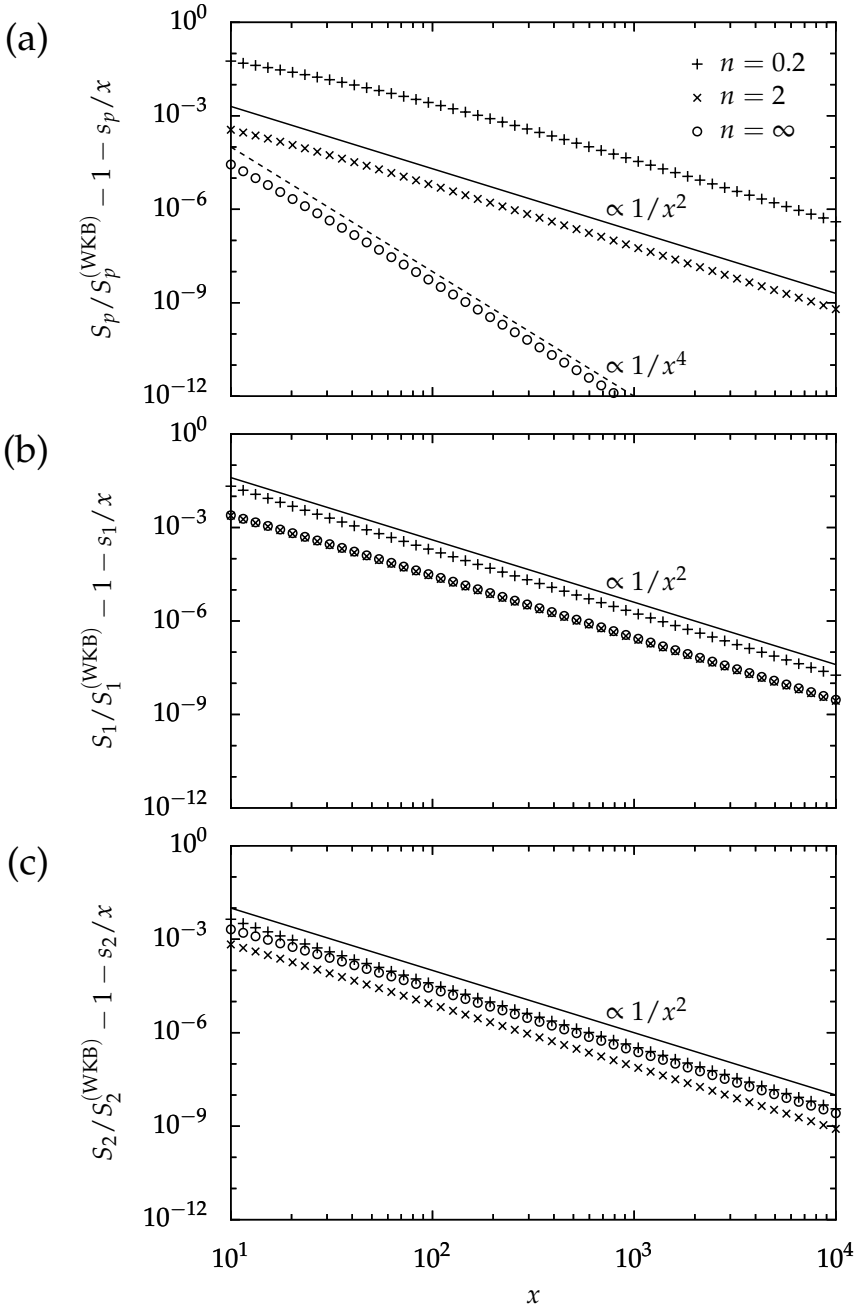

FIGURE 7.5: Next-to-leading order (NTLO) correction of the Mie scattering amplitudes S_p relative to the WKB approximation $S_p^{(\mathrm{WKB})}$ as a function of the imaginary size parameter x. The refractive index of $n = 0.2$, 2 and ∞ is represented by pluses, crosses and circles, respectively. (a) NTLO correction for $\cos(\Theta) = -1$. In this case, the result for S_1 and S_2 is identical. (b) and (c) NTLO correction of S_1 and S_2 for $\cos(\Theta) = -2$, respectively. The solid lines represent functions proportional to $1/x^2$, while the dashed line in (a) is proportional to $1/x^4$.

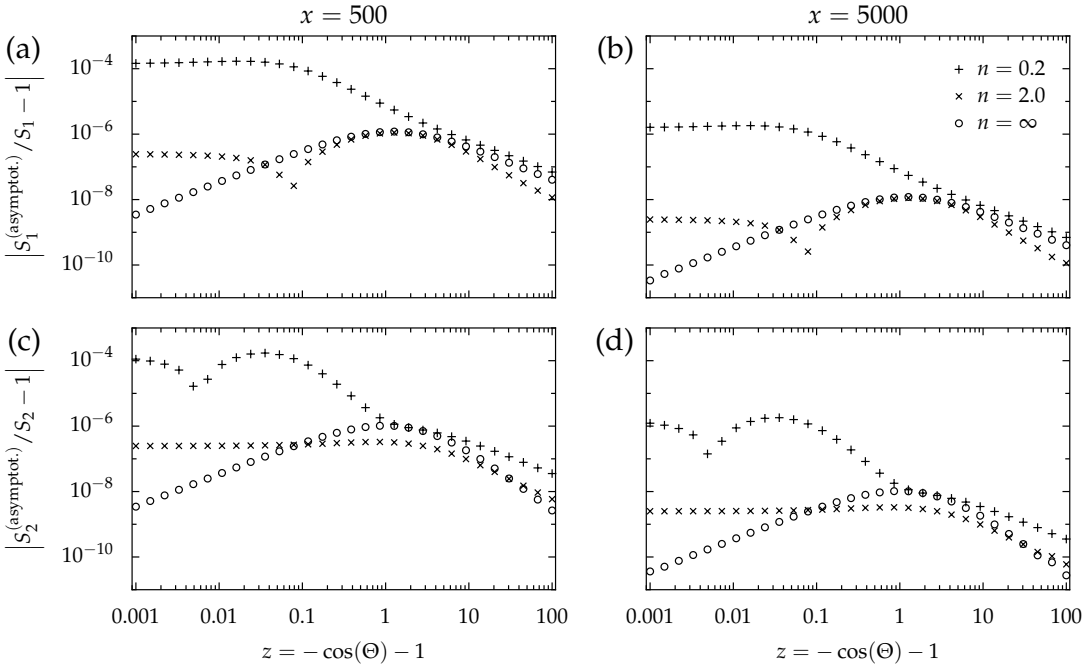

FIGURE 7.6: Relative error of the asymptotics of the Mie scattering amplitudes $S_p^{(\text{asymptot.})}$ compared to an numerical exact evaluation of the Mie scattering amplitudes S_p for a fixed refractive index n and size parameter x as a function of the scattering angle Θ through the parameter $z = -\cos(\Theta) - 1$. (a) and (b) show the relative error for the asymptotics of S_1, while in (c) and (d) the relative error is shown for the asymptotics of S_2. For (a) and (c) the size parameter is kept fixed at $x = 500$ and for (b) and (d) at $x = 5000$. Pluses, crosses and circles represent the refractive index of $n = 0.2$, 2 and ∞, respectively.

We now focus on the larger value of the size parameter $x = 5000$, i.e. Fig. 7.6 (b) and (d). For $n = 2$ and $n = \infty$, the relative error does not exceed 2×10^{-8} regardless of the value of $\cos(\Theta)$. For $n = 0.2$, the relative error becomes much larger for small values of z. In fact, by a further analysis, we find that the relative error may increase even more if $n = 0$ is approached. We generally find that if $n > 0.5$, the relative error is smaller than 2×10^{-8} when $x = 5000$ and smaller than 2×10^{-6} when $x = 500$, regardless of the value of $\cos(\Theta)$.

Based on this analysis, we decided to employ the asymptotics of the scattering amplitudes when $n > 0.5$ and $x > 5000$. Then, they are found within an accuracy of about eight digits. This accuracy is typically enough for analysis of the next-to-next-to-leading order asymptotics in the Casimir interaction which we will study in Secs. 8.2 and 8.3. For the computation of the Casimir interaction, the use of the asymptotic does not yield a significant speed-up for us. However, we observe that for large aspect ratios R/L, with the surface-to-surface distance L, the use of the asymptotics makes the evaluation of the Casimir interaction more stable, as it efficiently takes care of the cases where $\cos(\Theta)$ and x take rather extreme values.

Chapter 8

Applications

In this chapter, applications for the asymptotic expansion method derived in Ch. 6 and the plane-wave numerical method developed in Ch. 7 are given.

In section 8.1, we study the Casimir interaction in aqueous colloid systems involving polystyrene and mercury bodies in the plane-sphere and sphere-sphere geometry using our numerical method. Special attention is paid to the influence of variable salt concentrations. The accuracy of the PFA, which is typically used for predictions in experimental setup, is analyzed. Moreover, we study the geometry dependence and the influence of the salt concentration on the effective Hamaker parameter.

In section 8.2, the numerical accuracy of the asymptotic expansion for the Casimir interaction for large radii, which was derived in chapter 6, is studied by comparing its predictions with the ones obtained from our numerical exact method.

Finally, we analyze the PFA corrections for the Casimir energy at zero temperature in section 8.3. We investigate the asymptotic expansion of the Casimir energy beyond our analytical results. In the plane-sphere, we confirm the previously found rather surprising result that the next-to-leading order correction has a fractional power of $3/2$. For the sphere-sphere geometry, we come to similar conclusions. Finally, we provide a possible explanation for the emergence of that fractional power due to resummation of asymptotic higher order terms in the expansion.

8.1 Numerical results for the Casimir interaction in colloid systems

In this section, the plane-wave numerical method developed in chapter 7 will be applied to various colloidal systems suspended in an aqueous electrolyte solution. In particular, we will study the interaction between two spherical colloidal particles and the interaction of such a spherical particle with a plane wall. The analysis in this section is taken and adapted from Ref. [80], where the Casimir interaction is referred to as retarded van der Waals interaction.

For the analysis of colloid experiments the Lifshitz theory is most commonly employed, where the finite curvature of the spheres is accounted for by the proximity force approximation (PFA). In Sec. 4.1, we have seen that, within the PFA, the Casimir free energy is given by

$$\mathcal{F}_{\mathrm{PFA}} = 2\pi R_{\mathrm{eff}} \int_L^\infty \mathrm{d}l \, \mathcal{F}_{\mathrm{PP}}(l) \tag{8.1}$$

with the effective radius R_{eff} defined in (4.4) and the Casimir free energy per unit area between two parallel planes $\mathcal{F}_{\text{PP}}$ given in (3.29). By taking the negative derivative of (8.1) with respect to L, a corresponding expression for the force can be found

$$F_{\text{PFA}} = 2\pi R_{\text{eff}} \mathcal{F}_{\text{PP}}(L)\,. \tag{8.2}$$

As we have learned in chapter 6, the PFA is an asymptotic result valid only in the limit $L/R_{\text{eff}} \to 0$. At finite distances between the surfaces, there will always be some discrepancy between the exact result and the PFA.

The material dependence of the Casimir interaction is often expressed in terms of the Hamaker constant A [6]. Within Hamaker's microscopic theory, the non-retarded free energy per unit area for two parallel planes is given by

$$\mathcal{F}_{\text{PP}} = -\frac{A}{12\pi L^2}\,, \tag{8.3}$$

which is only valid for very small distances. For larger separations of the planes, retardation can no longer be neglected and the free energy needs to be computed using Eq. (3.29). This motivates the definition of an effective Hamaker parameter [60]

$$A_{\text{eff}}(L) = -12\pi L^2 \mathcal{F}_{\text{PP}}(L)\,, \tag{8.4}$$

which now has a non-trivial distance dependence through the exact plane-plane free energy per unit area. Usually A_{eff} is experimentally determined by measuring the force F between spherical surfaces [12]:

$$A_{\text{eff}}(L) = -\frac{6L^2}{R_{\text{eff}}} F\,. \tag{8.5}$$

Since the PFA expression (8.2) becomes exact in the small distance limit, the two definitions (8.4) and (8.5) are equivalent as far as the Hamaker constant $A = A_{\text{eff}}(0)$ is concerned. However, deviations from the PFA result make them differ at finite distances. In the following, we take the experimentally motivated Eq. (8.5) as our definition of the effective Hamaker parameter. In addition to the distance dependence associated to electrodynamical retardation, it also contains a geometry dependence which often translates into further reduction as the distance increases.

In the following, we will study colloidal systems involving polystyrene and mercury. The validity of the PFA will be analyzed for the plane-sphere and sphere-sphere geometry using the exactly calculated Casimir interaction through the numerical method developed above. Moreover, the geometry dependence of the effective Hamaker parameter (8.5) will be analyzed.

In our analysis, we will consider the two extreme cases of very low and very high salt concentrations in the aqueous suspensions. Only the zero-frequency Matsubara contribution is affected by the presence of ions in solution, since the corresponding plasma frequency is many orders of magnitude smaller than $k_{\text{B}}T/\hbar$ even when considering the highest possible concentrations. We follow the standard theoretical modeling of Casimir screening and consider the zero-frequency contribution to be completely suppressed by ionic screening in the case of high salt concentrations [23, 141, 142]. On the other hand, we model very low salt concentrations by summing over all Matsubara frequencies ξ_n including $n = 0$ and neglecting the effect of ions on the dielectric permittivities. Based on the scattering theory, an alternative result for the Casimir interaction in electrolytes has been derived [143]. This approach will not be discussed here further.

We model the dielectric function of polystyrene and water in terms of the oscillator model (3.16). For polystyrene, we take the parameters from data set 1 in Ref. [84] and, for water, we take the parameters from Ref. [85]. Where appropriate, we will compare our results to those obtained by using the Lorentz oscillator parameters for water suggested by Ref. [84] with the static relative permittivity $\epsilon(0) = 78.7$. Moreover, the temperature is assumed to be $T = 298\,\mathrm{K}$.

Polystyrene in water

The Casimir interaction between a polystyrene bead and a glass wall in an aqueous solution has been experimentally studied using the method of total internal reflection microscopy [15, 16]. With the colloidal probe technique, the interaction force between two latex spheres was measured [12]. Based on calculations presented in Refs. [59, 60], Elzbieciak-Wodka *et al.* assumed that the accuracy of the PFA for particles with diameters above $0.5\,\mu$m up to separations of 100 nm is within 1%. Deviations of the measured forces from the PFA result, which resulted in a smaller Hamaker constant, were attributed to the surface roughness of the spheres. Motivated by these experiments, we use the numerical method developed in this paper to study the Casimir interaction between two polystyrene bodies in an aqueous solution for the plane-sphere and sphere-sphere geometry.

The Casimir free energy and force between a plane and a sphere with radius $R = 1\,\mu$m as a function of the surface-to-surface distance L is depicted in Figs. 8.1 (a) and (b), respectively. The solid lines represent the numerically exact values, while the dashed lines correspond to the PFA. Here and in the following figures, the arrow indicates the direction of increasing screening. Thus, here, the upper curves represent strong screening while the lower curves refer to no screening. The Casimir interaction for intermediate screening then will follow a curve in the grey shaded area. Typical values of the free energies and forces are of the order of $k_\mathrm{B}T$ and 10^2 fN, respectively, and thus within reach of current experimental techniques [12, 15, 16]. For both observables, the PFA overestimates the interaction and the approximation agrees better with the exact values when the screening is strong.

The relative error of the PFA for the Casimir free energy and the Casimir force is quantified in Figs. 8.1 (c) and (d), respectively. We find that the PFA is more accurate for the force than for the free energy. The relative error of the PFA is larger than one percent above a separation of about 10 nm for the energy and above about 20 nm for the force regardless of the screening strength. The PFA performs worse when screening is negligible because the corrections to the PFA are particularly large for the zero-frequency contribution. This is consistent with our analytical results for the PFA correction for dielectrics which turned out to be particularly large at small separations (see Sec. 6.8).

The Casimir free energy and force, for two polystyrene spheres with equal radii $R_1 = R_2 = 1\,\mu$m, as a function of the surface-to-surface distance L is depicted in Figs. 8.1 (e) and (f), respectively. Again, the PFA overestimates the Casimir interaction and performs better when screening is strong. Overall, the free energy and the force are smaller for the two spheres than for the plane and the sphere. This can be explained by the fact that the effective interacting surface area analyzed in Sec. 6.10 is smaller in the former than in the latter.

The relative error of the PFA for the Casimir free energy and for the Casimir force are shown in Figs. 8.1 (g) and (h), respectively. Similar as in the plane-sphere geometry, the accuracy of the PFA is better when screening is strong and the PFA is more accurate for the force than for the energy. Above separations of 10 nm, the

relative error is larger than 1% for any screening strength. This is in particular true for distances below 100 nm, which is in contradiction to the assumption made in Ref. [12]. Compared to the plane-sphere geometry, the PFA is less accurate for two spheres. This is consistent with our findings in Sec. 6.9, where we have observed that the correction to the PFA is dominated by diffractive contributions. For two spheres, according to Eq. (6.38), these diffractive contributions are additive and thus lead to a larger correction to the PFA than in the plane-sphere geometry.

The effective Hamaker parameter for spherical surfaces is determined by Eq. (8.5) and depends not only on the chosen materials but also on the geometry used in its derivation. Figure 8.2 demonstrates this dependence for polystyrene and water. The dash-dotted and the solid curves represent the exact effective Hamaker parameter for the plane-sphere and sphere-sphere geometries, respectively, whereas the dashed curve corresponds to the PFA result, which is the same for both geometries. The upper curves do not take screening into account as they include the full contribution from the Matsubara frequency ξ_0. In contrast, in the lower curves the Matsubara frequency ξ_0 is omitted so that these curves correspond to the limit of a vanishingly small Debye screening length: $\lambda_D \to 0$. For any finite value of λ_D, the Hamaker parameter for each geometry first starts close to the upper curve at short distances ($L \ll \lambda_D$) and then is further suppressed by screening, approaching the lower curve for $L \gg \lambda_D$.

At small separations, the effective Hamaker parameters derived for the two different geometries asymptotically approach each other and the PFA curve as expected. As the distance increases, the reduction of the effective Hamaker parameter calculated within the PFA accounts for electrodynamical retardation only, whereas the exact curves display an additional reduction associated to curvature. Such geometrical reduction is more apparent in the absence of screening, since in this case the PFA curve at long distances defines a plateau associated to the contribution from the Matsubara frequency ξ_0, while the exact values decay to zero due to the curvature suppression.

We obtain the value $A = A_{\text{eff}}(L \to 0) = 1.40\, k_{\text{B}}T$ for the Hamaker constant. The limiting value is obtained from the short-distance plateau defined by the upper curves in Fig. 8.2 since they correspond to $L \ll \lambda_D$. On the other hand, the short-distance plateau associated to the lower curves yields the value $0.63\, k_{\text{B}}T$, representing the difference between the Hamaker constant and the contribution from the Matsubara frequency ξ_0, which in turn corresponds to the long-distance plateau defined by the upper PFA curve in Fig. 8.2. If we use the optical data from Ref. [84] for water instead, we obtain a somewhat larger Hamaker constant of $1.67\, k_{\text{B}}T$ and a corresponding short-distance plateau at $0.90\, k_{\text{B}}T$, for the lower curves in Fig. 8.2.

Our values for A are less than half of the theoretical value found in the literature [60]. This is because the optical data in Refs. [84] and [85] used here differ from Parsegian's optical data set [23]. It is interesting to observe that even though the difference between the permittivities of the data sets is small, namely less than 10%, the difference for the resulting Hamaker constants can be much bigger. This is because, at least within the PFA, the permittivities of the objects and the medium enter in terms of their differences. For polystyrene and water, the optical data almost match for UV frequencies. These frequencies become more and more important as the distance between the surfaces decreases, and then small differences in the optical data can result in relatively large differences in the Hamaker constant. The reduction of the Hamaker constant observed in the experiment of Ref. [12] could hence be partly due to uncertainties of the optical data.

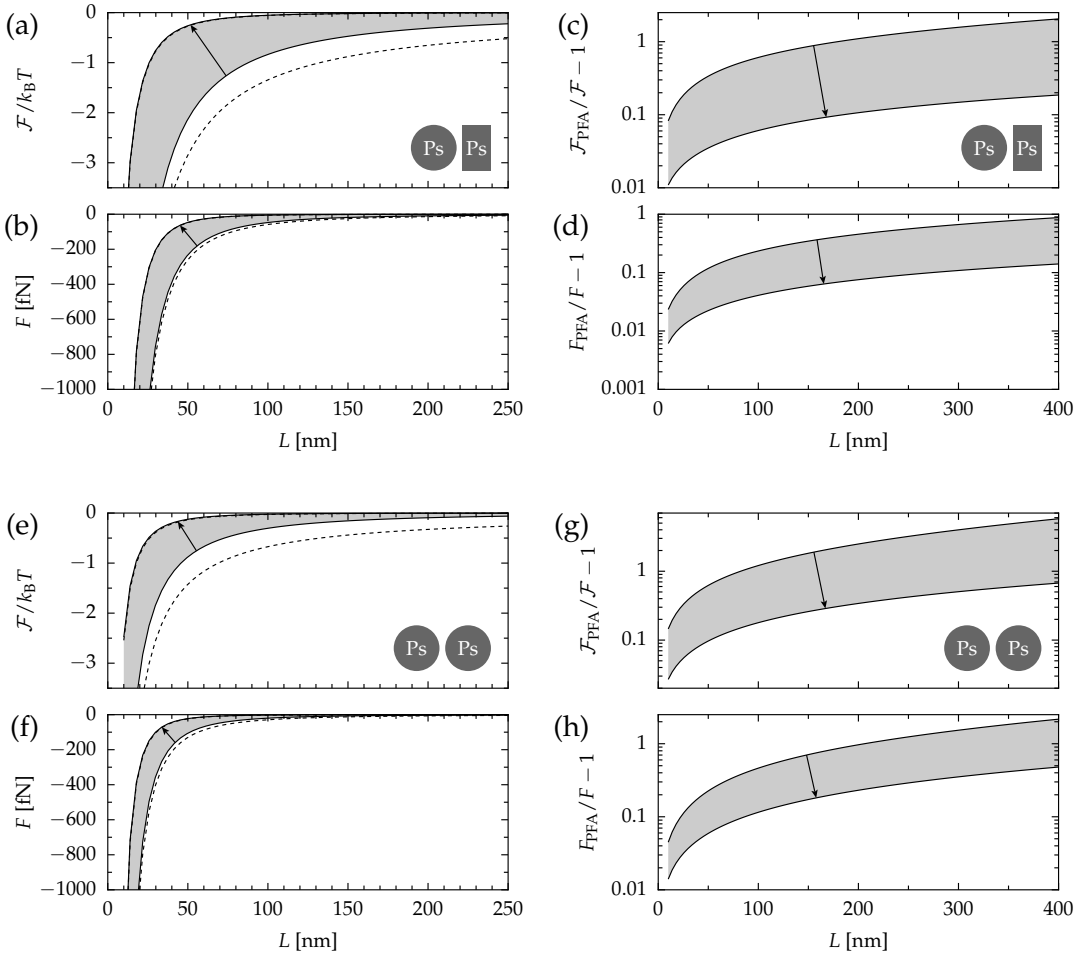

FIGURE 8.1: (a) Casimir free energy and (b) force for a polystyrene sphere with radius $R = 1\,\mu$m in front of a polystyrene plane in water as a function of the surface-to-surface distance L. Solid lines correspond to the numerically exact values and dashed lines to the PFA. The arrow indicates the direction of increasing screening so that the lower curve includes the Matsubara frequency ξ_0 while the upper curve does not. The grey shaded area indicates the interaction for any intermediate screening strength. The corresponding relative error of the PFA for (c) Casimir free energy and (d) force. Here, the upper curve corresponds to the absence of screening and screening increases through the grey area as indicated by the arrow. (e) Casimir free energy and (f) force for two polystyrene spheres with radii $R_1 = R_2 = 1\,\mu$m in water as a function of the surface-to-surface distance L. Corresponding relative error of the PFA for (g) the free energy and (h) the force. (from [80])

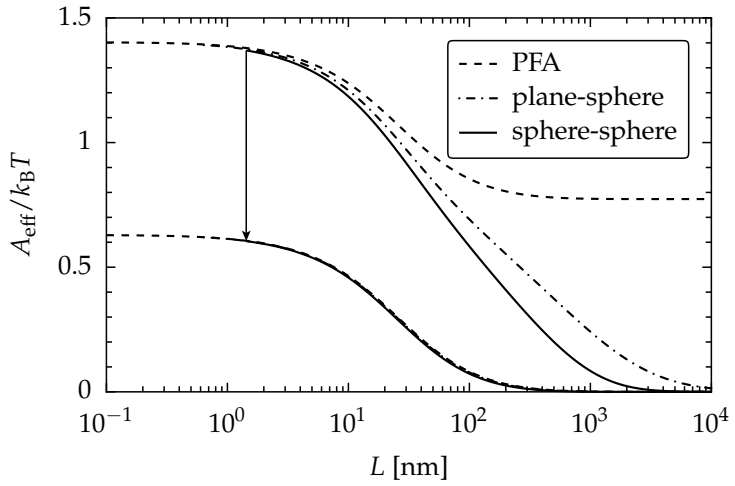

FIGURE 8.2: Effective Hamaker parameter for two polystyrene objects in water as a function of the surface-to-surface distance L. The dash-dotted and solid lines are derived from the exact plane-sphere and sphere-sphere interaction forces, respectively. The dashed line is computed within the PFA and is the same for both geometries. The radius of the sphere(s) is $1\,\mu$m. The arrow indicates the direction of increasing screening strength with the upper (lower) curve including (excluding) the Matsubara frequency ξ_0. (from [80])

Mercury and polystyrene in water

Mercury and polystyrene in an aqueous medium constitute an interesting colloid system, since the Casimir force can be tuned from repulsion to attraction depending on the screening of the zero frequency contribution [13]. Furthermore, due to the high surface tension mercury droplets have a small surface roughness and, thus, corrections due to roughness may play a minor role [90].

We study the interaction between a mercury droplet with radius $R = 1\,\mu$m and a polystyrene wall and the interaction between a mercury droplet with a polystyrene sphere with equal radii $R_1 = R_2 = 1\,\mu$m. The dielectric function of mercury is described by the Drude-Smith model (3.23) with parameters taken from Ref. [90]. Figures 8.3 (a) and (b) depict the Casimir free energy and force in the plane-sphere geometry, respectively. The corresponding quantities in the sphere-sphere geometry are shown in Figs. 8.3 (c) and (d).[1] Solid lines correspond to the numerically exact results, and the dashed lines to the PFA. We use the convention that a negative sign of the force corresponds to attraction and a positive sign corresponds to repulsion.

When screening is strong, the free energy and the force are negative and monotonic. For negligible screening, both quantities are non-monotonic and can change their sign. At intermediate distances, the force can be tuned from attractive to repulsive depending on the screening strength. Consistent with the discussion of polystyrene in water, the PFA is more accurate in the plane-sphere geometry than in the geometry of two spheres.

This becomes most evident when considering the points in which the observables vanish. For instance, according to the PFA the force vanishes at about $L = 138\,$nm for both geometries. The exact equilibrium distance is overestimated by about 3 nm for the plane-sphere geometry and underestimated by about 10 nm for

[1] Such calculations have been performed before in Ref. [13]. An implementation error affecting the Gaunt coefficient at large orders, however, lead to erroneous results for the Casimir force for small separations which were corrected in Ref. [54].

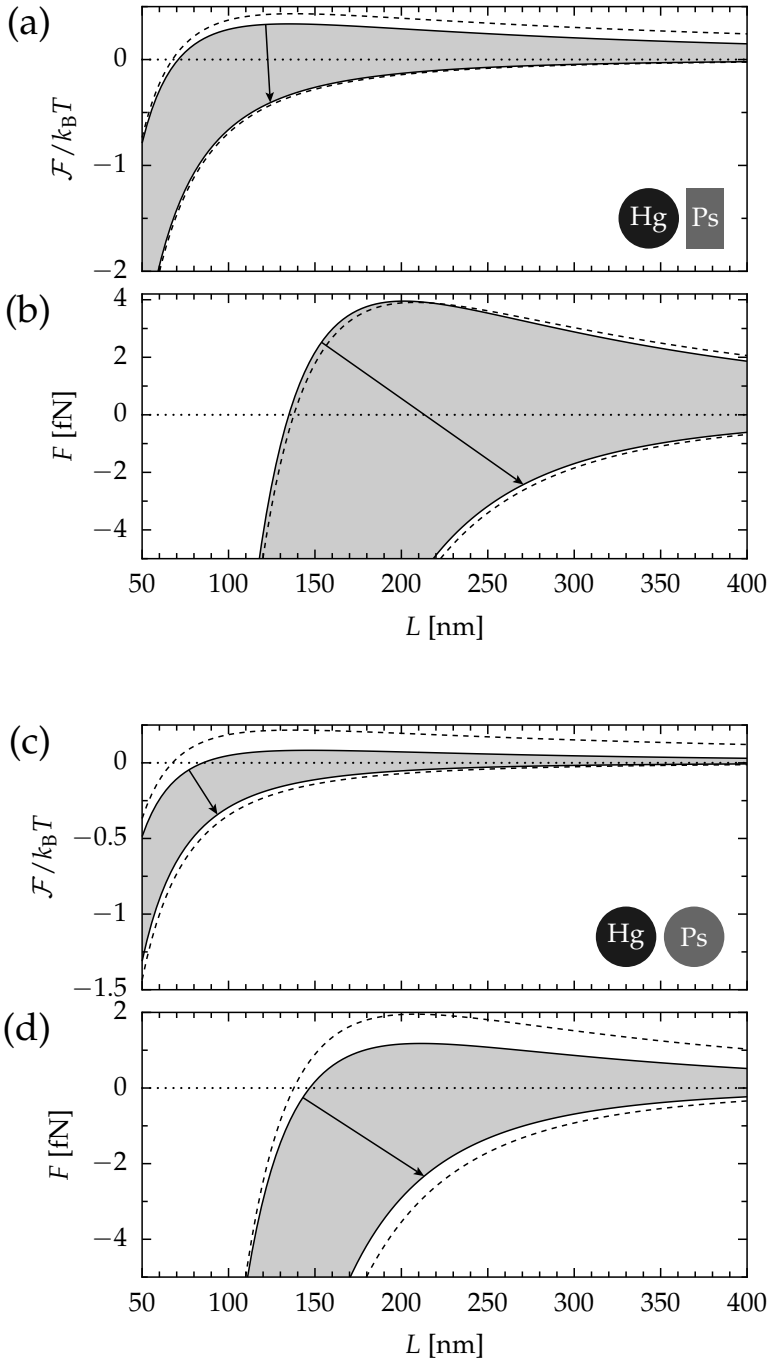

FIGURE 8.3: (a) Casimir free energy and (b) force between a mercury sphere of radius $R = 1\,\mu$m and a polystyrene plane in water. (c) Casimir free energy and (d) force between a mercury sphere and a polystyrene sphere with radii $R_1 = R_2 = 1\,\mu$m in water. For both scattering geometries, the quantities are presented as a function of the surface-to-surface distance L. The solid lines correspond to the numerically exact results and the dashed lines to the PFA. A positive (negative) sign of the force represents repulsion (attraction). The arrows indicate the direction of increasing screening strength with the upper (lower) curve including (excluding) the Matsubara frequency ξ_0. The grey shaded area indicates the interaction for any intermediate screening. (from [80])

the two spheres. When we use the optical data from Ref. [84] for water at a slightly different temperature ($T = 293\,\mathrm{K}$) instead, we find different values for the equilibrium distances. While the PFA would predict an equilibrium distance around $L = 178\,\mathrm{nm}$, its exact value would be shorter by about 4 nm for the plane-sphere geometry and larger by about 16 nm for the sphere-sphere geometry.

The determination of the equilibrium distance is particularly relevant for stable equilibria. This is the case for the materials considered in connection with ice particles [144] and gas bubbles [145] in liquid water near a planar interface. Our results suggest that beyond-PFA corrections in the nm range could appear when considering aspect ratios comparable to those taken in Fig. 8.3.

Figure 8.4 shows the effective Hamaker parameter for mercury and polystyrene in water. The effective Hamaker parameter has been computed through the exact force between a sphere and a plane (dash-dotted lines) and the exact force between two spheres (solid lines). We also show the results obtained within the PFA (dashed lines), which are the same for both geometries. The contribution from the Matsubara frequency ξ_0 is included in the lower lines but not in the upper ones. For any given Debye screening length, the Hamaker parameter exhibits a crossover from the lower curve to the upper one as the distance increases past λ_D. We find $A = A_{\mathrm{eff}}(L \to 0) = 4.11\,k_{\mathrm{B}}T$ for the Hamaker constant by following the lower short-distance plateau. In this configuration, the contribution $4.75\,k_{\mathrm{B}}T$ from non-zero Matsubara frequencies, associated to the short-distance upper plateau, is larger than the Hamaker constant. This is a consequence of the repulsive nature of the contribution from the Matsubara frequency ξ_0, which corresponds to the negative plateau defined by the lower PFA curve for the longer distances shown in Fig. 8.4. If we use the optical data for water from Ref. [84], we find a Hamaker constant of $5.17\,k_{\mathrm{B}}T$ and the upper short-distance plateau at $5.81\,k_{\mathrm{B}}T$ instead.

Again, the modification of the effective Hamaker parameter associated to the scattering geometry is most pronounced for larger distances provided that screening is negligible. The corresponding exact curves exhibit a non-monotonic behavior as they tend to zero at large distances.

8.2 Numerical accuracy of the asymptotic expansion

In chapter 6, we have derived the first two terms in the asymptotic expansion of the Casimir interaction between two spheres when the sphere radii become large compared to the surface-to-surface distance. It was shown that the leading term of the expansion corresponds to the PFA. The result for the asymptotic expansion holds for any dielectric materials of the spheres or the medium and at any temperature. It is given by the zero-frequency contribution (6.36) and the contributions for finite frequencies composed of (6.32) and (6.60). The asymptotic expansion for the plane-sphere geometry is contained as a limiting case, which was discussed in Sec. 6.6 in more detail. In the following, we will refer to the results for the asymptotic expansion with the acronym AE.

With the recent trend of experiments probing the Casimir interaction at larger distances [13, 30], it is important to utilize methods which predict the Casimir interaction beyond the PFA. This is because, by its asymptotic nature, the accuracy of the PFA becomes worse for larger distances. We have seen that this is true in the examples of the colloid setups in Sec. 8.1. Beyond-PFA predictions can be made by using numerical exact methods, such as our plane-wave numerical method, or by employing asymptotics beyond the PFA, like for instance our AE result.

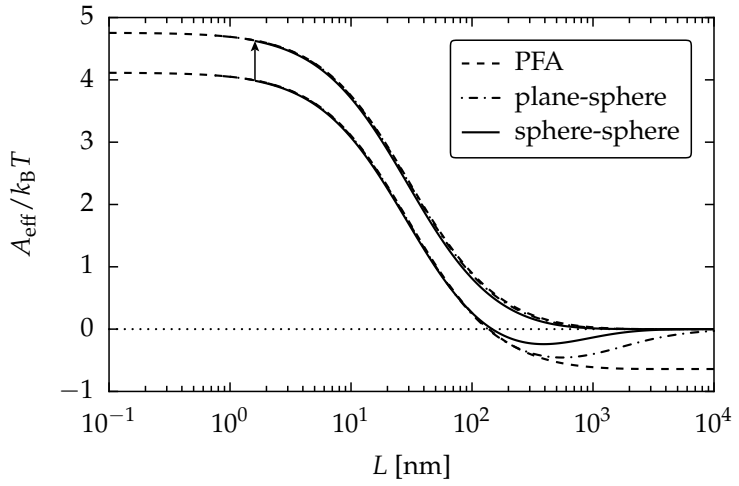

FIGURE 8.4: Effective Hamaker parameter for mercury and polystyrene in water as a function of the surface-to-surface distance L. The dash-dotted and solid lines are derived from the exact plane-sphere and sphere-sphere interaction forces, respectively. The dashed line is computed within the PFA and is the same for both geometries. The radius of the sphere(s) is 1 μm. The arrow indicates the direction of increasing screening strength with the lower (upper) curve including (excluding) the Matsubara frequency ξ_0. (from [80])

Before such asymptotic results can be employed, it is necessary to assess their numerical accuracy. In this section, we thus study the numerical accuracy of the AE in the plane-sphere and sphere-sphere geometry by comparing its predictions with the numerical exact results obtained from our plane-wave method, which was developed in Secs. 7.3 and 7.4. As example setups, we consider polystyrene in water, which was also discussed in Sec. 8.1 and is typical for colloid experiments [12, 15, 16], and gold in vacuum, which is commonly used in Casimir experiments [20, 22].

We first analyze the setups of polystyrene in water. Since in colloid experiments typically the Casimir free energy and the force are measured [12, 15, 16], we will analyze the accuracy of the AE for those observables. Like in the previous section, we model the dielectric function of polystyrene and water in terms of the oscillator model (3.16) with parameters from [84] and [85], respectively. The temperature is assumed to be $T = 298\,\mathrm{K}$ and the radius of the sphere(s) is $R = 1\,\mu\mathrm{m}$. We consider the same range of values for the surface-to-surface distance as in Fig. 8.1, i.e. $L = 10\,\mathrm{nm}$ up to $400\,\mathrm{nm}$. This distance range corresponds to rather small aspect ratios of $R/L = 100$ to 2.5

In Fig. 8.5, the relative error of the AE is depicted by the solid lines. For comparison, the dashed lines indicate the relative error of the PFA, which was also depicted in Fig. 8.1 for the same setup. Figures 8.5 (a) and (b) depict the relative error of the Casimir free energy $\mathcal{F}$ in the plane-sphere and the sphere-sphere geometry, respectively. Figures 8.5 (c) and (d) show the corresponding results for the Casimir force F. The arrows indicate the direction of increasing screening strength, so that the upper curves include the Matsubara frequency ξ_0, while the lower curves do not. For an intermediate screening strength, the relative error would follow a curve between the upper and lower lines.

Note that in Fig. 8.5 (a), the relative error of the AE for strong screening does not monotonically increase with the distance as one would expect. This reason why it falls off for distances larger than 200 nm, is that around 500 nm it passes through

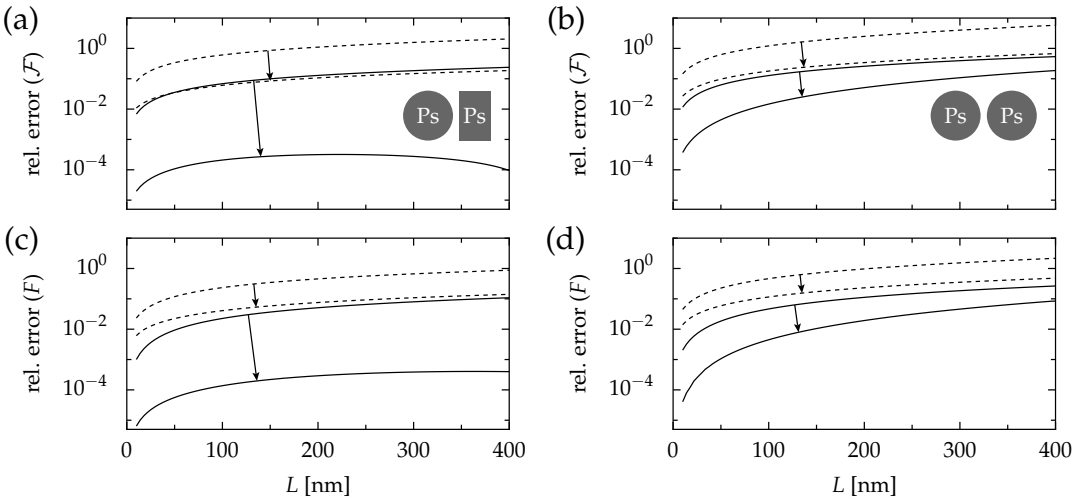

FIGURE 8.5: Relative error of the PFA (dashed lines) and the AE (solid lines) for polystyrene objects in water at $T = 298\,\mathrm{K}$ for (a) and (b) the Casimir free energy $\mathcal{F}$ in the plane-sphere and sphere-sphere geometry, respectively. (c) and (d) corresponding relative errors for the Casimir force F. The arrows indicate the direction of increasing screening strength so that the upper curves include the Matsubara frequency ξ_0, while the lower curves do not.

zero owing to the fact that the prediction by the AE and the numerical exact Casimir free energy coincidentally match at that value (see also Fig. 8.6).

We observe that the AE improves significantly on the PFA for the Casimir free energy and the force, regardless of geometry and screening strength. When comparing the accuracy of the AE between the observables, the geometries and screening strengths, we come to similar conclusions as for the PFA. Namely, that the accuracy of the AE is higher when screening is strong. In the plane-sphere geometry the AE performs slightly better than for two spheres and the AE is more accurate for the Casimir force than for the Casimir energy.

We now study the setup of gold in vacuum and take similar parameters as in the plane-sphere experiment of Ref. [30], i.e. room temperature $T = 293\,\mathrm{K}$, the radius of the sphere(s) of $R = 43\,\mu\mathrm{m}$ and the surface-to-surface distance range from 200 nm to one micron. This distance range corresponds to aspect ratios $R/L = 215$ to 43, which is rather small compared to the aspect ratios considered in earlier experiments [20, 22]. For the finite frequency contribution to the Casimir interaction, we use a dielectric function due to tabulated optical data for gold [121]. For the zero-frequency contribution, we consider the Drude and the plasma model separately.

In Fig. 8.6, the relative error of the PFA (dashed lines) and the AE (solid lines) is depicted for (a) and (b) the Casimir force in the plane-sphere and sphere-sphere geometry, respectively. Similarly, (c) and (d) show the corresponding relative errors for the Casimir force gradient. The blue lines correspond to the plasma and the black lines to the Drude prescription.

As for the colloid system, we find that the AE improves significantly upon the PFA for both observables in the two geometries. For Casimir force, the relative error is more than one magnitude smaller for the AE than for the PFA at shorter distances for both geometries. For the force gradient, the relative errors are smaller when compared to the force and it may even be two orders of magnitudes smaller for the AE compared to the PFA at the depicted distances.

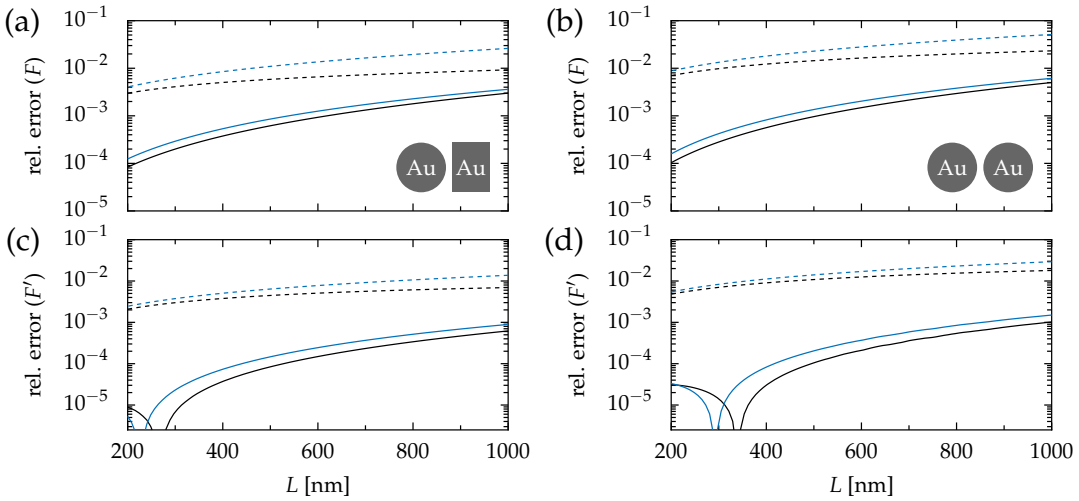

FIGURE 8.6: Relative error of the PFA (dashed lines) and the AE (solid lines) for gold in vacuum at $T = 293\,\mathrm{K}$ for (a) and (b) the Casimir force F in the plane-sphere and sphere-sphere geometry, respectively. (c) and (d) corresponding relative errors for the Casimir force gradient F'. The blue lines correspond to a plasma prescription and the black lines to a Drude prescription. The radius of the sphere(s) is $R = 43\,\mu\mathrm{m}$.

The results for the two geometries are rather similar. The relative errors for the plane-sphere geometry are slightly smaller when compared to the sphere-sphere geometry. When comparing the relative errors between the two observables, we see that they are generally smaller for the force gradient than for the force.

Note that the zero-frequency contribution in the AE, as given by (6.36), is identical to the PFA for Drude metals. Yet the AE provides a very accurate prediction of the Casimir interaction at the considered distances. At larger distances, the zero-frequency contribution becomes increasingly important. In this case, it might be beneficial to use the exact results known for the plane-sphere and sphere-sphere geometry [33–35]. We have not investigated this possibility here further and leave it for future work.

In conclusion, we have seen that the AE improves significantly on the PFA for the two exemplary setups corresponding to typical experimental situations. The AE may thus be useful for accurate predictions of the Casimir interaction for larger distances. Besides, the AE is an interesting alternative to numerical exact methods as it provides a way of computing the beyond-PFA Casimir interaction at a computational constant time, regardless of the separation.

8.3 Corrections beyond the PFA at zero temperature

In this section, we study the corrections beyond the PFA at zero temperature and generalize the results found for the plane-sphere geometry in [58] to the geometry of two spheres. In Ref. [58], it was found that at $T = 0$, the asymptotic expansion of the Casimir energy in the plane-sphere geometry for short distances is of the form

$$\frac{E}{E_{\mathrm{PFA}}} = 1 + \theta_1 \left(\frac{L}{R}\right) + \theta_2 \left(\frac{L}{R}\right)^{3/2} + \dots , \tag{8.6}$$

with the surface-to-surface distance L, the sphere radius R and the PFA energy E_{PFA}. For perfect reflectors, the PFA energy reads [37, 42, 104]

$$E_{\mathrm{PFA}} = -\frac{\hbar c \pi^3 R}{720 L^2} \,. \tag{8.7}$$

The next-to-leading order (NTLO) coefficient θ_1 is generally known in the literature [37, 38, 42, 104]. For perfect reflectors, it reads $\theta_1 = 1/3 - 20/\pi^2 \approx -1.69$, which can be obtained from (6.1) by taking the plane-sphere limit, $R_{\mathrm{eff}} \to R$ and $u \to 0$. The next-to-next-to-leading order (NNTLO) coefficient θ_2 was obtained in [58] by a fit to numerical exact data for the Casimir energy. For perfect reflectors in vacuum, it was then found that $\theta_2 \approx 2.65$. This result ruled out a previous suggestion made in [42], where, using a Padé approximation, the NNTLO term in the expansion was predicted to be of the form $\theta_2 (L/R)^2 \log(L/R)$ with $\theta_2 \approx -4.52$.

In Ref. [58], it was further shown that the NNTLO proportional to $(L/R)^{3/2}$ also appears when real materials at $T = 0$ are considered. For a simple Drude and plasma model, it was found that the NNTLO coefficient θ_2 in (8.6) depends on the values of the plasma frequency and the damping coefficient.

The derivative expansion (DE) approach, introduced in Sec. 4.2, generally predicts a NNTLO term proportional to $(L/R)^2$ at $T = 0$ [120, 146]. In the electromagnetic case, the perturbative kernel $\tilde{G}(k, L)$ given in (4.16) is non-analytic with respect to the in-plane wave number k and hence cannot be expanded beyond second order in k [44, 120]. While the DE provides the correct NTLO in the Casimir energy proportional to L/R [42, 43], it fails in the asymptotic expansion beyond that term due to this non-analyticity of the perturbative kernel function [120]. As the DE approach requires the Casimir interaction to be local, the NNTLO in (8.6) may stem from non-local contributions to the Casimir energy.

We now analyze the asymptotic series of the Casimir energy for two spheres with radii R_1 and R_2 at zero temperature for short distances. For simplicity, we assume perfect reflectors in vacuum. Before numerically analyzing the NNTLO term in the asymptotic expansion of the Casimir energy for two spheres, we demonstrate that our plane-wave numerical method produces the correct NTLO term in the asymptotic expansion given in (6.1).

In Fig. 8.7, the PFA correction is depicted as a function of L/R_2 with the surface-to-surface distance L. The circles represent our results for the plane-sphere limit, where $R_1/R_2 = \infty$, while the pluses, crosses and squares represent results for the ratios $R_1/R_2 = 1$, 2 and 4, respectively. The solid lines correspond to the NTLO term in (6.1) relative to the PFA with the just mentioned ratios R_1/R_2 increasing from to top to bottom. We see that, indeed, our numerical data is consistent with the asymptotics (6.1) for short distances.

We now analyze the correction to the NTLO term using our numerical data. In Fig. 8.8, the NTLO correction to the Casimir energy is shown as a function of L/R_{eff}. Pluses, crosses and squares correspond to numerical data with $R_1/R_2 = 1$, 2 and 4, respectively, while the circles represent numerical data in the plane-sphere geometry. The black solid line represents the function $2.65\,(L/R_{\mathrm{eff}})^{3/2}$, which corresponds to the NNTLO term determined in Ref. [58] when the plane-sphere limit, $R_{\mathrm{eff}} \to R$, is taken.

As the NTLO correction seems to be asymptotic to the solid black line, our numerical analysis suggests that the asymptotic expansion of the Casimir interaction is

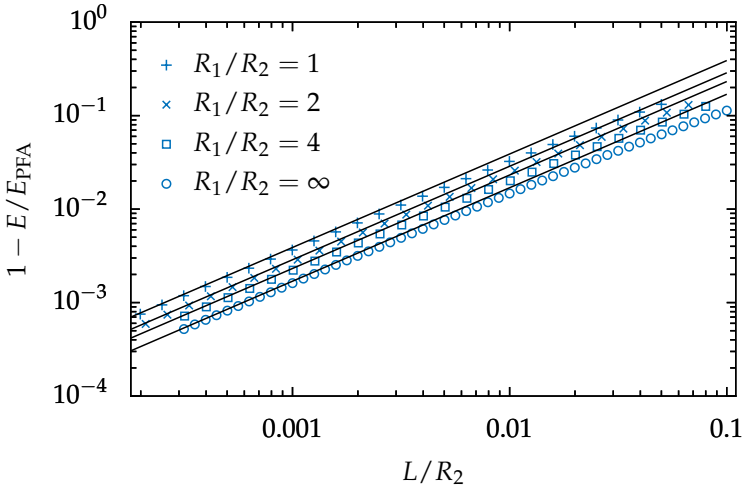

FIGURE 8.7: PFA correction for perfectly reflecting spheres with radii R_1 and R_2 in vacuum at zero temperature. The PFA correction is shown as a function of L/R_2 with the surface-to-surface distance L. The circles represent the plane-sphere limit, where $R_1/R_2 = \infty$, while the pluses, crosses and squares represent radii ratios of $R_1/R_2 = 1$, 2 and 4, respectively. The solid lines correspond to the asymptotics given by Eq. (6.1) where from top to bottom the radii ratio R_1/R_2 increases according to the numerical data.

of the form

$$\frac{E}{E_{\mathrm{PFA}}} = 1 + \theta_1 \left(\frac{L}{R_{\mathrm{eff}}}\right) + \theta_2 \left(\frac{L}{R_{\mathrm{eff}}}\right)^{3/2} + \dots \tag{8.8}$$

with the PFA energy (6.2) and the NTLO coefficient given in (6.1)

$$\theta_1 = \frac{1}{3} - \frac{20}{\pi^2} - \frac{R_1 R_2}{(R_1 + R_2)^2}\,. \tag{8.9}$$

As the numerical data points for different ratios of R_1/R_2 collapse, it seems that the NNTLO coefficient is consistent with $\theta_2 \approx 2.65$ for all values of R_1/R_2. It is interesting to observe that, while the NTLO coefficient θ_1 depends on the sphere radii, the NNTLO coefficient θ_2 seems to be independent of the radii.

Now we try to provide an explanation for the appearance of the $3/2$ power in the NNTLO asymptotic term of the Casimir energy. For simplicity, we will focus on the plane-sphere geometry in the following analysis and comment on the sphere-sphere case later. At first sight, in view of the asymptotic expansion of the Casimir interaction provided in Ch. 6, it seems that the NNTLO term should be proportional to $(L/R)^2$. This is because the NNTLO term of the Casimir energy should stem from the NNTLO term in the saddle-point approximation, the NNTLO term for the asymptotics of the scattering amplitudes and the combination of the NTLO terms in the saddle-point approximation with the NTLO term for the scattering amplitudes. The NNTLO of the saddle-point approximation going beyond (6.5) goes inversely quadratic in the large parameter which is the sphere radius here. In Sec. 7.5, we have seen that the NNTLO term in the scattering amplitudes is inversely proportional to the size parameter squared and thus also $\propto 1/R^2$. As the two NTLO terms contribute to the linear correction L/R, it is plausible that their combination contributes as $(L/R)^2$ to the asymptotic expansion of the Casimir energy. What is the mechanism giving rise to the numerical observed NNTLO term then?

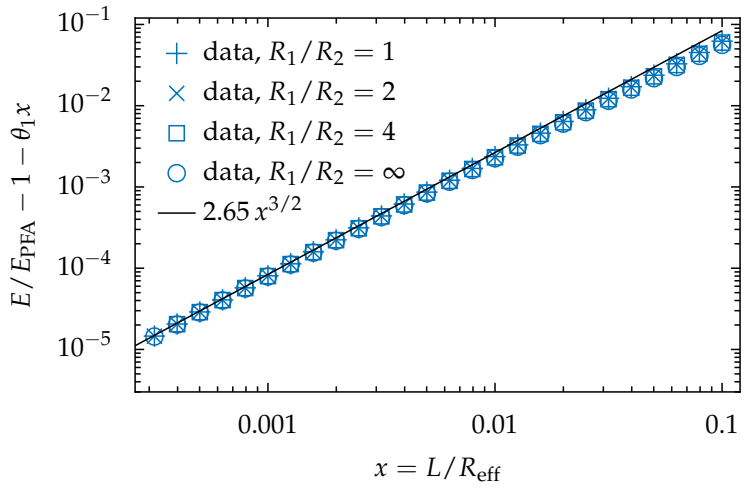

FIGURE 8.8: NTLO correction of the Casimir free energy for perfectly reflecting spheres with radii R_1 and R_2 in vacuum at zero temperature. The coefficient of the NTLO term is $\theta_1 = 1/3 - 20/\pi^2 - u$ with the dimensionless parameter $u = R_1 R_2/(R_1 + R_2)^2$. The NTLO correction is shown as a function of L/R_{eff} with the surface-to-surface distance L and the effective radius R_{eff}. The circles represent the plane-sphere limit, where $R_1/R_2 = \infty$, while the pluses, crosses and squares represent radii ratios of $R_1/R_2 = 1, 2$ and 4, respectively. The solid line corresponds to $2.65\,(L/R_{\mathrm{eff}})^{3/2}$.

An expansion of the Casimir energy in round trips seems to provide an answer to this question. In order to get insight, we numerically analyze the decomposition of the Casimir energy in round-trips. Specifically, we define the contribution to the Casimir energy for each round trip E_r by

$$E = \sum_{r=1}^{\infty} E_r\,, \tag{8.10}$$

where

$$E_r = -\hbar \int_0^\infty \frac{\mathrm{d}\xi}{2\pi} \frac{1}{r} \operatorname{tr} \mathcal{M}^r\,. \tag{8.11}$$

Numerically we can determine the trace over round trips, $\operatorname{tr} \mathcal{M}^r$, by first computing the round-trip matrix within the Nyström discretization as explained in Sec. 7.3 and 7.4 for the plane-sphere and sphere-sphere, respectively. The trace of the r-th round-trip is given by the sum over eigenvalues of the round trip matrix exponentiated by the power r.

By the arguments given above, it seems plausible to assume that E_r has an asymptotic expansion for small L/R of the form

$$\frac{E_r}{E_{r,\mathrm{PFA}}} \sim 1 + \theta_{r,1} \left(\frac{L}{R}\right) + \theta_{r,2} \left(\frac{L}{R}\right)^2 + \dots\,, \tag{8.12}$$

where we can determine $E_{r,\mathrm{PFA}}$ and $\theta_{r,1}$ from our analytical calculation in Sec. 6.5 by taking the plane-sphere limit, $R_{\mathrm{eff}} \to R$ and $u \to 0$. From (6.76) we can then read off that

$$E_{r,\mathrm{PFA}} = -\frac{\hbar c R}{8\pi L^2 r^4} \tag{8.13}$$

and from (6.78) we find

$$\theta_{r,1} = \frac{\frac{\hbar c}{24\pi L}\left(\frac{4}{r^2} - \frac{1}{r^4}\right)}{E_{r,\mathrm{PFA}}}\frac{R}{L} = -\frac{1}{3}\left(4r^2 - 1\right) . \tag{8.14}$$

We now investigate the NNTLO term in (8.12) numerically. To this end, we compute the round-trip contributions to the energy E_r for various number of round trips in the aspect ratio range $R/L = 0.002$ to 0.1. In Fig. 8.9 (a) these energy contributions are shown relative to the PFA expression (8.13). Purple, orange, blue, red and green lines correspond to 5, 10, 20, 30 and 40 round trips, respectively. Since the numerical data is shown as a function of the parameter $v = r^2 L/R$ and the distance range with respect to L/R is the same for each r, the lines corresponding to higher number of round trips depict function values further to right in the figure.

As v decreases, all lines approach the value one, indicating that the PFA expression becomes asymptotically correct. When v becomes large, the round-trip contribution becomes much smaller than the PFA expression even though L/R is small for the depicted data. This is because for large r, the asymptotic expansion breaks down, which can be seen by the fact that the NTLO term in (8.12) exceeds the leading order contribution when r is large enough. This is typical for asymptotic expansions for high dimensional integrals, which can be often improved by a resummation of higher order terms in the expansion [115, 116]. Indeed, the number of round trips r is proportional to the number of integrals appearing in the expression for the trace of the r-th round-trip, which can be seen in (6.9). The number of integrals is thus unbounded in the round-trip sum. Nevertheless, when the first two terms in (8.12) are summed over all round trips from $r = 1$ to infinity, the result yields the correct asymptotics of the Casimir interaction for small L/R, as we have seen in Fig. 8.7.

Fig. 8.9 (b) and (c) depict the correction to the PFA and NTLO term in the asymptotic series (8.12). Since for large values of v, the exact round-trip contribution to the energy becomes much smaller than the PFA, it is clear that in Fig. 8.9 (b) the PFA correction goes to 1 for large v. In this figure, when v becomes small the PFA correction approaches $4/3v$ as expected since this line corresponds to NTLO term in (8.12) for large r. Likewise, in Fig. 8.9 (c) since $4/3v$ becomes large compared to 1 for large v, the NTLO correction asymptotically approaches that line as v increases. For small values of v, the asymptotics of the numerical data does not seem to be consistent neither with $v^{3/2}$ nor with v^2. We will give an explanation for this below. Note that the lines all collapse on top of each other for depicted number of round trips. When the number of round trips is small the deviation between the lines becomes more prominent indicating that the NNTLO term in the asymptotic series of the Casimir energy depends only of the parameter v when r becomes large.

If we still hold on the form of the asymptotic series (8.12), this would suggest that $\theta_{r,2} \sim r^4$ for large r. The contribution to the Casimir energy due to that NNTLO term would then be

$$\left(\frac{L}{R}\right)^2 \sum_{r=1}^{\infty} E_{r,\mathrm{PFA}}\theta_{r,2} \tag{8.15}$$

which diverges since $E_{r,\mathrm{PFA}} \propto 1/r^4$. As there does not seem to be a good reason to assume an NNTLO term of a different form than the one given in (8.12), convergence of the round-trip sum can yet be ensured by a resummation of higher order terms in the expansion. The suggested resummation methods in Refs. [115, 116] did not give a conclusive result for us, which may be due to the rather complicated structure of our saddle-point integrals.

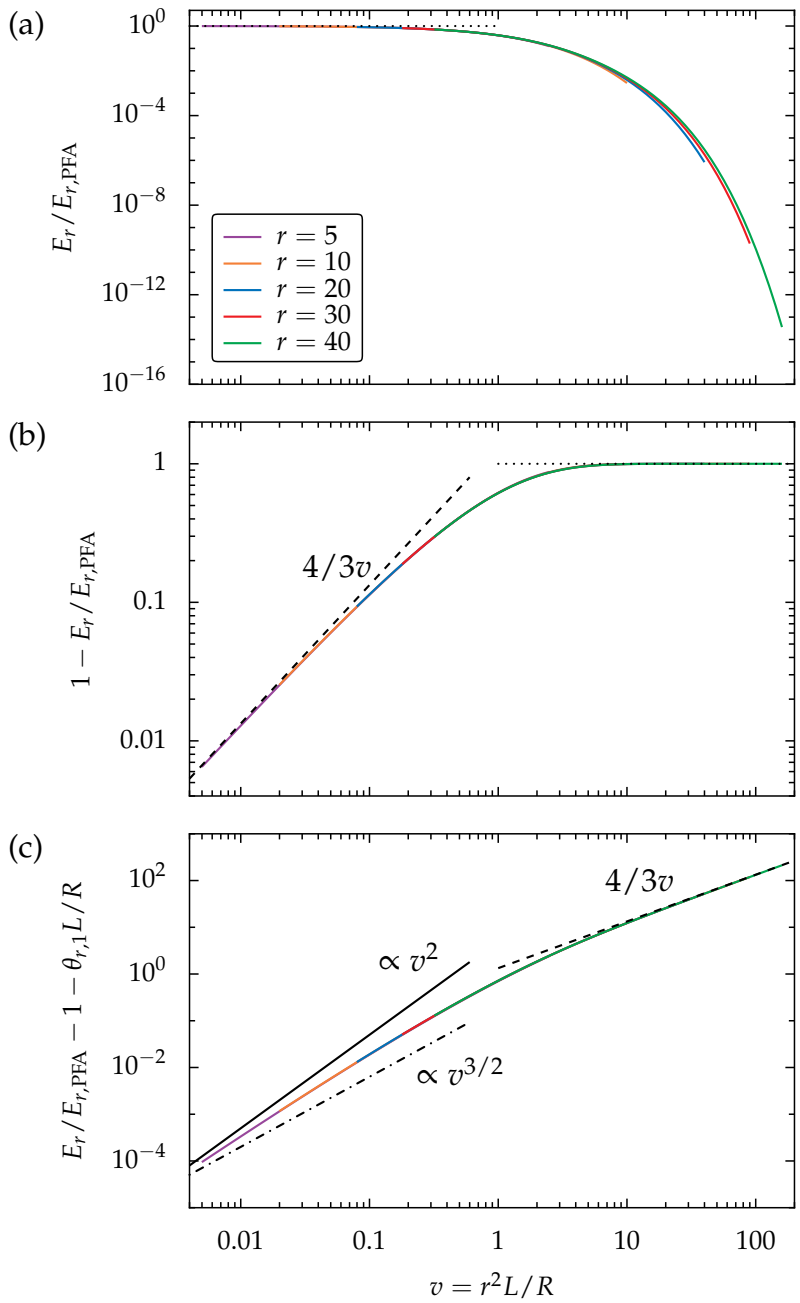

FIGURE 8.9: Round-trip contributions to the Casimir energy for a perfectly reflecting sphere and plane in vacuum at zero temperature as a function of $v = r^2 L/R$ with the round-trip index r, the surface-to-surface distance L and the sphere radius R. Purple, orange, blue, red and green lines correspond to 5, 10, 20, 30 and 40 round trips, respectively. (a) Numerical data relative to the PFA expression $E_{r,\mathrm{PFA}}$ defined in (8.13). (b) and (c) show the correction to the PFA and NTLO term in the asymptotic series of the round-trip contribution to the Casimir energy defined in (8.12). The dotted line corresponds to the constant value of 1, while the dashed line represents $4/3v$. The dash-dotted and solid line are proportional to $v^{3/2}$ and v^2, respectively.

However, by simply assuming that some resummation mechanism exists, which ensures the convergence of the round-trip sum in the NNTLO term, we can show that the corresponding contribution to the Casimir energy will indeed be proportional to $(L/R)^{3/2}$.

We first recall that in Sec. 6.5, the PFA and the NTLO term in the asymptotic expansion of the Casimir energy have been expressed in terms of integrals over the dimensionless variables s and t which were defined in (6.69) and (6.72), respectively. The variable s corresponds to the imaginary frequency and the variable t to the in-plane momenta representing the saddle-point manifold (6.16). Likewise, the PFA and the NTLO expression for the round-trip contribution to the Casimir energy are expressed as integrals over s and t. These integrals were already carried out when we wrote down Eqs. (8.13) and (8.14).

We assume that the NNTLO term in the round-trip contribution to the Casimir energy will also be expressed in terms of integrals over s and t. This assumption is not necessary to show that the NNTLO term in the Casimir energy is proportional to $(L/R)^{3/2}$, but it explains the observations made in Fig. 8.9 (c) for small values of r^2L/R. Incorporating the numerically observed universal behavior in v for large round-trips, we thus assume that the NNTLO term of the Casimir energy is of the form

$$E_{\mathrm{NNTLO}} = \sum_{r=1}^{\infty} \int_0^\infty \mathrm{d}s \int_s^\infty \mathrm{d}t\, f(v,s,t) \left(\frac{L}{R}\right)^2 , \tag{8.16}$$

where $v = r^2L/R$ as before and f is a function which ensures the convergence of the round-trip sum through resummation of asymptotic higher order terms. For instance, f could be of the form

$$\frac{g(s,t)}{1+h(s,t)v} = g(s,t)\left(1 - h(s,t)v + h^2(s,t)v^2 + \ldots\right) , \tag{8.17}$$

where on the right-hand side the fraction was expanded by means of the geometric series to illustrate the resummation procedure. Such fractional form would also encode that for $v \gg 1$, the NNTLO term becomes proportional to L/R, which is in agreement with the numerical observations we have made in Fig. 8.9 (c).

In the numerical data for the round-trip contributions, all in-plane momenta and frequencies are already considered. This would correspond to the evaluation of the integrals over s and t in the NNTLO expression (8.16). If we carry out the integrals in (8.16), its leading asymptotic behavior may then in general be different from $(L/R)^2$, which is precisely what we have observed in Fig. 8.9 (c).

When $L/R \ll 1$, the round trip sum in (8.16) can be replaced by an integral using the Euler-Maclaurin formula:

$$E_{\mathrm{NNTLO}} \sim \int_1^\infty \mathrm{d}r \int_0^\infty \mathrm{d}s \int_s^\infty \mathrm{d}t\, f(r^2L/R,s,t) \left(\frac{L}{R}\right)^2 \sim \int_0^\infty \mathrm{d}s \int_s^\infty \mathrm{d}t F(s,t) \left(\frac{L}{R}\right)^{3/2} \tag{8.18}$$

with the function

$$F(s,t) = \frac{1}{2}\int_0^\infty \frac{\mathrm{d}v}{\sqrt{v}} f(v,s,t) \tag{8.19}$$

which arose by changing the integration over r to $v = r^2L/R$ and by further setting the lower integration bound to zero to obtain the leading order asymptotic behavior. As the integrals over s and t over the function $F(s,t)$ are a numerical factor in (8.18), we have shown that indeed a resummation of higher order terms in the asymptotic

series explains the appearance of the fractional power of $3/2$ in the NNTLO contribution to the Casimir energy.

The precise value of its coefficient depends, however, on the details of the function f which we do not know. A possible candidate for the resummation procedure may be found by observing that the Mie coefficients (5.18) and (5.20) are expressed as fractions. We have expanded those fractions to obtain the asymptotics of the Mie scattering amplitudes (5.32) which is needed for the calculation of the PFA and the NTLO term in the asymptotic expansion of the Casimir energy. If we had not expanded that fraction, we would indeed find a fraction of the form (8.17), for which we would also know the function $h(s,t)$. Obtaining an expression for the function $g(s,t)$ in (8.17) seems like a difficult task as it involves the calculation of the NNTLO term in the saddle-point formula, as the calculation of the NTLO term in the saddle-point formula was already involved. On top of that, we do not know if the resummation due to the fractional representation of the asymptotics of the Mie coefficients would be enough to obtain the correct NNTLO coefficient of the energy. Perhaps another such resummation procedure will be necessary.

Finally, we would like to comment on the geometry of two spheres. In fact, by investigating the round-trip contributions to the energy, we find a universal behavior in $r^2 L/R_{\text{eff}}$ of its NTLO correction when LR_{eff} is small. By further assuming, that the NNTLO term is proportional to $(L/R_{\text{eff}})^2$ with a coefficient possibly depending on the sphere radii, we can use the same argument as above to show that the NNTLO term in the asymptotic expansion of the Casimir energy is proportional to $(L/R_{\text{eff}})^{3/2}$. On this level, we can, however, not argue that the coefficient does not depend on the sphere radii as we have observed numerically.

Chapter 9

Conclusions

In this thesis, we have explored a plane-wave approach to the Casimir interaction within the scattering formalism. Specializing on the plane-sphere and the sphere-sphere geometry, we have developed an analytical and a numerical method making predictions beyond the proximity-force approximation (PFA).

The analytical method is based on an asymptotic expansion of the exact Casimir interaction when the sphere radii become large compared to the surface-to-surface distance. In order to determine the asymptotic expansion, we employed a saddle-point approximation up to second order for the multidimensional integrals appearing in the calculation. As the leading order term in the asymptotic series, we recover the PFA, which can be described within a geometric optical picture of the plane-wave modes. We found that the subleading contribution to the Casimir interaction is mainly due to modifications of the geometric optical picture due to diffraction. By sending one sphere radius to infinity, we found a corresponding asymptotic expansion for Casimir interaction in the plane-sphere geometry. At zero temperature, we have recovered results, which were already known in the literature. As our result is also valid at finite temperatures for arbitrary materials, we found an analytical result, which has not been given in the literature before.

The derivative expansion approach, which assumes that the Casimir interaction is localized at the points of closest approach of the two surfaces, is an alternative approach, which makes beyond-PFA predictions for the Casimir interaction. We compared the results from our asymptotic expansion with the results from the derivative expansion approach. While we find good agreement for finite-frequency contributions to the Casimir interaction, we find that, in the example of aqueous systems involving dielectric bodies, the zero-frequency contribution within the derivative expansion approach does not make adequate predictions beyond the PFA. In contrast, our asymptotic expansion approach worked well in that case.

The derivation of the asymptotic expansion result entailed an estimation of the effective interaction area scaling as $R_1 L$, with the sphere radius of the smaller sphere R_1 and the surface-to-surface distance L. Apart from numerical factors, the same scaling law has been found earlier by heuristic geometric arguments. The scaling law shows that, within the asymptotic expansion, the Casimir interaction is, indeed, localized at the point of closest approach between the two surfaces.

On the numerical front, we have developed a novel scheme utilizing the plane-wave basis within the scattering formalism. The method is built on a Nyström discretization of the plane-wave momenta and it is applicable to in principle arbitrary geometries. We have shown that it can be improved by a discrete Fourier transform, when geometries exhibiting a cylindrical symmetry are considered. In comparison to the standard numerical approach built on the multipole basis, we have demonstrated that our approach has superior convergence properties. We have shown that,

in the example of the plane-sphere geometry, our method outperforms a state-of-the-art implementation of the multipole approach. As a result, the Casimir interaction for experimentally distances becomes now within reach of standard desktop computers when using our plane-wave numerical method.

We have then applied our new numerical method to study the accuracy of the PFA in aqueous colloid systems. Depending on the salt concentration, the zero-frequency contribution of the Casimir interaction is altered. We thus modeled the extreme cases of high and low salt concentration by excluding and including the zero-frequency contribution in the calculations. For polystyrene in water, we have found that the accuracy of the PFA is worse than often anticipated in the literature, especially for low salt concentrations. We demonstrated that in the system of mercury and polystyrene in water, the Casimir force can be repulsive or attractive depending on the distances of the two surfaces. Furthermore, our exact numerical approach allowed us to study the dependence of the effective Hamaker parameter on the geometries. We have found that the effective Hamaker parameter obtained from the Casimir interaction of the curved surfaces is reduced at larger distances when comparing to the usually found result obtained from the plane-plane interaction.

Then, we have studied the accuracy of the predictions made by our asymptotic expansion approach using exact data from the numerical plane-wave method. We found the result from the asymptotic expansion improves significantly on the PFA in typical experimental setups. Thus, it offers a precise alternative to our numerical approach on predicting the Casimir interaction.

Finally, we have studied the asymptotic series of the Casimir energy at zero temperature beyond the result obtained from our asymptotic expansion formula. We have found that in the sphere-sphere geometry the asymptotic next-to-next-to-leading order contribution to the Casimir energy has a fractional power, which is in agreement with a previously found result in the plane-sphere geometry. Interestingly, the coefficient of that next-to-next-to-leading order term does not depend on the sphere radii. By examining the round-trip contributions to the Casimir energy, we have found a possible explanation of the fractional power due to a resummation of higher order terms in the asymptotic series.

The analytical and numerical methods developed in this thesis leave room for future work. For instance, our methods may further be used for studying the Casimir interaction in setups involving magnetic and chiral materials or for other geometries involving cylinders, gratings, structured surfaces and layered surfaces.

Appendix A

Special functions

In this appendix, special functions and their properties, which are need in other parts of this thesis, are summarized.

A.1 Modified Bessel functions

Derivatives of the modified Bessel functions can be recursively expressed as [147, (10.29.2)]

$$I'_\lambda(z) = I_{\lambda-1}(z) - \frac{\lambda}{z} I_\lambda(z)\,, \tag{A.1a}$$

$$K'_\lambda(z) = -K_{\lambda-1}(z) - \frac{\lambda}{z} K_\lambda(z)\,. \tag{A.1b}$$

For large arguments $z \gg 1$, the asymptotics of the modified Bessel functions of first order read [147, (10.40.1)]

$$I_0(z) \sim \frac{\exp(z)}{\sqrt{2\pi z}} \left(1 + \frac{1}{8z} + \mathcal{O}(1/z^2)\right)\,, \tag{A.2a}$$

$$I_1(z) \sim \frac{\exp(z)}{\sqrt{2\pi z}} \left(1 + \mathcal{O}(1/z)\right)\,. \tag{A.2b}$$

For large orders $\lambda \gg 1$, the Debye uniform asymptotic expansion of the modified Bessel functions and their derivatives reads [147, (10.41.3) - (10.41.6)]

$$I_\lambda(\lambda z) \sim \frac{e^{\lambda\eta}}{(2\pi\lambda)^{1/2}(1+z^2)^{1/4}} \left(1 + \frac{U_1(p)}{\lambda} + \mathcal{O}(\lambda^{-2})\right)\,, \tag{A.3a}$$

$$K_\lambda(\lambda z) \sim \left(\frac{\pi}{2\lambda}\right)^{1/2} \frac{e^{-\lambda\eta}}{(1+z^2)^{1/4}} \left(1 - \frac{U_1(p)}{\lambda} + \mathcal{O}(\lambda^{-2})\right)\,, \tag{A.3b}$$

$$I'_\lambda(\lambda z) \sim \frac{(1+z^2)^{1/4} e^{\lambda\eta}}{(2\pi\lambda)^{1/2} z} \left(1 + \frac{V_1(p)}{\lambda} + \mathcal{O}(\lambda^{-2})\right)\,, \tag{A.3c}$$

$$K'_\lambda(\lambda z) \sim -\left(\frac{\pi}{2\lambda}\right)^{1/2} \frac{(1+z^2)^{1/4} e^{-\lambda\eta}}{z} \left(1 - \frac{V_1(p)}{\lambda} + \mathcal{O}(\lambda^{-2})\right)\,, \tag{A.3d}$$

where

$$\eta = (1+z^2)^{1/2} + \log \frac{z}{1+(1+z^2)^{1/2}} = (1+z^2)^{1/2} - \operatorname{arsinh}(1/z) \tag{A.4}$$

and

$$U_1(p) = \frac{1}{24}\left(3p - 5p^3\right) ,$$
$$V_1(p) = \frac{1}{24}\left(-9p + 7p^3\right)$$

with

$$p = (1+z^2)^{-1/2} . \tag{A.5}$$

Combining (A.3a) and (A.3c), we obtain

$$\frac{I'_\lambda(\lambda z)}{I_\lambda(\lambda z)} \sim \frac{\sqrt{1+z^2}}{z}\left(1 - \frac{z^2}{2(1+z^2)^{3/2}}\frac{1}{\lambda} + \mathcal{O}(\lambda^{-2})\right) , \tag{A.6}$$

which is valid uniformly in z for $\lambda \gg 1$.

A.2 Associated Legendre functions

The associated Legendre functions are defined as [147, (14.7.11)]

$$P_\ell^m(z) = (z^2-1)^{m/2}\frac{\mathrm{d}^m}{\mathrm{d}z^m}P_\ell(z) , \tag{A.7}$$

where $P_\ell(z) \equiv P_\ell^0(z)$ are the ordinary Legendre functions defined by [147, (14.7.13)]

$$P_\ell(z) = \frac{1}{2^\ell \ell!}\frac{\mathrm{d}^\ell}{\mathrm{d}z^\ell}(z^2-1)^\ell . \tag{A.8}$$

Note that the definition (A.7) is well adapted for arguments $|z| > 1$ and that we omit the Condon–Shortley phase.

The associated Legendre functions $P_\ell^m(z)$ satisfy the recurrence relations

$$\begin{aligned}(\ell - m + 1)P_{\ell+1}^m(z) &= (2\ell+1)zP_\ell^m(z) - (\ell+m)P_{\ell-1}^m(z) ,\\ (z^2-1)P_\ell^{m\prime}(z) &= \ell z P_\ell^m(z) - (\ell+m)P_{\ell-1}^m(z) .\end{aligned} \tag{A.9}$$

For $\ell = m$, they are given by

$$P_m^m(z) = \frac{(2m)!}{2^m m!}(z^2-1)^{m/2} . \tag{A.10}$$

For $\ell \gg 1$, the asymptotic expansion of the associated Legendre functions with $m = 0$ and 1 reads [139, §29.3.3]

$$P_\ell(\cosh u) \sim \left(\frac{u}{\sinh u}\right)^{1/2}\left(I_0(\lambda u) - \frac{1}{8}\frac{1-u\coth u}{u}\frac{I_1(\lambda u)}{\lambda} + \mathcal{O}(1/\lambda^2)\right) , \tag{A.11a}$$

$$P_\ell^1(\cosh u) \sim \frac{\ell(\ell+1)}{\lambda}\left(\frac{u}{\sinh u}\right)^{1/2}\left(I_1(\lambda u) + \frac{3}{8}\frac{1-u\coth u}{u}\frac{I_2(\lambda u)}{\lambda} + \mathcal{O}(1/\lambda^2)\right) , \tag{A.11b}$$

with $\lambda = \ell + \frac{1}{2}$. The asymptotic expansions (A.11) hold uniformly for $u \geq 0$.

A.3 Polylogarithm

The polylogarithm of order s is defined as [147, (25.12.10)]

$$\mathrm{Li}_s(z) = \sum_{n=1}^{\infty} \frac{z^n}{n^s}\,. \tag{A.12}$$

For certain integer values of the order, the polylogarithm can be expressed in terms of elementary functions. For instance,

$$\mathrm{Li}_1(z) = -\log(1-z)\,, \tag{A.13a}$$
$$\mathrm{Li}_0(z) = \frac{z}{1-z}\,, \tag{A.13b}$$
$$\mathrm{Li}_{-1}(z) = \frac{z}{(1-z)^2}\,, \tag{A.13c}$$
$$\mathrm{Li}_{-2}(z) = \frac{z(1+z)}{(1-z)^3}\,. \tag{A.13d}$$

We will often need to evaluate the polylogarithms of order 2 and 3. The evaluation of those polylogarithm cannot be reduced to the evaluation of elementary functions. For a fast and stable numerical evaluation we will make use of the integral representation [147, (25.12.11)]

$$\mathrm{Li}_s(z) = \frac{z}{\Gamma(s)} \int_0^\infty dx \frac{x^{s-1}}{e^x - z} \tag{A.14}$$

valid for $0 < z < 1$, which is also known as the Bose-Einstein integral. For $z = 1$, the polylogarithm reduces to the Riemann zeta function

$$\mathrm{Li}_s(1) = \zeta(s)\,. \tag{A.15}$$

Using the power series (A.12), the derivative of the polylogarithm can be expressed as

$$\frac{\mathrm{d}\,\mathrm{Li}_s(z)}{\mathrm{d}z} = \frac{1}{z}\,\mathrm{Li}_{s-1}(z)\,. \tag{A.16}$$

A.4 Angular functions

The angular functions (5.4) can be alternatively defined as

$$\pi_\ell(z) = \frac{1}{\sqrt{z^2-1}} P_\ell^1(z)\,, \tag{A.17a}$$
$$\tau_\ell(z) = -z\pi_\ell(z) + \ell(\ell+1)P_\ell(z)\,. \tag{A.17b}$$

The angular functions with negative arguments can be expressed in terms of the angular functions with positive arguments through the relations

$$\begin{aligned} \pi_\ell(-z) &= (-1)^{\ell-1}\pi_\ell(z)\,, \\ \tau_\ell(-z) &= (-1)^{\ell}\tau_\ell(z)\,. \end{aligned} \tag{A.18}$$

For $z = 1$, the angular functions take the special value

$$\pi_\ell(1) = \tau_\ell(1) = \frac{1}{2}\ell(\ell+1)\,. \tag{A.19}$$

In view of the alternative definition for the angular functions (A.17), a uniform asymptotic expansion for large order ℓ can be derived from (A.11). The expansion reads

$$\pi_\ell(\cosh u) \sim \frac{\ell(\ell+1)}{\lambda}\left(\frac{u}{\sinh^3 u}\right)^{1/2}\left(I_1(\lambda u)+\frac{3}{8}\frac{1-u\coth u}{u}\frac{I_2(\lambda u)}{\lambda}+\mathcal{O}(1/\lambda^2)\right), \tag{A.20a}$$

$$\tau_\ell(\cosh u) \sim \ell(\ell+1)\left(\frac{u}{\sinh u}\right)^{1/2}\left(I_0(\lambda u)-\frac{1}{8}\frac{1+7u\coth u}{u}\frac{I_1(\lambda u)}{\lambda}+\mathcal{O}(1/\lambda^2)\right), \tag{A.20b}$$

where $\lambda = \ell + \frac{1}{2}$. When $\lambda u \gg 1$, we can make use of (A.2) to find

$$\pi_\ell(\cosh u) \sim \frac{\ell(\ell+1)}{\lambda}\left(\frac{1}{2\pi\lambda\sinh^3 u}\right)^{1/2}\exp(\lambda u)\left(1+\mathcal{O}(1/\lambda)\right), \tag{A.21a}$$

$$\tau_\ell(\cosh u) \sim \ell(\ell+1)\left(\frac{1}{2\pi\lambda\sinh u}\right)^{1/2}\exp(\lambda u)\left(1-\frac{7}{8}\coth u\frac{1}{\lambda}+\mathcal{O}(1/\lambda^2)\right). \tag{A.21b}$$

In view of the definition of the angular functions (5.4), in which they are expressed in terms of the Legendre functions (A.8), their asymptotics for large arguments $|z| \gg 1$ reads

$$\begin{aligned}\pi_\ell(z) &\sim \frac{(2\ell)!}{2^\ell \ell!(\ell-1)!}z^{\ell-1},\\ \tau_\ell(z) &\sim \frac{(2\ell)!}{2^\ell[(\ell-1)!]^2}z^\ell.\end{aligned} \tag{A.22}$$

Appendix B

Supplementary material for chapter 2

B.1 Properties of a unitary matrix

Let $\mathbf{S}$ be a unitary matrix. The defining properties of a unitary matrix, $\mathbf{S}\mathbf{S}^\dagger = 1$ and $\mathbf{S}^\dagger\mathbf{S} = 1$, yield the equations

$$\mathbf{S}_{11}\mathbf{S}_{11}^\dagger + \mathbf{S}_{12}\mathbf{S}_{12}^\dagger = 1 \tag{B.1}$$

and

$$\mathbf{S}_{22}^\dagger\mathbf{S}_{22} + \mathbf{S}_{12}^\dagger\mathbf{S}_{12} = 1\,, \tag{B.2}$$

respectively.

The relation $\mathbf{S}^{-1} = \mathbf{S}^\dagger$ can be expressed as [63, Eq. (A6)]

$$\begin{pmatrix} \mathbf{S}_{11}^\dagger & \mathbf{S}_{21}^\dagger \\ \mathbf{S}_{12}^\dagger & \mathbf{S}_{22}^\dagger \end{pmatrix} = \begin{pmatrix} (\mathbf{S}/\mathbf{S}_{22})^{-1} & -(\mathbf{S}/\mathbf{S}_{22})^{-1}\mathbf{S}_{12}\mathbf{S}_{22}^{-1} \\ -\mathbf{S}_{22}^{-1}\mathbf{S}_{21}(\mathbf{S}/\mathbf{S}_{22})^{-1} & (\mathbf{S}/\mathbf{S}_{11})^{-1} \end{pmatrix}, \tag{B.3}$$

where

$$\begin{aligned} \mathbf{S}/\mathbf{S}_{11} &= \mathbf{S}_{22} - \mathbf{S}_{21}\mathbf{S}_{11}^{-1}\mathbf{S}_{12}\,, \\ \mathbf{S}/\mathbf{S}_{22} &= \mathbf{S}_{11} - \mathbf{S}_{12}\mathbf{S}_{22}^{-1}\mathbf{S}_{21}\,. \end{aligned} \tag{B.4}$$

B.2 Relation between the scattering and transfer matrix

In this appendix, we derive the formulae (2.27) and (2.26) relating the scattering and transfer matrix. Using Eq. (2.18), the corresponding inverted equation and Eq. (2.24), we can eliminate the fields $\mathbf{b}^\pm$. Comparison of the coefficients of the fields $\mathbf{a}^\pm$ then yields

$$\mathbf{T}_{11} = \mathbf{S}_{11} + \mathbf{S}_{12}\mathbf{T}_{21}\,, \tag{B.5a}$$

$$\mathbf{T}_{12} = \mathbf{S}_{12}\mathbf{T}_{22}\,, \tag{B.5b}$$

$$\mathbf{T}_{21} = \mathbf{S}_{12}^\dagger\mathbf{T}_{11}\,, \tag{B.5c}$$

$$\mathbf{T}_{22} = \mathbf{S}_{22}^\dagger + \mathbf{S}_{12}^\dagger\mathbf{T}_{12}\,. \tag{B.5d}$$

Using (B.1) and (B.2), we can solve for the entries of the transfer matrix and obtain

$$\mathbf{T}_{11} = (\mathbf{S}_{11}^{\dagger})^{-1}\,, \tag{B.6a}$$
$$\mathbf{T}_{12} = \mathbf{S}_{12}\mathbf{S}_{22}^{-1}\,, \tag{B.6b}$$
$$\mathbf{T}_{21} = \mathbf{S}_{12}^{\dagger}(\mathbf{S}_{11}^{\dagger})^{-1}\,, \tag{B.6c}$$
$$\mathbf{T}_{22} = \mathbf{S}_{22}^{-1}\,. \tag{B.6d}$$

Application of (B.3) to (B.6a) and (B.6c) then finally yields Eq. (2.26). Conversely, equation (2.26) can be straightforwardly solved for $\mathbf{S}$ to obtain (2.27)

B.3 Convergence analysis for the PSD

We study how the PSD converges as a function of the order of the Padé approximation N. For the analysis, we consider the Casimir free energy for the geometry of a plane and a sphere and the geometry of two spheres. The numerical evaluation of the Casimir free energy is based on the method developed in Ch. 7.

It turns out that convergence is reached when N takes values that scale as $\sqrt{\lambda_T/L}$, which motivates to write

$$N = \left\lceil \eta \left(\frac{\lambda_T}{L}\right)^{1/2} \right\rceil\,. \tag{B.7}$$

The coefficient η controls the numerical accuracy. For larger values of η the accuracy increases.

In Fig. B.1, the relative error of the PSD as a function of the coefficient η is shown for various system parameters. The error is computed relative to the free energy with $\eta = 7$. The radius of the sphere(s) is set to $R = 1\,\mu$m. In Fig. B.1 (a) the temperature is fixed at $T = 300\,$K, while in Fig. B.1 (b) the temperature is $T = 200\,$K. The geometries are represented by the shape of the symbols: circles and squares stand for the sphere-sphere geometry, and pluses and crosses stand for the plane-sphere geometry. The surface-to-surface distance for the crosses and circles is $L = 0.1\,\mu$m, while for the squares and pluses it is $L = 0.01\,\mu$m. Different colors represent different materials for the objects and the medium. The red, green and blue symbols correspond to the results for perfect reflectors in vacuum, gold in vacuum and polystyrene in water, respectively.

We observe that, for perfect reflectors in vacuum, the relative error only depends weakly on the geometries and on the surface-to-surface distance. For the other material choices this is no longer true and convergence is typically reached faster than for perfect reflectors. As Fig. B.1 (a) and (b) almost coincide, the temperature dependence on relative error as a function of η is very weak. Moreover, for other values for the radii of the sphere(s), we find that the depicted would change only weakly from those given in Fig. B.1. This shows that, for the two geometries composed of real materials, the curves for the relative error as a function of η depend to first order only on the distance L. Indeed, one expects that the convergence of the summation over imaginary frequencies depends on how the distance L between the two objects changes relative to the length scales introduced by the real materials. An example for such a length scale is the plasma wave length for gold.

For perfect reflectors in vacuum the convergence of the PSD-sum is determined by the translation factor between the two surfaces, which behaves like $\exp(-2\xi L/c)$ for large imaginary frequencies ξ. When real materials are involved the sum may

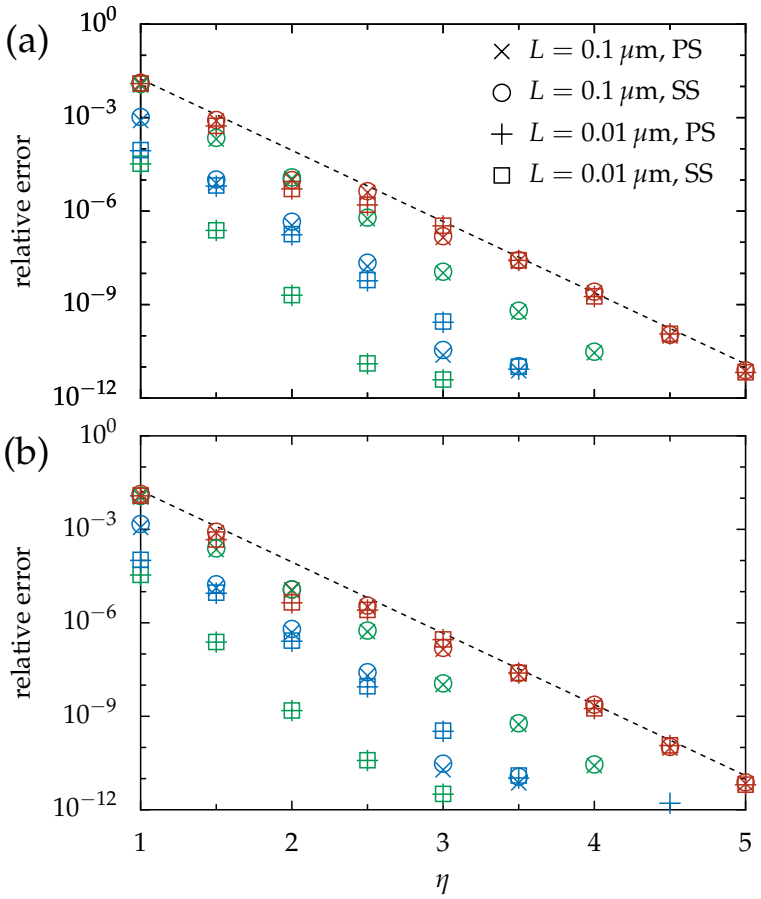

FIGURE B.1: The relative error of the Casimir free energy as a function of η at (a) $T = 300\,\mathrm{K}$ and (b) $T = 200\,\mathrm{K}$. The circles and squares represent the result for the sphere-sphere geometry (SS) and the pluses and crosses correspond to the plane-sphere geometry (PS). The radius of the sphere(s) is $R = 1\,\mu$m. For the crosses and circles the surface-to-surface distance is $L = 0.1\,\mu$m, while for the squares and pluses that distance is $L = 0.01\,\mu$m. The red, green and blue symbols represent the result for perfect reflectors in vacuum, gold in vacuum and polystyrene in water, respectively. The dashed lines serve as a guide to establish formula (B.8).

converge more rapidly since the objects become transparent at high enough frequencies. Thus, the curves for the relative errors of perfect reflectors in vacuum in Fig. B.1 can be understood as an upper bound for any materials. This allows us to establish a rule of thumb for choosing η for the plane-sphere and sphere-sphere geometry valid for any choice of material. From the dashed lines in Fig. B.1, we find the formula

$$\eta = -0.19 \log(0.30\,\epsilon) \tag{B.8}$$

where ϵ is the desired relative error.

Appendix C

Supplementary material for chapter 5

C.1 Explicit expressions for the polarization transformation coefficients

In this appendix, we derive explicit expressions for the polarization transformation coefficients (5.10).

First, we note that the basis vectors $\hat{\boldsymbol{\epsilon}}_\perp$ and $\hat{\boldsymbol{\epsilon}}_\parallel$ for the incident and scattered wave vectors are related by

$$\begin{aligned}
\hat{\boldsymbol{\epsilon}}_\parallel^{(\mathrm{in})} \cdot \hat{\boldsymbol{\epsilon}}_\parallel^{(\mathrm{sc})} &= \cos(\Theta)\,, \\
\hat{\boldsymbol{\epsilon}}_\perp^{(\mathrm{in})} \cdot \hat{\boldsymbol{\epsilon}}_\perp^{(\mathrm{sc})} &= 1\,, \\
\hat{\boldsymbol{\epsilon}}_\parallel^{(\mathrm{in})} \cdot \hat{\boldsymbol{\epsilon}}_\perp^{(\mathrm{sc})} &= 0\,, \\
\hat{\boldsymbol{\epsilon}}_\perp^{(\mathrm{in})} \cdot \hat{\boldsymbol{\epsilon}}_\parallel^{(\mathrm{sc})} &= 0\,.
\end{aligned} \tag{C.1}$$

With

$$\begin{aligned}
\hat{\boldsymbol{\epsilon}}_{\mathrm{TM}} &= \cos(\chi)\hat{\boldsymbol{\epsilon}}_\parallel - \sin(\chi)\hat{\boldsymbol{\epsilon}}_\perp\,, \\
\hat{\boldsymbol{\epsilon}}_{\mathrm{TE}} &= \sin(\chi)\hat{\boldsymbol{\epsilon}}_\parallel + \cos(\chi)\hat{\boldsymbol{\epsilon}}_\perp
\end{aligned} \tag{C.2}$$

and (C.1), the scalar products between the polarization vectors $\{\hat{\boldsymbol{\epsilon}}_{\mathrm{TM}}, \hat{\boldsymbol{\epsilon}}_{\mathrm{TE}}\}$ of the incident and scattered mode can be related to the polarization transformation coefficients (5.10). We find the relations

$$\begin{aligned}
\hat{\boldsymbol{\epsilon}}_{\mathrm{TM}}^{(\mathrm{in})} \cdot \hat{\boldsymbol{\epsilon}}_{\mathrm{TM}}^{(\mathrm{sc})} &= A\cos(\Theta) + B\,, \\
\hat{\boldsymbol{\epsilon}}_{\mathrm{TE}}^{(\mathrm{in})} \cdot \hat{\boldsymbol{\epsilon}}_{\mathrm{TE}}^{(\mathrm{sc})} &= A + B\cos(\Theta)\,, \\
\hat{\boldsymbol{\epsilon}}_{\mathrm{TM}}^{(\mathrm{in})} \cdot \hat{\boldsymbol{\epsilon}}_{\mathrm{TE}}^{(\mathrm{sc})} &= -C\cos(\Theta) - D\,, \\
\hat{\boldsymbol{\epsilon}}_{\mathrm{TE}}^{(\mathrm{in})} \cdot \hat{\boldsymbol{\epsilon}}_{\mathrm{TM}}^{(\mathrm{sc})} &= C + D\cos(\Theta)\,.
\end{aligned} \tag{C.3}$$

Solving for the coefficients A, B, C and D, we obtain

$$\begin{aligned} A &= \frac{\hat{\boldsymbol{\epsilon}}_{\mathrm{TE}}^{(\mathrm{in})} \cdot \hat{\boldsymbol{\epsilon}}_{\mathrm{TE}}^{(\mathrm{sc})} - \cos(\Theta)\hat{\boldsymbol{\epsilon}}_{\mathrm{TM}}^{(\mathrm{in})} \cdot \hat{\boldsymbol{\epsilon}}_{\mathrm{TM}}^{(\mathrm{sc})}}{1-\cos^2(\Theta)}\,, \\ B &= \frac{\hat{\boldsymbol{\epsilon}}_{\mathrm{TM}}^{(\mathrm{in})} \cdot \hat{\boldsymbol{\epsilon}}_{\mathrm{TM}}^{(\mathrm{sc})} - \cos(\Theta)\hat{\boldsymbol{\epsilon}}_{\mathrm{TE}}^{(\mathrm{in})} \cdot \hat{\boldsymbol{\epsilon}}_{\mathrm{TE}}^{(\mathrm{sc})}}{1-\cos^2(\Theta)}\,, \\ C &= \frac{\hat{\boldsymbol{\epsilon}}_{\mathrm{TE}}^{(\mathrm{in})} \cdot \hat{\boldsymbol{\epsilon}}_{\mathrm{TM}}^{(\mathrm{sc})} + \cos(\Theta)\hat{\boldsymbol{\epsilon}}_{\mathrm{TM}}^{(\mathrm{in})} \cdot \hat{\boldsymbol{\epsilon}}_{\mathrm{TE}}^{(\mathrm{sc})}}{1-\cos^2(\Theta)}\,, \\ D &= -\frac{\hat{\boldsymbol{\epsilon}}_{\mathrm{TM}}^{(\mathrm{in})} \cdot \hat{\boldsymbol{\epsilon}}_{\mathrm{TE}}^{(\mathrm{sc})} + \cos(\Theta)\hat{\boldsymbol{\epsilon}}_{\mathrm{TE}}^{(\mathrm{in})} \cdot \hat{\boldsymbol{\epsilon}}_{\mathrm{TM}}^{(\mathrm{sc})}}{1-\cos^2(\Theta)}\,. \end{aligned} \tag{C.4}$$

The remaining task is thus to find expressions for the scalar products between the TE and TM polarization components. They can be expressed in terms of the incident and scattered wave vectors through their definition (3.1). We find

$$\begin{aligned} \hat{\boldsymbol{\epsilon}}_{\mathrm{TM}}^{(\mathrm{in})} \cdot \hat{\boldsymbol{\epsilon}}_{\mathrm{TM}}^{(\mathrm{sc})} &= \frac{1}{k^{(\mathrm{in})}k^{(\mathrm{sc})}}\left[\mathbf{k}^{(\mathrm{in})} \cdot \mathbf{k}^{(\mathrm{sc})}\cos(\Theta) + \frac{1}{K^2}(\mathbf{k}^{(\mathrm{in})} \times \mathbf{k}^{(\mathrm{sc})})^2\right]\,, \\ \hat{\boldsymbol{\epsilon}}_{\mathrm{TE}}^{(\mathrm{in})} \cdot \hat{\boldsymbol{\epsilon}}_{\mathrm{TE}}^{(\mathrm{sc})} &= \frac{\mathbf{k}^{(\mathrm{in})} \cdot \mathbf{k}^{(\mathrm{sc})}}{k^{(\mathrm{in})}k^{(\mathrm{sc})}}\,, \\ \hat{\boldsymbol{\epsilon}}_{\mathrm{TM}}^{(\mathrm{in})} \cdot \hat{\boldsymbol{\epsilon}}_{\mathrm{TE}}^{(\mathrm{sc})} &= -\frac{\mathbf{K}^{(\mathrm{in})} \cdot (\mathbf{k}^{(\mathrm{in})} \times \mathbf{k}^{(\mathrm{sc})})}{k^{(\mathrm{in})}k^{(\mathrm{sc})}K}\,, \\ \hat{\boldsymbol{\epsilon}}_{\mathrm{TE}}^{(\mathrm{in})} \cdot \hat{\boldsymbol{\epsilon}}_{\mathrm{TM}}^{(\mathrm{sc})} &= \frac{\mathbf{K}^{(\mathrm{sc})} \cdot (\mathbf{k}^{(\mathrm{in})} \times \mathbf{k}^{(\mathrm{sc})})}{k^{(\mathrm{in})}k^{(\mathrm{sc})}K}\,. \end{aligned} \tag{C.5}$$

In polar coordinates, $\mathbf{k}^{(\mathrm{in})} = (k^{(\mathrm{in})}, \varphi^{(\mathrm{in})})$ and $\mathbf{k}^{(\mathrm{sc})} = (k^{(\mathrm{sc})}, \varphi^{(\mathrm{sc})})$, the scalar and cross products become

$$\begin{aligned} \mathbf{k}^{(\mathrm{in})} \cdot \mathbf{k}^{(\mathrm{sc})} &= k^{(\mathrm{in})}k^{(\mathrm{sc})}\cos(\varphi^{(\mathrm{sc})} - \varphi^{(\mathrm{in})})\,, \\ \mathbf{k}^{(\mathrm{in})} \times \mathbf{k}^{(\mathrm{sc})} &= \hat{\mathbf{z}}k^{(\mathrm{in})}k^{(\mathrm{sc})}\sin(\varphi^{(\mathrm{sc})} - \varphi^{(\mathrm{in})})\,. \end{aligned} \tag{C.6}$$

The polarization transformation coefficients then read

$$\begin{aligned} A &= \frac{K^4\cos(\varphi) - [k^{(\mathrm{in})}k^{(\mathrm{sc})}\cos(\varphi) + \phi^{(\mathrm{in})}\phi^{(\mathrm{sc})}k_z^{(\mathrm{in})}k_z^{(\mathrm{sc})}][k^{(\mathrm{in})}k^{(\mathrm{sc})} + \phi^{(\mathrm{in})}\phi^{(\mathrm{sc})}k_z^{(\mathrm{in})}k_z^{(\mathrm{sc})}\cos(\varphi)]}{K^4 - [k^{(\mathrm{in})}k^{(\mathrm{sc})}\cos(\varphi) + \phi^{(\mathrm{in})}\phi^{(\mathrm{sc})}k_z^{(\mathrm{in})}k_z^{(\mathrm{sc})}]^2}\,, \\ B &= \frac{K^2k^{(\mathrm{in})}k^{(\mathrm{sc})}\sin^2(\varphi)}{K^4 - [k^{(\mathrm{in})}k^{(\mathrm{sc})}\cos(\varphi) + \phi^{(\mathrm{in})}\phi^{(\mathrm{sc})}k_z^{(\mathrm{in})}k_z^{(\mathrm{sc})}]^2}\,, \\ C &= -K\sin(\varphi)\frac{k^{(\mathrm{in})}k^{(\mathrm{sc})}\phi^{(\mathrm{in})}k_z^{(\mathrm{in})}\cos(\varphi) - (k^{(\mathrm{in})})^2\phi^{(\mathrm{sc})}k_z^{(\mathrm{sc})}}{K^4 - [k^{(\mathrm{in})}k^{(\mathrm{sc})}\cos(\varphi) + \phi^{(\mathrm{in})}\phi^{(\mathrm{sc})}k_z^{(\mathrm{in})}k_z^{(\mathrm{sc})}]^2}\,, \\ D &= -K\sin(\varphi)\frac{k^{(\mathrm{in})}k^{(\mathrm{sc})}\phi^{(\mathrm{sc})}k_z^{(\mathrm{sc})}\cos(\varphi) - (k^{(\mathrm{sc})})^2\phi^{(\mathrm{in})}k_z^{(\mathrm{in})}}{K^4 - [k^{(\mathrm{in})}k^{(\mathrm{sc})}\cos(\varphi) + \phi^{(\mathrm{in})}\phi^{(\mathrm{sc})}k_z^{(\mathrm{in})}k_z^{(\mathrm{sc})}]^2}\,, \end{aligned} \tag{C.7}$$

where $\varphi = \varphi^{(\mathrm{sc})} - \varphi^{(\mathrm{in})}$.

For $\mathbf{k}^{(\mathrm{in})} = \mathbf{k}^{(\mathrm{sc})}$, they simplify to

$$A = 1\,, \quad B = C = D = 0\,. \tag{C.8}$$

C.2 Scattering amplitudes for large spheres

Here, the first two terms in the asymptotic series of the plane-wave scattering amplitudes (5.3) for a large sphere radius is derived. The derivation is within the imaginary frequency domain. The two cases of a finite and a vanishing imaginary frequency ξ are considered separately. First, the finite frequency case is considered and the calculation is demonstrated for a perfectly reflecting sphere. Then, the result is generalized to a dielectric sphere. Finally, the asymptotic expansion of the scattering amplitudes at vanishing frequencies is studied.

Finite imaginary frequencies

We recall that the scattering amplitudes are given by the expressions

$$\begin{aligned} S_1 &= \sum_{\ell=1}^{\infty} \frac{2\ell+1}{\ell(\ell+1)} \left[a_\ell(ix)\pi_\ell(\cos(\Theta)) + b_\ell(ix)\tau_\ell(\cos(\Theta)) \right] , \\ S_2 &= \sum_{\ell=1}^{\infty} \frac{2\ell+1}{\ell(\ell+1)} \left[a_\ell(ix)\tau_\ell(\cos(\Theta)) + b_\ell(ix)\pi_\ell(\cos(\Theta)) \right] . \end{aligned} \tag{C.9}$$

Inspired by the derivation of the asymptotic expansion in the real frequency domain, we make use the the localization principle [100] to argue that the important contributions to the ℓ-sum come from the neighborhood $\ell \lesssim x$ as the imaginary size parameter $x = \mathcal{K}R$ becomes large. Larger values of ℓ correspond to rays passing by the sphere and thus have a small contribution to the scattering amplitudes.

This motivates the replacement of the sum over ℓ by an integral

$$\sum_{\ell=1}^{\infty} \to \int_{1/2}^{\infty} \mathrm{d}\ell \tag{C.10}$$

for extracting the asymptotics of the scattering amplitudes. With suitable asymptotic expansions for the Mie coefficients and angular functions for $\ell \gg 1$, the integral can be evaluated by the saddle-point method described in Sec. 6.1, where x plays the role of the large parameter.

For positive arguments, a uniform asymptotic expansion of the angular functions for large order is given in (A.21). However, $\cos(\Theta)$ is always negative in the imaginary frequency domain, which can be seen from its defining equation (5.17). It is thus convenient to introduce the variable $u > 0$ in terms of $\cosh(u) = -\cos(\Theta)$. Using the reflection formulas (A.18), the asymptotic expansion of the angular functions then reads

$$\begin{aligned} \pi_\ell(\cos(\Theta)) &\sim (-1)^{\ell-1} \frac{\ell(\ell+1)}{\lambda} \left(\frac{1}{2\pi\lambda \sinh^3 u} \right)^{1/2} \exp(\lambda u) \\ \tau_\ell(\cos(\Theta)) &\sim (-1)^{\ell} \ell(\ell+1) \left(\frac{1}{2\pi\lambda \sinh u} \right)^{1/2} \exp(\lambda u) \left(1 - \frac{7}{8} \coth u \frac{1}{\lambda} \right) . \end{aligned} \tag{C.11}$$

for $\lambda \gg 1$ where $\lambda = \ell + 1/2$. Note that we have expanded τ_ℓ one order further than π_ℓ. This is because the leading order term of π_ℓ is asymptotically of the same order in λ as the subleading term of τ_ℓ.

The Mie coefficients and thus also their asymptotic behavior depend on the boundary conditions on the sphere. We first discuss the asymptotics of the Mie coefficients

for a perfectly conducting sphere and use the result to derive the asymptotic expansion of the scattering amplitudes. Then, we generalize these results to a dielectric sphere.

Perfectly conducting sphere

Using the identities for the derivatives of the modified Bessel functions (A.1), we can rewrite the Mie coefficient for electric polarization a_ℓ in (5.20). The Mie coefficients for a perfectly conducting sphere then read

$$\begin{aligned} a_\ell^{(\mathrm{PR})}(ix) &= (-1)^\ell \frac{\pi}{2} \frac{xI'_\lambda(x) + \frac{1}{2}I_\lambda(x)}{-xK'_\lambda(x) - \frac{1}{2}K_\lambda(x)}, \\ b_\ell^{(\mathrm{PR})}(ix) &= (-1)^{\ell-1} \frac{\pi}{2} \frac{I_\lambda(x)}{K_\lambda(x)}. \end{aligned} \tag{C.12}$$

where $\lambda = \ell + 1/2$. This form for the Mie coefficients is now suitable for employing the Debye asymptotic expansion of the modified Bessel functions and its derivatives (A.3). We find

$$\begin{aligned} a_\ell^{(\mathrm{PR})}(ix) &\sim (-1)^\ell \frac{1}{2} \exp(\psi) \frac{1 + \alpha/x}{1 - \alpha/x}, \\ b_\ell^{(\mathrm{PR})}(ix) &\sim (-1)^{\ell-1} \frac{1}{2} \exp(\psi) \frac{1 + \beta/x}{1 - \beta/x} \end{aligned} \tag{C.13}$$

where

$$\psi = 2x\left(\sqrt{1+\Lambda^2} - \Lambda \operatorname{arsinh}(\Lambda)\right) \tag{C.14}$$

with $\Lambda = \lambda/x$ and

$$\begin{aligned} \alpha &= \frac{1}{24}\left[\frac{3}{(1+\Lambda^2)^{1/2}} + \frac{7\Lambda^2}{(1+\Lambda^2)^{3/2}}\right], \\ \beta &= \frac{1}{24}\left[\frac{3}{(1+\Lambda^2)^{1/2}} - \frac{5\Lambda^2}{(1+\Lambda^2)^{3/2}}\right]. \end{aligned} \tag{C.15}$$

The fractions in (C.13) can be expanded for $x \gg 1$, which yields

$$\begin{aligned} a_\ell^{(\mathrm{PR})}(ix) &\sim (-1)^\ell \frac{1}{2} \exp(\psi) \left[1 + \frac{1}{4x}\left(\frac{1}{\sqrt{1+\Lambda^2}} + \frac{7}{3}\frac{\Lambda^2}{(1+\Lambda^2)^{3/2}}\right) + \mathcal{O}(1/x^2)\right], \\ b_\ell^{(\mathrm{PR})}(ix) &\sim (-1)^{\ell-1} \frac{1}{2} \exp(\psi) \left[1 + \frac{1}{4x}\left(\frac{1}{\sqrt{1+\Lambda^2}} - \frac{5}{3}\frac{\Lambda^2}{(1+\Lambda^2)^{3/2}}\right) + \mathcal{O}(1/x^2)\right]. \end{aligned} \tag{C.16}$$

Having replaced the sum over ℓ by an integral as given in (C.10) and using the substitution $\Lambda = \lambda/x = (\ell + 1/2)/x$, we can express the scattering amplitudes for perfectly conducting spheres as

$$S_{1/2}^{(\mathrm{PR})} = \int_{1/x}^{\infty} \mathrm{d}\Lambda \, g_{1/2}(\Lambda) \exp(-x f(\Lambda)) \tag{C.17}$$

with

$$f(\Lambda) = 2\Lambda \operatorname{arsinh}(\Lambda) - 2\sqrt{1+\Lambda^2} - \Lambda u \tag{C.18}$$

and

$$g_{1/2}(\Lambda) = \mp \left(\frac{x^3 \Lambda}{2\pi \sinh u}\right)^{1/2} \left[1 + g_{1/2}^{(1)}(\Lambda)\frac{1}{x} + \mathcal{O}(1/x^2)\right], \tag{C.19}$$

where

$$g_1^{(1)}(\Lambda) = \frac{1}{\Lambda \sinh u} - \frac{7 \coth u}{8\Lambda} + \frac{1}{4}\left(\frac{1}{\sqrt{1+\Lambda^2}} - \frac{5}{3}\frac{\Lambda^2}{(1+\Lambda^2)^{3/2}}\right),$$
$$g_2^{(1)}(\Lambda) = \frac{1}{\Lambda \sinh u} - \frac{7 \coth u}{8\Lambda} + \frac{1}{4}\left(\frac{1}{\sqrt{1+\Lambda^2}} + \frac{7}{3}\frac{\Lambda^2}{(1+\Lambda^2)^{3/2}}\right).$$

The first and second terms in the functions $g_1^{(1)}$ and $g_2^{(1)}$ come from the leading order contribution of π_ℓ and subleading contribution to τ_ℓ. They agree for the two functions. This is special to the perfect reflector case, because the leading order contributions of the Mie coefficients for the two polarizations just differ by a sign. The last terms in $g_1^{(1)}$ and $g_2^{(1)}$ differ because they come from the leading term in τ_ℓ and the subleading term of the Mie coefficients which are different for the two polarizations.

Now, the saddle-point method as described in Sec. 6.1 can be carried out. The saddle point for both scattering amplitudes is uniquely determined by

$$\Lambda_{\mathrm{sp}} = \sqrt{\frac{\cosh(u)-1}{2}} = i\cos(\Theta/2)\,. \tag{C.20}$$

For a more compact notation and also to allow for a direct comparison with the known results from the real-frequency domain, we write the expressions arising in the saddle-point approximation in terms of the scattering angle Θ. For instance, equation (C.20) precisely corresponds to the saddle-point $\ell_{\mathrm{sp}} = KR\cos(\Theta/2)$ appearing in the asymptotic expansion of the scattering amplitudes at real frequencies [108, 113]. Note that for imaginary frequencies $\cos(\Theta/2)$ is purely imaginary.

In order to find the asymptotic expansion of the scattering amplitudes by means of the saddle-point formula (6.6), we need to evaluate the functions f and $g_{1/2}$ and their derivatives at the saddle point. We find

$$\begin{aligned} f(\Lambda_{\mathrm{sp}}) &= -2\sin(\Theta/2)\,, \\ f''(\Lambda_{\mathrm{sp}}) &= \frac{2}{\sin(\Theta/2)}\,, \\ f'''(\Lambda_{\mathrm{sp}}) &= -\frac{i\sin(\Theta)}{\sin^4(\Theta/2)}\,, \\ f''''(\Lambda_{\mathrm{sp}}) &= -\frac{2[2+\cos(\Theta)]}{\sin^5(\Theta/2)} \end{aligned} \tag{C.21}$$

and

$$\begin{aligned} g_{1/2}(\Lambda_{\mathrm{sp}}) &\sim \mp\left(\frac{x^3\cos(\Theta/2)}{2\pi\sin(\Theta)}\right)^{1/2}\left[1 + g_{1/2}^{(1)}(\Lambda_{\mathrm{sp}})\frac{1}{x}\right], \\ g'_{1/2}(\Lambda_{\mathrm{sp}}) &\sim -\frac{i g_{1/2}(\Lambda_{\mathrm{sp}})}{2\cos(\Theta/2)}\,, \\ g''_{1/2}(\Lambda_{\mathrm{sp}}) &\sim \frac{g_{1/2}(\Lambda_{\mathrm{sp}})}{4\cos^2(\Theta/2)}\,, \end{aligned} \tag{C.22}$$

where

$$g_1^{(1)}(\Lambda_{\mathrm{sp}}) = \frac{25\cos(2\Theta) + 46\cos(\Theta) + 9}{48\sin(\Theta/2)\sin^2(\Theta)},$$
$$g_2^{(1)}(\Lambda_{\mathrm{sp}}) = \frac{\cos(2\Theta) - 50\cos(\Theta) - 63}{48\sin(\Theta/2)\sin^2(\Theta)}.$$

We then arrive at the asymptotic expansion of the scattering amplitudes

$$S_p^{(\mathrm{PR})} = S_{p,\mathrm{WKB}}^{(\mathrm{PR})}\left(1 + s_p^{(\mathrm{PR})}\frac{1}{x} + \mathcal{O}(1/x^2)\right) \tag{C.23}$$

with the geometric optical WKB approximation as the leading term

$$S_{p,\mathrm{WKB}}^{(\mathrm{PR})} = (-1)^p\frac{x}{2}\exp\left(2x\sin(\Theta/2)\right). \tag{C.24}$$

The subleading term has two distinct contributions: one contribution from the leading order saddle-point approximation with the subleading term in the function $g_{1/2}$, and the other contribution from the subleading term in the saddle-point approximation with the leading order term in $g_{1/2}$. The coefficient of the correction to the WKB approximation reads

$$s_1^{(\mathrm{PR})} = \frac{1}{2}\frac{\cos(\Theta)}{\sin^3(\Theta/2)},$$
$$s_2^{(\mathrm{PR})} = -\frac{1}{2}\frac{1}{\sin^3(\Theta/2)}.$$

Dielectric sphere

Now, we consider the case of a dielectric sphere with a finite refractive index n_{sphere}. The asymptotic expansion of the scattering amplitudes can be carried out in the same way as in the perfect reflector case, only that now the asymptotics of the Mie coefficients need to be replaced by the corresponding expressions for a dielectric sphere.

In deriving the asymptotics of the Mie coefficients the same strategy as in the perfect reflector case can be followed. With (A.1) the coefficients (5.19) can be expressed in terms of the modified Bessel functions and their derivatives with the same order λ. We find

$$a_\ell(ix) = (-1)^\ell\frac{\pi}{2}\frac{n^2 s_\ell^{(a)} - s_\ell^{(b)}}{n^2 s_\ell^{(c)} + s_\ell^{(d)}},$$
$$b_\ell(ix) = (-1)^{\ell+1}\frac{\pi}{2}\frac{s_\ell^{(b)} - s_\ell^{(a)}}{s_\ell^{(c)} + s_\ell^{(d)}}$$

with the relative refractive index $n = n_{\text{sphere}}/n_{\text{medium}}$ and

$$\begin{aligned}
s_\ell^{(a)} &= I_\lambda(nx)\left[\frac{1}{2}I_\lambda(x) + xI'_\lambda(x)\right], \\
s_\ell^{(b)} &= I_\lambda(x)\left[\frac{1}{2}I_\lambda(nx) + nxI'_\lambda(nx)\right], \\
s_\ell^{(c)} &= -I_\lambda(nx)\left[\frac{1}{2}K_\lambda(x) + xK'_\lambda(x)\right], \\
s_\ell^{(d)} &= K_\lambda(x)\left[\frac{1}{2}I_\lambda(nx) + nxI'_\lambda(nx)\right].
\end{aligned}$$

where again $\lambda = \ell + 1/2$.

Using the Debye asymptotic expansion (A.3), the asymptotics of the Mie coefficients reads

$$\begin{aligned}
a_\ell(ix) &\sim (-1)^\ell \frac{1}{2}\frac{n^2\sqrt{1+\Lambda^2} - \sqrt{n^2+\Lambda^2}}{n^2\sqrt{1+\Lambda^2} + \sqrt{n^2+\Lambda^2}} \exp(\psi)\left(1 + a^{(1)}\frac{1}{x} + \mathcal{O}(x^{-2})\right), \\
b_\ell(ix) &\sim (-1)^{\ell+1}\frac{1}{2}\frac{\sqrt{n^2+\Lambda^2} - \sqrt{1+\Lambda^2}}{\sqrt{n^2+\Lambda^2} + \sqrt{1+\Lambda^2}} \exp(\psi)\left(1 + b^{(1)}\frac{1}{x} + \mathcal{O}(x^{-2})\right)
\end{aligned}$$

with $\Lambda = \lambda/x$, ψ as defined in (C.14) and

$$\begin{aligned}
a^{(1)} &= \frac{1}{4}\frac{1}{\sqrt{1+\Lambda^2}} + \frac{7}{12}\frac{\Lambda^2}{(1+\Lambda^2)^{3/2}} \\
&\quad + \frac{\Lambda^2}{(n^2-1)[n^2+(n^2+1)\Lambda^2]}\left(\frac{n^2+\Lambda^2}{(1+\Lambda^2)^{3/2}} - \frac{n^2\sqrt{1+\Lambda^2}}{n^2+\Lambda^2}\right), \\
b^{(1)} &= \frac{1}{4}\frac{1}{\sqrt{1+\Lambda^2}} - \frac{5}{12}\frac{\Lambda^2}{(1+\Lambda^2)^{3/2}} + \frac{\Lambda^2}{n^2-1}\left(\frac{\sqrt{1+\Lambda^2}}{n^2+\Lambda^2} - \frac{1}{\sqrt{1+\Lambda^2}}\right).
\end{aligned}$$

In the limit $n \to i\infty$, the asymptotics of the Mie coefficients indeed coincides with the expressions from the perfect reflector limit (C.16).

Because the exponential in the asymptotics of the Mie coefficients is the same as in the perfect reflector case, the function f in the saddle-point formula is also the same. Carrying out the saddle-point integral, we find the asymptotic expansion for the scattering amplitudes

$$S_p \sim \frac{x}{2} r_p((\pi-\Theta)/2)\exp(2x\sin(\Theta/2))\left(1 + s_p\frac{1}{x} + \mathcal{O}(1/x^2)\right), \tag{C.25}$$

where r_p are the Fresnel coefficients (3.3) with $p = 1, 2$ corresponding to TE and TM modes, respectively, and

$$\begin{aligned}
s_1 &= s_1^{(\text{PR})} + \frac{1/s}{c^2 + s\sqrt{n^2-c^2}} - \frac{2n^2-c^2}{2(n^2-c^2)^{3/2}}, \\
s_2 &= s_2^{(\text{PR})} + \frac{1/s}{c^2 - s\sqrt{n^2-c^2}} - \frac{c^2}{s^3}\frac{2n^4s^2 - n^2c^2(1+s^2-s^4) + c^6}{(n^2-c^2)(n^2s^2-c^2)^2} \\
&\quad + \frac{n^2}{2(n^2-c^2)^{3/2}}\frac{2n^4 - n^2c^2(1+c^2) - c^4}{(n^2s^2-c^2)^2}
\end{aligned} \tag{C.26}$$

with the abbreviations

$$s \equiv \sin(\Theta/2)\,, \quad c \equiv \cos(\Theta/2)\,. \tag{C.27}$$

Notice that our result for the correction as given in (C.26) differs from those obtained in Ref. [110] or [111]. The results from those references does not agree mutually either for dielectric spheres. In Sec. 7.5, we numerically verify that our expressions correspond indeed to the correct asymptotic expansion of the scattering amplitudes.

For a comparison, we give their results in our notation. Khare's expression reads [110, §7.A]

$$\begin{aligned} s_1^{(\text{Khare})} &= s_1^{(\text{PR})} + \frac{1/s}{c^2 + s\sqrt{n^2-c^2}} - \frac{1}{2}\frac{2n^2-c^2}{(n^2-c^2)^{3/2}}\,, \\ s_2^{(\text{Khare})} &= s_2^{(\text{PR})} + \frac{2/s}{c^2 - s\sqrt{n^2-c^2}} - \frac{2c^2}{s^2}\frac{2n^4s^2 - n^2c^2(1+s^2-s^4)+c^6}{(n^2-c^2)(n^2s^2-c^2)^2} \\ &\quad + \frac{n^2 s}{(n^2-c^2)^{3/2}}\frac{2n^4 - n^2c^2(1+c^2)-c^4}{(n^2s^2-c^2)^2} \end{aligned} \tag{C.28}$$

and Grandy Jr. writes [111, §5.2]

$$\begin{aligned} s_1^{(\text{Grandy Jr.})} &= s_1^{(\text{PR})} + \frac{1/s^2}{c^2 + s\sqrt{n^2-c^2}} - \frac{1}{2}\frac{2n^2-c^2}{(n^2-c^2)^{3/2}}\,, \\ s_2^{(\text{Grandy Jr.})} &= s_2^{(\text{PR})} + \frac{2/s}{c^2 + s\sqrt{n^2-c^2}} - \frac{2c^2}{s^2}\frac{2n^4s^2 - n^2c^2(1+s^2-s^4)+c^6}{(n^2-c^2)(n^2s^2-c^2)^2} \\ &\quad + \frac{n^2 s}{(n^2-c^2)^{3/2}}\frac{2n^4 - n^2c^2(1+c^2)-c^4}{(n^2s^2-c^2)^2}\,. \end{aligned} \tag{C.29}$$

Vanishing frequencies

Recall that, in the low-frequency limit, the reflection matrix elements contain the scaled scattering amplitudes

$$\begin{aligned} \tilde{S}_1 &\sim \sum_{\ell=1}^{\infty} \mathcal{B}_\ell^{\text{model}} \frac{y^{2\ell}}{(2\ell)!}\,, \\ \tilde{S}_2 &\sim \sum_{\ell=1}^{\infty} \mathcal{A}_\ell^{\text{model}} \frac{y^{2\ell}}{(2\ell)!}\,, \end{aligned}$$

where $y = R\sqrt{2(k_1k_2 + \mathbf{k}_1\cdot\mathbf{k}_2)}$ and the coefficients $\mathcal{A}_\ell^{\text{model}}$ and $\mathcal{B}_\ell^{\text{model}}$ depend on the modeling of the sphere material and are given in Table 5.1 on page 48.

For large spheres, i.e. when $y \gg 1$, the dominant contributions to the scaled scattering amplitudes come from large momenta $\ell \gg 1$. Like in the derivation of the asymptotics for finite imaginary frequencies, we replace the sum over ℓ by an integral

$$\sum_{\ell=1}^{\infty} \to \int_{1/2}^{\infty} \mathrm{d}\ell\,. \tag{C.30}$$

Using the leading order Stirling approximation for the factorial,

$$n! \sim \sqrt{2\pi n}\left(\frac{n}{e}\right)^n\,, \tag{C.31}$$

the scaled scattering amplitudes can be expressed as

$$\tilde{S}_p \sim \frac{y}{2}\int_{1/y}^{\infty} d\Lambda\, g_p(\Lambda) e^{-y f(\Lambda)}\,, \tag{C.32}$$

where we have made the change of variables $\Lambda = 2\ell/y$. The functions f and g read

$$f(\Lambda) = \Lambda\left[\log(\Lambda) - 1\right] \tag{C.33}$$

and

$$g_1(\Lambda) = \frac{\mathcal{B}^{\text{model}}_{y\Lambda/2}}{\sqrt{2\pi y\Lambda}}\,, \tag{C.34}$$

$$g_2(\Lambda) = \frac{\mathcal{A}^{\text{model}}_{y\Lambda/2}}{\sqrt{2\pi y\Lambda}}\,. \tag{C.35}$$

The approximation of the scattering amplitudes as given in Eq. (C.32) is suitable for a saddle-point approximation where y plays the role of the large parameter. The saddle-point condition $f'(\Lambda_{\text{sp}}) = 0$ yields $\Lambda_{\text{sp}} = 1$. At this saddle point, the function f takes the value $f(\Lambda_{\text{sp}}) = 1$ which corresponds to a minimum since the second derivative is positive, $f''(\Lambda_{\text{sp}}) = 1$. To leading order in the saddle-point approximation (6.6) we then find

$$\tilde{S}_1 \sim \frac{1}{2}\mathcal{B}^{\text{model}}_{y/2} e^{y}\,, \tag{C.36a}$$

$$\tilde{S}_2 \sim \frac{1}{2}\mathcal{A}^{\text{model}}_{y/2} e^{y}\,. \tag{C.36b}$$

In the remaining part of this appendix, it is shown that the leading order asymptotic behavior of the scattering amplitudes $S_p = x\tilde{S}_p$ agrees with theWKB approximation

$$\tilde{S}_p \sim \frac{1}{2} r_p((\pi - \Theta)/2)\exp(2x\sin(\Theta/2)) \tag{C.37}$$

evaluated at $\xi = 0$. We start out by showing that the exponential functions agree for both expressions. Namely, in the limit of vanishing frequencies, the exponent in the exponential function can be expressed as

$$2x\sin(\Theta/2) = \sqrt{-2x^2\cos(\Theta)} = R\sqrt{2(k_1k_2 + \mathbf{k}_1\cdot\mathbf{k}_2)} = y\,. \tag{C.38}$$

Finally, it needs to be shown that the coefficients $\mathcal{A}^{\text{model}}_{y/2}$ and $\mathcal{B}^{\text{model}}_{y/2}$ reproduce the corresponding Fresnel coefficients in the low-frequency limit when expanded for $y \gg 1$.

When the coefficients $\mathcal{A}^{\text{model}}_{y/2}$ and $\mathcal{B}^{\text{model}}_{y/2}$ are equal to 1 or 0, there is nothing to do and they already agree with the corresponding Fresnel coefficients. Furthermore, by expanding the coefficients for perfect reflectors

$$\mathcal{B}^{(\text{PR})}_{y/2} = -\frac{y}{y+2} \sim -1 + \mathcal{O}(1/y) \tag{C.39}$$

and dielectrics

$$\mathcal{A}^{(\text{diel.})}_{y/2} = \frac{\varepsilon(0)-1}{\varepsilon(0)+2/y} \sim \frac{\varepsilon(0)-1}{\varepsilon(0)+1} + \mathcal{O}(1/y)\,, \tag{C.40}$$

we see that they agree to leading order with the corresponding Fresnel coefficients in (3.10) and (3.24). The coefficient $\mathcal{B}_\ell$ for the plasma model requires more work. Using A.1, we can express it as

$$\mathcal{B}_\ell^{(\text{plasma})} = -\frac{\ell}{\ell+1}\frac{\alpha I'_\lambda(\alpha) - \lambda I_\lambda(\alpha)}{\alpha I'_\lambda(\alpha) + \lambda I_\lambda(\alpha)} \tag{C.41}$$

with $\alpha = R\omega_p/c$. For $\lambda = \ell + 1/2 \gg 1$, we can employ the Debye asymptotic expansion (A.6). After setting $\lambda = y/2$, we find

$$\mathcal{B}_{y/2}^{(\text{plasma})} \sim \frac{y/2 - \sqrt{(y/2)^2+\alpha^2}}{y/2 + \sqrt{(y/2)^2+\alpha^2}}(1 + \mathcal{O}(1/y))\,. \tag{C.42}$$

Using that

$$\mathcal{K}\cos((\pi-\Theta)/2) = \mathcal{K}\sin(\Theta/2) = y/2R\,, \tag{C.43}$$

we find that the leading order term of $\mathcal{B}_{y/2}^{(\text{plasma})}$ is precisely the TE-Fresnel coefficient (3.3) at the incident angle $\theta_i = (\pi - \Theta)/2$ in the low-frequency limit when the plasma model is assumed.

Appendix D

Supplementary material for chapter 6

D.1 Uniqueness of the saddle-point condition

Here, we derive the saddle points of the $2r$-dimensional integral defined in Eq. (6.10). They are given by the points which minimize the function f defined in (6.11). We recall that f is composed of a sum over the functions

$$\eta_{j,j+1} = \kappa_j + \kappa_{j+1} - \sqrt{2\left[\mathcal{K}^2 + \kappa_j\kappa_{j+1} + \mathbf{k}_j \cdot \mathbf{k}_{j+1}\right]}\,. \tag{D.1}$$

It is thus enough to find a condition under which all $\eta_{j,j+1}$ are minimized simultaneously.

This condition can be found by successive application of inequalities. We start out by estimating the scalar-product as

$$\mathbf{k}_j \cdot \mathbf{k}_{j+1} \leq k_j k_{j+1}\,, \tag{D.2}$$

where equality holds if $\mathbf{k}_j$ and $\mathbf{k}_{j+1}$ are parallel. We then have

$$\eta_{j,j+1} \geq \kappa_j + \kappa_{j+1} - \sqrt{2\left[\mathcal{K}^2 + \kappa_j\kappa_{j+1} + k_j k_{j+1}\right]}\,. \tag{D.3}$$

Next, we make use of the inequality

$$\mathcal{K}^2 + k_j k_{j+1} \leq \kappa_j\kappa_{j+1} \tag{D.4}$$

where equality holds if $k_j = k_{j+1}$. This is true because after squaring, (D.4) becomes equivalent to $(k_j + k_{j+1})^2 \geq 0$. Together with the inequality of arithmetic and geometric means,

$$\frac{x+y}{2} \geq \sqrt{xy} \tag{D.5}$$

with equality if and only if $x = y$, we find that

$$\eta_{j,j+1} \geq 0\,. \tag{D.6}$$

The functions $\eta_{j,j+1}$ are thus minimized when $\mathbf{k}_j = \mathbf{k}_{j+1}$. Thus, the saddle-points are given by the condition

$$\mathbf{k}_0 = \cdots = \mathbf{k}_{2r-1}\,. \tag{D.7}$$

Note that the derivation entails that this saddle-point condition is unique and, therefore, there are no other points which minimize f.

D.2 Hessian matrix for Fourier transformed variables

For the asymptotic expansion of the Casimir energy, the Hessian matrix for the Fourier transformed variables is needed. After the change of variables, the Hessian becomes $\tilde{\mathsf{H}} = \mathsf{W}^T \mathsf{H} \mathsf{W}$ where, for the geometry of two spheres, the Hessian matrix is a $2r \times 2r$ matrix of the form

$$\mathsf{H} = \begin{pmatrix} a+b & -a & & & -b \\ -a & a+b & -b & & \\ & -b & \ddots & \ddots & \\ & & \ddots & \ddots & -a \\ -b & & & -a & a+b \end{pmatrix} \tag{D.8}$$

with $a, b > 0$ and the matrix elements not shown are zero. The Fourier matrix is given by

$$\mathsf{W}_{jk} = \frac{1}{\sqrt{2r}} \exp\left(\frac{2\pi i j k}{2r}\right) \tag{D.9}$$

for $j, k = 0, \ldots, 2r-1$.

Note that the Hessian matrix is composed of blocks of the form

$$\mathsf{M} = \begin{pmatrix} 1 & -1 & 0 & \ldots & 0 \\ -1 & 1 & 0 & & \\ 0 & 0 & 0 & \ddots & \vdots \\ \vdots & & \ddots & \ddots & 0 \\ 0 & & \ldots & 0 & 0 \end{pmatrix} \tag{D.10}$$

which are shifted along the diagonal. Those shifts can be expressed in terms of transformations with the permutation matrix

$$\mathsf{Z} = \begin{pmatrix} 0 & 1 & & & \\ & 0 & 1 & & \\ & & \ddots & \ddots & \\ & & & 0 & 1 \\ 1 & & & & 0 \end{pmatrix}. \tag{D.11}$$

For the blocks containing the parameter a and b, the transformation is applied an even and odd number of times, respectively. The Hessian matrix can thus be written as

$$\mathsf{H} = \sum_{n=0}^{r-1} \left[a \left(\mathsf{Z}^{2n}\right)^T \mathsf{M} \mathsf{Z}^{2n} + b \left(\mathsf{Z}^{2n+1}\right)^T \mathsf{M} \mathsf{Z}^{2n+1} \right]. \tag{D.12}$$

Using that the permutation matrix is diagonal after Fourier transform

$$\mathsf{W}^\dagger \mathsf{Z} \mathsf{W} = \mathsf{D}, \quad \mathsf{D} = \operatorname{diag}\left(\omega^0, \omega^1, \ldots, \omega^{2r-1}\right) \tag{D.13}$$

with $\omega = \exp(\pi i / r)$, and that the Fourier matrix is unitary $W^\dagger W = 1$, we can express the Hessian matrix for the transformed variables as

$$\tilde{\mathsf{H}} = \sum_{n=0}^{r-1} \left[a \mathsf{D}^{2n} \tilde{\mathsf{M}} \mathsf{D}^{2n} + b \mathsf{D}^{2n+1} \tilde{\mathsf{M}} \mathsf{D}^{2n+1} \right], \tag{D.14}$$

where $\tilde{\mathsf{M}} = \mathsf{W}^T \mathsf{M} \mathsf{W}$ with

$$\tilde{\mathsf{M}}_{jk} = \left(\mathsf{W}_{j,0} - \mathsf{W}_{j,1}\right)\left(\mathsf{W}_{k,0} - \mathsf{W}_{k,1}\right) . \tag{D.15}$$

The matrix elements of the transformed Hessian can be further expressed as

$$\tilde{\mathsf{H}}_{jk} = \left[a + b\exp(\pi i(j+k)/r)\right] \tilde{\mathsf{M}}_{jk} \sum_{n=0}^{r-1} \exp(2\pi i(j+k)n/r) , \tag{D.16}$$

where the sum over n can be evaluated yielding

$$\tilde{\mathsf{H}}_{jk} = r\left[a + (-1)^m b\right] \tilde{\mathsf{M}}_{jk} \tag{D.17}$$

if $j + k = mr$ for $m = 0, 1, 2, 3$. Otherwise the matrix elements vanish. Expressing $\tilde{\mathsf{M}}_{jk}$ in terms of trigonometric functions, we finally obtain

$$\tilde{\mathsf{H}}_{jk} = \begin{cases} 2i(b-a)\sin(\pi k/2r)\cos(\pi k/2r) & \text{for } j+k = r, 3r \\ 2(a+b)\sin^2(\pi k/2r) & \text{for } j+k = 0, 2r \\ 0 & \text{else} \end{cases} . \tag{D.18}$$

Appendix E

Derivation of the next-to-leading-order term in the saddle-point approximation

In this appendix, we present more details on the calculation of the NTLO term in the saddle-point approximation. Specifically, we calculate the contribution

$$g_{ij}\tilde{\mathsf{H}}^{ij} - \frac{1}{4}g_{\mathrm{sp}}f_{ijkl}\tilde{\mathsf{H}}^{ij}\tilde{\mathsf{H}}^{kl} + \frac{1}{6}g_{\mathrm{sp}}f_{ijk}f_{lmn}\tilde{\mathsf{H}}^{il}\tilde{\mathsf{H}}^{jm}\tilde{\mathsf{H}}^{kn} \equiv U^{(i)} + U^{(ii)} \tag{E.1}$$

which is relevant for the geometric optical correction to the trace of the r-th round trip in (6.48). Here, the same notation for the indices is used as in the main text in Sec. 6.4.

The term (E.1) is split into the two contributions $U^{(i)}$ and $U^{(ii)}$. This splitting is chosen such that $U^{(ii)}$ will only contain derivatives on the polarization transformation coefficients A, B, C and D and all other functions are evaluated at the saddle-point manifold, while for $U^{(i)}$ the polarization transformation coefficients are evaluated at the saddle-point manifold and derivatives are taken on the remaining functions. For convenience, the functions $U^{(i)}$ and $U^{(ii)}$ are further expressed as

$$U^{(i)} = U^{(i,0)} + \sum_p \left(U_p^{(i,1)} + U_p^{(i,2)}\right) \tag{E.2}$$

and

$$U^{(ii)} = U^{(ii,0)} + \sum_p \left(U_p^{(ii,1)} + U_p^{(ii,2)}\right) . \tag{E.3}$$

In the following, the splitting of (E.1) into the two contributions $U^{(i)}$ and $U^{(ii)}$ will be justified, and the terms constituting those two contributions will be defined.

Using the fact that single derivatives on symmetric functions with respect to the momenta $\mathbf{k}_j$ vanish (see Lemma 1.1 in App. E.5), we can split the second derivative of g as of (6.13) into two parts:

$$\begin{aligned} g_{ij} = \sum_p \left(r_p^{(1)} r_p^{(2)}\right)^r \left(\prod_{l=0}^{2r-1} \frac{e^{-\kappa_l L}}{\kappa_l}\right)_{ij} \\ + \frac{e^{-2r\kappa_{\mathrm{sp}}L}}{(\kappa_{\mathrm{sp}})^{2r}} \left(\sum_{p_0,\dots,p_{2r-1}} \prod_{l=0}^{r-1} \rho^{(1)}_{p_{2j+1},p_{2j}}(\mathbf{k}_{2j+1},\mathbf{k}_{2j})\rho^{(2)}_{p_{2j},p_{2j-1}}(\mathbf{k}_{2j},\mathbf{k}_{2j-1})\right)_{ij} , \end{aligned} \tag{E.4}$$

where it was used that $\rho^{(s)}_{pp'}|_{\rm sp} = r^{(s)}_p$ if $p = p'$ and $\rho^{(s)}_{pp'} = 0$ otherwise. Using Lemma 1.2 from App. E.5, the first term in (E.4) can be expressed as

$$\sum_p \left(r^{(1)}_p r^{(2)}_p\right)^r \left(\prod_{l=0}^{2r-1} \frac{e^{-\kappa_l L}}{\kappa_l}\right)_{ij} = -g_{\rm sp} \sum_{l=0}^{2r-1} (\kappa_l L + \log(\kappa_l))_{ij} \,. \tag{E.5}$$

Due to the evaluation at the saddle-point, $(\kappa_l L + \log(\kappa_l))_{ij}$ does not depend on the index l and thus the sum over l yields a factor of $2r$. Together with the contributions from the derivatives of the function f in (E.1), we define

$$U^{(i,0)} = g_{\rm sp} V \quad \text{with} \quad V = V_1 - \frac{V_2}{4} + \frac{V_3}{6} \tag{E.6}$$

where

$$\begin{aligned} V_1 &= -2r(\kappa_l L + \log(\kappa_l))_{ij} \tilde{\mathsf{H}}^{ij} \,, \\ V_2 &= f_{ijkl} \tilde{\mathsf{H}}^{ij} \tilde{\mathsf{H}}^{kl} \,, \\ V_3 &= f_{ijk} f_{lmn} \tilde{\mathsf{H}}^{il} \tilde{\mathsf{H}}^{jm} \tilde{\mathsf{H}}^{kn} \,. \end{aligned}$$

The remaining contributions to $U^{(i)}$ and $U^{(ii)}$ come from the second term in (E.4). We can further split this contribution into those terms for which the polarization is conserved for each reflection and into those for which polarization change is allowed.

Using Lemma 1.2 in App. E.5, the contributions in the second term of (E.4) corresponding to the polarization preserving terms can be expressed as

$$\sum_{s=1,2} \sum_p g_p \sum_{l=0}^{r-1} \left[\log\left(\rho^{(s)}_{pp}\right)\right]_{ij} \,. \tag{E.7}$$

In view of (E.20), it is important to keep track of the arguments of the function $\rho^{(s)}_{pp}$. The argument is $(\mathbf{k}_{2l+1}, \mathbf{k}_{2l})$ for $s = 1$ and $(\mathbf{k}_{2l}, \mathbf{k}_{2l-1})$ for $s = 2$. Using the fact that single derivatives on A and B vanish,

$$\left.\frac{\partial A}{\partial k_{j,\alpha}}\right|_{\rm sp} = \left.\frac{\partial B}{\partial k_{j,\alpha}}\right|_{\rm sp} = 0 \,, \tag{E.8}$$

which can be seen by the representation of A and B in (5.10) in terms of the angles, we can write

$$\left(\rho^{(s)}_{pp}\right)_{ij} = \left(r^{(s)}_p\right)_{ij} + r^{(s)}_p A_{ij} + r^{(s)}_{\bar{p}} B_{ij} \tag{E.9}$$

where $\bar{p}$ is the opposite polarization to p, i.e. $\bar{p} = \text{TE}$ when $p = \text{TM}$ and vice versa. Since further

$$\left(\rho^{(s)}_{pp}\right)_i = \left(r^{(s)}_p\right)_i \,, \tag{E.10}$$

we can write

$$\left[\log\left(\rho^{(s)}_{pp}\right)\right]_{ij} = \left[\log\left(r^{(s)}_p\right)\right]_{ij} + A_{ij} + \frac{r^{(s)}_{\bar{p}}}{r^{(s)}_p} B_{ij} \,. \tag{E.11}$$

Noting that the sum over l in (E.7) yields a factor of r, we can summarize those contributions to (E.1) as

$$U_p^{(i,s)} = r g_p \left[\log\left(r_p^{(s)}\right)\right]_{ij} \tilde{\mathsf{H}}^{ij},$$
$$U_p^{(ii,s)} = r\left(A_{ij} + \frac{r_{\bar{p}}^{(s)}|_{\mathrm{sp}}}{r_p^{(s)}|_{\mathrm{sp}}} B_{ij}\right) \tilde{\mathsf{H}}^{ij},$$

where the functions $r_p^{(s)}$, A and B depend on $(\mathbf{k}_{2l+1}, \mathbf{k}_{2l})$ for $s = 1$ and $(\mathbf{k}_{2l}, \mathbf{k}_{2l-1})$ for $s = 2$.

The remaining contribution comes from the terms which take polarization mixing into account. These terms are proportional to the polarization transformation coefficients C and D. Due to the trace in (6.10), the polarization can only change an even number of times upon reflection on the spheres. Since $C = D = 0$ at the saddle-point, the terms with four or more polarization changes vanish in the NTLO term to the saddle-point contribution. For the remaining term, the polarization change occurs exactly twice. It may only contribute when the derivatives with respect to the transformed variables acts on the functions C and D. We denote this contribution as $U^{(ii,0)}$.

Before we calculate the contributions constituting $U^{(i)}$ and $U^{(ii)}$ in (E.2) and (E.3), respectively, we introduce a differential operator, which frequently appears in the calculations, in the following section.

E.1 A differential operator and the chain rule

Since in the terms in the NTLO saddle-point contributions a second order derivative is always coupled to the inverse Hessian, it is convenient to define the differential operator

$$D \equiv \sum_{i,j=1}^{r-1} \left(\tilde{\mathsf{H}}^{-1}\right)_{ij} \frac{\partial^2}{\partial v_{i,\alpha} \partial v_{j,\alpha}} \tag{E.12}$$

for $\alpha = x, y$.

Because the functions f and g are defined with respect to the variables $k_{j,\alpha}$, we make use of the chain rule

$$\frac{\partial}{\partial v_{l,\alpha}} = \sum_{l=1}^{2r-1} W_{j,l} \frac{\partial}{\partial k_{j,\alpha}}. \tag{E.13}$$

The sums in (E.12) can then be performed leading to a simplified expression for D in terms of derivatives with respect to the variables $k_{j,\alpha}$.

In the following part of this section, we drop the index α and introduce the shorthand notation for the derivatives

$$\tilde{\partial}_j \equiv \frac{\partial}{\partial v_{j,\alpha}} \quad \text{and} \quad \partial_j \equiv \frac{\partial}{\partial k_{j,\alpha}}. \tag{E.14}$$

We start out by expressing (E.12) in terms of the non-vanishing matrix elements of the inverse Hessian (6.45) and (6.46). The second order derivatives can then be split into three parts

$$D = D_1 + D_2 + D_3 \tag{E.15}$$

with

$$D_1 \equiv \tilde{\mathsf{H}}^{-1}_{r,r}\tilde{\partial}_r\tilde{\partial}_r = \frac{\kappa_{\mathrm{sp}}}{R_1+R_2}\tilde{\partial}_r\tilde{\partial}_r\,,$$

$$D_2 \equiv \sum_{j=1}^{r-1}\left[\tilde{\mathsf{H}}^{-1}_{j,r-j}\tilde{\partial}_j\tilde{\partial}_{r-j} + \tilde{\mathsf{H}}^{-1}_{r+j,2r-j}\tilde{\partial}_{r+j}\tilde{\partial}_{2r-j}\right] = -i\frac{\kappa_{\mathrm{sp}}(R_1-R_2)}{4R_1R_2}\sum_{j=1}^{r-1}\frac{1}{s_jc_j}\left(\tilde{\partial}_j\tilde{\partial}_{r-j} - \tilde{\partial}_{r+j}\tilde{\partial}_{2r-j}\right)\,,$$

$$D_3 \equiv \sum_{j=1}^{r-1}\left[\tilde{\mathsf{H}}^{-1}_{j,2r-j}\tilde{\partial}_j\tilde{\partial}_{2r-j} + \tilde{\mathsf{H}}^{-1}_{r+j,r-j}\tilde{\partial}_{r+j}\tilde{\partial}_{r-j}\right] = \frac{\kappa_{\mathrm{sp}}}{2R_{\mathrm{eff}}}\sum_{j=1}^{r-1}\frac{1}{s_j^2}\tilde{\partial}_j\tilde{\partial}_{2r-j}\,,$$

where we have used in the last line that the second term proportional to $\tilde{\mathsf{H}}^{-1}_{r+j,r-j}$ is equal to the first one. This can be seen by reversing the summation over j.

The next step is to employ the chain rule (E.13). The first term D_1 then becomes

$$\begin{aligned} D_1 &= \frac{\kappa_{\mathrm{sp}}}{R_1+R_2}\sum_{m,n=0}^{2r-1} W_{m,r}W_{n,r}\partial_m\partial_n \\ &= \frac{\kappa_{\mathrm{sp}}}{2r(R_1+R_2)}\sum_{m,n=0}^{2r-1}(-1)^{m+n}\partial_m\partial_n\,, \end{aligned}$$

where we have used in the second line that $W_{n,r} = (-1)^n/\sqrt{2r}$. Likewise, the second term D_2 can be expressed as

$$\begin{aligned} D_2 &= -i\frac{\kappa_{\mathrm{sp}}(R_1-R_2)}{4R_1R_2}\sum_{m,n=0}^{2r-1}\sum_{j=1}^{r-1}\frac{1}{s_jc_j}\left(W_{m,j}W_{n,r-j} - W_{m,2r-j}W_{n,r+j}\right)\partial_n\partial_m \\ &= \frac{\kappa_{\mathrm{sp}}(R_1-R_2)}{2rR_1R_2}\sum_{m,n=0}^{2r-1}(-1)^n\sum_{j=1}^{r-1}\frac{\sin\left(\pi j(m-n)/r\right)}{\sin(\pi j/r)}\partial_n\partial_m\,. \end{aligned}$$

Using the identities (E.87) and (E.88) the summation over j can be performed and we find

$$D_2 = \frac{\kappa_{\mathrm{sp}}(R_1-R_2)}{2rR_1R_2}\sum_{m,n=0}^{2r-1}(-1)^n d_2(m-n)\partial_m\partial_n \tag{E.16}$$

with the $2r$-periodic function

$$d_2(k) = \begin{cases} r-k & \text{for } k \text{ odd} \\ 0 & \text{else} \end{cases} \tag{E.17}$$

for $k = 0,\ldots,2r-1$. Note that d_2 is anti-symmetric, i.e. $d_2(-k) = -d_2(k)$.

Making use of the chain rule, the third term D_3 can be written as

$$\begin{aligned} D_3 &= \frac{\kappa_{\mathrm{sp}}}{2R_{\mathrm{eff}}}\sum_{m,n=0}^{2r-1}\sum_{j=1}^{r-1}\frac{W_{m,j}W_{n,2r-j}}{s_j^2}\partial_m\partial_n \\ &= \frac{\kappa_{\mathrm{sp}}}{4rR_{\mathrm{eff}}}\sum_{m,n=0}^{2r-1}\sum_{j=1}^{r-1}\frac{\cos\left(\pi j(m-n)/r\right)}{\sin^2(\pi j/2r)}\partial_m\partial_n\,, \end{aligned}$$

where we have used in the last line that the imaginary parts of the complex exponentials cancel out due to the commutivity of the partial derivatives. The sum over

j can be performed using (E.89) and we obtain

$$D_3 = \frac{\kappa_{\mathrm{sp}}}{8rR_{\mathrm{eff}}} \sum_{m,n=0}^{2r-1} d_3(m-n)\partial_m\partial_n \tag{E.18}$$

with the $2r$-periodic function

$$d_3(k) = \frac{1}{3}\left(4r^2 - 12kr + 6k^2 - 1\right) - (-1)^k \tag{E.19}$$

for $k = 0, \ldots, 2r$. The function d_3 is symmetric, i.e. $d_3(-k) = d_3(k)$.

Summing up the expressions for D_1, D_2 and D_3, the differential operator (E.12) can be written as

$$D = \sum_{i,j=1}^{r-1} \left(\tilde{\mathsf{H}}^{-1}\right)_{ij} \frac{\partial^2}{\partial v_{i,\alpha}\partial v_{j,\alpha}} = \sum_{m,n=0}^{2r-1} d_\sigma(m-n) \frac{\partial^2}{\partial k_{m,\alpha}\partial k_{n,\alpha}} \tag{E.20}$$

for $\alpha = x, y$. The function d_σ is $2r$-periodic and defined as

$$d_\pm(k) = \frac{\kappa_{\mathrm{sp}}}{2r}\left[(-1)^k \frac{1}{R_1+R_2} \pm d_2(k)\frac{R_1-R_2}{R_1R_2} + \frac{d_3(k)}{4R_{\mathrm{eff}}}\right] \tag{E.21}$$

for $k = 0, \ldots, 2r$, where $\sigma = +$ is used when n is even and $\sigma = -$ when n is odd. The functions d_2 and d_3 as defined in (E.17) and (E.19), respectively. Since d_3 is symmetric and d_2 anti-symmetric, negative arguments of d_σ can be expressed in terms of positive arguments by flipping the sign σ, i.e.

$$d_\pm(-k) = d_\mp(k)\,. \tag{E.22}$$

When k is even, d_2 vanishes and thus the sign σ is dispensable. In this case, we will thus write $d(k)$ instead of $d_\sigma(k)$.

Most often, the coefficients $d_\sigma(k)$ are needed when $k = 0$ or 1. In these cases, the coefficients read

$$d(0) = \frac{\kappa_{\mathrm{sp}}}{2r}\left(\frac{1}{R_1+R_2} + \frac{r^2-1}{3R_{\mathrm{eff}}}\right), \tag{E.23}$$

$$d_\pm(1) = \frac{\kappa_{\mathrm{sp}}}{2r}\left(-\frac{1}{R_1+R_2} \pm (r-1)\frac{R_1-R_2}{R_1R_2} + \frac{(r-1)(r-2)}{3R_{\mathrm{eff}}}\right). \tag{E.24}$$

E.2 Derivation of V

Here, we calculate the contribution

$$V = V_1 - \frac{V_2}{4} + \frac{V_3}{6}\,, \tag{E.25}$$

where the terms

$$\begin{aligned} V_1 &= -\sum_{l=0}^{2r-1} \left(\kappa_l L + \log(\kappa_l)\right)_{ij} \tilde{\mathsf{H}}^{ij}\,, \\ V_2 &= f_{ijkl}\tilde{\mathsf{H}}^{ij}\tilde{\mathsf{H}}^{kl}\,, \\ V_3 &= f_{ijk}f_{lmn}\tilde{\mathsf{H}}^{il}\tilde{\mathsf{H}}^{jm}\tilde{\mathsf{H}}^{kn} \end{aligned} \tag{E.26}$$

are determined in the following subsections.

With the results (E.31), (E.38) and (E.51), we find

$$V = -\frac{rL\kappa_{\mathrm{sp}}(\kappa_{\mathrm{sp}}^2 + \mathcal{K}^2) + \mathcal{K}^2}{3r\kappa_{\mathrm{sp}}^3} \left(\frac{r^2-1}{R_{\mathrm{eff}}} + \frac{3}{R_1+R_2} \right) . \tag{E.27}$$

It is interesting that this expression is proportional to $d(0)$ even though V_2 and V_3 are not. This may be a mere coincidence or a hint on the existence of a representation of the term V for which the differential operator (E.20) is diagonal.

Derivation of V_1

We compute the term

$$V_1 = -2r \sum_{i,j=1}^{2r-1} \left(\tilde{\mathsf{H}}^{-1} \right)_{ij} \sum_{\alpha \in \{x,y\}} \frac{\partial^2 \left(\kappa_l L + \log(\kappa_l) \right)}{\partial v_{i,\alpha} \partial v_{j,\alpha}} . \tag{E.28}$$

Using the identity for the differential operator (E.20), we can write

$$V_1 = -2rd(0) \sum_{\alpha \in \{x,y\}} \frac{\partial^2 (\kappa_l L + \log(\kappa_l))}{\partial k_{l,\alpha} \partial k_{l,\alpha}} \bigg|_{\mathrm{sp}} . \tag{E.29}$$

With $d(0)$ as given in (E.23) and

$$\sum_{\alpha \in \{x,y\}} \frac{\partial^2 (\kappa_l L + \log(\kappa_l))}{\partial k_{l,\alpha} \partial k_{l,\alpha}} \bigg|_{\mathrm{sp}} = \frac{L\kappa_{\mathrm{sp}}(\kappa_{\mathrm{sp}}^2 + \mathcal{K}^2) + 2\mathcal{K}^2}{\kappa_{\mathrm{sp}}^4} , \tag{E.30}$$

we obtain the final result

$$V_1 = -\frac{L\kappa_{\mathrm{sp}}(\kappa_{\mathrm{sp}}^2 + \mathcal{K}^2) + 2\mathcal{K}^2}{\kappa_{\mathrm{sp}}^3} \left(\frac{1}{R_1+R_2} + \frac{r^2-1}{3R_{\mathrm{eff}}} \right) . \tag{E.31}$$

Derivation of V_2

We calculate the expression

$$V_2 = \sum_{\alpha,\beta \in \{x,y\}} \sum_{i,j,m,n=1}^{2r-1} \left(\tilde{\mathsf{H}}^{-1} \right)_{ij} \left(\tilde{\mathsf{H}}^{-1} \right)_{mn} \frac{\partial^4 f}{\partial v_{i,\alpha} \partial v_{j,\alpha} \partial v_{m,\beta} \partial v_{n,\beta}} . \tag{E.32}$$

Using the defining equation (6.11) for f we can split V_2 into two terms and write

$$V_2 = R_1 V_{2,1} + R_2 V_{2,2} . \tag{E.33}$$

Using (E.20), the two terms can be expressed as

$$V_{2,1} = \sum_{p=0}^{r-1} \sum_{i,j,m,n=2p}^{2p+1} d_{\sigma_j}(i-j) d_{\sigma_n}(m-n) e(i,j,m,n) , \tag{E.34}$$

$$V_{2,2} = \sum_{p=0}^{r-1} \sum_{i,j,m,n=2p-1}^{2p} d_{\sigma_j}(i-j) d_{\sigma_n}(m-n) e(i,j,m,n) , \tag{E.35}$$

where

$$e(i,j,m,n) = \sum_{\alpha,\beta=\{x,y\}} \left.\frac{\partial^4 \eta_{2p,2p+1}}{\partial k_{i,\alpha}\partial k_{j,\alpha}\partial k_{m,\beta}\partial k_{n,\beta}}\right|_{\mathrm{sp}} = \sum_{\alpha,\beta=\{x,y\}} \left.\frac{\partial^4 \eta_{2p-1,2p}}{\partial k_{i,\alpha}\partial k_{j,\alpha}\partial k_{m,\beta}\partial k_{n,\beta}}\right|_{\mathrm{sp}} .$$

Note that since the polarization does not play a role in the calculations of this and the following subsection, we use the variable p as an index running from 0 to $r-1$.

Due to the evaluation at the saddle-point manifold, the function e does not depend on the index p and is thus the same for the two terms $V_{2,1}$ and $V_{2,2}$. Depending on the values of i, j, m and n the function e falls into four different classes. These are listed in the second column of Tab. E.1. In the last column of this table the corresponding coefficients for $V_{2,1}$ are given which depend only on $d(0)$ and $d_\pm(\pm 1)$. Because these terms do not depend on the index p, the sum over p yields a factor of r. With property (E.22), we have $d_-(-1) = d_+(1)$. We then obtain

$$V_{2,1} = r\left\{2(e_1+e_4)\left[d(0)\right]^2 + 8e_2 d(0)d_+(1) + 4e_3\left[d_+(1)\right]^2\right\} . \tag{E.36}$$

Because for $V_{2,2}$ the order of the odd and even indices entering the functions d_σ is interchanged compared to $V_{2,1}$, we find an expression for $V_{2,2}$ by flipping the sign σ. By thus replacing $d_+(1)$ with $d_-(1)$ in (E.36), we obtain

$$V_{2,2} = r\left\{2(e_1+e_4)\left[d(0)\right]^2 + 8e_2 d(0)d_-(1) + 4e_3\left[d_-(1)\right]^2\right\} . \tag{E.37}$$

Using (E.23) and (E.24), the final result becomes

$$V_2 = \frac{4}{r\kappa_{\mathrm{sp}}^3}\left[\frac{(r-1)\left[\kappa_{\mathrm{sp}}^2\left(r^2-r+1\right) - 3\mathcal{K}^2 r^2\right]}{3R_{\mathrm{eff}}} - \frac{\mathcal{K}^2 r + \kappa_{\mathrm{sp}}^2(r-1)}{R_1+R_2}\right] . \tag{E.38}$$

Derivation of V_3

Here, we compute the term

$$V_3 = \sum_{\alpha,\beta,\gamma\in\{x,y\}} \sum_{ijklmn} \left(\tilde{\mathsf{H}}^{-1}\right)_{ij}\left(\tilde{\mathsf{H}}^{-1}\right)_{kl}\left(\tilde{\mathsf{H}}^{-1}\right)_{mn} \frac{\partial^3 f}{\partial v_{i,\alpha}\partial v_{k,\beta}\partial v_{m,\gamma}}\frac{\partial^3 f}{\partial v_{j,\alpha}\partial v_{l,\beta}\partial v_{n,\gamma}} , \tag{E.39}$$

where the indices $i,\ldots,n$ run from 1 to $2r-1$.

Since f can be split into two terms for the respective radii, we can express V_3 as a sum of three terms

$$V_3 = R_1^2 V_{3,11} + 2R_1R_2V_{3,12} + R_2^2 V_{3,22} . \tag{E.40}$$

4-tuple	$e(i,j,m,n)$	coefficient
$(0,0,0,0)$	$e_1 \equiv (\kappa_{\rm sp}^2 - 4\mathcal{K}^2)/\kappa_{\rm sp}^5$	$[d(0)]^2$
$(1,1,1,1)$	*	*
$(1,0,0,0)$	$e_2 \equiv \mathcal{K}^2/\kappa_{\rm sp}^5$	$d(0)d_+(1)$
$(0,1,0,0)$	*	*
$(0,0,1,0)$	*	*
$(0,0,0,1)$	*	*
$(0,1,1,1)$	*	$d(0)d_-(-1)$
$(1,0,1,1)$	*	*
$(1,1,0,1)$	*	*
$(1,1,1,0)$	*	*
$(1,0,1,0)$	$e_3 \equiv -(\kappa_{\rm sp}^2 - \mathcal{K}^2)/2\kappa_{\rm sp}^5$	$[d_+(1)]^2$
$(0,1,0,1)$	*	$[d_-(-1)]^2$
$(1,0,0,1)$	*	$d_+(1)d_-(-1)$
$(0,1,1,0)$	*	*
$(1,1,0,0)$	$e_4 \equiv -\mathcal{K}^2/\kappa_{\rm sp}^5$	$[d(0)]^2$
$(0,0,1,1)$	*	*

TABLE E.1: The sixteen terms of $V_{2,1}$ as defined in (E.34) for a given p. The first column represents the 4-tuple of the indices $(i-2p, j-2p, m-2p, n-2p)$ for which the values of the function $e(i,j,m,n)$ are given in the second column. The coefficients represented by a product containing the function $d_\sigma(k)$ is given in last column. The asterisk indicates that the entry is the same as the entry above.

where

$$
\begin{aligned}
V_{3,11} &= \sum_{p,q=0}^{r-1} \sum_{m,n,s=2p}^{2p+1} \sum_{t,u,w=2q}^{2q+1} d_t(m-t)d_u(n-u)d_w(s-w)e_{3,11}(m,n,s;t,u,w) \\
V_{3,12} &= \sum_{p,q=0}^{r-1} \sum_{m,n,s=2p}^{2p+1} \sum_{t,u,w=2q-1}^{2q} d_t(m-t)d_u(n-u)d_w(s-w)e_{3,12}(m,n,s;t,u,w) \\
V_{3,22} &= \sum_{p,q=0}^{r-1} \sum_{m,n,s=2p-1}^{2p} \sum_{t,u,w=2q-1}^{2q} d_t(m-t)d_u(n-u)d_w(s-w)e_{3,22}(m,n,s;t,u,w)
\end{aligned}
\tag{E.41}
$$

with

$$
\begin{aligned}
e_{3,11}(m,n,s;t,u,w) &= \sum_{\alpha,\beta,\gamma\in\{x,y\}} \frac{\partial^3 \eta_{2p,2p+1}}{\partial k_{m,\alpha}\partial k_{n,\beta}\partial k_{s,\gamma}} \frac{\partial^3 \eta_{2q,2q+1}}{\partial k_{t,\alpha}\partial k_{u,\beta}\partial k_{w,\gamma}}\bigg|_{\rm sp} \\
e_{3,12}(m,n,s;t,u,w) &= \sum_{\alpha,\beta,\gamma\in\{x,y\}} \frac{\partial^3 \eta_{2p,2p+1}}{\partial k_{m,\alpha}\partial k_{n,\beta}\partial k_{s,\gamma}} \frac{\partial^3 \eta_{2q-1,2q}}{\partial k_{t,\alpha}\partial k_{u,\beta}\partial k_{w,\gamma}}\bigg|_{\rm sp} \\
e_{3,22}(m,n,s;t,u,w) &= \sum_{\alpha,\beta,\gamma\in\{x,y\}} \frac{\partial^3 \eta_{2p-1,2p}}{\partial k_{m,\alpha}\partial k_{n,\beta}\partial k_{s,\gamma}} \frac{\partial^3 \eta_{2q-1,2q}}{\partial k_{t,\alpha}\partial k_{u,\beta}\partial k_{w,\gamma}}\bigg|_{\rm sp}
\end{aligned}
\tag{E.42}
$$

For given values of p and q each of the terms in (E.41) consists of 64 terms. There are however only three classes of arguments for which the functions in (E.42) do not

vanish.[1] These are given by the functions of the form

$$\begin{aligned} &e_{3,ab}(i_p, i_p, i_p; i_q, i_q, i_q) = e\,, \\ &e_{3,ab}(i_p+1, i_p, i_p; i_q, i_q, i_q) = e_{3,ab}(i_p, i_p, i_p; i_q+1, i_q, i_q) = -\frac{1}{3}e\,, \\ &e_{3,ab}(i_p+1, i_p, i_p; i_q+1, i_q, i_q) = \frac{1}{3}e \end{aligned} \tag{E.43}$$

with

$$e = \frac{3}{4}\frac{k_{\mathrm{sp}}^2}{\kappa_{\mathrm{sp}}^6}\,. \tag{E.44}$$

On the other hand, the vanishing functions are of the form

$$e_{3,ab}(i_p+1, i_p, i_p; i_q, i_q+1, i_q) = e_{3,ab}(i_p+1, i_p, i_p; i_q, i_q, i_q+1) = 0\,. \tag{E.45}$$

The dependencies of the indices i_p and i_q on p and q, respectively, is different for the three functions in (E.42) and will be discussed in more detail below. All other sets of arguments of the functions $e_{3,ab}$ can be reduced to the ones given above by using the following rules. One can perform the replacement $i_p \leftrightarrow i_p + 1$ and/or $i_q \leftrightarrow i_q + 1$ in each triple because the derivatives are evaluated at the saddle point. In this way, the argument $i_p + 1$ or $i_q + 1$ appears at most once. Moreover, the arguments within the two triples can be permuted since the partial derivatives commute. However, one has to perform that permutation simultaneously on both triples, for they are connected through the indices α, β and γ. Utilizing this rule, the argument $i_p + 1$ can be brought to the first position thus ending up with the set of arguments given above.

The coefficients composed of the products of the functions $d_\sigma(k)$ is different for each term in (E.41). In Table E.2 the arguments and values of the function $e_{3,11}$ along with the coefficients of the function $V_{3,11}$ are listed for fixed values of p and q. The function $V_{3,22}$ can be obtained from $V_{3,11}$ by the replacements $2p \leftrightarrow 2p+1$ and $2q \leftrightarrow 2q+1$, which interchanges the role of the even and odd indices. Thus, a corresponding table for the coefficients of $V_{3,22}$ can be obtained from Table E.2 by interchanging $d_+(k) \leftrightarrow d_-(k)$. The coefficients of the function $V_{3,12}$ are not related to the ones of $V_{3,11}$. For fixed values of p and q, they can be found in Table E.3.

Using the tables E.2 and E.3, the tree terms (E.41) can then be expressed as

$$V_{3,ab} = \sum_{p,q=0}^{r-1} A_{ab}(p-q) \tag{E.46}$$

for $ab = 11, 22, 12$ where

$$\begin{aligned} A_{11/22}(c) = e\big\{ &4[d(2c)]^3 + [d_\pm(2c+1)]^3 + [d_\mp(2c-1)]^3 + d_\pm(2c+1)[d_\mp(2c-1)]^2 \\ &+ d_\mp(2c-1)[d_\pm(2c+1)]^2 - 2[d(2c)]^2[d_\pm(2c+1) + d_\mp(2c-1)] \\ &- 2d(2c)\left([d_\pm(2c+1)]^2 + [d_\mp(2c-1)]^2\right)\big\} \end{aligned} \tag{E.47}$$

[1] These function values coincide with the corresponding ones in the plane-sphere geometry as given in Appendix A in Ref. [104].

and

$$\begin{aligned}A_{12}(c) = e\big\{&[d_-(2c+1)]^3 + [d_+(2c+1)]^3 + [d(2c)]^3 + [d(2c+2)]^3\\ &+ [d_-(2c+1) + d_+(2c+1)]\left[d_-(2c+1)d_+(2c+1) - [d(2c)]^2 - [d(2c+2)]^2\right]\\ &+ [d(2c) + d(2c+2)]\left[d(2c)d(2c+2) - [d_-(2c+1)]^2 - [d_+(2c+1)]^2\right]\big\}\,. \end{aligned} \tag{E.48}$$

Because the function d_σ is $2r$-periodic, each term $A_{ab}(c)$ appears r times in (E.46) allowing us to write

$$V_{3,ab} = r\sum_{c=0}^{r-1} A_{ab}(c) \tag{E.49}$$

which is a sum over polynomials in c. Before performing the summation machined, it is convenient to use $d_-(-1) = d_+(1)$ to write

$$A_{11/22}(0) = 4e[d(0) + d_\pm(1)][d(0) - d_\pm(1)]^2\,. \tag{E.50}$$

Then, within the sum in (E.49), the functions d_σ are evaluated at positive arguments $k = 0, \ldots, 2r$ and the $2r$-periodicity does not need to be explicitly implemented. The term $A_{12}(0)$ does not need special attention as the arguments of the coefficients d_σ do not become negative in (E.49).

As the final result we obtain

$$V_3 = \frac{2(r-1)k_{\mathrm{sp}}^2}{r\kappa_{\mathrm{sp}}^3}\left(\frac{r^2-r+1}{R_{\mathrm{eff}}} - \frac{3}{R_1+R_2}\right)\,. \tag{E.51}$$

E.3 Derivation of $U_p^{(i,1)}$ and $U_p^{(i,2)}$

We calculate the terms

$$U_p^{(1/2)} = rg_p \sum_{i,j=1}^{2r-1} \left(\tilde{\mathsf{H}}^{-1}\right)_{ij} \sum_{\alpha=x,y} \left.\frac{\partial^2 \log\left(r_p^{(1/2)}\right)}{\partial v_{i,\alpha}\partial v_{j,\alpha}}\right|_{\mathrm{sp}}\,. \tag{E.52}$$

Here, the Fresnel coefficients are understood as given in (3.3) evaluated at

$$\cos(\theta_i) = \sqrt{\frac{1-\cos(\Theta)}{2}}\,. \tag{E.53}$$

The scattering angle depends on $(\mathbf{k}_{2l+1}, \mathbf{k}_{2l})$ for $s = 1$ and $(\mathbf{k}_{2l}, \mathbf{k}_{2l-1})$ for $s = 2$. Note that the order of the odd and even indices matters for the coefficients of the differential operator (E.20). Using (E.20) and (E.22), we find

$$U_p^{(1/2)} = 2rg_p\left[d(0)Q_{p,0}^{(1/2)} + d_\pm(1)Q_{p,1}^{(1/2)}\right] \tag{E.54}$$

6-tuple	$e_{3,11}(m,n,s;t,u,w)$	coefficient
$(0,0,0;0,0,0)$	e	$[d(2c)]^3$
$(1,1,1;1,1,1)$	*	*
$(1,1,1;0,0,0)$	*	$[d_+(2c+1)]^3$
$(0,0,0;1,1,1)$	*	$[d_-(2c-1)]^3$
$(1,0,0;0,0,0)$	$-e/3$	$d_+(2c+1)\,[d(2c)]^2$
$(0,1,0;0,0,0)$	*	*
$(0,0,1;0,0,0)$	*	*
$(1,1,1;1,1,0)$	*	*
$(1,1,1;1,0,1)$	*	*
$(1,1,1;0,1,1)$	*	*
$(0,0,0;1,0,0)$	*	$d_-(2c-1)\,[d(2c)]^2$
$(0,0,0;0,1,0)$	*	*
$(0,0,0;0,0,1)$	*	*
$(1,1,0;1,1,1)$	*	*
$(1,0,1;1,1,1)$	*	*
$(0,1,1;1,1,1)$	*	*
$(1,1,0;0,0,0)$	*	$d(2c)\,[d_+(2c+1)]^2$
$(1,0,1;0,0,0)$	*	*
$(0,1,1;0,0,0)$	*	*
$(1,1,1;1,0,0)$	*	*
$(1,1,1;0,1,0)$	*	*
$(1,1,1;0,0,1)$	*	*
$(0,0,0;1,1,0)$	*	$d(2c)\,[d_-(2c-1)]^2$
$(0,0,0;1,0,1)$	*	*
$(0,0,0;0,1,1)$	*	*
$(1,0,0;1,1,1)$	*	*
$(0,1,0;1,1,1)$	*	*
$(0,0,1;1,1,1)$	*	*
$(1,0,0;1,0,0)$	$e/3$	$[d(2c)]^3$
$(0,1,0;0,1,0)$	*	*
$(0,0,1;0,0,1)$	*	*
$(0,1,1;0,1,1)$	*	*
$(1,0,1;1,0,1)$	*	*
$(1,1,0;1,1,0)$	*	*
$(1,0,0;0,1,1)$	*	$d_+(2c+1)\,[d_-(2c-1)]^2$
$(0,1,0;1,0,1)$	*	*
$(0,0,1;1,1,0)$	*	*
$(0,1,1;1,0,0)$	*	$d_-(2c-1)\,[d_+(2c+1)]^2$
$(1,0,1;0,1,0)$	*	*
$(1,1,0;0,0,1)$	*	*

TABLE E.2: The non-vanishing terms for $V_{3,11}$ in (E.41). The first column represents the 6-tuple of the indices $(m-2p, n-2p, s-2p; t-2q, u-2q, w-2q)$ and the values of the function $e_{3,11}(m,n,s;t,u,w)$ are given in the second column where $e = 3k_{\rm sp}^2/4\kappa_{\rm sp}^6$. The coefficients represented by a product containing the function $d_\sigma(k)$ is given in last column where the abbreviation $c \equiv p-q$ is used. The asterisk indicates that the table entry is identical to the entry above.

6-tuple	$e_{3,12}(m,n,s;t,u,w)$	coefficient
$(0,0,0;0,0,0)$	e	$[d_-(2c+1)]^3$
$(1,1,1;1,1,1)$	*	$[d_+(2c+1)]^3$
$(1,1,1;0,0,0)$	*	$[d(2c+2)]^3$
$(0,0,0;1,1,1)$	*	$[d(2c)]^3$
$(1,0,0;0,0,0)$	$-e/3$	$d(2c+2)\,[d_-(2c+1)]^2$
$(0,1,0;0,0,0)$	*	*
$(0,0,1;0,0,0)$	*	*
$(1,1,1;1,1,0)$	*	$d(2c+2)\,[d_+(2c+1)]^2$
$(1,1,1;1,0,1)$	*	*
$(1,1,1;0,1,1)$	*	*
$(0,0,0;1,0,0)$	*	$d(2c)\,[d_-(2c+1)]^2$
$(0,0,0;0,1,0)$	*	*
$(0,0,0;0,0,1)$	*	*
$(1,1,0;1,1,1)$	*	$d(2c)\,[d_+(2c+1)]^2$
$(1,0,1;1,1,1)$	*	*
$(0,1,1;1,1,1)$	*	*
$(1,1,0;0,0,0)$	*	$d_-(2c+1)\,[d(2c+2)]^2$
$(1,0,1;0,0,0)$	*	*
$(0,1,1;0,0,0)$	*	*
$(1,1,1;1,0,0)$	*	$d_+(2c+1)\,[d(2c+2)]^2$
$(1,1,1;0,1,0)$	*	*
$(1,1,1;0,0,1)$	*	*
$(0,0,0;1,1,0)$	*	$d_-(2c+1)\,[d(2c)]^2$
$(0,0,0;1,0,1)$	*	*
$(0,0,0;0,1,1)$	*	*
$(1,0,0;1,1,1)$	*	$d_+(2c+1)\,[d(2c)]^2$
$(0,1,0;1,1,1)$	*	*
$(0,0,1;1,1,1)$	*	*
$(1,0,0;1,0,0)$	$e/3$	$d_+(2c+1)\,[d_-(2c+1)]^2$
$(0,1,0;0,1,0)$	*	*
$(0,0,1;0,0,1)$	*	*
$(0,1,1;0,1,1)$	*	$d_-(2c+1)\,[d_+(2c+1)]^2$
$(1,0,1;1,0,1)$	*	*
$(1,1,0;1,1,0)$	*	*
$(1,0,0;0,1,1)$	*	$d(2c+2)\,[d(2c)]^2$
$(0,1,0;1,0,1)$	*	*
$(0,0,1;1,1,0)$	*	*
$(0,1,1;1,0,0)$	*	$d(2c)\,[d(2c+2)]^2$
$(1,0,1;0,1,0)$	*	*
$(1,1,0;0,0,1)$	*	*

TABLE E.3: The non-vanishing terms for $V_{3,12}$ in (E.41). The first column represents the 6-tuple of the indices $(m-2p, n-2p, s-2p; t-2q+1, u-2q+1, w-2q+1)$ and the values of the function $e_{3,11}(m,n,s;t,u,w)$ are given in the second column where $e = 3k_{\rm sp}^2/4\kappa_{\rm sp}^6$. The coefficients represented by a product containing the function $d_\sigma(k)$ is given in last column where the abbreviation $c \equiv p-q$ is used. The asterisk indicates that the table entry is identical to the entry above.

where the coefficients $d(0)$ and $d_\pm(1)$ are given in (E.23) and (E.24), respectively, and

$$Q^{(s)}_{\mathrm{TE},0} \equiv \sum_\alpha \left.\frac{\partial^2 \log\left(r^{(s)}_{\mathrm{TE}}\right)}{\partial k_{l,\alpha}\partial k_{l,\alpha}}\right|_{\mathrm{sp}} = Q^{(s)}_{\mathrm{TE},1} + \frac{k^2_{\mathrm{sp}}}{\kappa^3_{\mathrm{sp}}\varkappa_{\mathrm{sp}}} \tag{E.55}$$

$$Q^{(s)}_{\mathrm{TE},1} \equiv \sum_\alpha \left.\frac{\partial^2 \log\left(r^{(s)}_{\mathrm{TE}}\right)}{\partial k_{l,\alpha}\partial k_{l+1,\alpha}}\right|_{\mathrm{sp}} = \frac{k^2_{\mathrm{sp}} - 2\varkappa^2_{\mathrm{sp}}}{2\kappa_{\mathrm{sp}}\varkappa^3_{\mathrm{sp}}} \tag{E.56}$$

$$Q^{(s)}_{\mathrm{TM},0} \equiv \sum_\alpha \left.\frac{\partial^2 \log\left(r^{(s)}_{\mathrm{TM}}\right)}{\partial k_{l,\alpha}\partial k_{l,\alpha}}\right|_{\mathrm{sp}} = Q^{(s)}_{\mathrm{TM},1} - \frac{n_s^2 k^2_{\mathrm{sp}}\mathcal{K}^2}{\kappa^3_{\mathrm{sp}}\varkappa_{\mathrm{sp}}\left(\varkappa^2_{\mathrm{sp}} + n_s^2 k^2_{\mathrm{sp}}\right)} \tag{E.57}$$

$$Q^{(s)}_{\mathrm{TM},1} \equiv \sum_\alpha \left.\frac{\partial^2 \log\left(r^{(s)}_{\mathrm{TM}}\right)}{\partial k_{l,\alpha}\partial k_{l+1,\alpha}}\right|_{\mathrm{sp}} = n_s^2\mathcal{K}^2\frac{k^2_{\mathrm{sp}}(n_s^2 k^2_{\mathrm{sp}} - 3\varkappa^2_{\mathrm{sp}}) + 2\varkappa^4_{\mathrm{sp}}}{2\kappa_{\mathrm{sp}}\varkappa^3_{\mathrm{sp}}\left(\varkappa^2_{\mathrm{sp}} + n_s^2 k^2_{\mathrm{sp}}\right)^2} \tag{E.58}$$

with the relative refractive index n_s for sphere s and

$$\varkappa_{\mathrm{sp}} = \sqrt{n_s^2\mathcal{K}^2 + k^2_{\mathrm{sp}}}\,. \tag{E.59}$$

E.4 Derivation of $U^{(ii)}$

Derivation of $U_p^{(ii,1)}$ and $U_p^{(ii,2)}$

We calculate the term

$$U_p^{(ii,1/2)} = r g_p\left(u_1^{(1/2)} + \frac{r^{(s)}_{\check{p}}|_{\mathrm{sp}}}{r^{(s)}_p|_{\mathrm{sp}}}u_2^{(1/2)}\right) \tag{E.60}$$

with

$$u_1^{(1/2)} = \sum_{i,j=1}^{2r-1}\left(\tilde{\mathsf{H}}^{-1}\right)_{ij}\sum_{\alpha=x,y}\left.\frac{\partial^2 A}{\partial v_{i,\alpha}\partial v_{j,\alpha}}\right|_{\mathrm{sp}},$$
$$u_2^{(1/2)} = \sum_{i,j=1}^{2r-1}\left(\tilde{\mathsf{H}}^{-1}\right)_{ij}\sum_{\alpha=x,y}\left.\frac{\partial^2 B}{\partial v_{i,\alpha}\partial v_{j,\alpha}}\right|_{\mathrm{sp}}.$$

The functions A and B depend on $(\mathbf{k}_{2l+1}, \mathbf{k}_{2l})$ for $s = 1$ and $(\mathbf{k}_{2l}, \mathbf{k}_{2l-1})$ for $s = 2$. Thus, the results for the functions $u_1^{(s)}$ and $u_2^{(s)}$ is in general different for the two spheres. We find

$$u_1^{(1)} = -u_2^{(1)} = -[d(0) - d_+(1)]\frac{\mathcal{K}^2}{k^2_{\mathrm{sp}}\kappa_{\mathrm{sp}}} = -\frac{1}{r}\frac{\mathcal{K}^2}{k^2_{\mathrm{sp}}\kappa_{\mathrm{sp}}}\left(r + (r-1)\frac{R_2}{R_1}\right)\frac{1}{R_1+R_2},$$
$$u_1^{(2)} = -u_2^{(2)} = -[d(0) - d_-(1)]\frac{\mathcal{K}^2}{k^2_{\mathrm{sp}}\kappa_{\mathrm{sp}}} = -\frac{1}{r}\frac{\mathcal{K}^2}{k^2_{\mathrm{sp}}\kappa_{\mathrm{sp}}}\left(r + (r-1)\frac{R_1}{R_2}\right)\frac{1}{R_1+R_2},$$

where we used that

$$\sum_\alpha \frac{\partial^2 A}{\partial k_{l,\alpha}\partial k_{l,\alpha}}\bigg|_{\rm sp} = -\sum_\alpha \frac{\partial^2 A}{\partial k_{l,\alpha}\partial k_{l+1,\alpha}}\bigg|_{\rm sp} = -\frac{\mathcal{K}^2}{2k_{\rm sp}^2\kappa_{\rm sp}^2}\,,$$
$$\sum_\alpha \frac{\partial^2 B}{\partial k_{l,\alpha}\partial k_{l,\alpha}}\bigg|_{\rm sp} = -\sum_\alpha \frac{\partial^2 B}{\partial k_{l,\alpha}\partial k_{l+1,\alpha}}\bigg|_{\rm sp} = +\frac{\mathcal{K}^2}{2k_{\rm sp}^2\kappa_{\rm sp}^2}\,.$$

As the final result, we thus find

$$U_p^{(1/2)} = -g_p\frac{\mathcal{K}^2}{k_{\rm sp}^2\kappa_{\rm sp}}\left(r+(r-1)\frac{R_{2/1}}{R_{1/2}}\right)\frac{1}{R_1+R_2}\frac{r_p^{(1/2)}-r_{\bar p}^{(1/2)}}{r_p^{(1/2)}}\,, \tag{E.61}$$

where, as before, $\bar p = \text{TE}$ if $p = \text{TM}$ and vice versa.

Derivation of $U^{(ii,0)}$

The term $U^{(ii,0)}$ corresponds to the contribution to the saddle-point correction where a polarization change occurs precisely twice during the r round trips. Since the polarization change from TE to TM and back to TE can occur on any of the two spheres during the round trips, there are a total $2r(2r-1)$ terms to be considered.

Without loss of generality we may assume that the polarization change from TE to TM occurs in the zeroth round trip and the polarization back to TE at the l-th round trip. The terms for which the polarization change from TE to TM occurs in a different round trip yield an identical contribution and can thus be accounted for by multiplying the result by a factor of r.

It is then convenient to divide the contributions to $U^{(ii,0)}$ by specifying on which spheres the polarization changes occur:

$$U^{(ii,0)} = J^{(1,1)} + J^{(2,2)} + J^{(1,2)} + J^{(2,1)} \tag{E.62}$$

where $J^{(s,t)}$ stands for the contribution where the polarization from TE to TM occurs upon reflection on sphere s and the polarization change back to TE on sphere t.

We consider first the case that both polarization changes occur on sphere 1 which accounts for $r(r-1)$ terms in $U^{(ii,0)}$. This contribution reads

$$J^{(1,1)} = 2r\frac{\exp(-2r\kappa_{\rm sp}L)}{\kappa_{\rm sp}^{2r}}\sum_{l=1}^{r-1} x_{\rm TE}^{r-l-1}x_{\rm TM}^{l-1}r_{\rm TE}^{(2)}r_{\rm TM}^{(2)} \times\sum_{ij}\left(\tilde{\mathsf{H}}^{-1}\right)_{ij}\sum_\alpha \frac{\partial\rho^{(1)}_{\rm TETM}(\mathbf{k}_{2l+1},\mathbf{k}_{2l})}{\partial v_{i,\alpha}}\bigg|_{\rm sp}\frac{\partial\rho^{(1)}_{\rm TMTE}(\mathbf{k}_1,\mathbf{k}_0)}{\partial v_{j,\alpha}}\bigg|_{\rm sp} \tag{E.63}$$

where the factor of 2 is due to the identical contributions from the product rule for derivatives and

$$x_p \equiv r_p^{(1)}r_p^{(2)}\,. \tag{E.64}$$

Moreover, we have used that the polarization preserving contributions are given by $\rho_{pp}^{(1/2)}\big|_{\rm sp} = r_p^{(1/2)}$.

Using that

$$\sum_{\alpha} \frac{\partial \rho^{(1)}_{\mathrm{TETM}}}{\partial k_{2l,\alpha}}\bigg|_{\mathrm{sp}} \frac{\partial \rho^{(1)}_{\mathrm{TMTE}}}{\partial k_{0,\alpha}}\bigg|_{\mathrm{sp}} = \sum_{\alpha} \frac{\partial \rho^{(1)}_{\mathrm{TETM}}}{\partial k_{2l+1,\alpha}}\bigg|_{\mathrm{sp}} \frac{\partial \rho^{(1)}_{\mathrm{TMTE}}}{\partial k_{1,\alpha}}\bigg|_{\mathrm{sp}} = \frac{\mathcal{K}^2 \left[\Delta r^{(1)}\right]^2}{4k_{\mathrm{sp}}^2 \kappa_{\mathrm{sp}}^2}$$

$$\sum_{\alpha} \frac{\partial \rho^{(1)}_{\mathrm{TETM}}}{\partial k_{2l+1,\alpha}}\bigg|_{\mathrm{sp}} \frac{\partial \rho^{(1)}_{\mathrm{TMTE}}}{\partial k_{0,\alpha}}\bigg|_{\mathrm{sp}} = \sum_{\alpha} \frac{\partial \rho^{(1)}_{\mathrm{TETM}}}{\partial k_{2l,\alpha}}\bigg|_{\mathrm{sp}} \frac{\partial \rho^{(1)}_{\mathrm{TMTE}}}{\partial k_{1,\alpha}}\bigg|_{\mathrm{sp}} = -\frac{\mathcal{K}^2 \left[\Delta r^{(1)}\right]^2}{4k_{\mathrm{sp}}^2 \kappa_{\mathrm{sp}}^2}$$

where

$$\Delta r^{(s)} = r^{(s)}_{\mathrm{TE}} - r^{(s)}_{\mathrm{TM}}\,, \tag{E.65}$$

we can write

$$\sum_{ij} \left(\tilde{\mathsf{H}}^{-1}\right)_{ij} \frac{\partial \rho^{(1)}_{\mathrm{TETM}}(\mathbf{k}_{2l+1}, \mathbf{k}_{2l})}{\partial v_{i,\alpha}}\bigg|_{\mathrm{sp}} \frac{\partial \rho^{(1)}_{\mathrm{TMTE}}(\mathbf{k}_1, \mathbf{k}_0)}{\partial v_{j,\alpha}}\bigg|_{\mathrm{sp}}$$
$$= \left[2d(2l) - d_+(2l+1) - d_-(2l-1)\right] \frac{\mathcal{K}^2 \left[\Delta r^{(1)}\right]^2}{4k_{\mathrm{sp}}^2 \kappa_{\mathrm{sp}}^2}\,. \tag{E.66}$$

The brackets containing the functions d_σ is independent of l since it evaluates to

$$\left[2d(2l) - d_+(2l+1) - d_-(2l-1)\right] = -\frac{2R_2\kappa_{\mathrm{sp}}}{rR_1(R_1+R_2)}\,. \tag{E.67}$$

The sum over l can then be identified as a geometric sum for which we obtain

$$X \equiv \sum_{l=1}^{r-1} x_{\mathrm{TE}}^{r-l} x_{\mathrm{TM}}^{l} = \begin{cases} \frac{x_{\mathrm{TE}}^r x_{\mathrm{TM}} - x_{\mathrm{TM}}^r x_{\mathrm{TE}}}{x_{\mathrm{TE}} - x_{\mathrm{TM}}} & \text{for } x_{\mathrm{TE}} \neq x_{\mathrm{TM}} \\ (r-1) x_{\mathrm{TE}}^r & \text{for } x_{\mathrm{TE}} = x_{\mathrm{TM}}\,. \end{cases} \tag{E.68}$$

The contribution for which the polarization change occurs twice on sphere 1 can then be summarized as

$$J^{(1,1)} = -\frac{\mathcal{K}^2 \exp(-2r\kappa_{\mathrm{sp}}L)}{k_{\mathrm{sp}}^2 \kappa_{\mathrm{sp}}^{2r+1}} X \frac{\left[\Delta r^{(1)}\right]^2}{r_{\mathrm{TE}}^{(1)} r_{\mathrm{TM}}^{(1)}} \frac{R_2}{R_1(R_1+R_2)}\,. \tag{E.69}$$

The contribution $J^{(2,2)}$ where both polarization changes occur upon reflection on sphere 2 can be found by replacing $1 \leftrightarrow 2$ in $J^{(1,1)}$ which yields

$$J^{(2,2)} = -\frac{\mathcal{K}^2 \exp(-2r\kappa_{\mathrm{sp}}L)}{k_{\mathrm{sp}}^2 \kappa_{\mathrm{sp}}^{2r+1}} X \frac{\left[\Delta r^{(2)}\right]^2}{r_{\mathrm{TE}}^{(2)} r_{\mathrm{TM}}^{(2)}} \frac{R_1}{R_2(R_1+R_2)}\,. \tag{E.70}$$

The remaining terms represent the cases where the polarization changes occurs upon reflections on different spheres. The contribution where the polarization change from TE to TM occurs upon reflection on sphere 1 and the polarization change back

to TE on sphere 2 counts r^2 terms. These terms read

$$J^{(1,2)} = \frac{2r\exp(-2r\kappa_{\mathrm{sp}}L)}{\kappa_{\mathrm{sp}}^{2r}} \sum_{l=0}^{r-1} x_{\mathrm{TE}}^{r-l-1} x_{\mathrm{TM}}^{l} \times \sum_{ij} \left(\tilde{\mathsf{H}}^{-1}\right)_{ij} \sum_{\alpha} \left.\frac{\partial \rho^{(2)}_{\mathrm{TETM}}(\mathbf{k}_{2l+2}, \mathbf{k}_{2l+1})}{\partial v_{i,\alpha}}\right|_{\mathrm{sp}} \left.\frac{\partial \rho^{(1)}_{\mathrm{TMTE}}(\mathbf{k}_1, \mathbf{k}_0)}{\partial v_{j,\alpha}}\right|_{\mathrm{sp}} \tag{E.71}$$

where this time the sum over l starts at $l = 0$ allowing for the possibility that both polarization changes may occur within the same round trip. With

$$\begin{aligned} \sum_{\alpha} \left.\frac{\partial \rho^{(2)}_{\mathrm{TETM}}}{\partial k_{2l+1,\alpha}}\right|_{\mathrm{sp}} \left.\frac{\partial \rho^{(1)}_{\mathrm{TMTE}}}{\partial k_{0,\alpha}}\right|_{\mathrm{sp}} &= \sum_{\alpha} \left.\frac{\partial \rho^{(2)}_{\mathrm{TETM}}}{\partial k_{2l+2,\alpha}}\right|_{\mathrm{sp}} \left.\frac{\partial \rho^{(1)}_{\mathrm{TMTE}}}{\partial k_{1,\alpha}}\right|_{\mathrm{sp}} = -\frac{\mathcal{K}^2 \Delta r^{(1)} \Delta r^{(2)}}{4k_{\mathrm{sp}}^2 \kappa_{\mathrm{sp}}^2} \\ \sum_{\alpha} \left.\frac{\partial \rho^{(2)}_{\mathrm{TETM}}}{\partial k_{2l+2,\alpha}}\right|_{\mathrm{sp}} \left.\frac{\partial \rho^{(1)}_{\mathrm{TMTE}}}{\partial k_{0,\alpha}}\right|_{\mathrm{sp}} &= \sum_{\alpha} \left.\frac{\partial \rho^{(2)}_{\mathrm{TETM}}}{\partial k_{2l+1,\alpha}}\right|_{\mathrm{sp}} \left.\frac{\partial \rho^{(1)}_{\mathrm{TMTE}}}{\partial k_{1,\alpha}}\right|_{\mathrm{sp}} = \frac{\mathcal{K}^2 \Delta r^{(1)} \Delta r^{(2)}}{4k_{\mathrm{sp}}^2 \kappa_{\mathrm{sp}}^2} \end{aligned} \tag{E.72}$$

and the fact that

$$d(2l) + d(2l+2) - d_+(2l+1) - d_-(2l+1) = \frac{2\kappa_{\mathrm{sp}}}{r(R_1+R_2)} \tag{E.73}$$

is independent of l, we can perform the sum over l:

$$Y \equiv \sum_{l=0}^{r-1} x_{\mathrm{TE}}^{r-l-1} x_{\mathrm{TM}}^{l} = \begin{cases} \frac{x_{\mathrm{TE}}^r - x_{\mathrm{TM}}^r}{x_{\mathrm{TE}} - x_{\mathrm{TM}}} & \text{for } x_{\mathrm{TE}} \neq x_{\mathrm{TM}} \\ r x_{\mathrm{TE}}^{r-1} & \text{for } x_{\mathrm{TE}} = x_{\mathrm{TM}} \end{cases} . \tag{E.74}$$

We then obtain

$$J^{(1,2)} = \frac{\mathcal{K}^2 \exp(-2r\kappa_{\mathrm{sp}}L)}{k_{\mathrm{sp}}^2 \kappa_{\mathrm{sp}}^{2r+1}} Y \frac{\Delta r^{(1)} \Delta r^{(2)}}{R_1 + R_2} . \tag{E.75}$$

The remaining contribution for which the polarization change from TE to TM occurs upon reflection at sphere 2 and the polarization change back to TE on sphere 1 is given by interchanging the polarization components TE $\leftrightarrow$ TM in $J^{(1,2)}$. It turns out that the two contributions are identical:

$$J^{(2,1)} = J^{(1,2)} . \tag{E.76}$$

In total, we thus find

$$U^{(ii,0)} = \frac{\mathcal{K}^2 \exp(-2r\kappa_{\mathrm{sp}}L)}{k_{\mathrm{sp}}^2 \kappa_{\mathrm{sp}}^{2r+1}} \frac{1}{R_1+R_2} \times \left[2\Delta r^{(1)} \Delta r^{(2)} Y - X \left(\frac{\left[\Delta r^{(1)}\right]^2}{r_{\mathrm{TE}}^{(1)} r_{\mathrm{TM}}^{(1)}} \frac{R_2}{R_1} + \frac{\left[\Delta r^{(2)}\right]^2}{r_{\mathrm{TE}}^{(2)} r_{\mathrm{TM}}^{(2)}} \frac{R_1}{R_2} \right) \right] . \tag{E.77}$$

Perfect reflector case

The condition $x_{\mathrm{TE}} = x_{\mathrm{TM}}$, or equivalently

$$r_{\mathrm{TE}}^{(1)} r_{\mathrm{TE}}^{(2)} = r_{\mathrm{TM}}^{(1)} r_{\mathrm{TM}}^{(2)}\,, \tag{E.78}$$

is special which can already be seen by the fact that the functions X and Y defined in (E.68) and (E.74), respectively, take special values. For dielectric spheres, this condition is only satisfied in the perfect reflector limit.

We thus consider perfectly reflecting spheres in the following discussion. The Fresnel coefficients then become $r_{\mathrm{TE}} = -1$ and $r_{\mathrm{TM}} = 1$ and thus $X = r - 1$ and $Y = r$.

We can then write

$$\sum_p \left(U_p^{(ii,1)} + U_p^{(ii,2)} \right) = -\frac{\mathcal{K}^2 \exp(-2r\kappa_{\mathrm{sp}} L)}{k_{\mathrm{sp}}^2 \kappa_{\mathrm{sp}}^{2r+1}} \frac{1}{R_1 + R_2} \left[8r + 4(r-1) \left(\frac{R_2}{R_1} + \frac{R_1}{R_2} \right) \right] \tag{E.79}$$

and

$$U^{(ii,0)} = \frac{\mathcal{K}^2 \exp(-2r\kappa_{\mathrm{sp}} L)}{k_{\mathrm{sp}}^2 \kappa_{\mathrm{sp}}^{2r+1}} \frac{1}{R_1 + R_2} \left[8r + 4(r-1) \left(\frac{R_2}{R_1} + \frac{R_1}{R_2} \right) \right]. \tag{E.80}$$

The two term (E.79) and (E.80) precisely cancel each other. Thus, the contribution to the geometric optical correction due to the term $U^{(ii)}$ vanishes for perfect reflectors.

E.5 Useful identities

Identities for derivatives with respect to the Fourier transformed variables

Lemma 1.1: *Let X be a symmetric function of the momenta $\mathbf{k}_n$ for $n = 0, \ldots, 2r-1$ and $j \neq 0$, then*

$$\left. \frac{\partial X}{\partial v_{j,\alpha}} \right|_{\mathrm{sp}} = 0\,. \tag{E.81}$$

Proof: Using the chain rule, we can write

$$\left. \frac{\partial X}{\partial v_{j,\alpha}} \right|_{\mathrm{sp}} = \sum_{l=0}^{2r-1} W_{jl} \left. \frac{\partial X}{\partial k_{l,\alpha}} \right|_{\mathrm{sp}}. \tag{E.82}$$

Since now X is symmetric with respect to the $k_{l,\alpha}$, the derivative on the right-hand side evaluated at the saddle-point yields the same value for each l. The sum over l can then be written in terms of the geometric sum

$$\sum_{l=0}^{2r-1} W_{jl} = \frac{1}{\sqrt{2r}} \sum_{l=0}^{2r-1} \omega^l = \frac{1}{\sqrt{2r}} \frac{1-\omega^{2r}}{1-\omega} \tag{E.83}$$

where $\omega = \exp(\pi i j / r)$. Because $j \neq 0$ and $\omega^{2r} = 1$ the geometric sum evaluates to zero which proofs the lemma. □

Lemma 1.2: *Let $X = \prod_l X_l$ such that $\sum_l X_l$ is a symmetric function of the momenta $\mathbf{k}_n$ for*

$n = 0, \ldots, 2r-1$. *If further* $i, j \neq 0$ *then*

$$\left.\frac{\partial^2 X}{\partial v_{i,\alpha}\partial v_{j,\alpha}}\right|_{\text{sp}} = X|_{\text{sp}} \left.\frac{\partial^2 \log(X)}{\partial v_{i,\alpha}\partial v_{j,\alpha}}\right|_{\text{sp}} . \tag{E.84}$$

Proof: Using the product rule, we first express the second order derivative as

$$\left.\frac{\partial^2 X}{\partial v_{i,\alpha}\partial v_{j,\alpha}}\right|_{\text{sp}} = X|_{\text{sp}} \left[\frac{1}{X_l|_{\text{sp}}} \sum_l \left.\frac{\partial^2 X_l}{\partial v_{i,\alpha}\partial v_{j,\alpha}}\right|_{\text{sp}} + \frac{1}{X_l|^2_{\text{sp}}} \sum_{k\neq l} \left.\frac{\partial X_k}{\partial v_{i,\alpha}}\right|_{\text{sp}} \left.\frac{\partial X_l}{\partial v_{j,\alpha}}\right|_{\text{sp}}\right] . \tag{E.85}$$

Adding and subtracting the expression

$$\frac{1}{X_l|^2_{\text{sp}}} \sum_l \left.\frac{\partial X_l}{\partial v_{i,\alpha}}\right|_{\text{sp}} \left.\frac{\partial X_l}{\partial v_{j,\alpha}}\right|_{\text{sp}} \tag{E.86}$$

inside the brackets allows us to complete the sum of the second term. That second term then becomes proportional to $\partial X/\partial v_{i,\alpha}|_{\text{sp}}$ which vanishes according to Lemma 1.1. We thus write

$$\begin{aligned}\left.\frac{\partial^2 X}{\partial v_{i,\alpha}\partial v_{j,\alpha}}\right|_{\text{sp}} &= X|_{\text{sp}} \sum_l \left[\frac{1}{X_l|_{\text{sp}}} \sum_l \left.\frac{\partial^2 X_l}{\partial v_{i,\alpha}\partial v_{j,\alpha}}\right|_{\text{sp}} - \frac{1}{X_l|^2_{\text{sp}}} \left.\frac{\partial X_l}{\partial v_{i,\alpha}}\right|_{\text{sp}} \left.\frac{\partial X_l}{\partial v_{j,\alpha}}\right|_{\text{sp}}\right] \\ &= X|_{\text{sp}} \sum_l \left.\frac{\partial^2 \log(X_l)}{\partial v_{i,\alpha}\partial v_{j,\alpha}}\right|_{\text{sp}} .\end{aligned}$$

Expressing the sum of the logarithms as a logarithm of a product then completes the proof. □

Identities for sums over trigonometric functions

Lemma 2.1: *Let* k *and* r *be integers with* $0 \leq k < r$ *then*

$$\sum_{j=1}^{r-1} \frac{\sin(\pi j(2k+1)/r)}{\sin(\pi j/r)} = r - (2k+1) . \tag{E.87}$$

Proof: When $k = 0$, the sum trivially yields $r-1$. For $k > 0$, we can use the addition formula for the sine and express the sum as

$$\sum_{j=1}^{r-1} \frac{\sin(\pi j(2k+1)/r)}{\sin(\pi j/r)} = \sum_{j=1}^{r-1} \sin(2\pi kj/r)\cot(\pi j/r) + \sum_{j=1}^{r-1} \cos(2\pi jk/r) .$$

Using Corollary 4.2 from Ref. [148] the first sum yields $r-2k$. The cosine of the second sum can be expressed in terms of complex exponentials. The summation over j then yields -1. □

Lemma 2.2: *Let* k *and* r *be integers then*

$$\sum_{j=1}^{r-1} \frac{\sin(2\pi jk/r)}{\sin(\pi j/r)} = 0 . \tag{E.88}$$

Proof: The identity is easily proven by reversing the summation over j. The sum then goes over into the same sum with a negative sign, which can only be true if the

sum vanishes. □

Lemma 2.3: *Let k and r be integers with* $0 \leq k \leq 2r$ *then*

$$\sum_{j=1}^{r-1} \frac{\cos(\pi jk/r)}{\sin^2(\pi j/2r)} = \frac{1}{2}\left[\frac{1}{3}\left(4r^2 - 12kr + 6k^2 - 1\right) - (-1)^k\right] \tag{E.89}$$

Proof: Using

$$\sum_{j=1}^{r-1} \frac{\cos(\pi jk/r)}{\sin^2(\pi j/2r)} = \sum_{j=1}^{r-1} \frac{\cos(\pi(2r-j)k/r)}{\sin^2(\pi(2r-j)/2r)}$$

we can write

$$\sum_{j=1}^{r-1} \frac{\cos(\pi jk/r)}{\sin^2(\pi j/2r)} = \frac{1}{2}\left(\sum_{j=1}^{2r-1} \frac{\cos(2\pi jk/2r)}{\sin^2(\pi j/2r)} - (-1)^k\right) = \frac{1}{2}\left[\frac{1}{3}\left(4r^2 - 12kr + 6k^2 - 1\right) - (-1)^k\right]$$

where Corollary 5.4 from Ref. [148] was used to perform the sum over j in the last equality. □

Appendix F

Hybrid numerical approach

In this appendix, we discuss the hybrid numerical approach in more detail. This approach is a hybrid method between the plane-wave numerical approach discussed in chapter 7 and the commonly employed method based on spherical multipoles. For simplicity, we discuss the hybrid approach in the example of the plane-sphere geometry depicted in Fig. 7.1. This method may also be applied to any other geometry with cylindrical symmetry.

Within the plane-wave basis, the matrix elements of the reflection operator at the sphere can be expressed as [55, Appendix 5]

$$\begin{aligned}\langle \mathbf{k}', p', -|\mathcal{R}_S|\mathbf{k}, p, +\rangle = \frac{8\pi^2}{\mathcal{K}\kappa'} \sum_{\ell=1}^{\infty} \sum_{m=-\ell}^{\ell} \frac{i^{p-p'}}{\ell(\ell+1)} \\ \times \Bigg[a_\ell \left(\frac{m}{\sin\theta^-_{\mathbf{k}'}}\right)^{\delta_{p',1}} \left(\frac{\partial}{\partial\theta^-_{\mathbf{k}'}}\right)^{1-\delta_{p',1}} \left(\frac{m}{\sin\theta^+_{\mathbf{k}}}\right)^{\delta_{p,1}} \left(\frac{\partial}{\partial\theta^+_{\mathbf{k}}}\right)^{1-\delta_{p,1}} \\ + b_\ell \left(\frac{m}{\sin\theta^-_{\mathbf{k}'}}\right)^{\delta_{p',2}} \left(\frac{\partial}{\partial\theta^-_{\mathbf{k}'}}\right)^{1-\delta_{p',2}} \left(\frac{m}{\sin\theta^+_{\mathbf{k}}}\right)^{\delta_{p,2}} \left(\frac{\partial}{\partial\theta^+_{\mathbf{k}}}\right)^{1-\delta_{p,2}} \Bigg] Y_\ell^m(\theta^-_{\mathbf{k}'}, \varphi_{\mathbf{k}'}) Y_\ell^{m*}(\theta^+_{\mathbf{k}}, \varphi_{\mathbf{k}}) \,,\end{aligned} \tag{F.1}$$

where $p =$ TE and TM and associated with the indices 1 and 2, respectively. Here, a_ℓ and b_ℓ are the Mie coefficients given in (5.18),

$$\sin\theta^\pm_{\mathbf{k}} = -i\frac{k}{\mathcal{K}}, \quad \cos\theta^\pm_{\mathbf{k}} = \pm\frac{\kappa}{\mathcal{K}} \tag{F.2}$$

and the spherical harmonics are defined as [147, §14.30]

$$Y_\ell^m(\theta,\varphi) = \sqrt{\frac{2\ell+1}{4\pi}\frac{(\ell-m)!}{(\ell+m)!}}\, P_\ell^m(\cos\theta)\, e^{im\varphi} \tag{F.3}$$

with the associated Legendre functions defined in (A.7).

If objects different than spheres are involved, the Mie coefficients a_ℓ and b_ℓ appearing in (F.1) would need to be replaced with the corresponding partial-wave reflection coefficients. Note that the sum over the azimuthal numbers m in (F.1) can be performed analytically yielding the matrix elements (5.14) as outlined in [58, Appendix C]. Here, we perform the discrete Fourier transform discussed in 7.2 analytically and proceed as follows.

First, it is necessary to express the in-plane wave vector $\mathbf{k}$ appearing in the matrix elements (F.1) in polar coordinates with radial and angular component k and φ, respectively. The matrix elements depend on the angular components only through

the phase factor appearing in the spherical harmonics (F.3) and thus only on the difference of the angular components, $\Delta\varphi = \varphi' - \varphi$. Applying the trapezoidal rule for the angular components with a subsequent discrete Fourier transform as discussed in Sec. 7.2, the reflection matrix becomes block diagonal with respect to the azimuthal number and takes the form

$$\langle k', p', -|\mathcal{R}_S^{(m)}|k, p, +\rangle = \sum_{j=0}^{M-1} \frac{1}{M} e^{2\pi i j m/M} \langle k', 2\pi j/M, p', -|\mathcal{R}_S|k, 0, p, +\rangle \tag{F.4}$$

for $m = 0, \pm 1, \ldots$ up to $\pm(M-1)/2$ when M is odd or $M/2$ when M is even. Taking the limit $M \to \infty$, the sum over j becomes an integral over $\Delta\varphi$

$$\langle k', p', -|\mathcal{R}_S^{(m)}|k, p, +\rangle = \int_0^{2\pi} \frac{d\Delta\varphi}{2\pi} e^{im\Delta\varphi} \langle k', \Delta\varphi, p', -|\mathcal{R}_S|k, 0, p, +\rangle \,, \tag{F.5}$$

where the azimuthal numbers now run from $m = 0, \pm 1, \ldots$ to $\pm\infty$.

Switching the order of summation over ℓ and m in (F.1) by means of the relation

$$\sum_{\ell=1}^{\infty} \sum_{m=-\ell}^{\ell} = \sum_{m=-\infty}^{\infty} \sum_{\ell=\max(1,|m|)}^{\infty} \,, \tag{F.6}$$

we can perform the integration over $\Delta\varphi$ analytically yielding the matrix elements

$$\begin{aligned}
\langle k', \mathrm{TE}, -|\mathcal{R}_S^{(m)}|k, \mathrm{TE}, +\rangle &= -\frac{1}{\mathcal{K}\kappa'} \sum_{\ell=\max(1,|m|)}^{\infty} N_\ell^m \Big[a_\ell \frac{m^2\mathcal{K}^2}{kk'} P_\ell^m(-\kappa'/\mathcal{K}) P_\ell^m(\kappa/\mathcal{K}) \\
&\qquad + b_\ell \frac{kk'}{\mathcal{K}^2} \partial P_\ell^m(-\kappa'/\mathcal{K}) \partial P_\ell^m(\kappa/\mathcal{K}) \Big] \,, \\
\langle k', \mathrm{TM}, -|\mathcal{R}_S^{(m)}|k, \mathrm{TM}, +\rangle &= \frac{1}{\mathcal{K}\kappa'} \sum_{\ell=\max(1,|m|)}^{\infty} N_\ell^m \Big[a_\ell \frac{kk'}{\mathcal{K}^2} \partial P_\ell^m(-\kappa'/\mathcal{K}) \partial P_\ell^m(\kappa/\mathcal{K}) \\
&\qquad + b_\ell \frac{m^2\mathcal{K}^2}{kk'} P_\ell^m(-\kappa'/\mathcal{K}) P_\ell^m(\kappa/\mathcal{K}) \Big] \,, \\
\langle k', \mathrm{TE}, -|\mathcal{R}_S^{(m)}|k, \mathrm{TM}, +\rangle &= -\frac{im}{\mathcal{K}\kappa'} \sum_{\ell=\max(1,|m|)}^{\infty} N_\ell^m \Big[a_\ell \frac{k}{k'} P_\ell^m(-\kappa'/\mathcal{K}) \partial P_\ell^m(\kappa/\mathcal{K}) \\
&\qquad + b_\ell \frac{k'}{k} \partial P_\ell^m(-\kappa'/\mathcal{K}) P_\ell^m(\kappa/\mathcal{K}) \Big] \,, \\
\langle k', \mathrm{TM}, -|\mathcal{R}_S^{(m)}|k, \mathrm{TE}, +\rangle &= -\frac{im}{\mathcal{K}\kappa'} \sum_{\ell=\max(1,|m|)}^{\infty} N_\ell^m \Big[a_\ell \frac{k'}{k} \partial P_\ell^m(-\kappa'/\mathcal{K}) P_\ell^m(\kappa/\mathcal{K}) \\
&\qquad + b_\ell \frac{k}{k'} P_\ell^m(-\kappa'/\mathcal{K}) \partial P_\ell^m(\kappa/\mathcal{K}) \Big] \,,
\end{aligned} \tag{F.7}$$

where ∂P_ℓ^m denotes a derivative of the associated Legendre function with respect to its argument and

$$N_\ell^m = \frac{2\ell+1}{\ell(\ell+1)} \frac{(\ell-m)!}{(\ell+m)!} \,. \tag{F.8}$$

Using the reflection formulas

$$P_\ell^m(-x) = (-1)^\ell P_\ell^m(x) \quad \partial P_\ell^m(-x) = (-1)^{\ell+1} \partial P_\ell^m(x) \,, \tag{F.9}$$

the alternating sign of the Mie coefficients with respect to ℓ can be canceled out. In

the resulting sums over ℓ, the summands have a fixed sign and the sums can be numerically evaluated in a similar way as the summation over ℓ appearing in the Mie scattering amplitudes which is detailed in Sec. 7.5.

The reflection matrix elements (F.7) can now be used to compute the Casimir interaction between a plane and a sphere. To this end, we apply the Nyström discretization to the radial components of the wave-vectors as discussed in Sec. 7.3 and compute the contribution of the round-trip operator for each azimuthal number m until convergence is reached.

In our numerical implementation of the hybrid method, we calculate the associated Legendre functions and its derivative by means of the upward recurrence relations (A.9)

$$\begin{aligned}(\ell-m+1)P_{\ell+1}^m(z) &= (2\ell+1)zP_\ell^m(z)-(\ell+m)P_{\ell-1}^m(z)\,,\\ (z^2-1)\partial P_\ell^m(z) &= \ell z P_\ell^m(z)-(\ell+m)P_{\ell-1}^m(z)\end{aligned} \tag{F.10}$$

initiated with (A.10)

$$\begin{aligned}P_m^m(z) &= \frac{(2m)!}{2^m m!}(z^2-1)^{m/2}\,,\\ P_{m+1}^m(z) &= (2m+1)zP_m^m(z)\,,\\ \partial P_m^m(z) &= \frac{(2m)!}{2^m(m-1)!}z(z^2-1)^{m/2-1}\,.\end{aligned} \tag{F.11}$$

In principle, the evaluation of the sum over ℓ can be sped up by the use of asymptotics for the evaluation of the associated Legendre functions since then we would not need to calculate the sum from $\ell=\max(1,|m|)$ to $\ell_{\max}$. We, however, did not investigate this possibility further.

For a fair comparison between the plane-wave and the hybrid method, we evaluated the Mie scattering amplitudes (5.3) in the plane-wave method also with an upward summation of the angular functions starting at $\ell=1$. In both the hybrid and plane-wave methods the sums over ℓ were truncated by the same value $\ell_{\max}=\lceil 10R/L\rceil$. We found that the hybrid method performed slower than the plane-wave method. This may be explained by the fact that in the plane-wave method the round-trip matrix has to be constructed for fewer values of m than in the hybrid method. This is related to the convergence rate of the summation over m in the hybrid approach and the convergence of the quadrature order M in the plane-wave method, respectively, which we will discuss in the following.

For a comparison of the convergence rates, we truncate the summation over the contribution of m in the hybrid method by some highest value $m_{\max}$. The choice of $m_{\max}$ determines how well the result converges. For simplicity, we study the convergence for a given frequency contribution to the Casimir free energy for a perfectly reflecting sphere and plane in vacuum. The frequency is set to $\xi=0.1\,c/L$ and the radial quadrature order is set to $N=\lceil 6\sqrt{R/L}\rceil$ which yields a numerical accuracy between 10^{-6} and 10^{-7} (cf. Tab. 7.1).

In Fig. F.1, we compare the convergence of $m_{\max}$ in the hybrid approach with the convergence of the quadrature order M in the plane-wave approach for aspect ratios $R/L=100$ and 10. For a given $m_{\max}$ or M the error of the contribution to the Casimir free energy is shown relative to a numerical value with higher numerical accuracy with $M=100$ for $R/L=10$ and $M=250$ for $R/L=100$. The results for the hybrid method are represented by the circles and squares and the results for

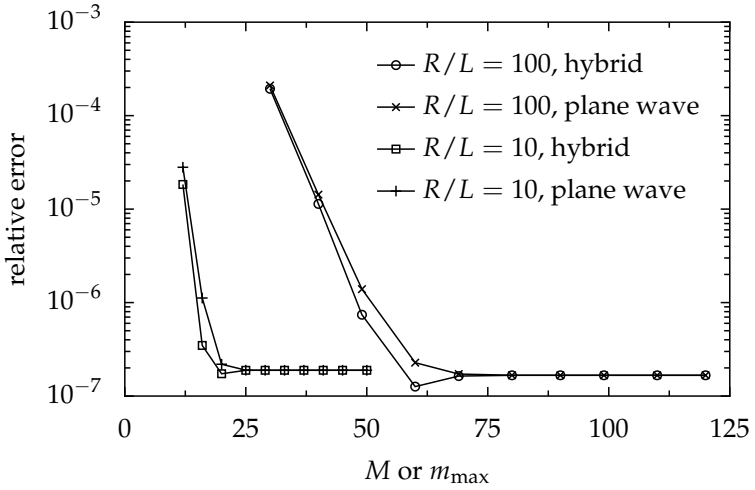

FIGURE F.1: Numerical relative error for the evaluation of the frequency contribution to the Casimir free energy in the plane-sphere geometry as a function of the highest azimuthal number $m_{\max}$ included in the hybrid method and angular quadrature order M in the plane-wave method. The object are assumed to be perfectly reflecting and the medium to be vacuum. The imaginary frequency is set to $\xi = 0.1\, c/L$ with the surface-to-surface distance L. The circles and squares (crosses and pluses) represent data points obtained in the hybrid (plane-wave) method for $R/L = 100$ and $R/L = 10$, respectively. For the data points, the numerical error is calculated relative to the result obtained by setting $M = 100$ when $R/L = 10$ and $M = 250$ when $R/L = 100$ in the plane-wave method.

the plane-wave method by the crosses and pluses. The circles and crosses show the result for the aspect ratio $R/L = 100$ and the pluses for the aspect ratio of $R/L = 10$.

We observe that for the two methods convergence is reached for about the same values of M and $m_{\max}$. For $R/L = 10$, this is at about $M = m_{\max} = 25$ and, for $R/L = 100$, at about $M = m_{\max} = 70$. For larger values of M and $m_{\max}$, the relative error stays constant as it is determined by the relative error induced by discretization order of the radial component of the wave vector which is fixed here. Though convergence is reached when $M = m_{\max}$, this means that in the plane-wave method about half of the matrix elements and matrix computations have to be performed compared to the hybrid method.

Due to symmetry in $\Delta\varphi$, we only need to compute half of the matrix elements. After then applying the discrete Fourier transform, the contributions to the Casimir energy correspond to azimuthal numbers $m = 0, \pm, \ldots$ to about $M/2$. Since positive and negative azimuthal numbers contribute equally, we only need to compute half of the determinants of the round-trip matrices.

Note that, for a fixed M, expression (F.4) yields a worse and worse approximation of the exact result (F.5) as m increases. This is because the Fourier factor becomes more and more oscillatory and the fixed quadrature order resolves these oscillations worse and worse. This is illustrated in Fig. F.2, where the numerical value of the contribution to the free energy is shown as a function of the azimuthal number m. In the figure, the frequency is set to $\xi = 0.1\, c/L$ and the aspect ratio to $R/L = 100$. Circles and crosses represent the data points of the hybrid and plane-wave method respectively. For the plane-wave method, numerical data corresponding to the angular quadrature order $M = 40$ and $M = 60$ is shown.

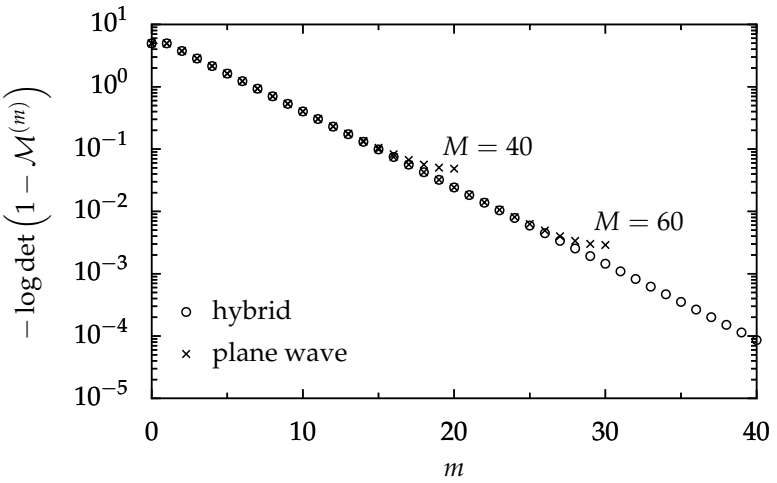

FIGURE F.2: The numerical value of the contribution to the free energy in the plane-sphere geometry as a function of the azimuthal number m for a fixed frequency $\xi = 0.1\, c/L$. The objects are assumed to be perfect reflectors in vacuum and the ratio of the sphere radius R to the surface-to-surface distance L is set to $R/L = 100$. Circles and crosses represent the data points of the hybrid and plane-wave method respectively. For the plane-wave method, data corresponding to the quadrature order $M = 40$ and $M = 60$ is depicted.

One can nicely observe the exponential convergence of the m-sum in the hybrid method. For $M = 40$, the data points from the plane-wave method agree well with the results from the hybrid method for small m. For larger m, the deviation increases. The deviation is largest for the last data point at $m = 20$. The situation is similar for the quadrature order $M = 60$, which contains data for azimuthal numbers up to $m = 30$. If we were interested in the Casimir contribution for a given azimuthal number, the hybrid approach is certainly to be preferred, as one can directly compute the contribution. Interestingly, in the plane-wave approach the loss of accuracy in the calculation of higher azimuthal numbers makes the summation over all azimuthal numbers converge fast. For $M = 40$, the summation over the crosses from $m = 0$ to 20 yield the contribution to the Casimir energy to the same accuracy as all circles in the figure stemming from the hybrid method.

Bibliography

[1] J. N. Israelachvili, *Intermolecular and Surface Forces* (Academic Press, London, 2011).

[2] A. Milling, P. Mulvaney, and I. Larson, "Direct Measurement of Repulsive van der Waals Interactions Using an Atomic Force Microscope", J. Colloid Interface Sci. **180**, 460–465 (1996), DOI: 10.1006/jcis.1996.0326.

[3] J. N. Munday, F. Capasso, and V. A. Parsegian, "Measured long-range repulsive Casimir–Lifshitz forces", Nature **457**, 170–173 (2009), DOI: 10.1038/nature07610.

[4] R. F. Tabor, R. Manica, D. Y. C. Chan, F. Grieser, and R. R. Dagastine, "Repulsive van der Waals Forces in Soft Matter: Why Bubbles Do Not Stick to Walls", Phys. Rev. Lett. **106**, 064501 (2011), DOI: 10.1103/PhysRevLett.106.064501.

[5] H. Butt and M. Kappl, *Surface and Interfacial Forces* (John Wiley & Sons, Ltd, 2010), DOI: 10.1002/9783527629411.

[6] H. Hamaker, "The London—van der Waals attraction between spherical particles", Physica **4**, 1058–1072 (1937), DOI: 10.1016/S0031-8914(37)80203-7.

[7] P. Rodriguez-Lopez, "Pairwise summation approximation of Casimir energy from first principles", Phys. Rev. E **80**, 061128 (2009), DOI: 10.1103/PhysRevE.80.061128.

[8] K. A. Milton, P. Parashar, and J. Wagner, "Exact Results for Casimir Interactions between Dielectric Bodies: The Weak-Coupling or van der Waals Limit", Phys. Rev. Lett. **101**, 160402 (2008), DOI: 10.1103/PhysRevLett.101.160402.

[9] H. B. G. Casimir, "On the attraction between two perfectly conducting plates", Proc. K. Ned. Akad. Wet. **51**, 793 (1948).

[10] E. M. Lifshitz, "The Theory of Molecular Attractive Forces between Solids", Sov. Phys. JETP (Engl. Transl.) **2**, 73 (1956).

[11] I. Dzyaloshinskii, E. Lifshitz, and L. Pitaevskii, "The general theory of van der Waals forces", Adv. Phys. **10**, 165–209 (1961), DOI: 10.1080/00018736100101281.

[12] M. Elzbieciak-Wodka et al., "Measurements of dispersion forces between colloidal latex particles with the atomic force microscope and comparison with Lifshitz theory", J. Chem. Phys. **140**, 104906 (2014), DOI: 10.1063/1.4867541.

[13] D. S. Ether et al., "Probing the Casimir force with optical tweezers", Europhys. Lett. **112**, 44001 (2015), DOI: 10.1209/0295-5075/112/44001.

[14] F. J. M. Ruiz-Cabello, M. Moazzami-Gudarzi, M. Elzbieciak-Wodka, and P. Maroni, "Forces between different latex particles in aqueous electrolyte solutions measured with the colloidal probe technique", Microsc. Res. Tech. **80**, 144–152 (2017), DOI: 10.1002/jemt.22656.

[15] M. A. Bevan and D. C. Prieve, "Direct Measurement of Retarded van der Waals Attraction", Langmuir **15**, 7925–7936 (1999), DOI: 10.1021/la9813811.

[16] P. M. Hansen, J. K. Dreyer, J. Ferkinghoff-Borg, and L. Oddershede, "Novel optical and statistical methods reveal colloid–wall interactions inconsistent with DLVO and Lifshitz theories", J. Colloid Interface Sci. **287**, 561–571 (2005), DOI: 10.1016/j.jcis.2005.01.098.

[17] G. L. Klimchitskaya, U. Mohideen, and V. M. Mostepanenko, "The Casimir force between real materials: Experiment and theory", Rev. Mod. Phys. **81**, 1827–1885 (2009), DOI: 10.1103/RevModPhys.81.1827.

[18] R. Decca, V. Aksyuk, and D. López, "Casimir Force in Micro and Nano Electro Mechanical Systems", Lect. Notes Phys. **834**, 287 (2011), DOI: 10.1007/978-3-642-20288-9_9.

[19] S. K. Lamoreaux, "Progress in Experimental Measurements of the Surface–Surface Casimir Force: Electrostatic Calibrations and Limitations to Accuracy", Lect. Notes Phys. **834**, 219 (2011), DOI: 10.1007/978-3-642-20288-9_7.

[20] G. L. Klimchitskaya and V. M. Mostepanenko, "Recent measurements of the Casimir force: Comparison between experiment and theory", Mod. Phys. Lett. A **35**, 2040007 (2020), DOI: 10.1142/S0217732320400076.

[21] B. Derjaguin, "Untersuchungen über die Reibung und Adhäsion, IV", Kolloid-Zeitschrift **69**, 155–164 (1934), DOI: 10.1007/BF01433225.

[22] M. Bordag, G. Klimchitskaya, U. Mohideen, and V. Mostepanenko, *Advances in the Casimir effect* (Oxford University Press, 2009).

[23] V. A. Parsegian, *Van der Waals Forces: A Handbook for Biologists, Chemists, Engineers, and Physicists* (Cambridge University Press, 2005), DOI: 10.1017/CBO9780511614606.

[24] I. Antoniadis, N. Arkani-Hamed, S. Dimopoulos, and G. Dvali, "New dimensions at a millimeter to a fermi and superstrings at a TeV", Phys. Lett. B **436**, 257–263 (1998), DOI: 10.1016/S0370-2693(98)00860-0.

[25] R. S. Decca et al., "Novel constraints on light elementary particles and extra-dimensional physics from the Casimir effect", Eur. Phys. J. C **51**, 963–975 (2007), DOI: 10.1140/epjc/s10052-007-0346-z.

[26] Y.-J. Chen et al., "Stronger Limits on Hypothetical Yukawa Interactions in the 30–8000 nm Range", Phys. Rev. Lett. **116**, 221102 (2016), DOI: 10.1103/PhysRevLett.116.221102.

[27] V. M. Mostepanenko and G. L. Klimchitskaya, "The State of the Art in Constraining Axion-to-Nucleon Coupling and Non-Newtonian Gravity from Laboratory Experiments", Universe **6** (2020), DOI: 10.3390/universe6090147.

[28] N. Ashcroft and N. Mermin, *Solid State Physics* (Saunders College Publishing, 1976).

[29] M. Liu, J. Xu, G. L. Klimchitskaya, V. M. Mostepanenko, and U. Mohideen, "Examining the Casimir puzzle with an upgraded AFM-based technique and advanced surface cleaning", Phys. Rev. B **100**, 081406 (2019), DOI: 10.1103/PhysRevB.100.081406.

[30] M. Liu, J. Xu, G. L. Klimchitskaya, V. M. Mostepanenko, and U. Mohideen, "Precision measurements of the gradient of the Casimir force between ultraclean metallic surfaces at larger separations", Phys. Rev. A **100**, 052511 (2019), DOI: 10.1103/PhysRevA.100.052511.

[31] A. Lambrecht, P. A. Maia Neto, and S. Reynaud, "The Casimir effect within scattering theory", New J. Phys. **8**, 243–243 (2006), DOI: 10.1088/1367-2630/8/10/243.

[32] T. Emig, N. Graham, R. L. Jaffe, and M. Kardar, "Casimir Forces between Arbitrary Compact Objects", Phys. Rev. Lett. **99**, 170403 (2007), DOI: 10.1103/PhysRevLett.99.170403.

[33] G. Bimonte and T. Emig, "Exact Results for Classical Casimir Interactions: Dirichlet and Drude Model in the Sphere-Sphere and Sphere-Plane Geometry", Phys. Rev. Lett. **109**, 160403 (2012), DOI: 10.1103/PhysRevLett.109.160403.

[34] R. Zhao, Y. Luo, A. I. Fernández-Domínguez, and J. B. Pendry, "Description of van der Waals Interactions Using Transformation Optics", Phys. Rev. Lett. **111**, 033602 (2013), DOI: 10.1103/PhysRevLett.111.033602.

[35] T. Schoger and G.-L. Ingold, *to be submitted*.

[36] M. Bordag, "Casimir effect for a sphere and a cylinder in front of a plane and corrections to the proximity force theorem", Phys. Rev. D **73**, 125018 (2006), DOI: 10.1103/PhysRevD.73.125018.

[37] L. P. Teo, M. Bordag, and V. Nikolaev, "Corrections beyond the proximity force approximation", Phys. Rev. D **84**, 125037 (2011), DOI: 10.1103/PhysRevD.84.125037.

[38] L. P. Teo, "Material dependence of Casimir interaction between a sphere and a plate: First analytic correction beyond proximity force approximation", Phys. Rev. D **88**, 045019 (2013), DOI: 10.1103/PhysRevD.88.045019.

[39] G. Bimonte, "Classical Casimir interaction of a perfectly conducting sphere and plate", Phys. Rev. D **95**, 065004 (2017), DOI: 10.1103/PhysRevD.95.065004.

[40] L. P. Teo, "Casimir effect between two spheres at small separations", Phys. Rev. D **85**, 045027 (2012), DOI: 10.1103/PhysRevD.85.045027.

[41] C. D. Fosco, F. C. Lombardo, and F. D. Mazzitelli, "Proximity force approximation for the Casimir energy as a derivative expansion", Phys. Rev. D **84**, 105031 (2011), DOI: 10.1103/PhysRevD.84.105031.

[42] G. Bimonte, T. Emig, R. L. Jaffe, and M. Kardar, "Casimir forces beyond the proximity approximation", Europhys. Lett. **97**, 50001 (2012), DOI: 10.1209/0295-5075/97/50001.

[43] G. Bimonte, T. Emig, and M. Kardar, "Material dependence of Casimir forces: Gradient expansion beyond proximity", Appl. Phys. Lett. **100**, 074110 (2012), DOI: 10.1063/1.3686903.

[44] C. D. Fosco, F. C. Lombardo, and F. D. Mazzitelli, "Derivative-expansion approach to the interaction between close surfaces", Phys. Rev. A **89**, 062120 (2014), DOI: 10.1103/PhysRevA.89.062120.

[45] C. D. Fosco, F. C. Lombardo, and F. D. Mazzitelli, "Derivative expansion for the electromagnetic Casimir free energy at high temperatures", Phys. Rev. D **92**, 125007 (2015), DOI: 10.1103/PhysRevD.92.125007.

[46] G. Bimonte, "Beyond-proximity-force-approximation Casimir force between two spheres at finite temperature", Phys. Rev. D **97**, 085011 (2018), DOI: 10.1103/PhysRevD.97.085011.

[47] G. Bimonte, "Beyond-proximity-force-approximation Casimir force between two spheres at finite temperature. II. Plasma versus Drude modeling, grounded versus isolated spheres", Phys. Rev. D **98**, 105004 (2018), DOI: 10.1103/PhysRevD.98.105004.

[48] P. A. Maia Neto, A. Lambrecht, and S. Reynaud, "Casimir energy between a plane and a sphere in electromagnetic vacuum", Phys. Rev. A **78**, 012115 (2008), DOI: 10.1103/PhysRevA.78.012115.

[49] T Emig, "Fluctuation-induced quantum interactions between compact objects and a plane mirror", J. Stat. Mech. **2008**, P04007 (2008), DOI: 10.1088/1742-5468/2008/04/p04007.

[50] A. Canaguier-Durand, P. A. Maia Neto, A. Lambrecht, and S. Reynaud, "Thermal Casimir effect for Drude metals in the plane-sphere geometry", Phys. Rev. A **82**, 012511 (2010), DOI: 10.1103/PhysRevA.82.012511.

[51] A. Canaguier-Durand, "Multipolar scattering expansion for the Casimir effect in the sphere-plane geometry.", Ph.D. thesis (Université Pierre et Marie Curie - Paris VI, Sept. 2011).

[52] A. Canaguier-Durand et al., "Classical Casimir interaction in the plane-sphere geometry", Phys. Rev. A **85**, 052501 (2012), DOI: 10.1103/PhysRevA.85.052501.

[53] S. Umrath, M. Hartmann, G.-L. Ingold, and P. A. Maia Neto, "Disentangling geometric and dissipative origins of negative Casimir entropies", Phys. Rev. E **92**, 042125 (2015), DOI: 10.1103/PhysRevE.92.042125.

[54] S. Umrath, "Der Casimir-Effekt in der Kugel-Kugel-Geometrie: Theorie und Anwendung auf das Experiment", Ph.D. thesis (Universität Augsburg, 2016).

[55] R. Messina, P. A. Maia Neto, B. Guizal, and M. Antezza, "Casimir interaction between a sphere and a grating", Phys. Rev. A **92**, 062504 (2015), DOI: 10.1103/PhysRevA.92.062504.

[56] M. Hartmann, G.-L. Ingold, and P. A. Maia Neto, "Plasma versus Drude Modeling of the Casimir Force: Beyond the Proximity Force Approximation", Phys. Rev. Lett. **119**, 043901 (2017), DOI: 10.1103/PhysRevLett.119.043901.

[57] M. Hartmann, G.-L. Ingold, and P. A. Maia Neto, "Advancing numerics for the Casimir effect to experimentally relevant aspect ratios", Phys. Scr. **93**, 114003 (2018), DOI: 10.1088/1402-4896/aae34e.

[58] M. Hartmann, "Casimir effect in the plane-sphere geometry: Beyond the proximity force approximation", Ph.D. thesis (Universität Augsburg, 2018).

[59] B. Pailthorpe and W. Russel, "The retarded van der Waals interaction between spheres", J. Colloid Interface Sci. **89**, 563 –566 (1982), DOI: 10.1016/0021-9797(82)90208-9.

[60] W. B. Russel, D. A. Saville, and W. R. Schowalter, *Colloidal Dispersions*, Cambridge Monographs on Mechanics (Cambridge University Press, 1989), DOI: 10.1017/CBO9780511608810.

[61] C. Genet, A. Lambrecht, and S. Reynaud, "Casimir force and the quantum theory of lossy optical cavities", Phys. Rev. A **67**, 043811 (2003), DOI: 10.1103/PhysRevA.67.043811.

[62] G.-L. Ingold and A. Lambrecht, "Casimir effect from a scattering approach", Am. J. Phys. **83**, 156–162 (2015), DOI: 10.1119/1.4896197.

[63] R. Guérout, G.-L. Ingold, A. Lambrecht, and S. Reynaud, "Accounting for Dissipation in the Scattering Approach to the Casimir Energy", Symmetry **10** (2018), DOI: 10.3390/sym10020037.

[64] M. Nieto-Vesperinas, *Scattering and Diffraction in Physical Optics*, 2nd (World Scientific, 2006), DOI: 10.1142/5833.

[65] A. I. Alekseev and Y. P. Nikitin, "Quantization of the Electromagnetic Field in a Dispersive Medium", Sov. Phys. JETP **23**, 608–614 (1966).

[66] M. Agu, "On Phenomenological Quantization of Electromagnetic Field in a Dispersive Medium", Japanese Journal of Applied Physics **18**, 2143–2156 (1979), DOI: 10.1143/jjap.18.2143.

[67] L. D. Landau, L. P. Pitaevskii, and E. Lifshitz, *Electrodynamics of Continuous Media 2nd Edition*, Vol. 8 (Pergamon Press, 1984).

[68] I. Brevik and K. A. Milton, "Casimir energies: Temperature dependence, dispersion, and anomalies", Phys. Rev. E **78**, 011124 (2008), DOI: 10.1103/PhysRevE.78.011124.

[69] K. A. Milton, J. Wagner, P. Parashar, and I. Brevik, "Casimir energy, dispersion, and the Lifshitz formula", Phys. Rev. D **81**, 065007 (2010), DOI: 10.1103/PhysRevD.81.065007.

[70] S. Weinberg, *The Quantum Theory of Fields*, Vol. 1 (Cambridge University Press, 1995), DOI: 10.1017/CBO9781139644167.

[71] F. Mandl and G. Shaw, *Quantum Field Theory, 2nd Edition* (Wiley, 2013).

[72] S. Souma and A. Suzuki, "Local density of states and scattering matrix in quasi-one-dimensional systems", Phys. Rev. B **65**, 115307 (2002), DOI: 10.1103/PhysRevB.65.115307.

[73] A. G. Akritas, E. K. Akritas, and G. I. Malaschonok, "Various proofs of Sylvester's (determinant) identity", Math. Comput. Simul. **42**, Sybolic Computation, New Trends and Developments, 585–593 (1996), DOI: https://doi.org/10.1016/S0378-4754(96)00035-3.

[74] S. J. Rahi, T. Emig, N. Graham, R. L. Jaffe, and M. Kardar, "Scattering theory approach to electrodynamic Casimir forces", Phys. Rev. D **80**, 085021 (2009), DOI: 10.1103/PhysRevD.80.085021.

[75] V. V. Nesterenko and I. G. Pirozhenko, "Lifshitz formula by a spectral summation method", Phys. Rev. A **86**, 052503 (2012), DOI: 10.1103/PhysRevA.86.052503.

[76] M. T. Jaekel and S. Reynaud, "Casimir force between partially transmitting mirrors", J. Phys. I France, 1395–1409 (1991), DOI: 10.1051/jp1:1991216.

[77] C. Genet, A. Lambrecht, and S. Reynaud, "Temperature dependence of the Casimir effect between metallic mirrors", Phys. Rev. A **62**, 012110 (2000), DOI: 10.1103/PhysRevA.62.012110.

[78] R. Guérout, A. Lambrecht, K. A. Milton, and S. Reynaud, "Derivation of the Lifshitz-Matsubara sum formula for the Casimir pressure between metallic plane mirrors", Phys. Rev. E **90**, 042125 (2014), DOI: 10.1103/PhysRevE.90.042125.

[79] J. Hu, R.-X. Xu, and Y. Yan, "Communication: Padé spectrum decomposition of Fermi function and Bose function", J. Chem. Phys. **133**, 101106 (2010), DOI: 10.1063/1.3484491.

[80] B. Spreng, P. A. Maia Neto, and G.-L. Ingold, "Plane-wave approach to the exact van der Waals interaction between colloid particles", J. Chem. Phys. **153**, 024115 (2020), DOI: 10.1063/5.0011368.

[81] C. F. Bohren and D. R. Huffman, *Absorption and Scattering of Light by Small Particles* (John Wiley & Sons, Ltd, 2007), DOI: 10.1002/9783527618156.

[82] A. Lambrecht and S. Reynaud, "Casimir force between metallic mirrors", Eur. Phys. J. D **8**, 309 (2000), DOI: 10.1007/s100530050041.

[83] V. Parsegian and G. H. Weiss, "Spectroscopic parameters for computation of van der waals forces", J. Colloid Interface Sci. **81**, 285–289 (1981), DOI: 10.1016/0021-9797(81)90325-8.

[84] P. J. van Zwol and G. Palasantzas, "Repulsive Casimir forces between solid materials with high-refractive-index intervening liquids", Phys. Rev. A **81**, 062 502 (2010), DOI: 10.1103/PhysRevA.81.062502.

[85] J. Fiedler et al., "Full-Spectrum High-Resolution Modeling of the Dielectric Function of Water", J. Phys. Chem. B **124**, PMID: 32208624, 3103–3113 (2020), DOI: 10.1021/acs.jpcb.0c00410.

[86] R. Buchner, J. Barthel, and J. Stauber, "The dielectric relaxation of water between 0 °C and 35 °C", Chem. Phys. Lett. **306**, 57–63 (1999), DOI: 10.1016/S0009-2614(99)00455-8.

[87] H. Ikezi, K. Schwarzenegger, A. L. Simons, A. L. Passner, and S. L. McCall, "Optical properties of expanded fluid mercury", Phys. Rev. B **18**, 2494–2499 (1978), DOI: 10.1103/PhysRevB.18.2494.

[88] T. Inagaki, E. T. Arakawa, and M. W. Williams, "Optical properties of liquid mercury", Phys. Rev. B **23**, 5246–5262 (1981), DOI: 10.1103/PhysRevB.23.5246.

[89] N. V. Smith, "Classical generalization of the Drude formula for the optical conductivity", Phys. Rev. B **64**, 155106 (2001), DOI: 10.1103/PhysRevB.64.155106.

[90] R. Esquivel-Sirvent and J. V. Escobar, "Casimir force between liquid metals", Europhys. Lett. **107**, 40004 (2014), DOI: 10.1209/0295-5075/107/40004.

[91] A.-F. Bitbol, A. Canaguier-Durand, A. Lambrecht, and S. Reynaud, "Pairwise summation approximation for Casimir potentials and its limitations", Phys. Rev. B **87**, 045413 (2013), DOI: 10.1103/PhysRevB.87.045413.

[92] J. Błocki, J. Randrup, W. Świątecki, and C. Tsang, "Proximity forces", Ann. Phys. **105**, 427–462 (1977), DOI: 10.1016/0003-4916(77)90249-4.

[93] A. Scardicchio and R. Jaffe, "Casimir effects: an optical approach I. Foundations and examples", Nuclear Physics B **704**, 552 –582 (2005), DOI: https://doi.org/10.1016/j.nuclphysb.2004.10.017.

[94] M Bordag and V Nikolaev, "Casimir force for a sphere in front of a plane beyond proximity force approximation", Journal of Physics A: Mathematical and Theoretical **41**, 164002 (2008), DOI: 10.1088/1751-8113/41/16/164002.

[95] G. Bimonte, "Going beyond PFA: A precise formula for the sphere-plate Casimir force", Europhys. Lett. **118**, 20002 (2017), DOI: 10.1209/0295-5075/118/20002.

[96] A Voronovich, "Small-slope approximation for electromagnetic wave scattering at a rough interface of two dielectric half-spaces", Waves in Random Media **4**, 337–367 (1994), DOI: 10.1088/0959-7174/4/3/008.

[97] P. A. Maia Neto, A. Lambrecht, and S. Reynaud, "Casimir effect with rough metallic mirrors", Phys. Rev. A **72**, 012115 (2005), DOI: 10.1103/PhysRevA.72.012115.

[98] Wolfram Research, Inc., *Mathematica, Version 11.1*, Champaign, IL, 2017.

[99] C. D. Fosco, F. C. Lombardo, and F. D. Mazzitelli, "Derivative expansion for the Casimir effect at zero and finite temperature in $d+1$ dimensions", Phys. Rev. D **86**, 045021 (2012), DOI: 10.1103/PhysRevD.86.045021.

[100] H. C. van de Hulst, *Light scattering by small particles* (Dover Publications, 1981).

[101] H. Weyl, "Ausbreitung elektromagnetischer Wellen über einem ebenen Leiter", Ann. Phys. **365**, 481–500 (1919), DOI: 10.1002/andp.19193652104.

[102] W. C. Chew, *Waves and Fields in Inhomogenous Media* (Wiley-IEEE Press, 1999).

[103] K. Kvien, "Angular spectrum representation of fields diffracted by spherical objects: physical properties and implementations of image field models", J. Opt. Soc. Am. A **15**, 636–651 (1998), DOI: 10.1364/JOSAA.15.000636.

[104] V. Henning, B. Spreng, M. Hartmann, G.-L. Ingold, and P. A. Maia Neto, "Role of diffraction in the Casimir effect beyond the proximity force approximation", J. Opt. Soc. Am. B **36**, C77–C87 (2019), DOI: 10.1364/JOSAB.36.000C77.

[105] R. Carminati, M. Nieto-Vesperinas, and J.-J. Greffet, "Reciprocity of evanescent electromagnetic waves", J. Opt. Soc. Am. A **15**, 706–712 (1998), DOI: 10.1364/JOSAA.15.000706.

[106] R. Messina and M. Antezza, "Scattering-matrix approach to Casimir-Lifshitz force and heat transfer out of thermal equilibrium between arbitrary bodies", Phys. Rev. A **84**, 042102 (2011), DOI: 10.1103/PhysRevA.84.042102.

[107] A. Canaguier-Durand, P. A. Maia Neto, A. Lambrecht, and S. Reynaud, "Erratum: Thermal Casimir effect for Drude metals in the plane-sphere geometry [Phys. Rev. A 82, 012511 (2010)]", Phys. Rev. A **83**, 039905 (2011), DOI: 10.1103/PhysRevA.83.039905.

[108] H. M. Nussenzveig, *Diffraction Effects in Semiclassical Scattering*, Montroll Memorial Lecture Series in Mathematical Physics (Cambridge University Press, 1992), DOI: 10.1017/CBO9780511599903.

[109] V. Khare and H. M. Nussenzveig, "Theory of the Rainbow", Phys. Rev. Lett. **33**, 976–980 (1974), DOI: 10.1103/PhysRevLett.33.976.

[110] V. Khare, "Short-wavelength scattering of electromagnetic waves by a homogeneous dielectric sphere", Ph.D. thesis (University of Rochester, Rochester, NY, 1975).

[111] W. T. Grandy Jr, *Scattering of Waves from Large Spheres* (Cambridge University Press, 2000), DOI: 10.1017/CBO9780511524158.

[112] H. M. Nussenzveig, "High-Frequency Scattering by a Transparent Sphere. I. Direct Reflection and Transmission", J. Math. Phys. **10**, 82–124 (1969), DOI: 10.1063/1.1664764.

[113] H. Nussenzveig, "High-frequency scattering by an impenetrable sphere", Ann. Phys. **34**, 23–95 (1965), DOI: 10.1016/0003-4916(65)90041-2.

[114] B. Spreng, M. Hartmann, V. Henning, P. A. Maia Neto, and G.-L. Ingold, "Proximity force approximation and specular reflection: Application of the WKB limit of Mie scattering to the Casimir effect", Phys. Rev. A **97**, 062504 (2018), DOI: 10.1103/PhysRevA.97.062504.

[115] Z. Shun and P. McCullagh, "Laplace Approximation of High Dimensional Integrals", J. R. Stat. Soc. Series B Stat. Methodol. **57**, 749–760 (1995).

[116] E. Evangelou, Z. Zhu, and R. L. Smith, "Estimation and prediction for spatial generalized linear mixed models using high order Laplace approximation", J. Stat. Plan. Inference **141**, 3564–3577 (2011), DOI: 10.1016/j.jspi.2011.05.008.

[117] R. H. Schafer and R. G. Kouyoumjian, "Higher order terms in the saddle point approximation", Proc. IEEE **55**, 1496–1497 (1967).

[118] C. Bender and S. Orszag, *Advanced Mathematical Methods for Scientists and Engineers I: Asymptotic Methods and Perturbation Theory*, Advanced Mathematical Methods for Scientists and Engineers (Springer, 1999), DOI: 10.1007/978-1-4757-3069-2.

[119] I. Florescu, *Probability and Stochastic Processes* (Wiley, 2014).

[120] G. Bimonte, "Exact Casimir interaction of perfectly conducting three-spheres in four euclidean dimensions", Phys. Rev. D **94**, 085021 (2016), DOI: 10.1103/PhysRevD.94.085021.

[121] E. Palik, *Handbook of Optical Constants of Solids*, Academic Press handbook series (Academic Press, 1998).

[122] A. O. Sushkov, W. J. Kim, D. A. R. Dalvit, and S. K. Lamoreaux, "Observation of the thermal Casimir force", Nat. Phys. **7**, 230–233 (2011), DOI: 10.1038/nphys1909.

[123] R. S. Decca et al., "Tests of new physics from precise measurements of the Casimir pressure between two gold-coated plates", Phys. Rev. D **75**, 077101 (2007), DOI: 10.1103/PhysRevD.75.077101.

[124] C.-C. Chang et al., "Gradient of the Casimir force between Au surfaces of a sphere and a plate measured using an atomic force microscope in a frequency-shift technique", Phys. Rev. B **85**, 165443 (2012), DOI: 10.1103/PhysRevB.85.165443.

[125] A. A. Banishev, G. L. Klimchitskaya, V. M. Mostepanenko, and U. Mohideen, "Demonstration of the Casimir Force between Ferromagnetic Surfaces of a Ni-Coated Sphere and a Ni-Coated Plate", Phys. Rev. Lett. **110**, 137401 (2013), DOI: 10.1103/PhysRevLett.110.137401.

[126] J. L. Garrett, D. A. T. Somers, and J. N. Munday, "Measurement of the Casimir Force between Two Spheres", Phys. Rev. Lett. **120**, 040401 (2018), DOI: 10.1103/PhysRevLett.120.040401.

[127] W. J. Kim, A. O. Sushkov, D. A. R. Dalvit, and S. K. Lamoreaux, "Surface contact potential patches and Casimir force measurements", Phys. Rev. A **81**, 022505 (2010), DOI: 10.1103/PhysRevA.81.022505.

[128] G.-L. Ingold, A. Lambrecht, and S. Reynaud, "Quantum dissipative Brownian motion and the Casimir effect", Phys. Rev. E **80**, 041113 (2009), DOI: 10.1103/PhysRevE.80.041113.

[129] A. Weber and H. Gies, "Nonmonotonic Thermal Casimir Force from Geometry-Temperature Interplay", Phys. Rev. Lett. **105**, 040403 (2010), DOI: 10.1103/PhysRevLett.105.040403.

[130] C. P. Boyer, E. G. Kalnins, and W. Miller, "Symmetry and separation of variables for the Helmholtz and Laplace equations", Nagoya Math. J. **60**, 35—80 (1976), DOI: 10.1017/S0027763000017165.

[131] F. Bornemann, "On the numerical evaluation of Fredholm determinants", Math. Comp. **79**, 871–915 (2010), DOI: 10.1090/S0025-5718-09-02280-7.

[132] Q. I. Rahman and G. Schmeisser, "Characterization of the speed of convergence of the trapezoidal rule", Numer. Math. **57**, 123–138 (1990), DOI: 10.1007/BF01386402.

[133] J. A. C. Weideman, "Numerical Integration of Periodic Functions: A Few Examples", Am. Math. Mon. **109**, 21–36 (2002), DOI: 10.1080/00029890.2002.11919836.

[134] J. P. Boyd, "Exponentially convergent Fourier-Chebshev quadrature schemes on bounded and infinite intervals", J. Sci. Comput. **2**, 99–109 (1987), DOI: 10.1007/BF01061480.

[135] S. van der Walt, S. C. Colbert, and G. Varoquaux, "The NumPy Array: A Structure for Efficient Numerical Computation", Comput. Sci. Eng. **13**, 22–30 (2011), DOI: 10.1109/MCSE.2011.37.

[136] P. Virtanen et al., "SciPy 1.0: fundamental algorithms for scientific computing in Python", Nat. Methods **17**, 261–272 (2020), DOI: 10.1038/s41592-019-0686-2.

[137] S. K. Lam, A. Pitrou, and S. Seibert, "Numba: A LLVM-Based Python JIT Compiler", in Proceedings of the Second Workshop on the LLVM Compiler Infrastructure in HPC, LLVM '15 (2015), DOI: 10.1145/2833157.2833162.

[138] M. Hartmann and G.-L. Ingold, "CaPS: Casimir Effect in the Plane-Sphere Geometry", J. Open Source Softw. **5**, 2011 (2020), DOI: 10.21105/joss.02011.

[139] N. M. Temme, *Asymptotic Methods for Integrals* (World Scientific, 2014), DOI: 10.1142/9195.

[140] I. Bogaert, B. Michiels, and J. Fostier, "$\mathcal{O}(1)$ Computation of Legendre Polynomials and Gauss–Legendre Nodes and Weights for Parallel Computing", SIAM J. Sci. Comput. **34**, C83–C101 (2012), DOI: 10.1137/110855442.

[141] D. Mitchell and P Richmond, "A general formalism for the calculation of free energies of inhomogeneous dielectric and electrolytic systems", J. Colloid and Interface Sci. **46**, 118–127 (1974), DOI: 10.1016/0021-9797(74)90031-9.

[142] J. Mahanty and B. Ninham, *Dispersion Forces*, Colloid Science: a series of monographs (Academic Press, 1976).

[143] P. A. Maia Neto et al., "Scattering theory of the screened Casimir interaction in electrolytes", Eur. Phys. J. D **73**, 178 (2019), DOI: 10.1140/epjd/e2019-100225-8.

[144] P. Thiyam et al., "Ice Particles Sink below the Water Surface Due to a Balance of Salt, van der Waals, and Buoyancy Forces", J. Phys. Chem. C **122**, 15311–15317 (2018), DOI: 10.1021/acs.jpcc.8b02351.

[145] V. Esteso et al., "Trapping of Gas Bubbles in Water at a Finite Distance below a Water–Solid Interface", Langmuir **35**, 4218–4223 (2019), DOI: 10.1021/acs.langmuir.8b04176.

[146] C. D. Fosco, F. C. Lombardo, and F. D. Mazzitelli, "Fourth order perturbative expansion for the Casimir energy with a slightly deformed plate", Phys. Rev. D **86**, 125018 (2012), DOI: 10.1103/PhysRevD.86.125018.

[147] *NIST Digital Library of Mathematical Functions*, http://dlmf.nist.gov/, Release 1.0.26 of 2020-03-15, F. W. J. Olver, A. B. Olde Daalhuis, D. W. Lozier, B. I. Schneider, R. F. Boisvert, C. W. Clark, B. R. Miller, B. V. Saunders, H. S. Cohl, and M. A. McClain, eds.

[148] B. C. Berndt and B. P. Yeap, "Explicit evaluations and reciprocity theorems for finite trigonometric sums", Adv. Appl. Math. **29**, 358–385 (2002), DOI: 10.1016/S0196-8858(02)00020-9.

List of Abbreviations

AE	**A**symptotic **E**xpansion, see chapter 6
DA	**D**eraguin **A**pproximation, see section 4.1
DE	**D**erivative **E**xpansion, see section 4.2
in	**in**cident (plane wave)
LO	**L**eading **O**rder
MSD	**M**atsubara **S**pectrum **D**ecomposition, see section 2.6
NTLO	**N**ext-**T**o-**L**eading-**O**rder
NNTLO	**N**ext-**T**o-**N**ext-**T**o-**L**eading-**O**rder
PFA	**P**roximity **F**orce **A**pproximation, see section 4.1
PR	**P**erfect **R**eflector
PSD	**P**adé **S**ectrum **D**ecomposition, see section 2.7
sc	**sc**attered (plane wave)
sp	**s**addle **p**oint
TE	**T**ransverse **E**lectric, see equation (3.1)
TM	**T**ransverse **M**agnetic, see equation (3.1)
WKB	**W**entzel–**K**ramers–**B**rillouin (approximation), see section 5.4

List of Symbols

Physical constants

c	speed of light in vacuum	$2.997\,924\,58 \times 10^{8}\,\mathrm{m\,s^{-1}}$
$\hbar$	reduced Planck constant	$1.054\,571\,817 \times 10^{-34}\,\mathrm{J\,s} = 6.582\,119\,569 \times 10^{-16}\,\mathrm{eV\,s}$
k_B	Boltzmann constant	$1.380\,649 \times 10^{-23}\,\mathrm{J\,K^{-1}} = 8.617\,333\,262\,145 \times 10^{-5}\,\mathrm{eV\,K^{-1}}$
ε_0	vacuum permittivity	$8.854\,187\,812\,8(13) \times 10^{-12}\,\mathrm{F\,m^{-1}}$
μ_0	vacuum permeability	$1.256\,637\,062\,12(19) \times 10^{-6}\,\mathrm{H\,m^{-1}}$

Special functions

$I_\nu(x)$	modified Bessel function of the first kind, see appendix A.1
$K_\nu(x)$	modified Bessel function of the second kind, see appendix A.1
$\mathrm{Li}_s(x)$	polylogarithm of order s, see appendix A.3
$P_\ell(x)$	ordinary Legendre function, see equation (A.8)
$P_\ell^m(x)$	associated Legendre function, see appendix A.2
$Y_\ell^m(\theta, \varphi)$	spherical harmonics, see equation F.3
$\Gamma(z)$	Gamma function, see [147, §5]
$\pi_\ell(x)$, $\tau_\ell(x)$	angular functions, see equation (5.4) and appendix A.4

Typographical symbols

$f \sim g$	function f is asymptotic to function g
$x \propto y$	x is proportional to y
$f\|_\mathrm{sp}$	evaluation of the function f at the saddle-point manifold (6.16)
$\sum_{n=0}^{\infty}{}'$	primed Matsubara sum, see equation (2.53)

Calligraphic symbols

$\mathcal{A}$, $\mathcal{B}$	coefficients of the Mie coefficients in the zero-frequency limit, see Eq. (5.22) and Tab. 5.1
$\mathcal{F}$	Casimir free energy, see equations (2.44) and (2.52)
$\mathcal{F}_\mathrm{PP}$	Casimir free energy per unit area between parallel planes, see equation (3.29)
$\mathcal{K}$	imaginary wave number, $\mathcal{K} = iK = \sqrt{\varepsilon_\mathrm{m}}\xi/c$
$\mathcal{L}$	center-to-center distance in sphere-sphere geometry, $\mathcal{L} = L + R_1 + R_2$
$\mathcal{M}$	round-trip operator, see equation (2.41)
$\mathcal{R}$	reflection operator, see round-trip operator $\mathcal{M}$
$\mathcal{T}$	translation operator, see round-trip operator $\mathcal{M}$

Greek symbols

$\varepsilon(\omega)$	dielectric function, see section 3.2
ε_{m}	dielectric function of the medium
$\hat{\boldsymbol{\epsilon}}_p$	plane-wave polarization vector, see equation (2.11)
κ	$\kappa = \sqrt{\mathcal{K}^2 + k^2}$
ϕ	plane-wave propagation direction with respect to the z-axis, $K_z = \phi k_z$
λ_T	thermal wavelength, $\lambda_T = \hbar c / k_{\mathrm{B}} T$
ξ	imaginary frequency, $\xi = -i\omega$
ξ_n	Matsubara frequency, $\xi_n = 2\pi n k_{\mathrm{B}} T / \hbar$ for $n \in \mathbb{Z}$
Θ	scattering angle
ω	(angular) frequency
χ	angle between scattering and Fresnel plane

Latin symbols

a_ℓ, b_ℓ	Mie coefficients, see equation (5.18)
A, B, C, D	polarization transformation coefficients, see equations (5.10) and (5.15)
A_{eff}	effective Hamaker parameter, see equations (8.4) and (8.5)
$\mathbf{B}$	magnetic field
E	Casimir energy, $E = \mathcal{F}(T = 0)$
$\mathbf{E}$	electric field
F	Casimir force, $F = -\partial\mathcal{F}/\partial L$
F_{PP}	Casimir pressure between parallel planes, see equation (3.30)
F'	Casimir force gradient, $F' = \partial F/\partial L = -\partial^2\mathcal{F}/\partial L^2$
$\mathbf{K}$	wave vector, $\mathbf{K} = (K_x, K_y, K_z)$
K	wave number, magnitude of the wave vector $\mathbf{K}$, $K = \lvert\mathbf{K}\rvert$
$\mathbf{k}$	projection of $\mathbf{K}$ onto the x-y-plane, $\mathbf{k} = (K_x, K_y, 0)$
k	magnitude of the wave vector $\mathbf{k}$, $k = \lvert\mathbf{k}\rvert$
k_z	modulus of the wave vector's z-component $k_z = \lvert K_z\rvert$
ℓ	multipole order, see spherical harmonics $Y_\ell^m(\theta, \varphi)$
L	surface-to-surface distance
m	azimuthal number, see spherical harmonics $Y_\ell^m(\theta, \varphi)$
p	polarization
R	sphere radius
$\mathbf{R}$	spatial coordinates, $\mathbf{R} = (x, y, z)$
R_{eff}	effective radius in the sphere-sphere geometry, $R_{\mathrm{eff}} = R_1 R_2/(R_1 + R_2)$
r_p	Fresnel coefficients, see section 3.1
S_1, S_2	Mie scattering amplitudes, see equation (5.3)
$\tilde{S}_1$, $\tilde{S}_2$	scaled Mie scattering amplitudes in the zero-frequency limit, see Eq. (5.26)
s_1, s_2	coefficients for the WKB correction, see equation (5.34)
$\mathbf{S}$	scattering matrix, see equation (2.18)
T	temperature
$\mathbf{T}$	transfer matrix, see equation (2.24)
u	dimensionless parameter in the sphere-sphere geometry, $u = R_1 R_2/(R_1 + R_2)^2$

Acknowledgements

First of all, I would like to thank my advisor Gert-Ludwig Ingold for giving me the opportunity to do my PhD with him. He taught me a lot in how to approach physical problems and numerical computation with python.

I want to thank Paulo Maia Neto for the hospitality during my research visits at the UFRJ, Rio de Janeiro. His experience in research and our discussions have taught me a lot.

Special thanks goes to Vinicius Henning with whom I closely collaborated during my stay in Rio de Janeiro and his visit to our group in Augsburg. Thanks for keeping me motivated. During our time together he has become a very good friend and I am grateful that he introduced me to Amanda.

I also want to thank Prof. Dr. Thilo Kopp for examining this thesis and Prof. Dr. Ulrich Eckern and Prof. Dr. Hubert Krenner for being part of the oral examination board.

I would like to thank my former and current group members, Eva Geiger, Peter Hänggi, Peter Talkner, Wolfgang Häusler, Sergey Denisov, Luca Magazzú, Juan Jaramillo, Michael Hartmann, Alexander Geiseler, Katharina Kopper, Fabian Pauly, Leon Martin, Werner Schosser, Tanja Schoger, and also the former and current group members of TP2, Marion Amling, Ulrich Eckern, Klaus Ziegler, Andreas Sinner, Michael Dzierzawa, Sebastian Tölle, Wilhelm Appelt, Andreas Weh, Andreas Prinz-Zwick, Christian Schiegg for providing a productive and pleasant atmosphere at the institute. Moreover, I want to thank Ralf Utermann for technical support.

I gratefully acknowledge financial support from the German Academic Exchange Service (DAAD) on my two research visits at the UFRJ in Rio de Janeiro.

A huge thanks goes to Vinicius Henning and Amanda Nicotina for the careful proof reading of this work.

Last but not least, I would like to thank my family and my girlfriend Amanda for their love and constant support, in particular during the dark times of writing this thesis.